

**UNIVERSITÀ DEGLI STUDI DI GENOVA**

**FACOLTÀ DI INGEGNERIA**



**CORSO DI LAUREA IN INGEGNERIA MECCANICA  
AERONAUTICA**

**DICAT – Dipartimento di Ingegneria delle Costruzioni, dell’Ambiente e  
del Territorio**

**TESI DI LAUREA IN FLUIDODINAMICA AVANZATA**

**Large-Eddy Simulations of Turbulent Channel  
Flows Over Rough Patches**

**Relatori: Prof. Ugo Piomelli & Prof. Alessandro Bottaro**

**Allievo: Roberto Zonza**

Anno Accademico 2011/2012  
Genova, Marzo 2012

**QUEEN'S UNIVERSITY**

**FACOLTY OF ENGINEERING AND APPLIED  
SCIENCE**



**MCLAUGHLIN HALL – Department of Mechanical and Materials  
Engineering**

**Large-Eddy Simulations of Turbulent Channel  
Flows Over Rough Patches**

**by**

**Roberto Zonza**

Kingston, Ontario, Canada

# Abstract

In this thesis we proposed to carry out large-eddy simulations, to study the effects of local roughness in turbulent open channel flows.

At first, we summarized the theory of turbulent channel flows, which is at the base of this work. Then, the current knowledge about roughness is presented and discussed widely, comparing laboratory and atmospheric rough-wall studies within a single framework.

After that, we discuss our sand-grain roughness model, with the no-slip boundary condition modeled by an immersed boundary method. The properties and accuracies of the scheme are studied, the roughness model is validated, and the spatial-resolution requirements are determined. The model is applied to open channel flow, with simulations carried out underlining the effects of two parameters: the roughness height and the geometry of the rough and smooth patches.

Finally, results are presented: the roughness effects are limited to the roughness sublayer; its blockage effect extends only to  $y = d$  in the mean flow; the roughness significantly affects the inner-layer quantities like the friction velocity  $u_\tau$  and the friction coefficient  $C_f$ , while the local Reynolds number, the outer-layer mean velocity, as well as the Reynolds stresses beyond the roughness sublayer, are not sensitive to the roughness. The comparison between  $\tau_w$  from momentum balance and  $\tau_w$  from the log law assumption matches everywhere, except in the smooth-rough and rough-smooth transition regions where  $\tau_w$  from the log law can't capture the local variation of flow quantities close to the wall, and thus the log law is not valid. Studying mean velocity profiles for the patch cases at different  $x$  locations, we observed the influence of the number of patches: while low roughness height cases are not influenced by this parameter, when the roughness is higher the 8 patch case mean velocity profile, above smooth regions, is lower than the the corresponding 2 and 4 patch cases within the buffer layer, thus the influence of rough patch frequency more significantly affects the ability of the flow to adapt from rough to smooth than from smooth to rough and, under this conditions, the critical number of patches is between 4 and 8.

# Prefazione

Per realizzare questa tesi mi sono recato alla Queen's University, Kingston, Ontario, Canada, in particolare presso McLaughlin Hall, Department of Mechanical and Materials Engineering, dove ho lavorato come ricercatore sotto la supervisione del Prof. Ugo Piomelli, per una durata complessiva di 6 mesi.

Lo scopo che ci siamo proposti è stato quello di effettuare uno studio numerico, tramite l'utilizzo di Large-Eddy Simulations, su rugosità localizzata all'interno di un canale aperto attraversato da un flusso in regime turbolento. La rugosità è, infatti, un importante parametro che influenza numerosi applicazioni in fluidodinamica; in generale, quando un flusso lambisce una parete rugosa, il flusso stesso è alterato in maniera difficile da prevedere. A causa delle sue caratteristiche impronte, per esempio, una pallina da golf può viaggiare molto più lontano di una versione liscia della stessa pallina: le impronte inducono turbolenza e ritardano la separazione dello strato limite, riducendo in questo modo la resistenza di forma che si genera.

Un esempio più ingegneristico sull'importanza della rugosità è quello delle palette di una turbina, dove la rugosità superficiale aumenta lo scambio termico e favorisce il raffreddamento delle palette, allungando loro la vita. Strati limite caratterizzati da rugosità sono tipici anche nei flussi geofisici: la superficie sottostante è quasi sempre rugosa, come nel caso di foreste, città o fondali marini, e questo può influenzare numerosi studi, come le previsioni meteorologiche.

Nella prima parte della tesi è riassunta la teoria dei flussi turbolenti in canale; il channel flow è un flusso di parete tipico di applicazioni ingegneristiche, ed è alla base di questa tesi. Dopo una breve descrizione del flusso, sono riportate e descritte le equazioni di bilancio di massa e di quantità di moto, che portano a definire la tensione di taglio di parete  $\tau_w$ , il coefficiente di attrito  $C_f$  e altri importanti parametri. Sono poi definite e analizzate le varie regioni di parete, con particolare attenzione all'outer layer dove la log-law è valida. In seguito, è analizzata l'influenza del numero di Reynolds sul flusso, in particolare sui profili di velocità media e sulle tensioni di Reynolds. Infine, vengono riportate considerazioni di natura energetica, definendo il bilancio dell'energia cinetica turbolenta e analizzando il comportamento dei termini di produzione, dissipazione, trasporto, diffusione e convezione nelle varie regioni di parete, al variare del numero di Reynolds.

Nel capitolo successivo la rugosità superficiale è introdotta e sono riportati le più recenti considerazioni e studi a riguardo: flussi turbolenti su superfici rugose sono stati studiati già a partire dai lavori di Hagen (1854) and Darcy (1857), che erano interessati alle perdite di pressione all'interno di condotti d'acqua. Tuttavia, durante l'ultimo secolo di ricerca, flussi su pareti rugose hanno ricevuto molta meno attenzione dei corrispondenti flussi su pareti lisce, il che è giustificabile col fatto che si è voluto prima studiare le condizioni di parete più semplici possibili, e solo in seguito introdurre complessità come rugosità, gradienti di pressione, curvature... Tuttavia, questa negligenza può aver oscurato il potenziale contributo della rugosità alla ricerca su flussi di parete, in generale. In questa sezione, infatti, è riportato un dettagliato studio di flussi turbolenti su pareti rugose, con particolare attenzione alle interazioni tra inner e outer layers; un modo di porre il problema è questo: pareti lisce e pareti rugose inducono essenzialmente alla stessa struttura turbolenta nell'outer layer, ovvero ad una regione con debole sforzo di taglio, pochi meccanismi di instabilità e debole produzione di energia cinetica turbolenta. Al contrario, vicino alla parete, dove lo sforzo di taglio e la generazione di turbolenza sono elevate, i due flussi

sono nettamente diversi e controllati da lunghezze di scala diverse. Come possono due diversi processi nell'energetico inner layer portare essenzialmente agli stessi risultati nel più passivo outer layer? In questa stessa sezione abbiamo anche descritto diversi tipi di superfici rugose che sono state usate in letteratura nel passato per modellizzare la rugosità cercando di introdurre il minor numero di parametri possibile.

Nel capitolo successivo viene presentata la formulazione numerica del problema: abbiamo implementato Large-Eddy Simulation (LES) con un dynamic sub-grid scale model, in cui un fractional time-step method (Chorin, 1968; Kim & Moin, 1985) e second-order central differencing sono usati per risolvere le equazioni di bilancio. Per quanto riguarda le condizioni al contorno, periodic boundary conditions sono usate nelle spanwise e streamwise directions, free-slip conditions nel limite superiore del canale e no-slip conditions alla parete, con l'utilizzo di un Immersed Boundary Method (IBM) nell'interfaccia tra fluido e rugosità superficiale.

Il modello è stato poi validato, concentrandosi in particolar modo sull'accuratezza spaziale e temporale dell'IBM; in primo luogo è stato studiato un canale 2D inclinato rispetto alla parete, per analizzare il comportamento dell'IBM quando il flusso al contorno non è allineato con le celle. Dopodichè abbiamo studiato l'accuratezza del modello in un flusso instazionario attorno ad un cilindro. Infine, abbiamo analizzato il flusso nel nostro open-channel con superficie rugosa, validando il modello e determinando i requisiti richiesti dalla griglia per avere una adeguata risoluzione della rugosità.

Infine, i risultati delle nostre simulazioni sono presentati nell'ultimo capitolo: dall'andamento in direzione streamwise della tensione di taglio di parete  $\tau_w$  e del coefficiente di attrito  $C_f$  abbiamo osservato elevate fluttuazioni in corrispondenza delle superfici rugose, dovute ad un problema di sampling: benchè gli ellissoidi generati col metodo di Scotti siano orientati in maniera casuale, esistono delle strutture favorevoli e ricorrenti; questo fenomeno può essere limitato incrementando il dominio in direzione spanwise o filtrando il segnale tramite trasformate wavelet. Confrontando  $\tau_w$  ottenuta dal bilancio di quantità di moto con  $\tau_w$  ottenuta dall'assunzione a priori della log law, si nota come le due funzioni siano in ottimo accordo ovunque eccetto nelle regioni di transizioni tra superficie rugosa e liscia (e viceversa), dove avvengono fenomeni locali complessi vicino alla parete, e la log law non è, quindi, più valida.

Studiando i profili di velocità media abbiamo osservato l'influenza del numero di patch: per bassa rugosità ( $h^+ = 20$ ) le simulazioni non sono influenzate da questo parametro, mentre per elevata rugosità ( $h^+ = 40$ ) il profilo di velocità per il caso con 8 patch si differenzia dai corrispondenti casi con 4 e 2 patch, permettendoci di concludere che la frequenza delle patch influenza maggiormente la capacità del flusso di adattarsi da rugoso a liscio che viceversa, e che, sotto queste condizioni, il numero critico di patch sia tra 4 e 8. In generale, gli effetti della rugosità sono limitati al sublayer rugoso; il suo effetto di ostruzione si estende solo fino a  $y = d$  nel flusso medio; la rugosità influenza significativamente le quantità dell' inner-layer come la velocità di attrito  $u_\tau$  e il coefficiente di attrito  $C_f$ , mentre il numero di Reynolds locale, la velocità media nell'outer-layer e le tensioni di Reynolds al di sopra del sublayer rugoso non sono sensibile alla rugosità.

## Acknowledgments

My special thanks go to Professor Ugo Piomelli for his guidance and his help in the achievement of this thesis. Besides, thanks to Professor Alessandro Bottaro, who gave me the possibility to know Professor Piomelli and join him in Canada for an incredible experience.

My gratitude also goes to the friends I met in McLaughlin Hall that made me feel like home: Carlo Scalo, Junlin Yuan, Mohammad Omidyeganeh, Matthew Ford, Wen Wu, Rayhaneh Banyassady and Amirreza Rouhi. In particular, a special thanks to Carlo Scalo, who taught me the code, and to Junlin Yuan, without whom I wouldn't surely have finished this thesis in only six months.

At last, I express my gratitude to my family: my parents, my grandmother and my brother Marco; for their support, understanding and tenderness through the duration of my studies.

# Table of Contents

|  |           |
|--|-----------|
| <b>1. INTRODUCTION .....</b>   | <b>1</b>  |
| <b>2. TURBULENT CHANNEL FLOW.....</b>                                      | <b>4</b>  |
| 2.1 A DESCRIPTION OF THE FLOW .....  | 4         |
| 2.2 THE BALANCE OF MEAN FORCES .....                                       | 5         |
| 2.3 THE NEAR-WALL SHEAR STRESS.....  | 7         |
| 2.4 MEAN VELOCITY PROFILES .....   | 9         |
| 2.4.1 <i>The law of the wall</i> .....                                     | 10        |
| 2.4.2 <i>The viscous sublayer</i> .....                                    | 11        |
| 2.4.3 <i>The log law</i> .....   | 12        |
| 2.4.4 <i>The velocity-defect law</i> .....                                 | 14        |
| 2.5 THE FRICTION LAW AND THE REYNOLDS NUMBER .....                         | 16        |
| 2.6 REYNOLDS STRESSES .....  | 20        |
| 2.7 LENGHTSCALES AND THE MIXING LENGTH .....                               | 25        |
| <b>3. EFFECT OF ROUGHNESS .....</b>  | <b>28</b> |
| 3.1 MEAN VELOCITY ABOVE THE ROUGHNESS SUBLAYER .....                       | 29        |
| 3.1.1 <i>Dimensional considerations and the logarithmic profile</i> .....  | 29        |
| 3.1.2 <i>Fully rough flow</i> .....  | 33        |
| 3.1.3. ' <i>K</i> '-Roughness.....   | 39        |
| 3.1.4. ' <i>D</i> '-Roughness.....   | 41        |
| 3.1.5 <i>Transitional Roughness</i> .....                                  | 44        |
| 3.2 TURBULENCE ABOVE THE ROUGHNESS SUBLAYER .....                          | 46        |
| 3.2.1 <i>Wall similarity</i> .....   | 47        |
| 3.2.2. <i>Turbulence velocity scales, length scales, and spectra</i> ..... | 50        |
| 3.2.3 <i>The attached-eddy hypothesis</i> .....                            | 55        |
| 3.2.4 <i>Observations of velocity variances</i> .....                      | 56        |
| 3.2.5 <i>Wake Intensity</i> .....  | 57        |
| 3.2.6 <i>Theoretical models</i> .....                                      | 57        |
| 3.3 FLOW CLOSE TO AND WITHIN THE ROUGHNESS .....                           | 59        |
| 3.3.1 <i>Mean velocity</i> .....   | 59        |
| 3.3.2 <i>Basic properties of the turbulence</i> .....                      | 62        |
| 3.3.3 <i>Measurement problems</i> .....                                    | 63        |
| 3.3.4 <i>Second-moment budgets</i> .....                                   | 64        |
| 3.4 ORGANIZED MOTION IN ROUGH-WALL BOUNDARY LAYERS.....                    | 68        |
| 3.4.1 <i>Two-point velocity correlation functions</i> .....                | 68        |

|   |            |
|---|------------|
| 3.4.2 Manifestations of organized motion.....                                     | 71         |
| 3.4.3 Inferred structure of the organized motion.....                             | 75         |
| <b>4. PROBLEM FORMULATION .....</b>   | <b>78</b>  |
| 4.1 GOVERNING EQUATIONS .....   | 78         |
| 4.2 SUB-GRID SCALE MODEL .....  | 79         |
| 4.3 TIME-ADVANCEMENT AND DISCRETIZATION .....                                     | 80         |
| 4.4 BOUNDARY CONDITIONS .....   | 82         |
| 4.5 IMMERSED BOUNDARY METHOD .....  | 83         |
| <b>5. MODEL VALIDATION .....</b>  | <b>85</b>  |
| 5.1 TILTED PLANE-CHANNEL FLOW .....   | 85         |
| 5.2 FLOW OVER A TWO-DIMENSIONAL CIRCULAR CYLINDER.....                            | 90         |
| 5.3 ROUGH-WALL CHANNEL FLOW.....  | 94         |
| <b>6. RESULTS .....</b>   | <b>99</b>  |
| 6.1 CASE SETUP .....  | 99         |
| 6.2 PATCHES GENERATION .....  | 100        |
| 6.3 PRELIMINARY CALCULATION .....   | 105        |
| 6.3.1 Calculation of zero-plane displacement $d$ .....                            | 105        |
| 6.3.2 Calculation of $\tau_w$ .....   | 106        |
| 6.4 DESCRIPTION OF THE FLOW .....   | 107        |
| 6.4.1 Streamwise development of $\tau_w$ and $C_f$ - smooth and rough cases ..... | 107        |
| 6.4.2 $\tau_w$ from the log law assumption .....                                  | 113        |
| 6.4.3 Streamwise development of $\tau_w$ and $C_f$ - patch cases .....            | 115        |
| 6.5 MEAN VELOCITY .....   | 126        |
| 6.6 REYNOLDS STRESSES .....   | 134        |
| 6.7 TURBULENT STRUCTURES .....  | 141        |
| 6.7.1 The $Q$ -criterion.....   | 146        |
| <b>7. CONCLUSIONS .....</b>   | <b>152</b> |
| <b>BIBLIOGRAPHY .....</b>   | <b>154</b> |



# 1. Introduction

Hydrodynamically rough boundary layers are found in many applications: dimples on golf balls, cholesterol in blood vessels, skyscraper-studded grids of a large city... In general when there's fluid flow over a rough surface, the flow is affected in ways that are challenging to predict. Because they are dimpled, for example, golf balls fly much farther than would a smooth version of the same ball. The dimples induce turbulence and delay the separation of the boundary layer that forms near the ball's surface thus reducing the drag (Fig. 1.1).

A more telling example of why roughness matters in engineering applications is turbine blades, where surface roughness improves heat transfer and decreases temperature of the turbine, extending the life of the blades. In that case, roughness has the same effect of ribs or pins, which have been largely studied in the past years (Fig. 1.2). On the other hand, roughness and accumulated debris could affect the performance of turbine blades and lead to a faster deterioration. To replace one blade of a power-generating turbine can cost up to a million dollars when considering lost flight time.

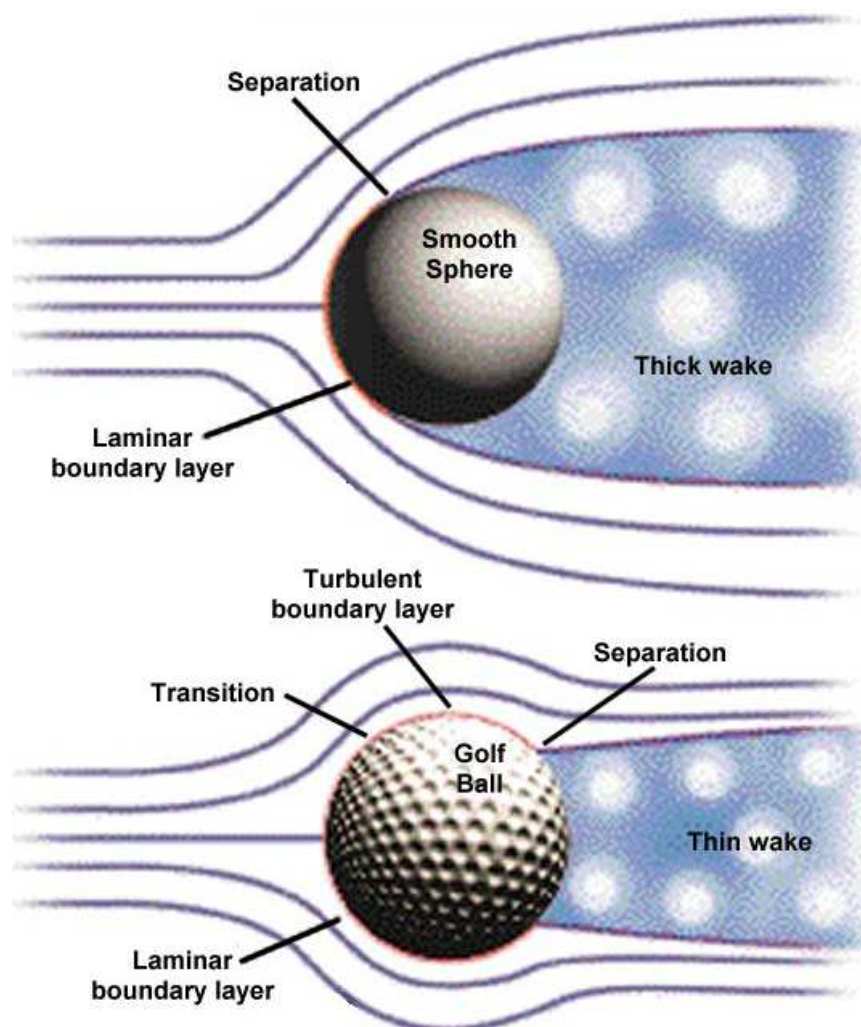


Fig. 1.1 - Effect of dimples in a sphere.

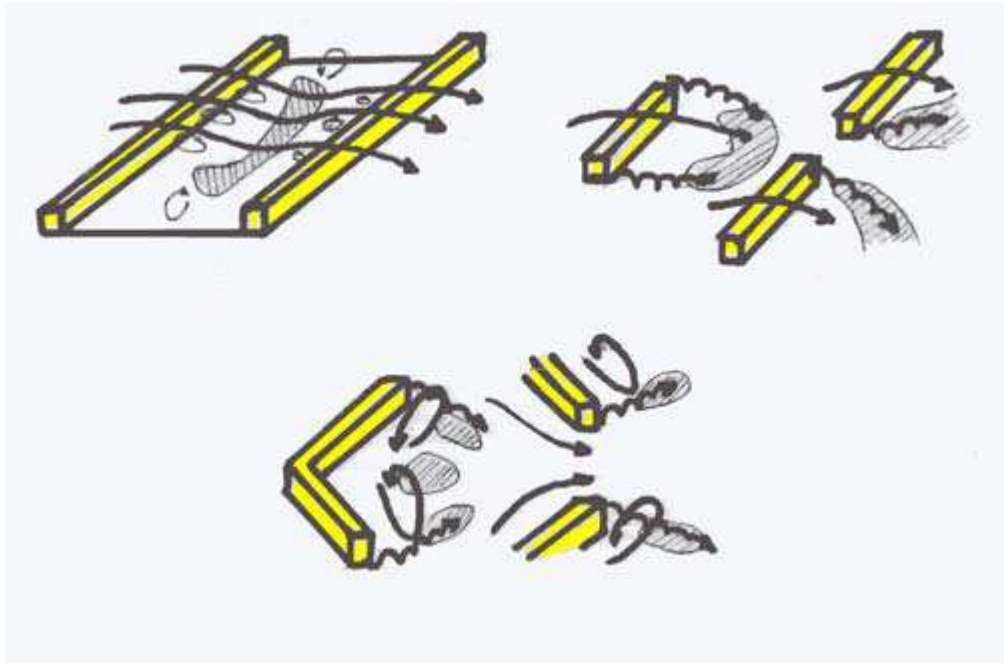


Fig. 1.2 - Effect of different rib configurations in turbine blades.

Rough boundary layers are usually the norm in geophysical flows, too: the underlying surface is almost always rough, like woods and cities (Fig. 1.3), and that can affect weather forecast, prediction of air pollution, dispersion of volatile materials...

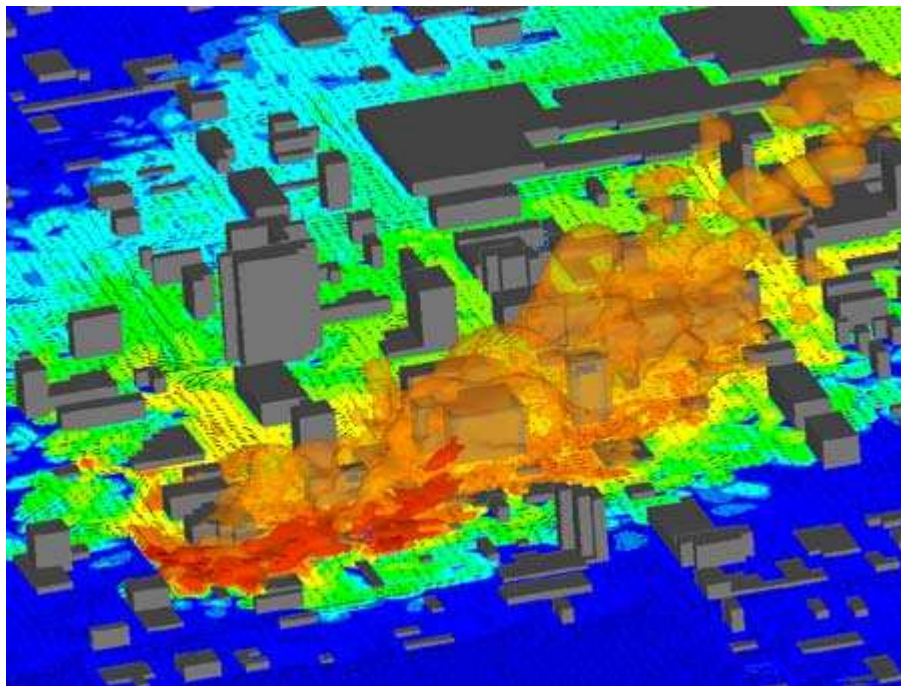


Fig. 1.3 - Flow visualization in an urban area.

In addition to the engineering and meteorological motivations for research on the rough-wall boundary layers, there are basic considerations: for a smooth-wall boundary layer, many investigations have been carried out to study the relative importance of the inner and outer regions of the boundary layer. Rough-wall boundary layers may help the understanding of this interaction, since both the smooth-wall and rough-wall boundary layers have essentially the same structure in the outer layer while, close to the wall, they are very different, and are controlled by different length scales: the roughness introduces a layer where the turbulent structure is significantly influenced by the viscous length scale and roughness length scales. So, if, more generally, the turbulence structure over a significant part of the layer is essentially unchanged in spite of significant alterations of the wall, this perspective would imply even less communication between the wall region and the outer region of a boundary layer than may be normally assumed.

To study the inner/outer layer interaction, a systematic study is required with both isolated and combined alterations of the inner and outer layer flow conditions, which leads to the idea of studying boundary layers with alternate rough and smooth patches developed along the streamwise direction.

Till present day, it is known that surface roughness, in addition to increasing the skin friction characteristics, has significant effects on mass and heat transport in the flow. Nevertheless, the effects of roughness on momentum, heat and mass transfer characteristics are not well understood. The problem of surface roughness is complicated by the fact that the geometry and length scales of roughness elements vary widely, from regularly spaced two-dimensional ribs to random three-dimensional roughness, such as manufacturing roughness and riverbeds. In the past, two-dimensional ribs were employed a lot, because, thanks to their geometrical simplicity, it was possible to apply direct numerical simulation (DNS) or large eddy simulation (LES) to thoroughly study the flow fields.

However, during the last years, more elaborate models of roughness has been used in simulations, thanks to development of the immersed boundary method: this gave an advantage in the knowledge of the physics involved, because it allows to know what's happening very near the wall, where in experiment it's difficult to insert a probe to measure the flow effects.

To look closely into the physical effect of surface roughness, we carry out large-eddy simulations with varying the roughness height and the length of the rough and smooth patches, to cover a wide range of values, enabling direct interaction of roughness disturbance and typical smooth-wall boundary layer.

Complete data of the flow field are provided from numerical simulations, and thus the mean and instantaneous properties of the flow can be studied in action.

## 2. Turbulent Channel Flow

In this chapter we summarize the theory of turbulent channel flow over smooth surface, which is at the very base of this thesis. Channel flow is a wall flow and it is often found in engineering applications, like flow through ducts or boundary layers.

### 2.1 A description of the flow

As sketched in Fig. 2.1, we consider the flow through a rectangular duct of height  $h = 2\delta$ . The duct is long ( $L/\delta \gg 1$ ) and has a large aspect ratio ( $b/\delta = 10$  in Fig. 2.1). The mean flow is predominantly in the axial direction ( $x$ ), with the mean velocity varying mainly in the cross-stream direction ( $y$ ). The bottom and the top walls are at  $y = 0$  and  $y = 2\delta$ , respectively, with the mid-plane being  $y = \delta$ . The extent of the channel in the spanwise ( $z$ ) direction is large compared with  $\delta$  so that (remote from the end walls) the flow is statistically independent of  $z$ . The centerline is defined by  $y = \delta, z = 0$ . The velocities in the three coordinate direction are  $(U, V, W)$  with fluctuations  $(u, v, w)$ . The mean cross-stream velocity  $W$  is zero.

Near the entry of the duct ( $x = 0$ ) there is a flow-development region. We, however, confine our attention to the fully developed region (large  $x$ ), in which velocity statistics no longer vary with  $x$ . Hence the fully developed channel flow being considered is statistically stationary and statistically one-dimensional, with velocities statistics depending on  $y$ . Experiments confirm the natural expectation that the flow is statistically symmetric about the mid-plane  $y = \delta$ ; the statistics of  $(U, V, W)$  at  $y$  are the same as those of  $(U, -V, W)$  at  $2\delta - y$ .

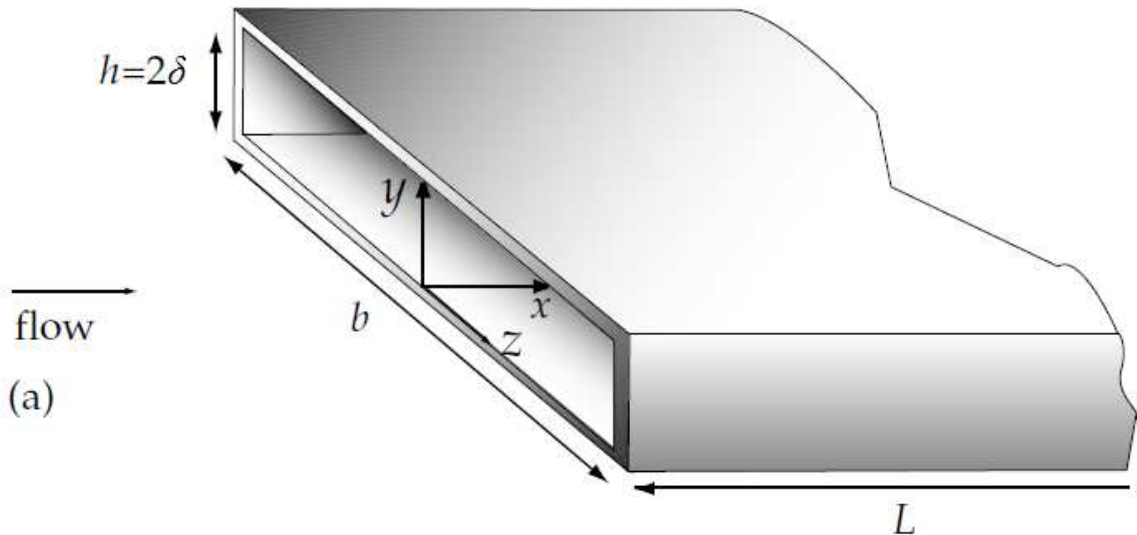


Fig. 2.1 - Sketch of channel flow.

The Reynolds numbers used to characterize the flow are

$$\text{Re} = (2\delta)\bar{U}/\nu \quad (2.1)$$

$$\text{Re}_0 = U_0\delta/\nu \quad (2.2)$$

where  $U_0$  is the centerline velocity,  $\bar{U}$  is the bulk velocity

$$\bar{U} = \frac{1}{\delta} \int_0^\delta \langle U \rangle dy \quad (2.3)$$

The flow is laminar for  $\text{Re} < 1350$  and fully turbulent for  $\text{Re} > 1800$ , although transitional effects are evident up to  $\text{Re} = 3000$ .

## 2.2 The balance of mean forces

The mean continuity equation reduces to

$$\frac{d\langle V \rangle}{dy} = 0 \quad (2.4)$$

since  $\langle W \rangle$  is zero,  $\langle U \rangle$  is independent of  $x$ . With the boundary condition  $\langle V \rangle_{y=0} = 0$ , this dictates that  $\langle V \rangle$  is zero for all  $y$ , so that the boundary condition at the top wall  $\langle V \rangle_{y=2\delta} = 0$  is satisfied.

The lateral mean-momentum equation reduces to

$$0 = -\frac{d\langle v^2 \rangle}{dy} - \frac{1}{\rho} \frac{d\langle p \rangle}{dy} \quad (2.5)$$

which, with the boundary condition  $\langle v^2 \rangle_{y=2\delta} = 0$ , integrates to

$$\langle v^2 \rangle + \frac{\langle p \rangle}{\rho} = \frac{p_w(x)}{\rho} \quad (2.6)$$

where  $p_w = \langle p(x, 0, 0) \rangle$  is the mean pressure on the bottom wall. An important deduction from this equation is that the mean axial pressure gradient is uniform across the flow:

$$\frac{d\langle p \rangle}{dx} = \frac{dp_w}{dx} \quad (2.7)$$

The axial mean-momentum equation,

$$0 = \nu \frac{d^2 \langle U \rangle}{dy^2} - \frac{d\langle uv \rangle}{dy} - \frac{1}{\rho} \frac{d\langle p \rangle}{dx} = 0 \quad (2.8)$$

can be written

$$\frac{d\tau}{dy} = \frac{dp_w}{dx} \quad (2.9)$$

where the total shear stress  $\tau(y)$  is

$$\tau = \rho v \frac{d\langle U \rangle}{dx} - \rho \langle uv \rangle \quad (2.10)$$

For this flow there is no mean acceleration, so the mean momentum equation (2.9) amounts to a balance of forces: the stress is balanced by the pressure gradient.

Since  $\tau$  is a function only of  $y$ , and  $p_w$  is a function only of  $x$ , it is evident from equation (2.9) that both the first member and the second one are constant. The solutions for  $\tau(y)$  and  $dp_w/dx$  can be written explicitly in terms of the wall shear stress

$$\tau_w = \tau(0) \quad (2.11)$$

Because  $\tau(y)$  is antisymmetric about the mid-plane, it follows that  $\tau(\delta)$  is zero; and at the top wall the stress is  $\tau(2\delta) = -\tau_w$ . Hence, the solution to equation (2.9) is

$$-\frac{dp_w}{dx} = \frac{\tau_w}{\delta} \quad (2.12)$$

and

$$\tau(y) = \tau_w \left( 1 - \frac{y}{\delta} \right) \quad (2.13)$$

The wall shear stress normalized by a reference velocity is called a skin-friction coefficient. On the basis of the centerline velocity and the bulk velocity we define

$$c_f = \tau_w / \left( \frac{1}{2} \rho U_0^2 \right) \quad (2.14)$$

$$C_f = \tau_w / \left( \frac{1}{2} \rho \bar{U}^2 \right) \quad (2.15)$$

To summarize: the flow is driven by the drop in pressure between the entrance and the exit of the channel. In the fully developed region there is a constant (negative) mean pressure gradient  $\partial \langle p \rangle / \partial x = dp_w/dx$ , which is balanced by the shear-stress gradient  $\partial \tau / \partial y = -\tau_w/\delta$ . For a given pressure gradient  $dp_w/dx$  and channel half-width  $\delta$ , the linear shear-stress profile is given by equations (2.12) and (2.13) independent of the fluid properties (for instance turbulent). Note that, if the flow is defined by  $\rho$ ,  $\delta$ ,  $v$  and  $dp_w/dx$ , then  $U_0$  and  $\bar{U}$  are not known a priori. Alternatively, in an experiment  $\bar{U}$  can be imposed and then the

pressure gradient is unknown. In both cases the skin-friction coefficient is not known a priori. Of course all these quantities are readily determined for laminar flow.

### 2.3 The near-wall shear stress

Figure 2.2 shows the mean velocity profiles obtained by Kim et al. (1987) from direct numerical simulations of fully developed turbulent channel flow at  $Re = 5600$  and  $Re = 13750$  (Reynolds bulk number, as defined in equation (2.1)). The objective of this and the next subsection is to explain and quantify these profiles.

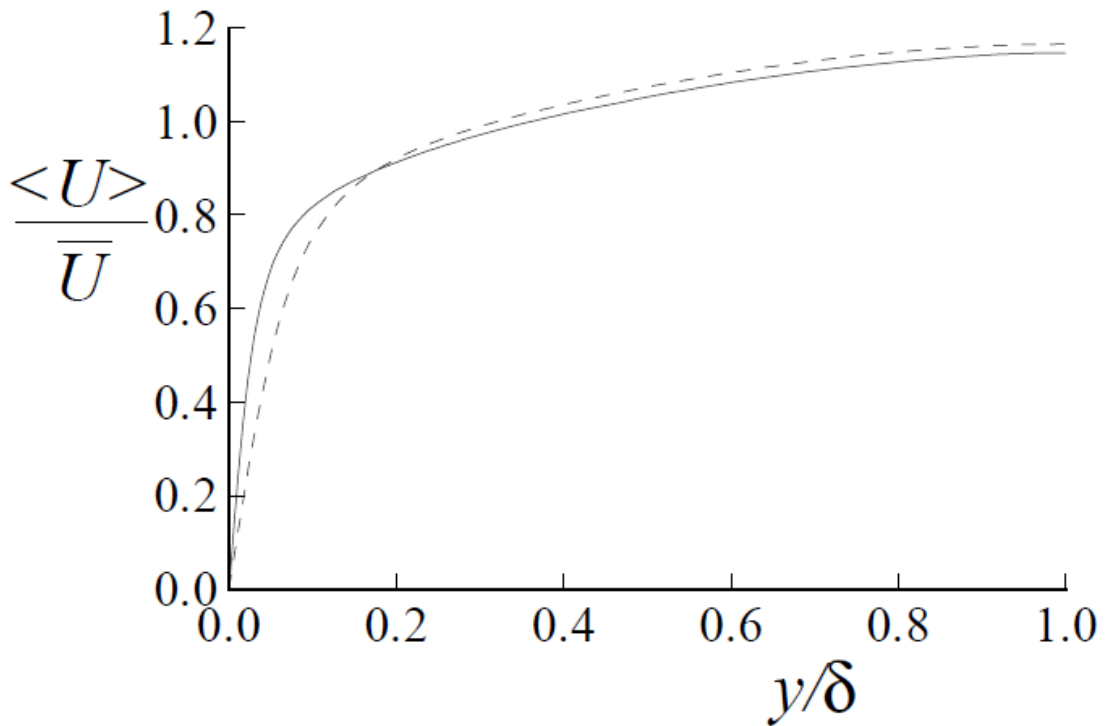


Fig. 2.2 - Mean velocity profiles in fully developed turbulent channel flow from the DNS of Kim et al. (1987); dashed line  $Re = 5600$ , solid line  $Re = 13750$ .

The total shear stress  $\tau(y)$  is the sum of the viscous stress and the Reynolds stress, as written in equation (2.10). At the wall, the boundary condition  $U(x,t) = 0$  dictates that all the Reynolds stresses are zero. Consequently the wall shear stress is due entirely to the viscous contribution,

$$\tau_w = \rho\nu \left( \frac{d\langle U \rangle}{dx} \right)_{y=0} \quad (2.16)$$

Profiles of the viscous and Reynolds shear stresses are shown in Figure 2.3.



The important observation that the viscous stress dominates at the wall is in contrast to the situation in free shear flows. There, at high Reynolds number, the viscous stresses are everywhere negligibly small compared with the Reynolds stresses. Also, near the wall, since the viscosity is an influential parameter, the velocity profiles depends upon the Reynolds number (as may be observed in Figure 2.2) and this is again in contrast to free shear flows.

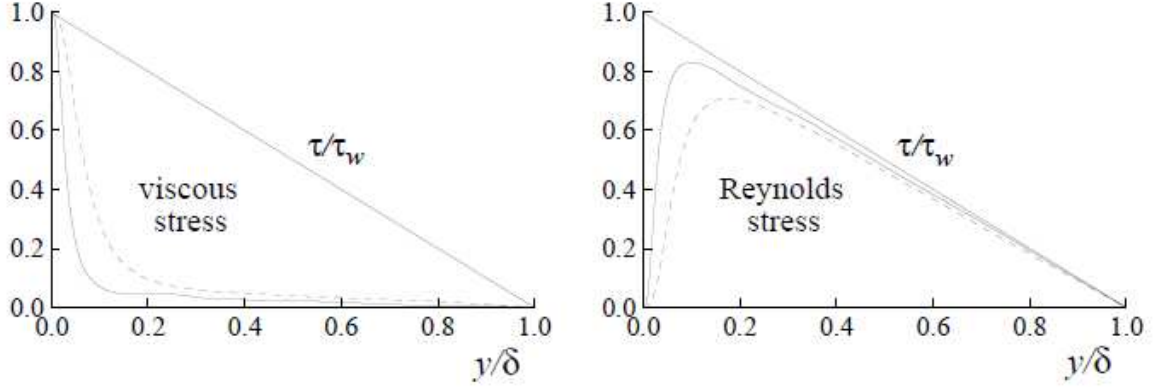


Fig. 2.3 - Profiles of viscous shear stress and Reynolds shear stress in turbulent channel flow. DNS data of Kim et al. (1987); dashed line  $Re = 5600$ , solid line  $Re = 13750$ .

It is evident that, close to the wall, the viscosity  $\nu$  and the wall shear stress  $\tau_w$  are important parameters. From these quantities (and  $\rho$ ) we define viscous scales that are appropriate velocity scales and lengthscales in the near-wall region. These are the friction velocity

$$u_\tau = \sqrt{\frac{\tau_w}{\rho}} \quad (2.17)$$

and the viscous lengthscale

$$\delta_\nu = \nu \sqrt{\frac{\rho}{\tau_w}} = \frac{\nu}{u_\tau} \quad (2.18)$$

The Reynolds number based on the viscous scales  $u_\tau \delta_\nu / \nu$  is identically unity, while the friction Reynolds number is defined by

$$Re_\tau = \frac{u_\tau \delta}{\nu} = \frac{\delta}{\delta_\nu} \quad (2.19)$$

The distance from the wall measured in viscous lengths (or wall units) is denoted by

$$y^+ = \frac{y}{\delta_\nu} = \frac{u_\tau y}{\nu} \quad (2.20)$$



Notice that  $y^+$  is similar to a local Reynolds number, so its magnitude can be expected to determine the relative importance of viscous and turbulent processes. In support of this supposition, Fig. 2.4 shows the fractional contributions to the total stress from the viscous and Reynolds stresses in the near-wall region of channel flow. When they are plotted against  $y^+$ , the profiles for the two Reynolds number almost collapse. The viscous contribution drops from 100% at the wall ( $y^+ = 0$ ) to 50% at  $y^+ \approx 12$  and is less than 10% by  $y^+ = 50$ .

Different regions, or layers, in the near-wall flow are defined on the basis of  $y^+$ . In the wall region  $y/\delta < 0.1$ , there is a direct effect of molecular viscosity on the shear stress; whereas, conversely, in the outer layer  $y/\delta > 0.1$  the direct effect of viscosity is negligible. Within the viscous wall region, in the viscous sublayer  $y^+ < 5$ , the Reynolds shear stress is negligible compared with the viscous stress. As the Reynolds number of the flow increases, the fraction of the channel occupied by the wall region decreases, since  $\delta_v/\delta$  varies as  $Re_\tau^{-1}$  (from equation 2.19).

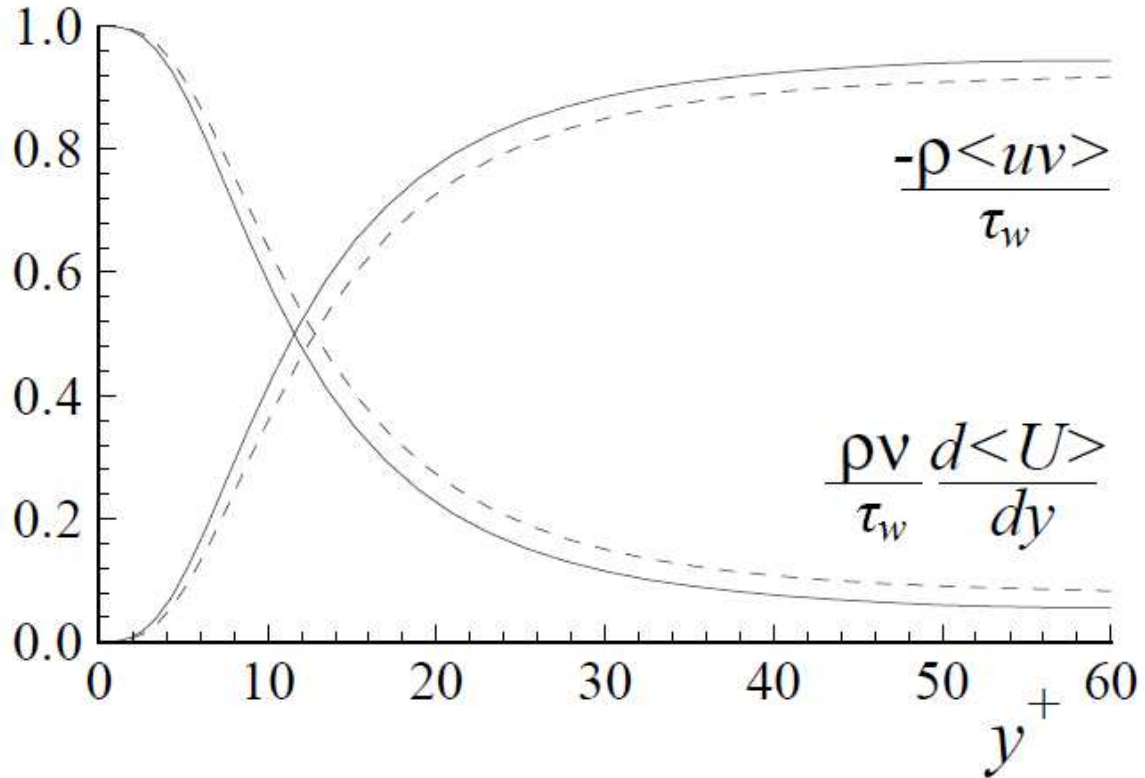


Fig. 2.4 - Profiles of the fractional contributions of the viscous and Reynolds stresses to the total stress. DNS data of Kim et al. (1987); dashed line  $Re = 5600$ , solid line  $Re = 13750$ .

## 2.4 Mean velocity profiles

Fully developed channel flow is completely specified by  $\rho$ ,  $\delta$ ,  $\nu$  and  $dp_w/dx$ ; or, equivalently, by  $\rho$ ,  $\delta$ ,  $\nu$  and  $u_\tau$ , since we have

$$u_\tau = \left( -\frac{\delta}{\rho} \cdot \frac{dp_w}{dx} \right)^{1/2} \quad (2.21)$$

There are just two independent non-dimensional groups that can be formed from  $\rho$ ,  $\delta$ ,  $\nu$ ,  $u_\tau$  and  $y$  and consequently the mean velocity profile can be written

$$\langle U \rangle = u_\tau \cdot F_0 \left( \frac{y}{\delta}, \text{Re}_\tau \right) \quad (2.22)$$

where  $F_0$  is a universal non-dimensional function to be determined.

While this approach to determining the mean velocity profile appears natural, it is, however, preferable to proceed somewhat differently. Instead of  $\langle U \rangle$ , we consider the velocity gradient  $d\langle U \rangle/dy$ , which is the dynamically important quantity. The viscous stress and the turbulence production, for example, are both determined by  $d\langle U \rangle/dy$ . Again on dimensional grounds,  $d\langle U \rangle/dy$  depends on just two non-dimensional parameters, so that (without any assumption) we can write

$$\frac{d\langle U \rangle}{dy} = \frac{u_\tau}{y} \cdot \Phi \left( \frac{y}{\delta_\nu}, \frac{y}{\delta} \right) \quad (2.23)$$

where  $\Phi$  is a universal non-dimensional function. The idea behind the choice of the two parameters is that  $\delta_\nu$  is the appropriate lengthscale in the wall region, while  $\delta$  is the appropriate scale in the outer layer. The relation

$$\left( \frac{y}{\delta_\nu} \right) / \left( \frac{y}{\delta} \right) = \text{Re}_\tau \quad (2.24)$$

shows, as is inevitable, that these two parameters contain the same information as  $y/\delta$  and  $\text{Re}_\tau$  (equation 2.22).

#### 2.4.1 The law of the wall

Prandtl (1925) postulated that, at high Reynolds number, close to the wall ( $y/\delta \ll 1$ ) there is an inner layer in which the mean velocity profile is determined by the viscous scale, independent of  $\delta$  and  $U_0$ . Mathematically, this implies that the function  $\Phi(y/\delta_\nu, y/\delta)$  in equation 2.23 tends asymptotically to a function of  $y/\delta_\nu$  only, as  $y/\delta$  tends to zero, so that equation 2.23 becomes

$$\frac{d\langle U \rangle}{dy} = \frac{u_\tau}{y} \cdot \Phi_I \left( \frac{y}{\delta_\nu} \right) \quad \text{for } y/\delta \ll 1 \quad (2.25)$$

where

$$\Phi_I\left(\frac{y}{\delta_\nu}\right) = \lim_{y/\delta \rightarrow 0} \Phi\left(\frac{y}{\delta_\nu}, \frac{y}{\delta}\right) \quad (2.26)$$

With  $y^+ = y/\delta_\nu$  and  $u^+(y^+)$  defined by

$$u^+ = \frac{\langle U \rangle}{u_\tau} \quad (2.27)$$

equation (2.25) can alternatively be written

$$\frac{du^+}{dy^+} = \frac{1}{y^+} \cdot \Phi_I(y^+) \quad (2.28)$$

The integral of equation (2.28) is the law of the wall:

$$u^+ = f_w(y^+) \quad (2.29)$$

where

$$f_w(y^+) = \int_0^{y^+} \frac{1}{y'} \cdot \Phi_I(y') dy' \quad (2.30)$$

The important point is not equation (2.30), but the fact that (according to Prandtl's hypothesis)  $u^+$  depends solely on  $y^+$  for  $y/\delta \ll 1$ .

For Reynolds numbers not too close to transition, there is abundant experimental verification that the function  $f_w(y^+)$  can be determined for small and large values of  $y^+$ .

#### 2.4.2 The viscous sublayer

The no-slip condition  $\langle U \rangle_{y=0}$  corresponds to  $f_w(0) = 0$ , while the viscous stress law at the wall, equation (2.16), yields for the derivative

$$f'_w(0) = 1 \quad (2.31)$$

Note that this is simply a result of the normalization by the viscous scales. Hence, the Taylor-series expansion for  $f_w(y^+)$  for small  $y^+$  is

$$f_w(y^+) = y^+ + O(y^{+2}) \quad (2.32)$$

In fact, closer examination reveals that, after the linear term, the next non-zero term is of order  $y^{+4}$ .

Figure 2.5 shows the profiles of  $u^+$  in the near-wall region obtained from direct numerical simulations. The departures from the linear relation  $u^+ = y^+$  are negligible in the viscous sublayer ( $y^+ < 5$ ), but are significant (greater than 25%) for  $y^+ > 12$ .

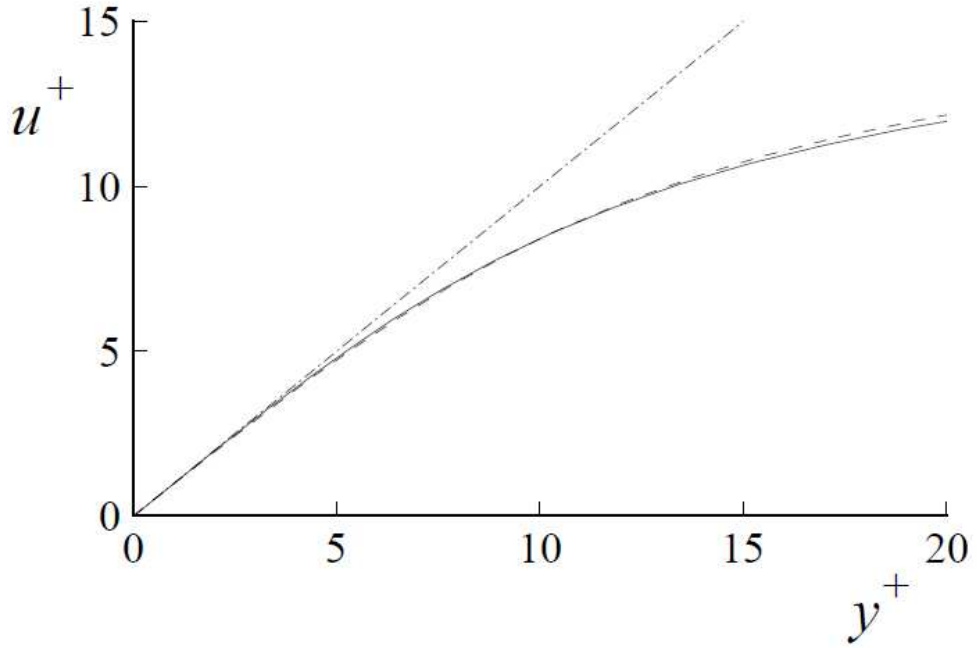


Fig. 2.5 - Near-wall profiles of mean velocity from the DNS data of Kim et al. (1987); dashed line  $Re = 5600$ , solid line  $Re = 13750$ , dot-dashed line  $u^+ = y^+$ .

### 2.4.3 The log law

The inner layer is usually defined as  $y/\delta < 0.1$ . At high Reynolds number, the outer part of the inner layer corresponds to large  $y^+$ . As has already been discussed, for large  $y^+$  it can be supposed that viscosity has little effect. Hence, in equation (2.25), the dependence of  $\Phi_I(y/\delta_v)$  on  $\nu$  (through  $\delta_v$ ) vanishes, so that  $\Phi_I$  adopts a constant value denoted by  $k^{-1}$ :

$$\Phi_I(y^+) = \frac{1}{k} \quad \text{for } y/\delta \ll 1 \text{ and } y^+ \gg 1 \quad (2.33)$$

Thus, in this region, the mean velocity gradient is

$$\frac{du^+}{dy^+} = \frac{1}{k \cdot y^+} \quad (2.34)$$

which integrates to

$$u^+ = \frac{1}{k} \cdot \ln y^+ + B \quad (2.35)$$

Where  $B$  is a constant. This is the logarithmic law of the wall due to von Kàrmàn (1930), or simply the log law, and  $k$  is the von Kàrmàn constant. In the literature, there is some

variation in the values ascribed to the log-law constants, but generally they are within 5% of  $k = 0.41$  and  $B = 5.2$ .

The log law is revealed in a semi-log plot; Fig. 2.6 shows measured profiles of  $u^+(y^+)$  for turbulent channel flow at Reynolds numbers between  $Re_0 \approx 3000$  and  $Re_0 \approx 40000$ . It may be seen that the data collapse to a single curve, in confirmation of the law of the wall, and that for  $y^+ > 30$  the data conform to the log law, except near the channel's mid-plane (the last few data points for each Reynolds number).

The region between the viscous sublayer ( $y^+ < 5$ ) and the log law region ( $y^+ > 30$ ) is called buffer layer. It is the transition region between the viscosity-dominated and the turbulence-dominated parts of the flow. The various regions and layers that are used to describe near-wall flows are summarized in Fig. 2.7.

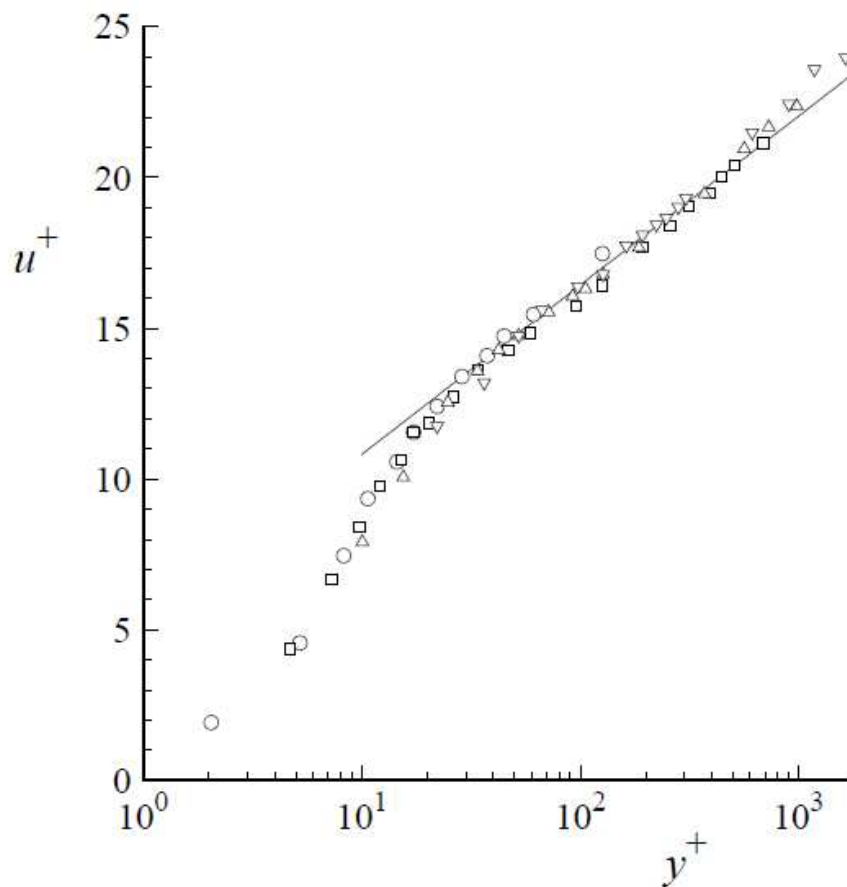


Fig. 2.6 - Mean velocity profiles in fully developed turbulent channel flow measured by Wei and Willmarth (1989); line the log law, symbols different Reynolds numbers.

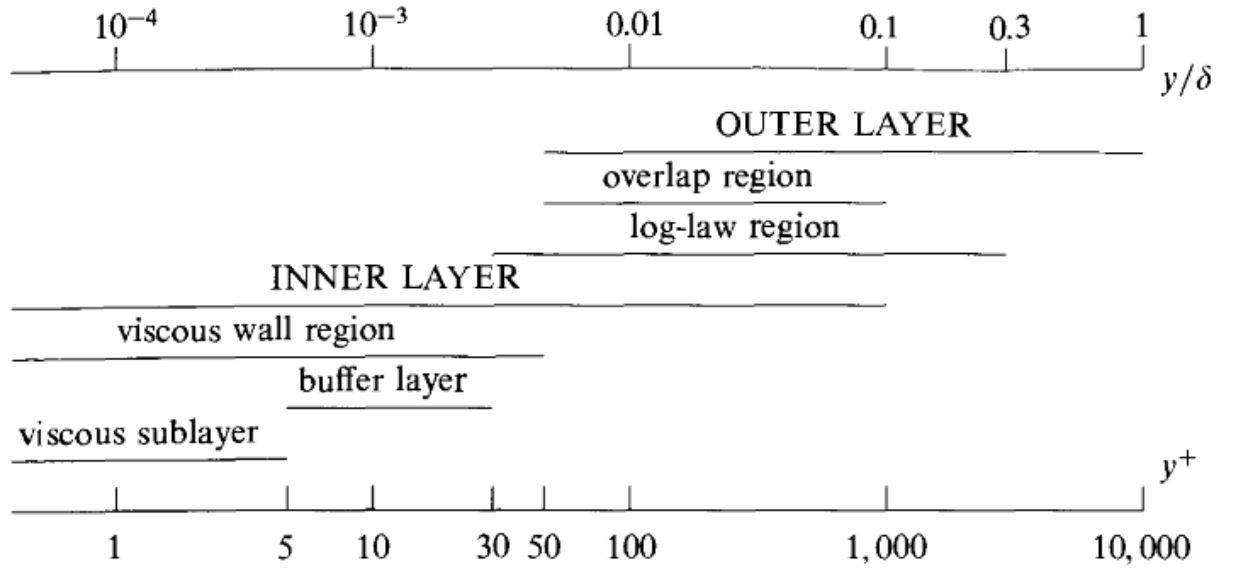


Fig. 2.7 - A sketch showing the various wall regions and layers defined in terms of  $y^+$  and  $y/\delta$ , for turbulent channel flow at high Reynolds number.

#### 2.4.4 The velocity-defect law

In the outer layer ( $y^+ > 50$ ), the assumption that  $\Phi(y/\delta_v, y/\delta)$  is independent of  $v$  implies that, for large  $y/\delta_v$ ,  $\Phi$  tends asymptotically to a function of  $y/\delta$  only:

$$\lim_{y/\delta_v \rightarrow \infty} \Phi\left(\frac{y}{\delta_v}, \frac{y}{\delta}\right) = \Phi_0\left(\frac{y}{\delta}\right) \quad (2.36)$$

Substituting  $\Phi_0$  for  $\Phi$  in equation (2.23) and integrating between  $y$  and  $\delta$  then yields the velocity-defect law due to von Kàrmàn (1930):

$$\frac{U_0 - \langle U \rangle}{u_\tau} = F_D\left(\frac{y}{\delta}\right) \quad (2.37)$$

where

$$F_D\left(\frac{y}{\delta}\right) = \int_{y/\delta}^1 \frac{1}{y'} \cdot \Phi_0(y') dy' \quad (2.38)$$

By definition, the velocity defect is the difference between the mean velocity  $\langle U \rangle$  and the centerline velocity  $U_0$ . The velocity-defect law states that this velocity defect normalized by  $u_\tau$  depends on  $y/\delta$  only. Unlike the law-of-the-wall function  $f_w(y^+)$ , here there is no suggestion that  $F_D(y/\delta)$  is universal: it is different in different flows.

At sufficiently high Reynolds number (approximately  $Re > 20000$ ) there is an overlap region between the inner layer ( $y/\delta > 0.1$ ) and the outer layer ( $y/\delta_v > 50$ ) (see Fig. 2.7). In this region, both equation (2.25) and (2.36) are valid, yielding (from equation (2.23))

$$\frac{y}{u_\tau} \cdot \frac{d\langle U \rangle}{dy} = \Phi_I \left( \frac{y}{\delta_v} \right) = \Phi_0 \left( \frac{y}{\delta} \right) \quad \text{for } \delta_v \ll y \ll \delta \quad (2.39)$$

This equation can be satisfied in the overlap region only by  $\Phi_I$  and  $\Phi_0$  being constant, which leads to

$$\frac{y}{u_\tau} \cdot \frac{d\langle U \rangle}{dy} = \frac{1}{k} \quad \text{for } \delta_v \ll y \ll \delta \quad (2.40)$$

This argument, due to Millikan (1938), provides an alternative derivation of the log law. It also established the form of the velocity-defect law for small  $y/\delta$ :

$$\frac{U_0 - \langle U \rangle}{u_\tau} = F_D \left( \frac{y}{\delta} \right) = -\frac{1}{k} \cdot \ln \left( \frac{y}{\delta} \right) + B_1 \quad \text{for } y/\delta \ll 1 \quad (2.41)$$

where  $B_1$  is a flow-dependent constant.

Figure 2.8 shows the velocity defect in the DNS of turbulent channel flow. It may be seen that the log law is followed quite closely between  $y/\delta = 0.08$  ( $y^+ \approx 30$ ) and  $y/\delta = 0.3$ . Even in the central part of the channel ( $0.3 < y/\delta < 1.0$ ) the deviations from the log law are quite small; but it should be appreciated that the arguments leading to the log law are not applicable in this region.

Let  $U_{0,\log}$  denote the value of  $\langle U \rangle$  on the centerline obtained by extrapolation of the log law. For  $y/\delta = 1$ , equation (2.41) then yields

$$\frac{U_0 - U_{0,\log}}{u_\tau} = B_1 \quad (2.42)$$

which provides a convenient way to determining  $B_1$ . It may be seen from Fig. 2.8 that the difference  $U_0 - U_{0,\log}$  is very small (about 1% of  $U_0$ ) which makes  $B_1$  difficult to measure. The DNS data yields to  $B_1 \approx 0.2$ , but from a survey of many measurements, Dean (1978) suggested  $B_1 \approx 0.7$ . The uncertainty in  $B_1$  is of little consequence: the point is that it is small.

However, we must take in account that in the outer layer of boundary layers, the deviations from the log law are more substantial.

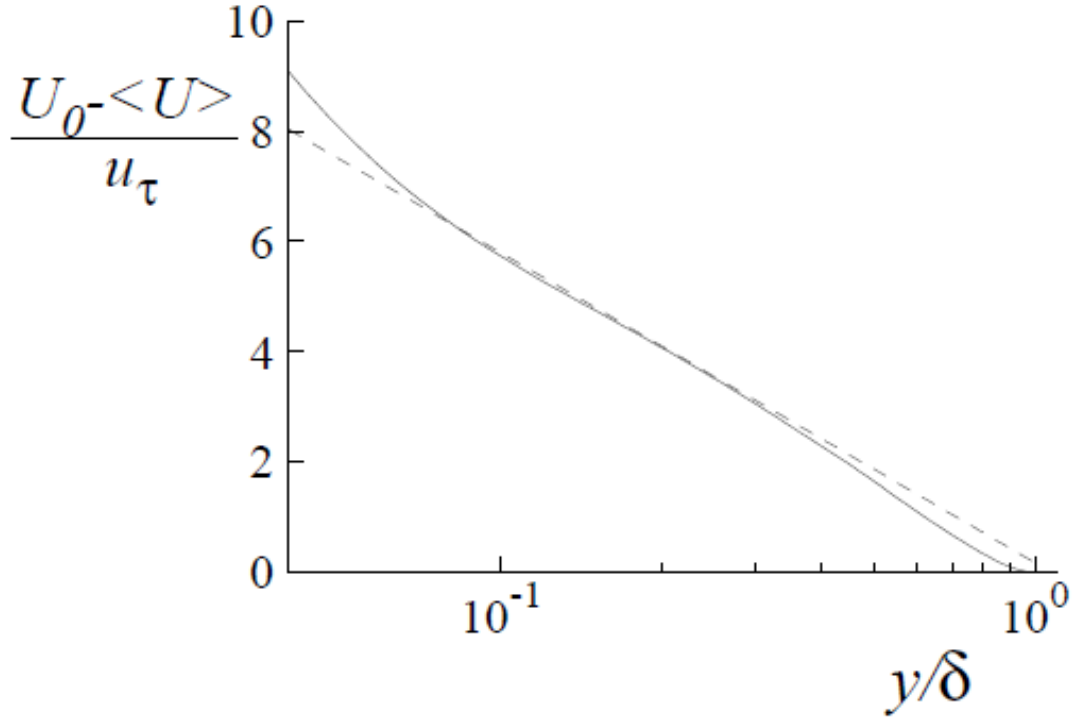


Fig. 2.8 - Mean velocity defect in turbulent channel flow. Solid lines, DNS of Kim et al. (1987)  $Re = 13750$  and dashed line log law from equation (2.35).

## 2.5 The friction law and the Reynolds number

Having characterized the mean velocity profile, we are now in position to determine the Reynolds-number dependence of the skin-friction coefficient and other quantities. The primary task is to establish relationships among the velocities  $U_0$ ,  $\bar{U}$  and  $u_\tau$ .

A good estimate of the bulk velocity is obtained by using the log law (equation 2.50) to approximate  $\langle U \rangle$  over the whole channel (for consistency at  $y = \delta$ ), this requires taking  $B_1 = 0$ ). As we have seen, in the center of the channel, the departures from the log law are quite small (Fig. 2.8): near the wall ( $y^+ < 30$ ) the approximation is poor (Fig. 2.6), but this region makes a negligible contribution to the integral of  $\langle U \rangle$ , except at very low Reynolds number. The result obtained with this approximation is

$$\frac{U_0 - \bar{U}}{u_\tau} = \frac{1}{\delta} \int_0^\delta \frac{U_0 - \langle U \rangle}{u_\tau} dy \approx \frac{1}{\delta} \int_0^\delta -\frac{1}{k} \cdot \ln\left(\frac{y}{\delta}\right) dy = \frac{1}{k} \approx 2.4 \quad (2.43)$$

This estimate agrees well with the experimental data which are scattered between 2 and 3 (Dean 1978), and the DNS values of 2.6, at  $Re = 13750$ .

The log law in the inner layer (equation 2.35) can be written



$$\frac{\langle U \rangle}{u_\tau} = \frac{1}{k} \cdot \ln \left( \frac{y}{\delta_v} \right) + B_1 \quad (2.44)$$

whereas in the outer layer is it (equation 2.41)

$$\frac{U_0 - \langle U \rangle}{u_\tau} = -\frac{1}{k} \cdot \ln \left( \frac{y}{\delta} \right) + B_1 \quad (2.45)$$

When these two equations are added together the  $y$  dependence vanishes to yield

$$\frac{U_0}{u_\tau} = \frac{1}{k} \cdot \ln \left( \frac{\delta}{\delta_v} \right) + B + B_1 = \frac{1}{k} \cdot \ln \left[ \text{Re}_0 \left( \frac{U_0}{u_\tau} \right)^{-1} \right] + B + B_1 \quad (2.46)$$

For given  $\text{Re}_0$  this equation can be solved for  $U_0/u_\tau$ , hence determining the skin-coefficient  $c_f = \tau_w / (0.5 \rho U_0^2) = 2(u_\tau / U_0)^2$ . With the aid of the approximation equation (2.43),  $\text{Re}$ , defined in equation (2.1) and  $C_f$ , as defined in equation (2.15), can also be determined. Figure 2.9 shows the skin friction coefficient  $c_f$  obtained from equation (2.46) as a function of  $\text{Re}$  (solid line). Also shown is the laminar relation and the experimental data compiled by Dean (1978) (symbols). The dashed line is, instead, the laminar friction coefficient  $c_f = 16/(3\text{Re})$ . For  $\text{Re} > 3000$ , equation (2.46) provides a good representation of the skin-friction coefficient. It is interesting to note that Patel and Head (1969) found that  $\text{Re} = 3000$  is the lowest Reynolds number at which a log law with universal constants is observed.

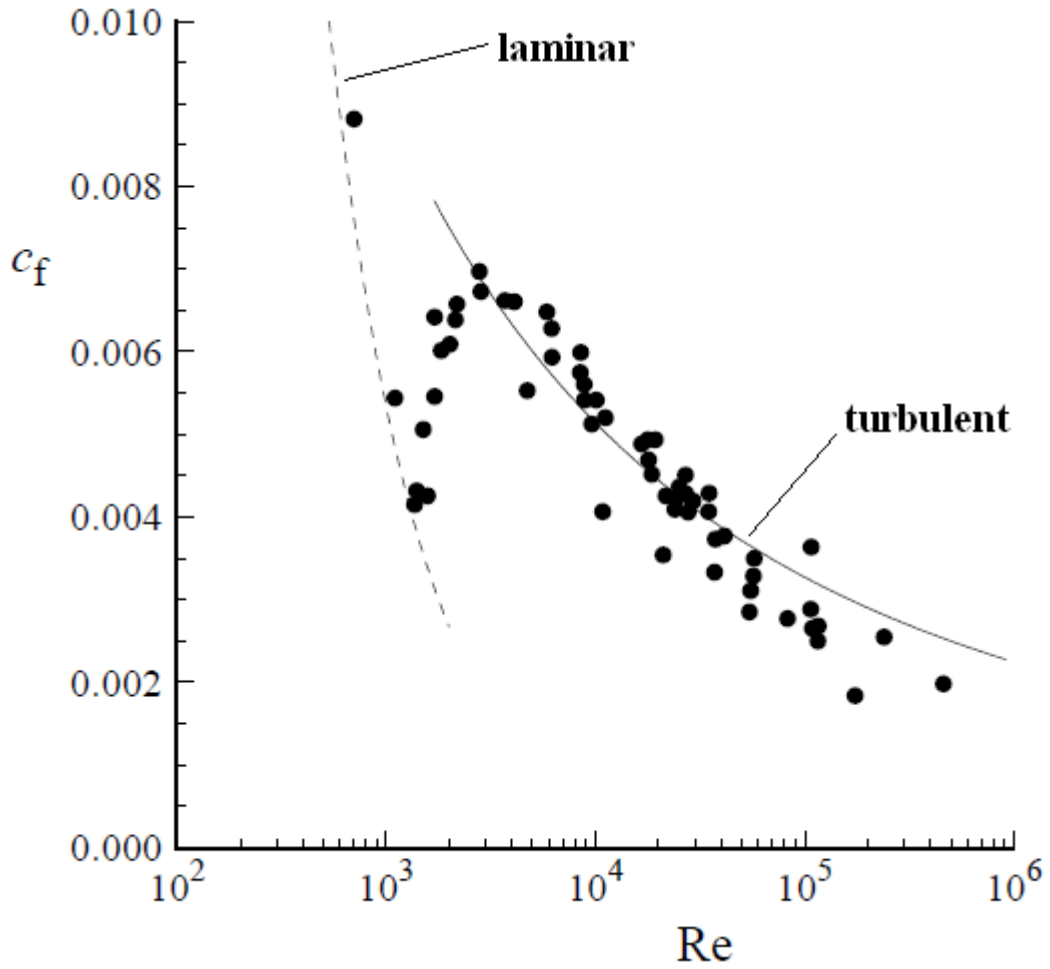


Fig. 2.9 - The skin-friction coefficient  $c_f = \tau_w / (0.5\rho U_0^2)$  against the Reynolds number  $Re = (2\delta)\bar{U}/\nu$  for channel flow.

The ratios of the mean flow to viscous scales are shown in Fig. 2.10 and 2.11. The lengthscales ratio  $\delta/\delta_v = Re_\tau$  increases almost linearly with  $Re$ , a good approximation being  $Re_\tau \approx 0.09Re^{0.88}$ . Consequently, at high Reynolds number the viscous lengthscale can be very small. As an example, for a channel with  $\delta = 2$  cm, at  $Re = 10^5$  the viscosity scale is  $\delta_v \approx 10^{-5}$  m, so the location  $y^+ = 100$  is just 1 mm from the wall. Needless to say, there are considerable difficulties in making measurements in the viscous wall region of high-Reynolds-number laboratory flows.

In contrast, the velocity ratios increase very slowly with  $Re$  (Fig. 2.11). As a consequence, a significant fraction of the increase in the mean velocity between the wall and the centerline occurs in the viscous wall region. In the example introduced above ( $\delta = 2$  cm,  $Re = 10^5$ ) it follows that, at  $y^+ = 10$ , the mean velocity is over 30% of the centerline value,  $U_0$ .

Figure 2.12 shows the Reynolds-number dependence of the  $y$  locations that delineate the various regions and layers. According to this plot, a log-law region ( $30\delta_v < y < 0.3\delta$ ) exists for  $Re > 3000$ , in agreement with the experimental observations of Patel and Head (1969). On the other hand, a Reynolds number in excess of 20000 is required for there to be an

overlap region, according to the criterion  $50\delta_v < y < 0.1\delta$ . As has already been observed, the log law persists beyond the region suggested by the overlap argument.

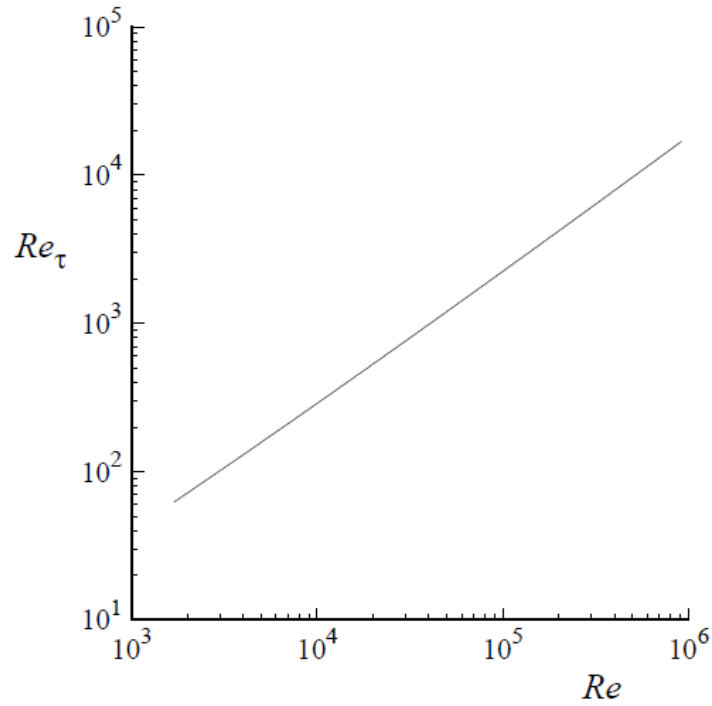


Fig. 2.10 - The outer-to-inner lengthscale ratio  $\delta/\delta_v = Re_\tau$  for turbulent channel flow as a function of the Reynolds number.

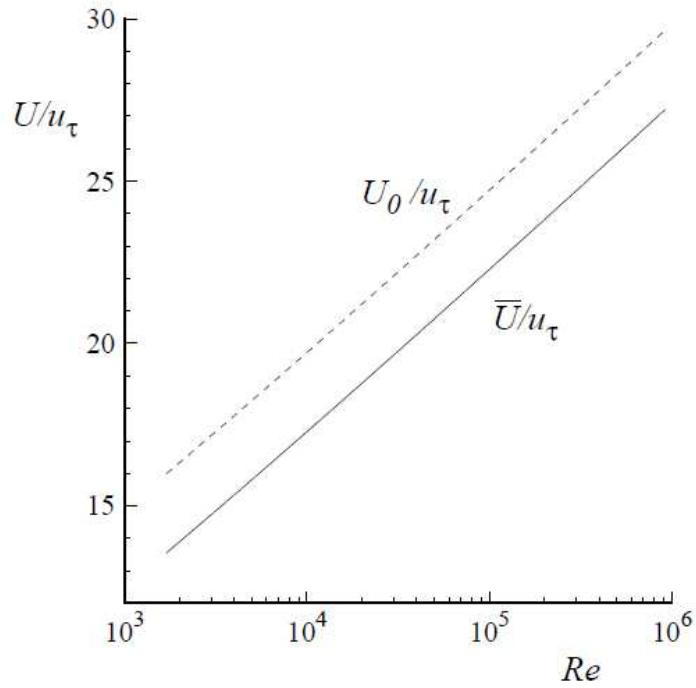


Fig. 2.11 - Outer-to-inner velocity-scale ratio for turbulent channel flow as functions of the Reynolds number.

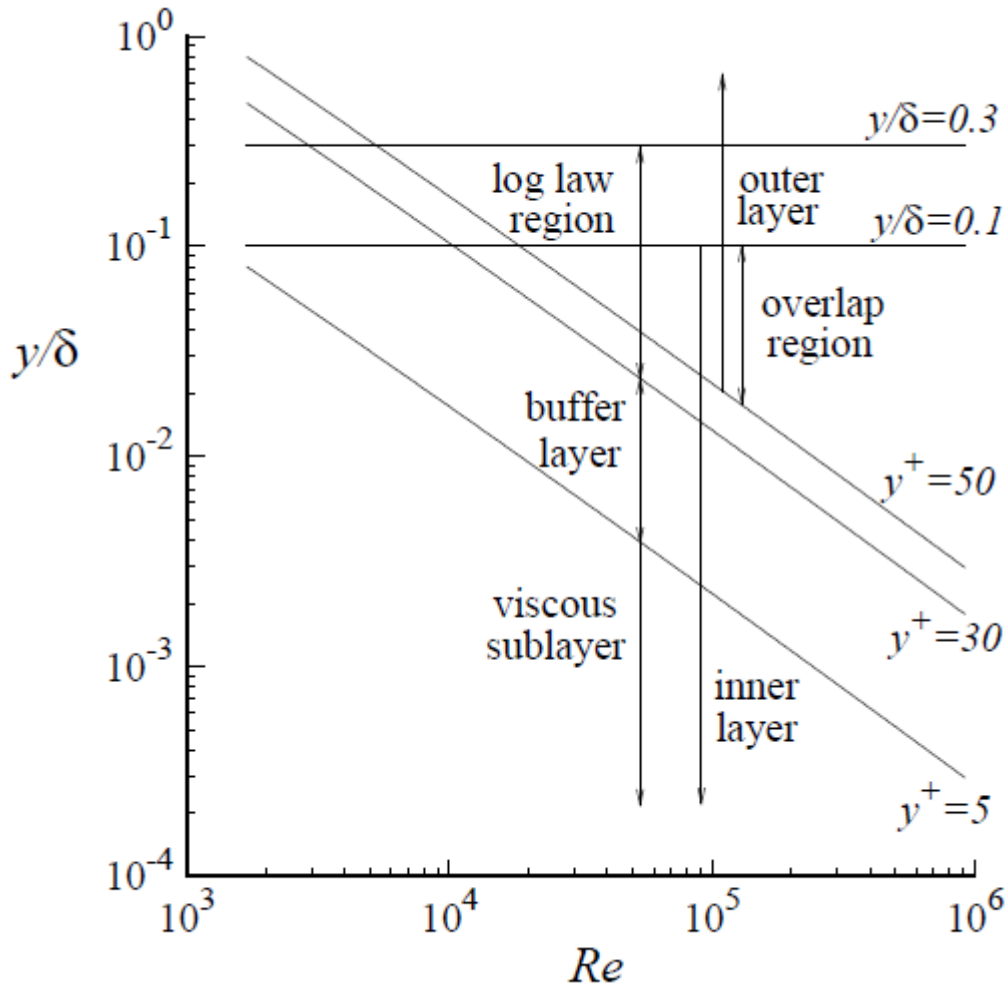


Fig. 2.12 - Regions and layers in turbulent channel flow as a function of the Reynolds number.

## 2.6 Reynolds stresses

Figure 2.13, 2.14 and 2.15 show the Reynolds stresses and some related statistics obtained from the DNS of channel flow at  $Re = 13750$ . In order to discuss these statistics, it is useful to divide the flow into three regions: the viscous wall region ( $y^+ < 50$ ); the log-law region ( $50\delta_v < y < 0.3\delta$ , or  $50 < y^+ < 120$  at this Reynolds number); and the core ( $y > 0.3\delta$ ). In the log-law region there is approximate self-similarity. The normalized Reynolds stresses  $\langle u_i u_j \rangle / k$  are essentially uniform, as are the production-to-dissipation ratio,  $P/\epsilon$ , and the normalized mean shear rate,  $Sk/\epsilon$  (where  $S = \partial \langle U \rangle / \partial y$ ). It is possible to observe that the values from experimental data that the values of  $\langle u_i u_j \rangle / k$  are within a few percent of those measured by Tavoularis and Corrsin (1981) in homogeneous shear flow. Production  $P$  and dissipation  $\epsilon$  are almost in balance, the viscous and turbulent transport of  $k$  being very small in comparison.

On the centerline, both the mean velocity gradient and the shear stress vanish, so that the production  $P$  is zero. Fig. 2.15 shows the gradual changes of  $P/\epsilon$ ,  $Sk/\epsilon$  and  $\rho_w$  from their

log-law values to zero on the centerline. Fig. 2.14 indicates that the Reynolds stresses are anisotropic on the centerline, but considerably less so than in the log-law region.

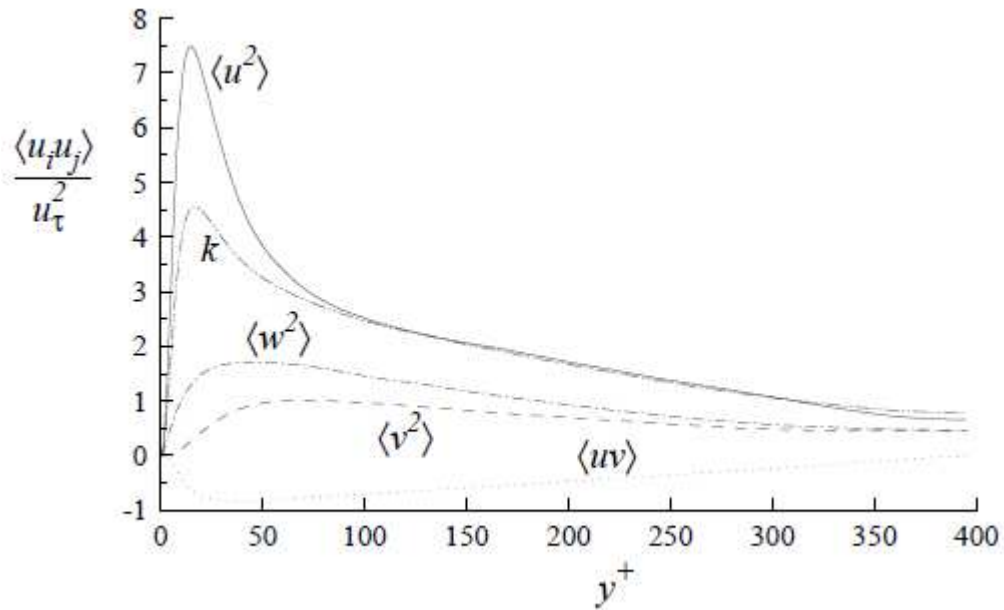


Fig. 2.13 - Reynolds stresses and kinetic energy normalized by the friction velocity against  $y^+$  from DNS of channel flow at  $Re = 13750$  (Kim et al. 1987).

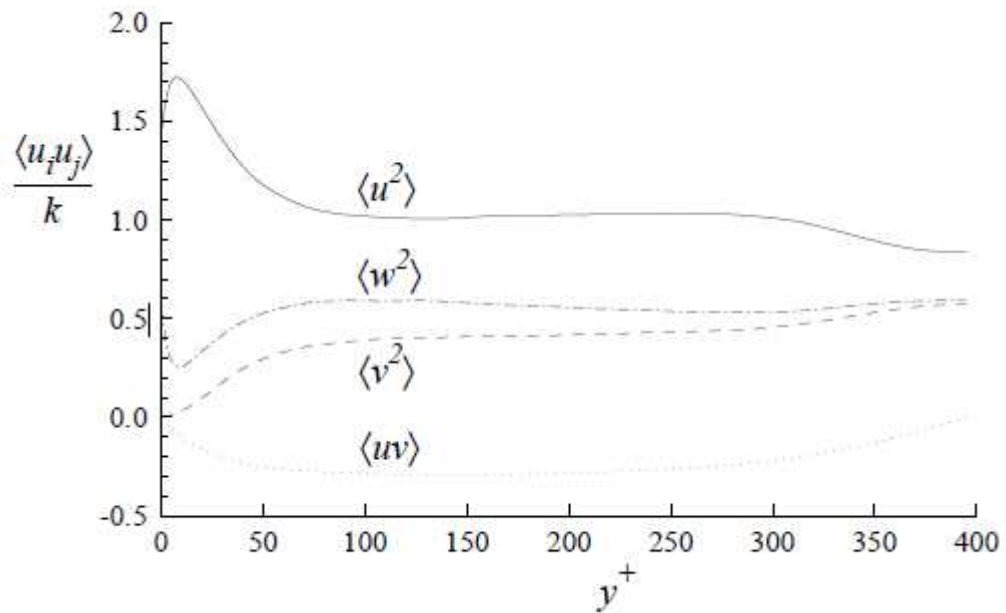


Fig. 2.14 - Profiles of Reynolds stresses normalized by the turbulent kinetic energy against  $y^+$  from DNS of channel flow at  $Re = 13750$  (Kim et al. 1987).

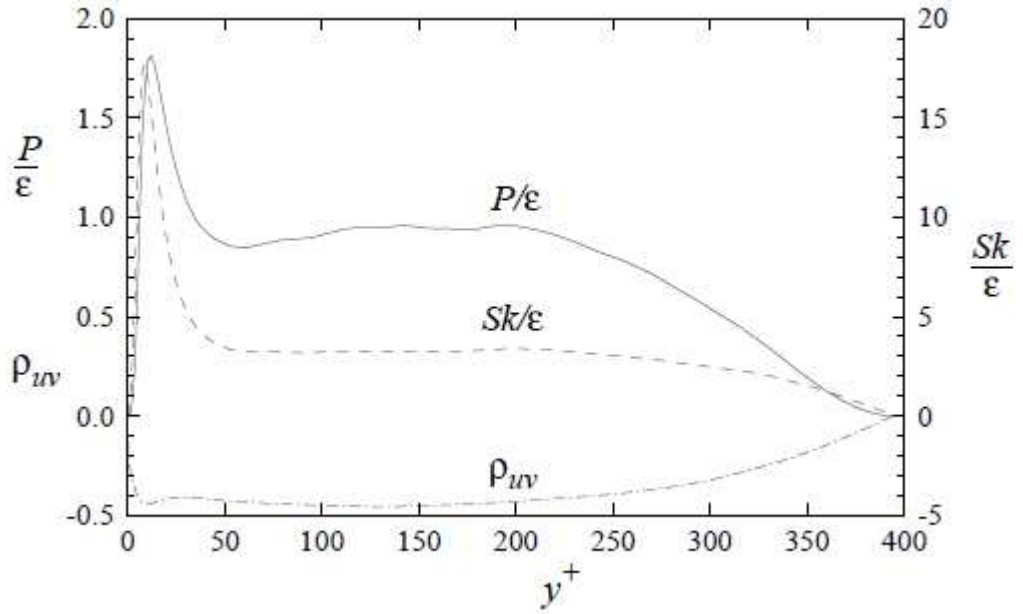


Fig. 2.15 - Profiles of the ratio production to dissipation ( $P/\epsilon$ ), normalized mean shear rate ( $Sk/\epsilon$ ), and shear stress correlation ( $\rho_w$ ) from DNS of channel flow at  $Re = 13750$  (Kim et al. 1987).

The wall region contains the most vigorous turbulent activity. The production, dissipation, turbulent kinetic energy and anisotropy all achieve their peak values at  $y^+$  less than 20. We shall examine the behavior in this region in more detail.

The boundary condition  $U = 0$  at the wall determines the way in which the Reynolds stresses depart from zero to small  $y$ . For fixed  $x$ ,  $z$  and  $t$ , and for small  $y$ , the fluctuating velocity components can be written as Taylor series of the forms

$$u = a_1 + b_1 y + c_1 y^2 + \dots \quad (2.47)$$

$$v = a_2 + b_2 y + c_2 y^2 + \dots \quad (2.48)$$

$$w = a_3 + b_3 y + c_3 y^2 + \dots \quad (2.49)$$

The coefficients are zero-mean random variables, and, for fully developed channel flow, they are statistically independent of  $x$ ,  $z$  and  $t$ . For  $y = 0$ , the no-slip condition yields  $u = a_1 = 0$  and  $w = a_3 = 0$ ; and similarly the impermeability condition yields  $v = a_2 = 0$ . At the wall, since  $u$  and  $w$  are zero for all  $x$  and  $z$ , the derivatives  $(\partial u / \partial x)_{y=0}$  and  $(\partial w / \partial z)_{y=0}$  are also zero. Hence the continuity equation yields

$$\left( \frac{\partial v}{\partial y} \right)_{y=0} = b_2 = 0 \quad (2.50)$$

The significance of the coefficient  $b_2$  being zero is that, very close to the wall, there is a two-component flow. That is, to order  $y$ ,  $v$  is zero whereas  $u$  and  $w$  are non-zero. The

resulting motion corresponds to flow in planes parallel to the wall. This is called two-component flow, rather than two-dimensional flow, because  $u$  and  $w$  vary in  $y$  direction. The Reynolds stresses can be obtained from the expansions of equations (2.47), (2.48) and (2.49) simply by taking the means of the products of the series. Taking account of the coefficients that are zero, to leading order in  $y$  the Reynolds stresses are

$$\langle u^2 \rangle = \langle b_1^2 \rangle y^2 + \dots \quad (2.51)$$

$$\langle v^2 \rangle = \langle c_2^2 \rangle y^4 + \dots \quad (2.52)$$

$$\langle w^2 \rangle = \langle b_3^2 \rangle y^2 + \dots \quad (2.53)$$

$$\langle uv \rangle = \langle b_1 c_2 \rangle y^3 + \dots \quad (2.54)$$

Thus, while  $\langle u^2 \rangle$ ,  $\langle w^2 \rangle$  and  $k$  increase from zero as  $y^2$ ,  $-\langle uv \rangle$  and  $\langle v^2 \rangle$  increase more slowly, as  $y^3$  and  $y^4$ , respectively. These behaviors can be clearly seen in log-log plots of  $\langle u_i u_j \rangle$  against  $y$ ; they are also evident in figure 2.16, which shows the profiles of  $\langle u_i u_j \rangle$  and  $k$  in the viscous wall region.

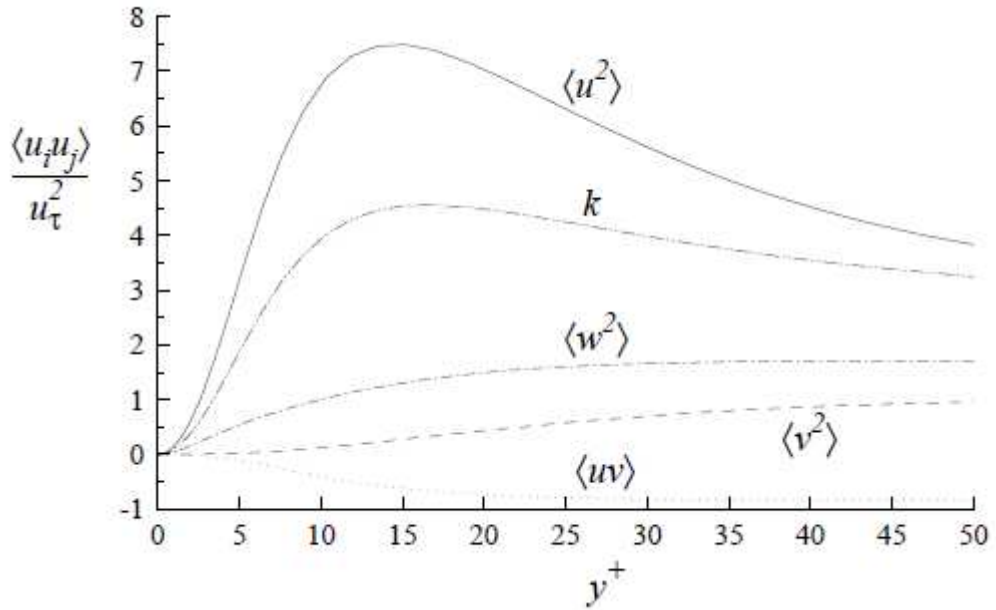


Fig. 2.16 – Profiles of Reynolds stresses and kinetic energy normalized by the friction velocity in the viscous wall region of a turbulent channel flow: DNS data of Kim et al. (1987).  $Re = 13750$ .

For fully developed channel flow, the balance equation for turbulent kinetic energy is

$$0 = P - \tilde{\epsilon} + \nu \frac{d^2 k}{dy^2} - \frac{d}{dy} \left\langle \frac{1}{2} \nu u \cdot u \right\rangle - \frac{1}{\rho} \cdot \frac{d}{dy} \langle \nu p' \rangle \quad (2.55)$$

Fig. 2.17 shows the terms in this equation for the viscous wall region. In order, the terms are production, pseudo-dissipation, viscous diffusion, turbulent convection and pressure transport.

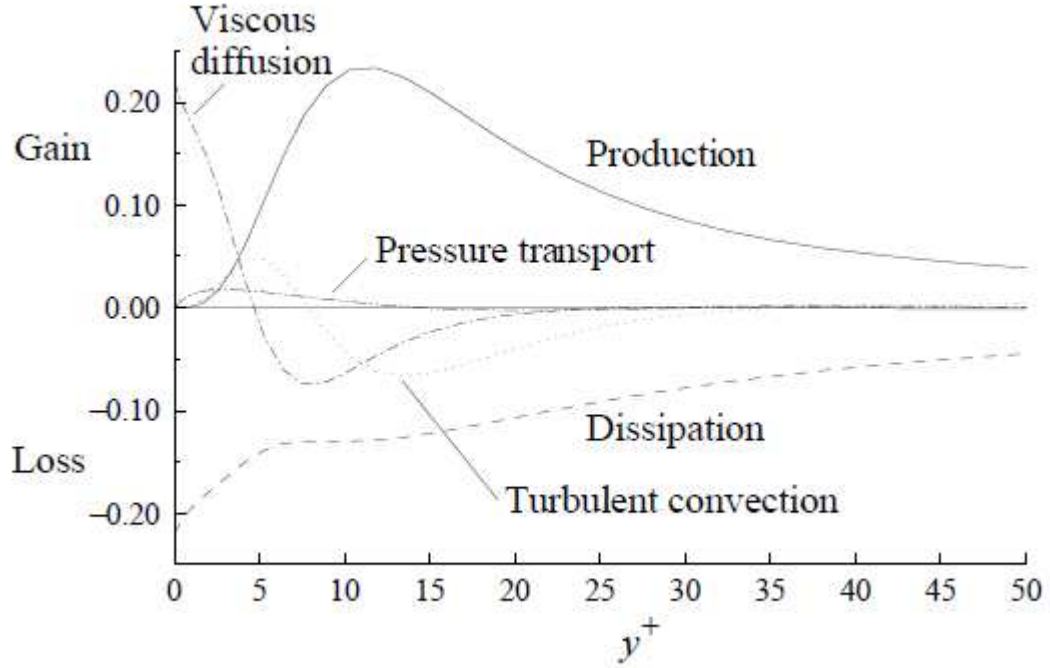


Fig. 2.17 – The turbulent-kinetic-energy budget in the viscous wall region of channel flow; terms in equation (2.64) normalized by viscous scale. From the DNS data of Kim et al. (1987).  $Re = 13750$ .

Like  $-\langle uv \rangle$ , the production  $P$  increases from zero as  $y^+$ . It reaches its peak value well within the buffer layer, at  $y^+ \approx 12$ . In fact, it can be shown that the peak production occurs precisely where the viscous stress and the Reynolds shear stress are equal. Around this peak, production exceeds dissipation ( $P/\epsilon \approx 1.8$ ), and the excess energy produced is transported away. Pressure transport is small, while turbulent convection transports energy both toward the wall and into the log-law region. Viscous transport transports kinetic energy all the way to the wall.

We can notice that the peak dissipation occurs at the wall, where the kinetic energy is zero. Although the fluctuating velocity vanishes at  $y = 0$ , the fluctuating strain rate  $s_{ij}$  and hence the dissipation do not. The dissipation at the wall is balanced by viscous transport

$$\epsilon = \tilde{\epsilon} = \nu \frac{d^2 k}{dy^2} \quad \text{for } y = 0 \quad (2.56)$$

the other terms in equation (2.56) being zero.

For fully turbulent flow, the statistics considered here (normalized by the viscous scale) have only a weak dependence on Reynolds number in the inner layer ( $y/\delta < 0.1$ ). Figure 2.18 shows profiles of the r.m.s. of  $u$  and  $v$  measured at various Reynolds numbers. The peak value of  $u'/u_\tau$  appears independent of  $Re$ ; but at  $y^+ = 50$  (which is within the inner layer for all but the lowest Reynolds number) the value of  $u'/u_\tau$  increases by 20% between



$Re_0 = 14914$  and  $Re_0 = 39582$ . These and other Reynolds number effects are discussed by Wei and Willmarth (1989) and Antonia et al. (1992).

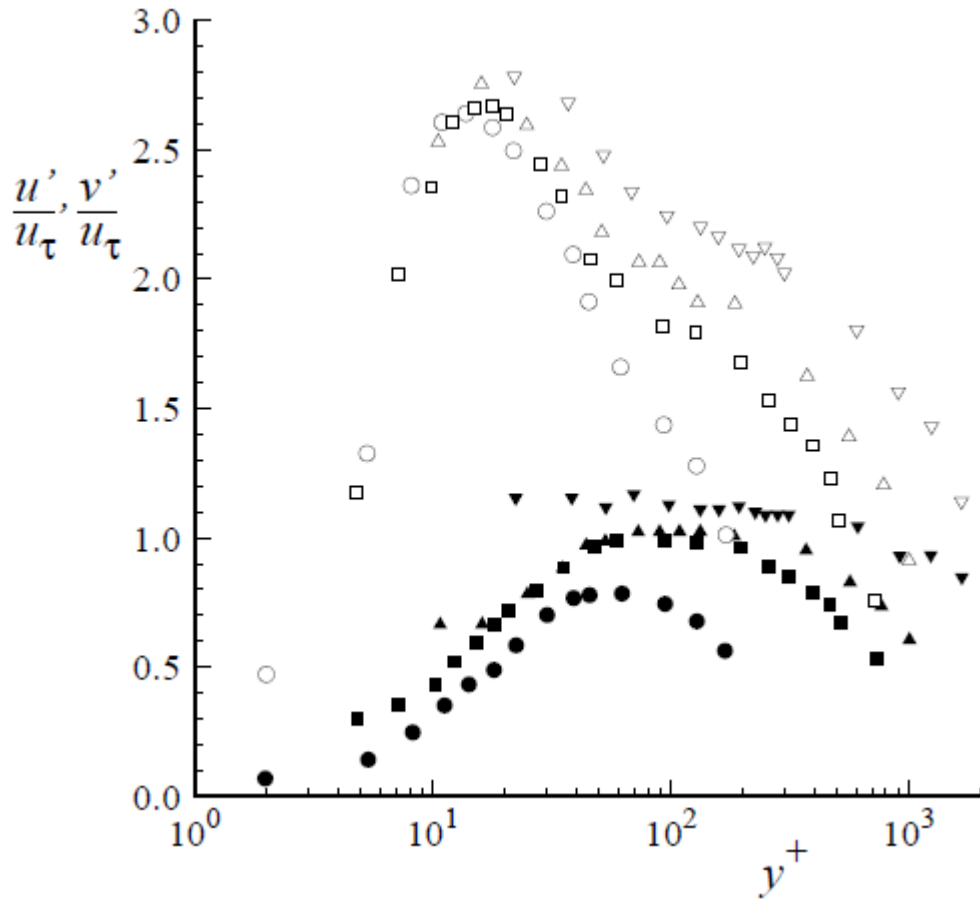


Fig. 2.18 – Profiles of r.m.s. velocity measured in channel flow at various Reynolds numbers by Wei and Willmarth (1989). Open symbols  $u'/u_\tau$ , solid symbols  $v'/u_\tau$  at different Reynolds number.

## 2.7 Lengthscales and the mixing length

Three fundamental properties of the log-law region are the form of the mean velocity gradient:

$$S = \frac{d\langle U \rangle}{dy} = \frac{u_\tau}{ky} \quad \text{or} \quad \frac{du^+}{dy^+} = \frac{1}{ky^+} \quad (2.57)$$

the fact that production and dissipation are almost in balance:

$$P/\varepsilon \approx 1 \quad (2.58)$$

and the near constancy of the normalized Reynolds shear stress:

$$-\langle uv \rangle / k \approx 0.3 \quad (2.59)$$

A fourth property, that follows from these three, is the near constancy of the turbulence-to-mean-shear timescale ratio:

$$\frac{Sk}{\epsilon} = \left| \frac{k}{\langle uv \rangle} \right| \cdot \frac{P}{\epsilon} \approx 3 \quad (2.60)$$

From these relations, it is a matter of algebra to deduce that the turbulence lengthscale  $L = k^{3/2}/\epsilon$  varies as

$$L = ky \cdot \frac{|\langle uv \rangle|^{1/2}}{u_\tau} \cdot \left( \frac{P}{\epsilon} \right) \cdot \left| \frac{\langle uv \rangle}{k} \right|^{-3/2} \quad (2.61)$$

At high Reynolds number, in the overlap region ( $50\delta_v < y < 0.1\delta$ ), the Reynolds stress is essentially constant, so that then  $L$  varies linearly with  $y$ :

$$L = C_L y \quad (2.62)$$

with

$$C_L \approx k \cdot \left( \frac{P}{\epsilon} \right) \cdot \left| \frac{\langle uv \rangle}{k} \right|^{-3/2} \approx 2.5 \quad (2.63)$$

Notice that  $S$ ,  $P$ , and  $\epsilon$  vary inversely with  $y$ , whereas  $L$  and  $\tau = k/\epsilon$  vary linearly with  $y$ . However, at the moderate Reynolds number accessible in DNS, there is no overlap region, and the shear stress changes appreciably over the log-law region. This, together with imperfections in the approximations equations (2.57), (2.58) and (2.59), results in equation (2.62) providing a poor approximation to  $L$  obtained from DNS.

The turbulent viscosity  $\nu_T(y)$  is defined so that the Reynolds shear stress is given by

$$-\langle uv \rangle = \nu_T \frac{d\langle U \rangle}{dy} \quad (2.64)$$

It can be expressed as the product of a velocity scale  $u^*$  and a lengthscale  $l_m$ :

$$\nu_T = u^* \cdot l_m \quad (2.65)$$

One of these scales can be specified at will, and then the other determines  $\nu_T$ . A propitious (implicit) specification is

$$u^* = |\langle uv \rangle|^{1/2} \quad (2.66)$$

By substituting equation (2.65) and (2.66) into (2.64) and taking the absolute value we obtain the explicit relation

$$u^* = l_m \cdot \left| \frac{d\langle U \rangle}{dy} \right| \quad (2.67)$$

Note that in the upper half of the channel ( $\delta < y < 2\delta$ ) the velocity gradient  $d\langle U \rangle/dy$  is negative and the Reynolds stress  $\langle uv \rangle$  is positive. The absolute value in equation (2.66) and (2.67) ensure that  $u^*$  is non-negative for all  $y$ .

In the overlap region ( $50\delta_v < y < 0.1\delta$ ) that occurs at high Reynolds number, the shear stress  $-\langle uv \rangle$  differs little from  $u_\tau^2$ , and the mean velocity gradient is  $u_\tau/(ky)$ . Consequently,  $u^*$  equals  $u_\tau$ , and then equation (2.89) determines  $l_m$  to be

$$l_m = ky \quad (2.68)$$

Like  $L = k^{3/2}/\epsilon$ , the lengthscale  $l_m$  varies linearly with  $y$ .

The above relations constitute Prandtl's mixing-length hypothesis (Prandtl 1925). In summary, the turbulent viscosity is given by

$$\nu_T = u^* \cdot l_m = l_m^2 \cdot \left| \frac{d\langle U \rangle}{dy} \right| \quad (2.69)$$

where  $l_m$  is the mixing length. In the overlap region,  $l_m$  varies linear with  $y$ , the constant of proportionality being the Kàrmàn constant,  $k$ .

In order to use the mixing-length hypothesis as a model of turbulence, it is necessary to specify  $l_m$  outside the overlap region, like in the viscous wall region and in the core.

### 3. Effect of Roughness

Turbulent flows over rough walls have been studied since the early works of Hagen (1854) and Darcy (1857), who were concerned with pressure losses in water conduits. They have been important in the history of turbulence. Had those conduits not been fully rough, turbulence theory would probably have developed more slowly. The pressure loss in pipes only becomes independent of viscosity in the fully rough limit, and this independence was the original indication that something was amiss with laminar theory. Flows over smooth walls never become fully turbulent, and their theory is correspondingly harder.

However, during the last century of basic turbulence research, boundary layer over a rough wall has received far less attention than turbulent layer over a smooth wall with zero pressure gradient (see, for example, the review by Kovasznay (1970), Willmarth (1975), Cantwell (1981), Kline (1978), Sreenivasan (1989), and Kline and Robinson (1990)).

That situation at first sight appears justifiable on the grounds that one should try to understand wall-bounded flow with the simplest possible boundary condition before introducing complexities such as roughness, pressure gradients, curvature, and so on. However, this comparative neglect may obscure the potential contribution of rough-wall boundary layer studies to some continuing problems of boundary-layer research in general. Over either a smooth or a rough wall, the turbulent boundary layer consists (in the simplest view) of an outer region where the length scale is the boundary-layer thickness  $\delta$ , and a wall or inner region where the length scale is  $\nu/u_\tau$  in the case of a smooth wall, as explained profusely in chapter 2. Kline (1978) has suggested that neither the dominant-inner-layer view (in which the outer layer is regarded as a collection of "tired turbulence diffused outward from events" near the smooth wall) nor the dominant-outer-layer view (in which the inner region is driven by the outer layer) is tenable. It is much more likely that the inner and outer regions interact, a notion which can be evaluated (Kline and Robinson 1990) not only with data from the canonical smooth-wall boundary layer, but also from boundary layers subjected to perturbations such as roughness transitions, pressure gradient changes, or wall suction.

Much of the literature before 1990 regarding roughness concerns itself with the universal aspects of flows over rough walls; more recent research has emphasized the differences between different types of roughness. It has been suggested that the details of the wall may influence the flow across the whole boundary layer, and part of this review is dedicated to sorting those claims and their significance in understanding wall turbulence. Because of space limitations we restrict ourselves to the fluid dynamics of fully turbulent flows over rough walls, neglecting other important topics. One of them is transition, which can be promoted (Schlichting 1968, pp. 509–15) or delayed by roughness (Wassermann & Kloker 2002). Another one is the role of roughness in enhancing heat transfer, recently reviewed by Kalinin & Dreitzer (1998), which is a field by itself.

In this chapter, a study of turbulence in rough-wall boundary layers is carried out for understanding degree and nature of the interaction between the inner and outer layers. One way of posing the problem is this: smooth-wall and rough-wall boundary layers have (as will be shown) essentially the same turbulence structure in the outer layer, a region of weak shear and therefore not the site of the dominant instability mechanisms which generate the turbulence, nor of the strongest production of turbulent kinetic energy. Yet close to the wall, where the shear is large and turbulence generation is strong, the two kinds of boundary layer have quite different structures and are controlled by quite different length scales. How do such different processes in the energetic inner layer lead to

essentially identical results in the more passive outer layer? In addition to these basic considerations, there are a host of practical engineering and meteorological motivations for research on rough-wall boundary layers. In the atmosphere the underlying surface is almost always rough, leading micrometeorologists to study the flow above and within vegetation canopies (certainly rough walls in the fluid mechanical sense), both in field experiments and in wind tunnel models. By contrast, mainstream or engineering fluid mechanics has almost always relegated the roughness to a property of the wall which is not of direct concern other than through its influence on the boundary layer well above the surface. The usual laboratory realizations of roughness, such as sand-roughened walls, do not admit measurements within the roughness envelope or canopy. In this respect, studies of real or model vegetation canopies make a unique contribution. One reason for slower progress in rough-wall than in smooth-wall boundary layer studies is that there are two intrinsic difficulties for both measurements and theory in the vicinity of the roughness. The high turbulence intensities encountered near the roughness cause many standard measurement techniques (X-wire anemometry in particular) to suffer from substantial errors that have often proved difficult to diagnose and correct. Second, because the flow near the roughness is spatially heterogeneous at the length scales of individual roughness elements, spatial averaging is required in both theory and experiment to eliminate the resulting "noise." In this chapter, our aim is to place laboratory and atmospheric rough-wall studies within a single framework and summarize the existing studies about the effect of roughness. Sections 3.1 and 3.2 consider, respectively, the mean velocity profile and turbulence statistics in a rough-wall boundary layer well above the roughness, while section 3.3 discusses the mean and turbulent velocity fields close to and within the roughness layer. Section 3.4 considers organized motion.

## 3.1 Mean Velocity above the roughness sublayer

### 3.1.1 Dimensional considerations and the logarithmic profile

The bulk properties of the mean velocity distribution  $U(y)$  in both smooth-wall and rough-wall boundary layers are derivable by a classical asymptotic matching process (Millikan 1938, Wooding et al 1973, Yaglom 1979). Suppose that the flow is in the state called "moving equilibrium" by Yaglom (1979), in which  $\delta$  and  $u_\tau$  vary sufficiently slowly with  $x$  that their variation with  $x$  can be disregarded; then both  $\delta$  and  $u_\tau$  can be considered as local scales at any particular  $x$ . The asymptotic matching analysis postulates that the boundary layer consists of two overlapping regions: an outer layer scaling with  $u_\tau$  and  $\delta$ , and an inner layer scaling with  $u_\tau$  and a set  $S$  of length scales characterizing the surface. For a smooth surface, as we saw in chapter 2,  $S$  consists only of the viscous length scale  $\nu/u_\tau$ , whereas, for a rough surface,  $S$  consists of  $\nu/u_\tau$  together with the roughness height  $h$  and all additional lengths  $L_i$ , needed to completely characterize the roughness. Typically,  $L_i$  includes at least the roughness element dimensions in the  $x$  and  $y$  directions, and the mean element separation distance. Other lengths may also be relevant in some circumstances. Of course,  $U(y)$  also depends on  $y$  itself. However, care is necessary in defining the origin of  $y$  for a rough surface, since the roughness itself displaces the entire flow upwards. To account for this, we define the displaced height  $Y = y - d$ , where  $d$  is the fluid-dynamic height origin or zero-plane displacement, dependent on both the flow and the roughness, as Jiménez (2004) did. Thorn (1971) proposed, and Jackson (1981) verified theoretically, that

$d$  is the mean height of momentum absorption by the surface; in the absence of an external horizontal pressure gradient, the mean stress experienced by the base of the wall layer must equal the average horizontal force per unit plan area,  $\tau_0$ , acting on the surface. If the average moment per unit plan area exerted by these forces is  $M$ , then the level of action of  $\tau_0$  is a distance  $M/\tau_0$  above any arbitrary origin for the vertical axis. In this context, we can define  $d = M/\tau_0$ . It follows that  $d$  automatically satisfies the constraints  $0 < d < h$  and  $d = 0$  for a smooth surface. Also, the definition yields a method for the measurement of  $d$ , by calculating the geometrical centre of the drag profile in the roughness (Thorn 1971). Digressing briefly, it is noteworthy that several other techniques for defining or measuring  $d$  have been proposed. Monin and Yaglom (1971, p 293) pointed out how  $d$  can be defined in principle by requiring that first-order departures from the logarithmic velocity profile over a rough surface should vanish; however, this does not lead to a practical way of measuring  $d$ . Furuya et al (1976) and Bandyopadhyay (1987) described a method for determining  $d$  in laboratory rough-wall boundary layers, by fitting measured profiles to an assumed form for  $U(y)$  across the entire boundary layer. In micrometeorology, the standard method (choosing  $d$  so that measurements of  $U(y)$  above the canopy conform to a logarithmic law) is well known to be inaccurate (Thorn 1975, Raupach et al 1980). Molion and Moore (1983) and de Bruin and Moore (1985) suggested that  $d$  can be calculated for tall vegetation from the assumption of mass conservation imposed on a logarithmic wind profile, but there is no theoretical basis for this. The asymptotic matching analysis for  $U(Y)$  now proceeds thus: in the outer layer,  $U(Y)$  depends only on  $u_\tau$ ,  $\delta$ , and the (displaced) height  $Y$ , leading to the velocity-defect law:

$$\frac{U(Y) - U_\infty}{u_\tau} = G(\eta) \quad (3.1)$$

Where  $U_\infty$  is the free-stream velocity and  $\eta = Y/\delta$ . In the inner layer, on the other hand,  $U(Y)$  depends only on  $Y$ ,  $u_\tau$ , and the set  $S$  of surface length scales, leading to the law of the wall

$$\frac{U(Y)}{u_\tau} = F(Y_+, h_+, L_{i+}) \quad (3.2)$$

where  $+$  subscripts denote lengths normalized with  $v/u_\tau$ . The viscous length scale is chosen from the set  $S$  as the normalizing length scale in (3.2) to preserve generality over both smooth and rough walls. In the overlap region between the inner and outer layers, (3.1) and (3.2) must be valid simultaneously. Because the dimensionless laws (3.1) and (3.2) have no independent variables in common, matching is possible only if

$$\frac{Y}{u_\tau} \cdot \frac{dU}{dY} = Y_+ \cdot \frac{dF}{dY_+} = \eta \cdot \frac{dG}{d\eta} = \frac{1}{k} \quad (3.3)$$

where  $K$  is the von Kannan constant, here taken as 0.40 (though experimental values vary between 0.35 and 0.42). Integrating (3.3) gives the familiar logarithmic law

$$\frac{U(Y)}{u_\tau} = \frac{\ln Y_+}{k} + C(h_+, L_{i+}) \quad (3.4)$$

where  $C$  is a function of the roughness. For a smooth surface,  $C$  takes a constant value  $C_0$ , here taken as 5 (though experimental values between 5 and 5.5 are common). The overlap layer, in which (3.3) and (3.4) are valid, can be called the inertial sublayer (Tennekes and Lumley 1972). In this layer the flow is independent of all lengths except  $Y$ , whereas in the roughness sublayer immediately below, the flow depends explicitly on the surface scales  $h$  and  $L_{i+}$ . A crucial condition for the existence of an inertial sublayer is  $\delta \gg (v/u_\tau, h, L_{i+})$ , to ensure that the outer-layer length scale  $\delta$  is confined to (3.1) and the inner-layer length scales to (3.2). The logarithmic law is usually reformulated from (3.4) in one of two equivalent ways. The engineering approach (eg, Perry et al 1969) emphasizes the departure of a rough-wall flow from that over a smooth wall, by writing (3.4) as

$$\frac{U(Y)}{u_\tau} = \frac{\ln Y_+}{k} + C_0 - \left[ \frac{\Delta U}{u_\tau} \right] (h_+, L_{i+}) \quad (3.5)$$

where  $\Delta U/u_\tau$  is the roughness function, equal to zero for a smooth wall and increasing with wall roughness; it is the increment between (parallel) smooth-wall and rough-wall velocity profiles on a Clauser plot. The relationship between  $\Delta U/u_\tau$ , and  $h_+$  has been obtained experimentally for a wide variety of rough surfaces; see Fig. 3.1, which shows both laboratory data and atmospheric data from several vegetation surfaces. The atmospheric data extend the  $h_+$  range by about 2 orders of magnitude. When  $h_+$  is sufficiently large (more than about 70 for sand roughness),  $\Delta U/u_\tau$  varies logarithmically with  $h_+$ ; the reason becomes clear from the following. The meteorological approach to (3.4) (eg, Wooding et al 1973) is to note that at high Reynolds numbers, flow over a rough wall approaches Reynolds number similarity and viscosity becomes irrelevant. In these circumstances, usual in the atmosphere, it is not sensible to nondimensionalize (3.2) with the length scale  $v/u_\tau$ ; a better choice is  $h$  leading to the law of the wall in the form

$$\frac{U(Y)}{u_\tau} = f(\zeta, h_+, \sigma_i) \quad (3.6)$$

where  $\sigma_i = L_i/h$  are the aspect ratios necessary to characterize the roughness, and  $\zeta = Y/h$ . Combining the form (3.6) for the law of the wall with the outer-layer law (3.1) in the inertial sublayer, we can obtain the logarithmic law in the form

$$\frac{U(Y)}{u_\tau} = \frac{\ln \zeta}{k} + c(h_+, \sigma_i) \quad (3.7)$$

It is convenient to reexpress the constant  $c$  in terms of a roughness length  $y_0$ , writing

$$\frac{U(Y)}{u_\tau} = \frac{1}{k} \cdot \frac{\ln Y}{y_0} = \frac{1}{k} \cdot \ln \frac{(y-d)}{y_0} \quad (3.8)$$

where  $y_0$  is related to the other integration constants in (3.4), (3.5), and (3.7) by

$$\ln\left(\frac{y_0}{h}\right) = -k \cdot c(h_+, \sigma_i) = -k \cdot C(h_+, L_{i+}) - \ln(h_+) = -k \cdot \left( C_0 - \left[ \frac{\Delta U}{u_\tau} \right] (h_+, L_{i+}) \right) - \ln(h_+) \quad (3.9)$$

so that  $C$ ,  $\Delta U/u_\tau$ ,  $c$  and  $y_0/h$  are all equivalent measures of the capacity of the surface to absorb momentum. The functional form of the logarithmic law becomes simpler in the high and low Reynolds number limits. When  $h_+ \rightarrow \infty$ , the flow is dynamically fully rough, and Reynolds number similarity ensures that

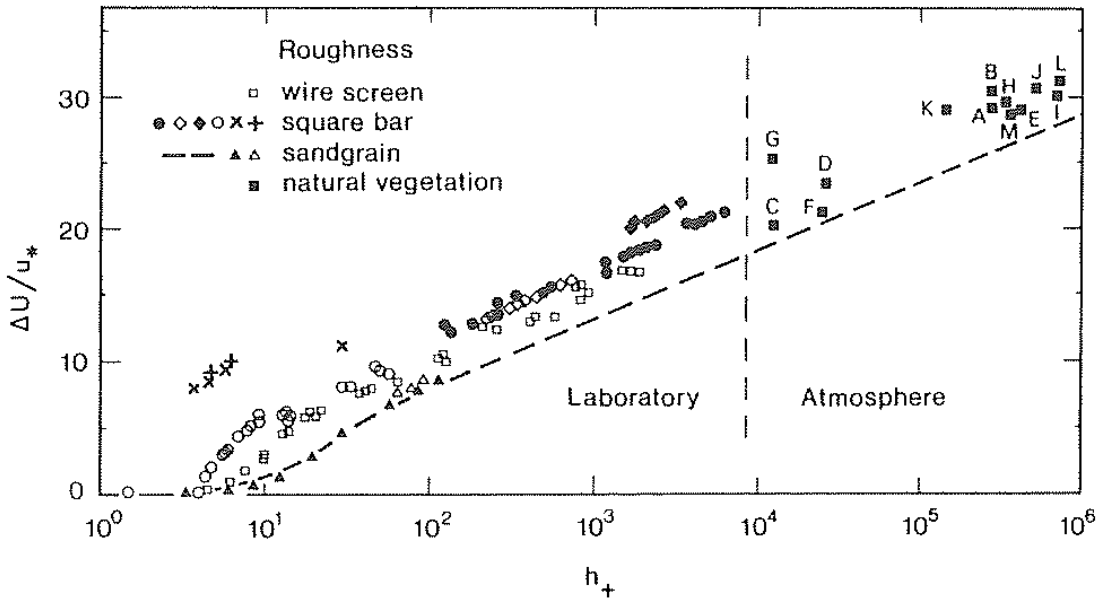


Fig. 3.1 - The relationship between  $\Delta U/u_\tau$  and the roughness Reynolds number  $h_+$ . Laboratory data from survey by Bandyopadhyay (1987).

$$\begin{aligned} y_0/h &\rightarrow \exp[-k \cdot c_\infty(\sigma_i)] \\ \Delta U/u_\tau &\rightarrow -c_\infty(\sigma_i) + C_0 + \frac{1}{k} \cdot \ln h_+ \end{aligned} \quad (3.10)$$

Where  $c_\infty(\sigma_i)$  is the limit of  $c$  as  $h_+ \rightarrow \infty$ . In this limit  $c(h_+, \sigma_i)$  and  $y_0$  become independent of  $h_+$ , depending only on roughness geometry through  $\sigma_i$ , and  $\Delta U/u_\tau$  varies logarithmically with  $h_+$  (see Fig. 3.1). When  $h_+ \rightarrow 0$  (but with  $u_\tau$  remaining nonzero), the flow is dynamically smooth and approaches that over a smooth wall, so that  $C \rightarrow C_0$ ,  $\Delta U/u_\tau \rightarrow 0$  and

$$y_0 \rightarrow \frac{\nu}{u_\tau} \exp[-k \cdot C_0] = 0.14 \cdot \frac{\nu}{u_\tau} \quad (3.11)$$



Therefore,  $y_0$  remains defined for dynamically smooth flow but is flow-dependent, unlike the fully rough limit where  $y_0$  depends on roughness geometry alone. For the homogeneous sand roughness studied by Nikuradse (1933), dynamically smooth flow is observed for  $0 < h_+ < 5$  and dynamically fully rough flow for  $h_+ > 70$ . At intermediate values of  $h_+$ , the flow is called transitional. In the fully rough state, the data for sand roughness show that  $c_\infty = 8.5$ , giving  $y_0 \sim h/30$  from (3.10). It is also useful to define a Reynolds number based on  $y_0$  by writing (consistent with previous notation)  $y_{0+} = y_0 u_\tau / \nu$ . (This is sometimes called the roughness Reynolds number, but we reserve that term for  $h_+$ .) From (3.11), the minimum value of  $y_{0+}$  is 0.14, on a smooth wall. The relation between the roughness function  $\Delta U/u_\tau$  and the roughness length  $y_0$  is most easily expressed in terms of  $y_{0+}$ :

$$\frac{\Delta U}{u_\tau} = C_0 + \frac{1}{k} \cdot \ln y_{0+} \quad (3.12)$$

which permits simple conversion between the engineering and meteorological measures of roughness.

From the previous equations we can say that the most important effect of roughness is the change of the mean velocity profile near the wall, with the consequent modification of the friction coefficient.

Before leaving the dimensional analysis, it is necessary to consider the zero-plane displacement  $d$ , which is required to fix the origin of  $Y$  in (3.4)-(3.8). From the definition of  $d$  as the mean level of momentum absorption by the (rough) surface, it follows that  $d$  is a fluid-dynamic property of the surface which obeys dimensional constraints similar to those on  $y_0$ . Hence, when  $\delta \gg (\nu/u_\tau, h, L_i)$ , the normalized displacement  $d/h$  is a function only of the surface properties  $h_+$  and  $\sigma_i$ , independent of  $h_+$  as  $h_+ \rightarrow \infty$ , like  $y_0/h$  from (3.9) and (3.10).

Virtually all surfaces of geophysical or meteorological interest are rough. The characteristic height of the roughness elements in natural terrains ranges from a few microns in the case of snow and fresh mud, to several centimeters in open rural terrain, and to tens of meters over forests and cities (Monin 1970). The thickness of the atmospheric boundary layer is  $\delta \approx 500$  m (Counihan 1975), so that the ratio  $\delta/h$  is large in open rural areas, but not necessarily so over cities or forests (Chen & Castro 2002).

Besides the obvious effects of roughness just discussed there are subtler possibilities. Researchers have known for some time that structures with outer length scales penetrate into the buffer region (Hites 1997, Del Alamo & Jiménez 2003), and it has also been suggested that those outer-layer structures grow from “hairpin” eddies generated near the wall (Head & Bandyopadhyay 1981, Adrian et al. 2000). It is therefore possible that at least some rough walls may influence the whole layer by modifying the form of the hairpins (Bandyopadhyay & Watson 1988), and the behavior of the roughness layer in other cases may be directly modified by events coming from the outside. Both mechanisms have been proposed.

### 3.1.2 Fully rough flow

At Reynolds numbers large enough for the flow to obey Reynolds number similarity, the problem of determining the mean velocity profile in the logarithmic region devolves to

finding the functional dependence of  $y_0/h$  (or  $\Delta U/u_\tau$ ) and  $d/h$  upon the roughness geometry as specified by  $\sigma_i$ . The question of whether there are kinds of roughness which do not achieve a fully rough state (even at very high Reynolds numbers) is considered here. The earliest approach to the problem of characterizing  $y_0/h$  or  $\Delta U/u_\tau$  was to define roughness by analogy with particular, well-studied forms such as the sand roughness of Nikuradse (1933), for which  $c_\infty = 8.5$  and  $y_0 \sim h/30$ . It is still common in engineering to define roughness in terms of the "equivalent sandgrain roughness height"  $h_s = 32.6y_0$  introduced by Schlichting (1936). The three quantities  $h_s^+$ ,  $\Delta U^+$ , and  $y_0^+$  characterize roughness interchangeably. The first one is most often used in engineering applications, the second one in wind-tunnel research, and the last one in geophysics.

Note that, even if in Nikuradse's case  $h_s$  is the grain size of the sand, it is in general only a convenient way of characterizing the drag increment due to the roughness. Consider the skin friction generated by two boundary layers, one rough and the other one smooth, with identical mean velocities  $U$  at a given location  $y$  within the logarithmic layer. In the smooth and rough cases the logarithmic velocity distribution for the mean velocity profile can be written as

$$U_l^+ + \frac{1}{k} \cdot \ln U_l^+ = \frac{1}{k} \cdot \ln R + 5.1 = B_l \quad (3.13)$$

and

$$U_r^+ + \frac{1}{k} \cdot \ln U_r^+ = \frac{1}{k} \cdot \ln \left( \frac{R}{h_s^+} \right) + 8.5 = B_r \quad (3.14)$$

where  $R = Uy/\nu$ , and the subindices  $l$  and  $r$  refer to smooth and rough values. These two equations have to be solved for  $U^+ = U/u_\tau$ , and higher values of  $U^+$  imply lower skin frictions. They both have the same form with different right-hand sides  $B$ . It is easy to check that  $U^+$  is a monotonically increasing function of  $B$ , so that the difference in wall drag between smooth and rough walls is controlled by the difference

$$B_l - B_r = \frac{1}{k} \cdot \ln h_s^+ - 3.4 \quad (3.15)$$

For  $h_s^+ \leq 4$  the skin friction of the rough wall would be less than that of the smooth one. There is no obvious reason why this should not be the case, but the opposite is usually true. Roughness elements seem to be more efficient generators of skin friction than smooth walls, presumably because they generate more turbulent dissipation than the relatively delicate viscous cycle. This is not an absolute rule, and some moderately rough surfaces reduce drag (Tani 1988, Sirovich & Karlsson 1997, Bechert et al. 2000). A well-documented example is the flow over riblets, which are narrow grooves aligned with the mean flow. They decrease drag by up to 10% (Walsh 1990), and are discussed below. In most cases  $h_s^+ \approx 4$  is however a lower limit below which the drag is the same as over a smooth wall.

In the limit  $B_l \gg B_r$  the viscous component of the skin friction is negligible compared with the drag of the roughness elements, and the flow becomes asymptotically independent of viscosity. In this limit

$$\frac{u_{\tau,r}}{u_{\tau,l}} = \frac{B_l}{B_r} \quad (3.16)$$

so that to have a skin friction larger than twice that of a smooth wall we need  $B_r \leq B_l/\sqrt{2}$ . Because  $B_l$  is approximately 20–30 in the logarithmic layer, this implies  $B_l - B_r \geq 7.5$  and  $h_s^+ \geq 80$ . In practice  $h_s/h$  becomes independent of  $h_s^+$  around that threshold, beyond which the flow is considered fully rough.

We stress that the previous argument deals with the drag properties of the flow, and that the equivalent sand roughness is a hydrodynamic concept that needs to be related to the surface geometry before it can be used.

Rather than, in micrometeorology surveys of early data by Tanner and Pelton (1960) and Stanhill (1969) gave  $y_0/h = 0.13$  ( $c_\infty = 5.10$ ) and  $d/h = 0.64$  for field crops and grass canopies, which have proved to be good rules-of-thumb in many cases and are still in widespread use. For forests, measurements reviewed by Jarvis et al (1976) suggested the rather different typical values  $y_0/h \sim 0.06$ ,  $d/h \sim 0.8$ .

The large differences between sandgrain, crop, and forest values of  $y_0/h$  and  $d/h$  reinforces the need for understanding the influence of geometry. To do this, it is necessary to identify and study experimentally the particular aspect ratios  $\sigma_i$ , which dominate the behavior of the roughness as a momentum absorber. The main ones studied are the element aspect ratios  $\sigma_x = l_x/h$ ,  $\sigma_z = l_z/h$ , and the roughness density  $\lambda$ , defined as the total roughness frontal area per unit ground area, or (frontal area per element)/(ground area per element) (Koloseus and Davidian 1966, Wooding et al 1973, Raupach et al 1980). For three-dimensional roughness  $\lambda = hl_z/D^2$ , whereas for transverse two-dimensional roughness such as ribs or grooves  $\sigma_z \rightarrow \infty$  and  $\lambda = h/D$ . Data on the influence of these aspect ratios on  $y_0/h$  are available for several broad classes of roughness.

*Three-dimensioned laboratory roughness:* An early and extensive study of the effect of roughness density  $\lambda$  on  $y_0/h$  was made by Koloseus and Davidian (1966); some of their data for three-dimensional roughness are shown in Fig. 3.2a, along with data from O'Loughlin (1965) and Raupach et al (1980). Comparable data also appear in Segner (1974). In general,  $y_0/h$  increases with increasing  $\lambda$  to a maximum value (at  $\lambda_{\max}$ , say) beyond which declines with further increase in  $\lambda$ . This behavior can be attributed to mutual sheltering of roughness elements when  $\lambda > \lambda_{\max}$  (Wooding et al 1973). However, the function  $[y_0/h](\lambda)$  and the location of  $\lambda_{\max}$  depend on the type of roughness, indicating that other aspect ratios besides  $\lambda$  are required for a complete specification.

At low roughness densities ( $\lambda < \lambda_{\max}$ ) Fig 3.2a suggests that  $y_0/h$  varies linearly with  $\lambda$ . Lettau (1969), in an early investigation of roughness-geometry effects in the atmosphere, concluded from data on flow over bushel baskets on a frozen lake (Kutzbach 1961) that  $y_0/h = 0.5\lambda$ ; however, he imposed no restriction analogous to  $\lambda \ll \lambda_{\max}$ . There is theoretical support for a linear relationship when  $\lambda \ll \lambda_{\max}$  (Wooding et al 1973), but the coefficient of proportionality depends on the drag coefficient of an isolated individual roughness element on an otherwise smooth surface.

Much less is known about the influence of other aspect ratios than  $\lambda$  on  $y_0/h$  for three-dimensional roughness. A comparison of data for three- and two-dimensional roughness (see below) suggests that the effect of  $\sigma_z$  is significant, but it seems that a definitive experiment on  $\sigma_z$  has yet to be done. The role of  $\sigma_x$  was studied by Wooding et al (1973),

using the extensive data set of Marshall (1971); they proposed  $y_0/h$  is proportional to  $\sigma_x^{-0.38}$  for  $\lambda \ll \lambda_{\max}$ .

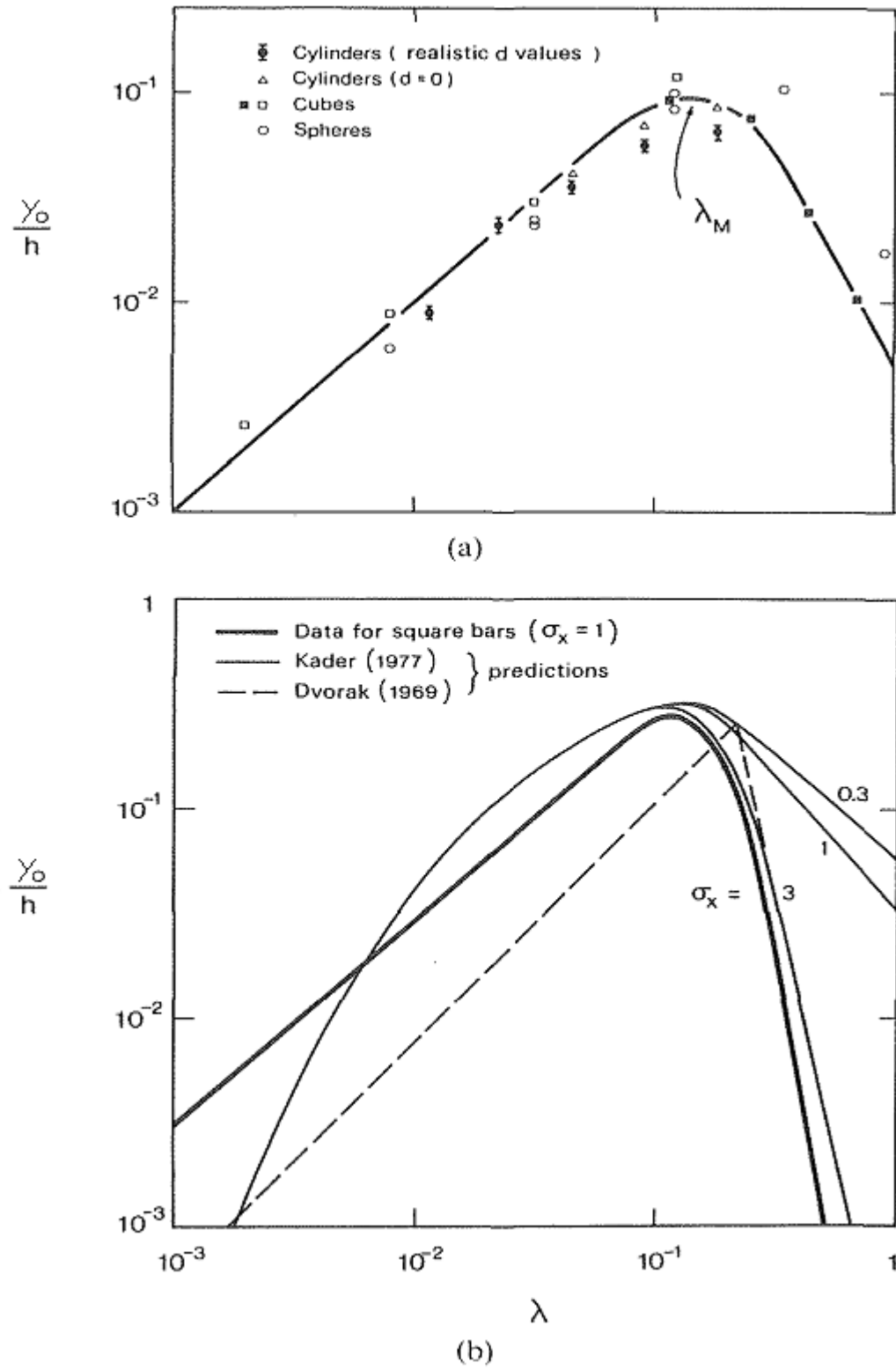


Fig. 3.2 - Normalized roughness length  $y_0/h$  as a function of roughness density  $\lambda$ .

*Two-dimensional laboratory roughness:* For transverse rectangular two-dimensional "bar" roughness, the relevant length scales are the streamwise "wavelength"  $D$ , the length  $l_x$  of the bars in the  $x$  direction, and the gap space  $D - l_x$ ; these give two independent dimensionless aspect ratios,  $\lambda = h/D$  and  $\sigma_x = l_x/h$ . The influence of  $\lambda$  on  $\Delta U/u_\tau$  or  $y_0/h$  has been extensively studied. In the case of square-bar roughness ( $\sigma_x = 1$ ), Bettermann (1966) and Liu et al (1966) showed that  $\Delta U/u_\tau$  and therefore  $y_0/h$  has a maximum for a particular spacing between elements approximately corresponding to  $\lambda_{\max} = 0.2$ ; this is a qualitatively similar finding to the three-dimensional case (Fig. 3.2a). Simpson (1973) referred to flow visualizations by Liu et al (1966) to explain this behavior, arguing that for  $\lambda > 0.2$ , permanent separated vortices occupy the entire cavity between adjacent square bars, whereas for  $\lambda < 0.2$ , reattachment occurs some distance before the next bar. Dvorak (1969) recommended, using data from various sources (Bettermann 1966, Liu et al 1966, Schlichting 1968 and others), the following formulas for square-bar roughness (see also Cebeci and Smith 1974, p 131):

$$\frac{\Delta U}{u_\tau} - \frac{1}{k} \cdot \ln h_+ = 17.35 \left( 0.706 \cdot \ln \frac{1}{\lambda} - 1 \right) \quad \text{for } 0.2 \leq \lambda \leq 1 \quad (3.17a)$$

$$\frac{\Delta U}{u_\tau} - \frac{1}{k} \cdot \ln h_+ = -5.95 \left( 0.479 \cdot \ln \frac{1}{\lambda} - 1 \right) \quad \text{for } \lambda \leq 0.2 \quad (3.17b)$$

with the qualification that (3.17b) may require further verification. Later, Kader (1977) combined several data sets on twodimensional transverse roughness of arbitrary aspect ratio  $\sigma_x$  and concluded that

$$c_\infty = 0.5 \cdot e^{-0.4s} + s^{0.45} \quad (3.18)$$

where  $s$  is a function of the surface geometric length scales.

In this formulation,  $c_\infty$  is a function not only of  $\lambda$  but also of  $\sigma_x$ , the only other aspect ratio. Equations (3.17) and (3.18) are compared in Fig. 3.2b with data from Koloseus and Davidian (1966).

*Vegetation:* For natural vegetated surfaces in the atmosphere, the data are scattered not only because of roughness element variations but also because of measurement difficulties associated with both  $y_0$  and (especially) with  $\lambda$ . One fairly widely available surrogate for  $\lambda$  is the "leaf area index" (LAI), defined as the (one-sided) cumulative leaf area per unit ground area. Stems are sometimes included (depending on the purpose of the measurement) to produce a "plant area index" (PAI). If each leaf or stem is regarded as a roughness element, and leaves and stems are assumed to be isotropically oriented, then  $\lambda = \text{PAI}/2$  (or  $\text{LAI}/2$  if only LAI is available).

Figure 3.3 shows data on the variation of  $y_0/h$  and  $d/h$  with  $\lambda$  for vegetated surfaces, from Jarvis et al (1976) and Garratt (1977), using  $\lambda = \text{LAI}/2$  where appropriate. There is a clear increase of  $d/h$  with  $\lambda$ , which is intuitively expected and is consistent with the definition of  $d$  as the mean level of momentum absorption. The  $y_0/h$  data form a qualitatively similar peaked curve against  $\lambda$  to the laboratory data (Fig. 3.2a), but with more scatter. However,

$y_0/h$  for vegetation does not fall off as rapidly at high  $\lambda$ , and has a higher  $\lambda_{\max}$  ( $\ll 0.3$ ) than for laboratory roughness (for which  $0.05 < \lambda_{\max} < 0.2$ , from Fig. 3.2). This suggests a difference in mutual sheltering properties between vegetation and solid laboratory roughness elements, which may be associated with the "porosity," or much more scattered distribution of roughness elements through space, of vegetation relative to laboratory roughness.

There have been many attempts to model turbulent flow and momentum absorption in vegetation canopies, and thence to model  $y_0/h$  and  $d/h$ . As an example, Fig. 3.4 shows results on  $y_0/h$  and  $d/h$  from a higher-order closure model by Shaw and Pereira (1982). They assumed a triangular distribution of leaf area with height, with a peak at normalized height  $y_{\max}/h$ . The results suggest a substantial dependence of both  $y_0/h$  and  $d/h$  on  $y_{\max}/h$ , but for typical values ( $0.6 < y_{\max}/h < 0.8$ ) the agreement between the model and the field data (Fig. 3.3) is reasonable.

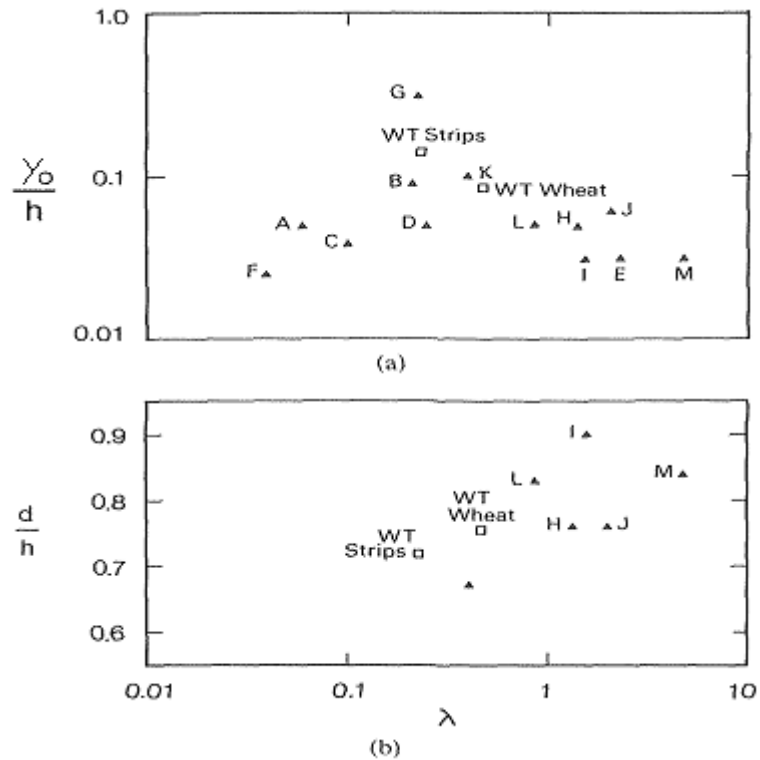


Fig. 3.3 -  $y_0/h$  and  $d/h$  as a function of roughness density  $\lambda$  for field vegetation. Surfaces A-G from Garratt (1977) and H-M from Jarvis et al (1976).

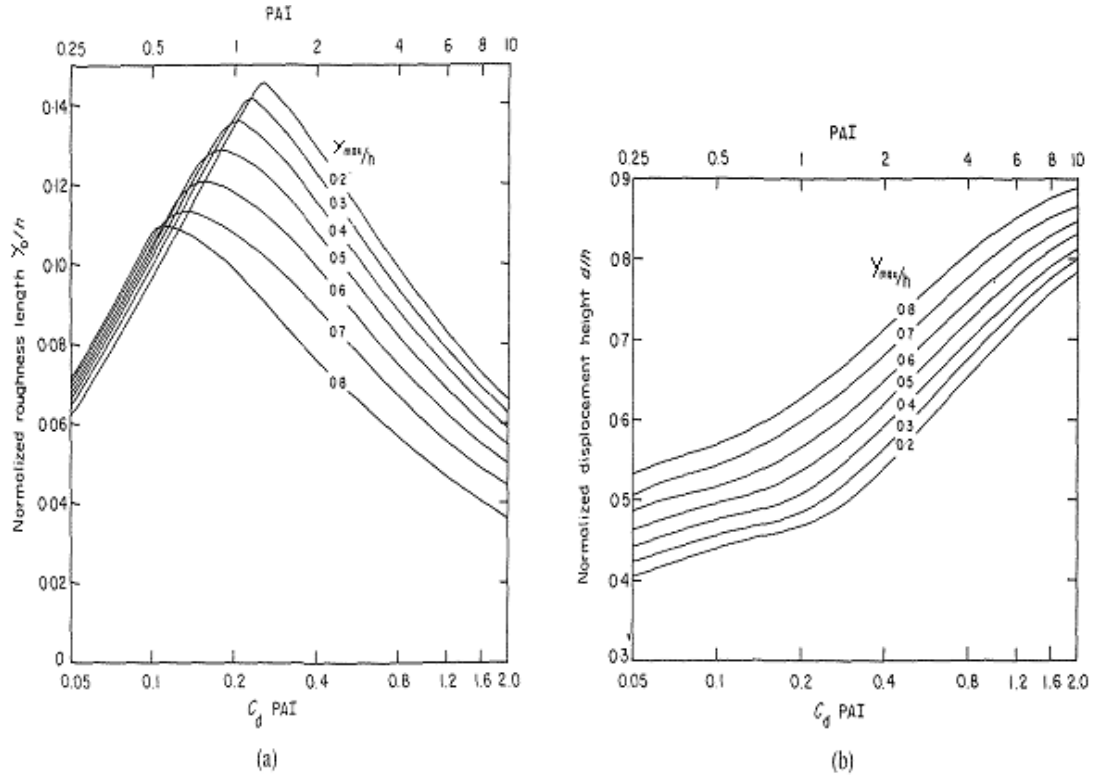


Fig. 3.4 - Predictions from a second-order closure model (Shaw and Pereira 1982) of (a) normalized roughness length  $y_0/h$  and (b) zeroplane displacement  $d/h$ , for field vegetation.

### 3.1.3.'K'-Roughness

Much consideration has been given to the question of whether there exist roughness geometries which (unlike the forms just considered) do not achieve a fully rough state at high Reynolds numbers, in the sense of obeying (3.10) as  $h_+ \rightarrow \infty$ .

Dimensional analysis suggests that in the limit in which  $h^+ \gg 1$  and viscosity becomes irrelevant,  $h_s$  should be proportional to the dimensions of the roughness elements. The "normal" surfaces for which this is true are called  $k$ -rough, to distinguish them from the  $d$ -roughness described below. The ratio  $h_s/h$  depends on the geometry of the roughness, and particularly on its surface density, which was quantified by Schlichting (1936) by the solidity  $\lambda$ , which is the total projected frontal roughness area per unit wall-parallel projected area. He performed a fairly complete set of experiments designed to test this effect, which are still often used to test theories and empirical correlations. They are presented, together with a few others, in figure 3.5. There are two regimes: the sparse one below  $\lambda \approx 0.15$ , for which the effect of the roughness increases with the solidity, and the dense one for which it decreases because the roughness elements shelter each other. In the sparse region it is intuitively clear that the extra roughness drag should be proportional to the frontal surface of the roughness elements, and  $h_s/h \approx \lambda$ . Much of the scatter of the original experiments in that range can be accounted for by scaling the drag of each surface by an appropriate drag coefficient of the individual elements. Following Tillman (1944), we use  $c_D \approx 1.25$  for two-dimensional spanwise obstacles, and  $c_D \approx 0.15$ – $0.3$  for three-dimensional rounded ones.

A re-evaluation of Schlichting's results was published by Coleman et al. (1984), and has occasionally been used instead of the original experiments. The differences are only significant for very sparse roughness, and they are used in figure 3.5 to compute the error bars.

The solidity has often been used for engineering correlations, but it cannot by itself fully characterize a surface. For example, the mutual sheltering of the roughness elements depends on other geometric factors, and correlations such as those in Figure 1a apply only to particular sets of experiments. There is not even a qualitative theory for the power of  $\lambda$ , which should describe the dense regime. Figure 3.5 uses  $\lambda^{-2}$ , which is close to some engineering correlations, but powers down to  $\lambda^{-5}$  have been proposed (Dvorak 1969). There have been many attempts to improve the empirical correlations by choosing better parameters to describe the surface (Simpson 1973, Bandyopadhyay 1987). Waigh & Kind's (1998) is a particularly complete compilation.

Most correlations are restricted to surfaces whose geometry is easily described, and cannot easily cope with irregular surfaces that are often only known by their mode of preparation. Townsin (1991) attempted to correlate the drag of such surfaces with the moments of the spectra of the roughness height while analyzing surfaces of interest in naval construction, and Raupauch et al. (1991) gave empirical correlations for plant canopies. Taylor et al. (1995) pioneered an approach in which the flow in the layer below the roughness top is approximated by a series of two-dimensional wall-parallel slices, computing the drag in each of them using a turbulence model. They had some success in the initial determination of the drag characteristics of sparse roughness (Scraggs et al. 1988).

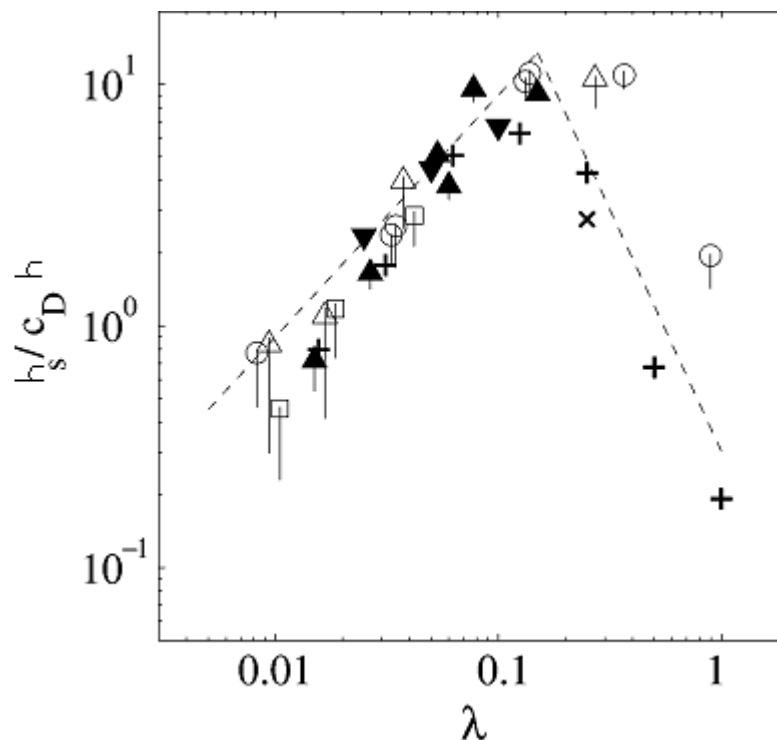


Fig. 3.5 - Equivalent sand roughness for various  $k$ -surfaces versus the solidity  $\lambda$ , corrected with empirical drag coefficients. See Jiménez (2004) for primary references.



### 3.1.4. ‘D’-Roughness

The distinction between  $d$ - and  $k$ -roughness was first made by Perry et al. (1969), who also summarized previous evidence for  $d$ -type behavior. They observed that, in several boundary layers over plates that had been roughened by narrowspanwise square grooves, the effective roughness  $h_s$  was not proportional to the roughness height (the  $h$ ), but to the boundary-layer thickness (the  $d$ ),

$$h_s \approx 0.02\delta \quad (3.19)$$

This result has to be taken with care because it was only documented for a single zero-pressure-gradient case in which the ratio of the boundary layer thickness to the groove depth was 10–20, and where asymptotic scaling laws should not be expected.

This criticism is not valid for their adverse-pressure-gradient boundary layers, which were thicker, but the only correlation in those cases was that  $h_s$  was proportional to the offset  $\Delta y$  of the logarithmic layer’s origin with respect to the top of the grooves, which could not be related to other physical lengths. It is nevertheless interesting that the value of  $\Delta y$  measured at the downstream end of some boundary layers was twice larger than either the groove width or the depth.

Figure 3.6 shows a compilation of effective roughness heights for  $d$ -surfaces, and only partially supports the conclusion that the effective roughness is independent of the roughness dimensions. In the individual experiments, represented by open symbols,  $k_s$  is not proportional to  $h$ , but neither is the overall picture consistent with a constant value for  $h_s/\delta$ . The problem is in part the narrow range of  $h/\delta$  in each experiment, but also that in most cases  $h/\delta$  is relatively large. Only Bandyopadhyay’s (1987) experiments satisfy the criterion set in the introduction that  $h/\delta > 40$ , and they are also the ones that behave less like  $d$ -walls. Simpson (1973) studied the effect of  $h/\delta$  on the drag of a particular  $k$ -surface, and suggested that

$$\Delta_0 U^+ = \Delta U^+ - 25 \cdot h/\delta \quad (3.20)$$

where  $\Delta_0 U^+$  would be an ideal value at  $h/\delta = 0$ . That correction has been applied to the solid symbols in figure 3.6, and the resulting values are in somewhat better agreement with  $d$ -behavior, but the magnitude of the correction suggests that there is a need for a definitive set of experiments with emphasis on sufficiently high values of both  $\delta/h$  and  $h^+$ .

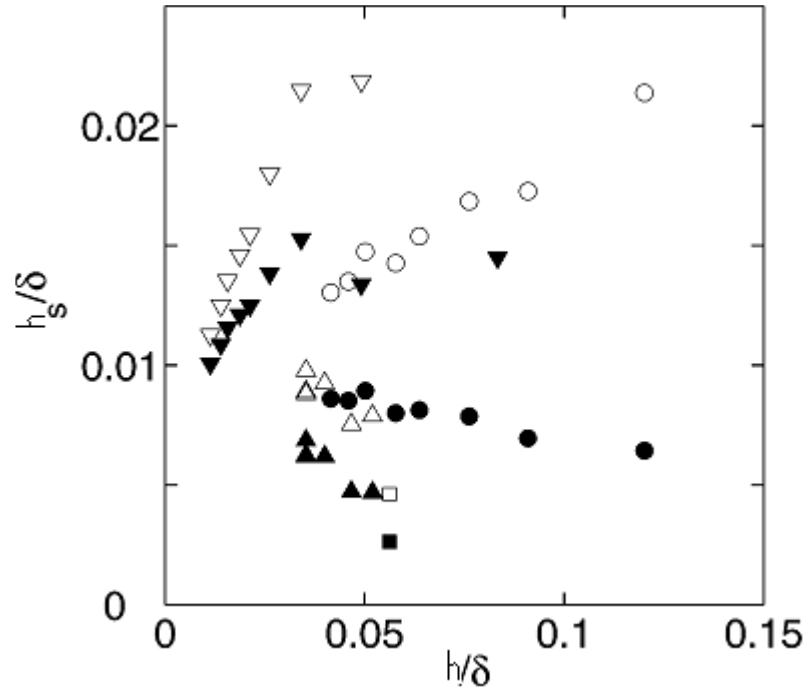


Fig. 3.6 - Equivalent sand roughness for various  $d$ -surfaces versus the solidity  $h/\delta$ . The solid symbols are corrected for the effect of  $h/\delta$ . See Jiménez (2004) for primary references.

Even with these uncertainties  $d$ -roughness has been studied extensively, both because it is difficult to understand how the origin of the logarithmic layer could be offset by more than the physical roughness dimensions, and because it promises a way of constructing boundary layers with a single length scale. Because much of the complication of wall-bounded flows is due to the interplay between two independent length scales, the proportionality in Equation 3.19 implies that  $d$ -type layers have only outer scales and are, in a sense, pure core flows.

The grooves in  $d$ -type walls are roughly square, with a solidity  $\lambda \approx 0.5$ , which is in the limit of extreme mutual sheltering in Fig. 3.5. The usual explanation for their behavior is that they sustain stable recirculation vortices that isolate the outer flow from the roughness (Fig. 3.7). Walls with grooves wider than  $3-4h$  behave like  $k$ -type surfaces, and also have recirculation bubbles that reattach ahead of the next rib, exposing it to the outer flow. Perry et al. (1969) explicitly observed the difference in recirculation lengths, and Djenidi et al. (1994) and Liou et al. (1990) confirmed it in flow visualizations of individual grooves.

Although this model explains how the flow becomes isolated from the interior of the grooves, making  $h_s$  independent of their depth, the role of the boundary-layer thickness is harder to understand. In the limit of ideally stable groove vortices, the outer flow sees a boundary condition that alternates between no slip at the rib tops and partial slip over the cavities, and the relevant length scales would seem to be the groove width and pitch, both of which are proportional to  $h$ . To get around this difficulty, it has been proposed that groups of grooves occasionally eject their vorticity into the wall layer, and that these ejections are triggered by large-scale sweeps originating in the outer flow (Townsend 1976, p. 142). There has been a lot of discussion on whether the outer flow structures couple directly with near-wall events, with various investigators finding that the periods

between buffer-layer “bursts” over smooth walls scale in outer units (Laufer & Narayanan 1971), inner units (Luchik & Tiederman 1987), or their geometric mean (Shah & Antonia 1989). A full discussion is beyond this review, but it is conceivable that a length scale  $\delta$  could arise from those interactions.

Djenidi et al. (1994) visualized ejections from individual groove vortices under turbulent boundary layers, and Taniguchi & Evans (1993) gave evidence of their modulation by passing turbulence. Ghaddar et al. (1986a) analyzed the simpler system of a grooved laminar channel and found that the vortices bifurcate spontaneously to an oscillatory state at fairly low Reynolds numbers and that the bifurcation eventually leads to subharmonic behavior in which several grooves eject collectively. Ghaddar et al. (1986b) later enhanced the heat transfer in the channel by pulsating the flow at frequencies resonating with the natural instability, supporting the idea that similar resonances could occur naturally over *d*-type surfaces.

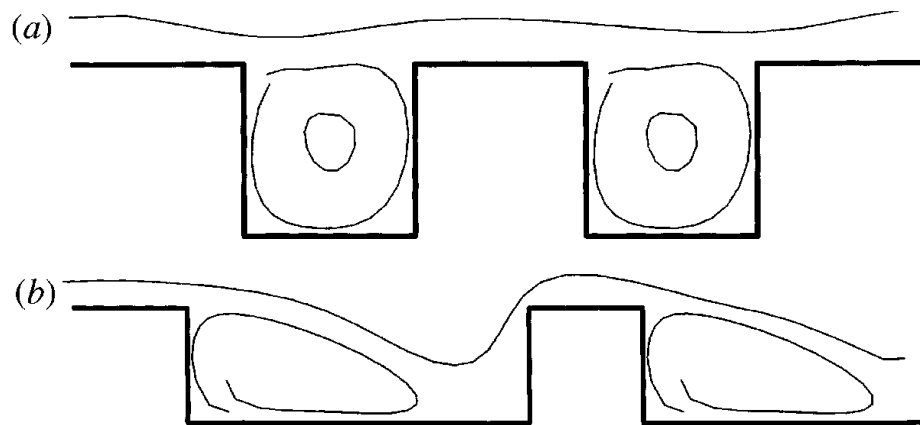


Fig. 3.7 - Geometry of (a) *d*-type and (b) *k*-type slotted walls. Flow is from left to right.

It is likely that the observed behavior of “d-type” roughness is related to the difficulty of simultaneously achieving high roughness Reynolds numbers and a large separation between  $\delta$  and roughness length scales in laboratory boundary layers. Several experiments have shown that with limited fetch  $x$  (from the start of the roughness at  $x = 0$ ),  $h - d$  varies linearly with  $x$  for “d-type” roughness (Perry et al 1969, Wood and Antonia 1975, Osaka et al 1982, Bandyopadhyay 1987). Since  $\delta$  is also approximately proportional to  $x$ , this behavior is consistent [through (3.15)] with a roughness scaling on  $\delta$ , as implied by the “d-type” nomenclature. However, it is also clear that such scaling can only operate for limited  $x$ , because  $h - d$  cannot increase beyond  $h$  whereas  $\delta$  can increase without limit in principle. At some downstream distance, both  $y_0$  and  $h - d$  must approach a limiting value determined by roughness geometry alone; only beyond this distance is the scale separation criterion  $\delta \gg (v/u_\tau, h, L_i)$  properly satisfied.

The wide interest in “d-type” roughness has been motivated partly by the possibility of generating an exactly self-preserving boundary layer. Rotta (1962) showed that, for self-preservation to exist,  $u_\tau / U_\infty$  and  $d\delta/dx$  must be independent of  $x$ . These requirements cannot be met on a smooth wall with zero pressure gradient, and in the case of a rough wall, can only be met if the roughness scale varies linearly with  $x$  (see also Townsend

1976). The observations described above suggest that "d-type" roughness fulfills the self-preservation criteria in the range of  $x$  where  $(h - d)$  is the same order of  $x$ .

### 3.1.5 Transitional Roughness

The flow regime in which  $h^+$  is not large enough for a fully rough behavior is, somewhat confusingly, called "transitionally" rough. The name has nothing to do with transition to turbulence, which is controlled by  $\delta^+$ .

Transitional roughness functions for several surfaces are collected in figure 3.8, but it is important to realize that the Reynolds number used in the abscissae is not based on the equivalent sand roughness  $h_s$ . We in the previous section that  $h_s^+$  is a flow property that univocally determines  $\Delta U^+$ . What is done in practice, and what is done in Fig. 3.8, is to assign to each surface a single "geometric" sand roughness, which is the fixed value that corresponds to its skin friction in the fully rough regime at high Reynolds numbers. This geometric roughness  $h_{s\infty}$  is a property of the surface, and can be used to characterize the Reynolds number of the flow. It guarantees the collapse of all the roughness functions in the fully rough regime. Nikuradse (1933) observed that, for graded sand, the roughness function vanishes at  $h_{s\infty}^+ \approx 4$ , which has often been incorrectly quoted as meaning that all surfaces below  $h^+ = 4$  are hydrodynamically smooth. Colebrook (1939) collected results for several industrial pipes and found more gradual transitions, also included in Fig. 3.8. His results depend on the particular surface, but to simplify their practical use, he proposed a "universal" interpolation formula

$$\Delta U^+ = \frac{1}{k} \cdot \ln(1 + 0.26 \cdot h_{s\infty}^+) \quad (3.21)$$

which Moody (1944) later used to compute his commonly used skin-friction diagram for pipes. The discrepancy between the two results was already noted by Schlichting (1968), but became lost in practice. Surfaces below  $h^+ \approx 4$  are still often considered "smooth," whereas engineers use Moody's more gradual formula.

Bradshaw (2000) revived the question, noting that a minimum transitional height was unlikely for sparse roughness because the drag of the roughness elements in a shear is proportional to  $h^2$  even in the low Reynolds number limit, and this should be reflected in  $\Delta U^+$ . In recent years the matter has become topical because some of the experiments undertaken to clarify the high Reynolds number behavior of flows over smooth walls have surfaces that would be hydrodynamically smooth or rough depending on which criterion is used (Barenblatt & Chorin 1998, Perry et al. 2001). Figure 3.8 shows that there is no "true" answer, and that each surface has to be treated individually.

The solid symbols in figure 3.8 correspond to triangular riblets measured by Bechert et al. (1997). The drag-reducing property of streamwise-aligned riblets is a transitional roughness effect (Tani 1988). When they exceed  $h^+ \approx 10$  they lose effectiveness, and their behavior when  $h^+ \gg 1$  is that of regular  $k$ -surfaces. Their drag-reducing mechanism is reasonably well understood. Luchini, Manzo & Pozzi (1991) showed that, in the limit  $h^+$  is very much less than 1, the effect of the riblets is to impose an offset for the no-slip boundary condition which is further into the flow for the spanwise velocity fluctuations than for the streamwise ones. They reasoned that this would move the quasi-streamwise vortices away from the wall, thickening the viscous sublayer and lowering the drag. They computed the relative offset  $\Delta y/h$  for several riblet families and estimated that

$$\Delta U^+ \approx 0.8 \Delta y^+ \quad (3.22)$$

assuming that the depth of the sublayer increases exactly by  $\Delta y$ . Jiménez (1994) carried out direct numerical simulations of turbulent channels incorporating the offset of the boundary conditions, and confirmed that all the transverse velocity fluctuations are shifted by  $\Delta y$ , obtaining a drag law  $\Delta U^+ \approx 0.9 \Delta y^+$ . Actual riblets satisfy a linear law similar to Equation 13 with somewhat lower experimental slopes, which Bechert et al. (1997) showed to be due to the mechanical rounding of their tips. Because  $\Delta y/h$  is constant for each riblet shape, this implies a linear behavior of the roughness function at low  $h^+$ . This is faster than the quadratic one suggested by Bradshaw (2000), showing that there are roughness effects that go beyond simple aerodynamic drag. Luchini et al.'s (1991) argument and Jiménez's (1994) simulations are antisymmetric in  $\Delta y$  when  $\Delta y \ll 1$ , and imply that the drag of spanwise-mounted riblets should increase linearly with  $h^+$ .

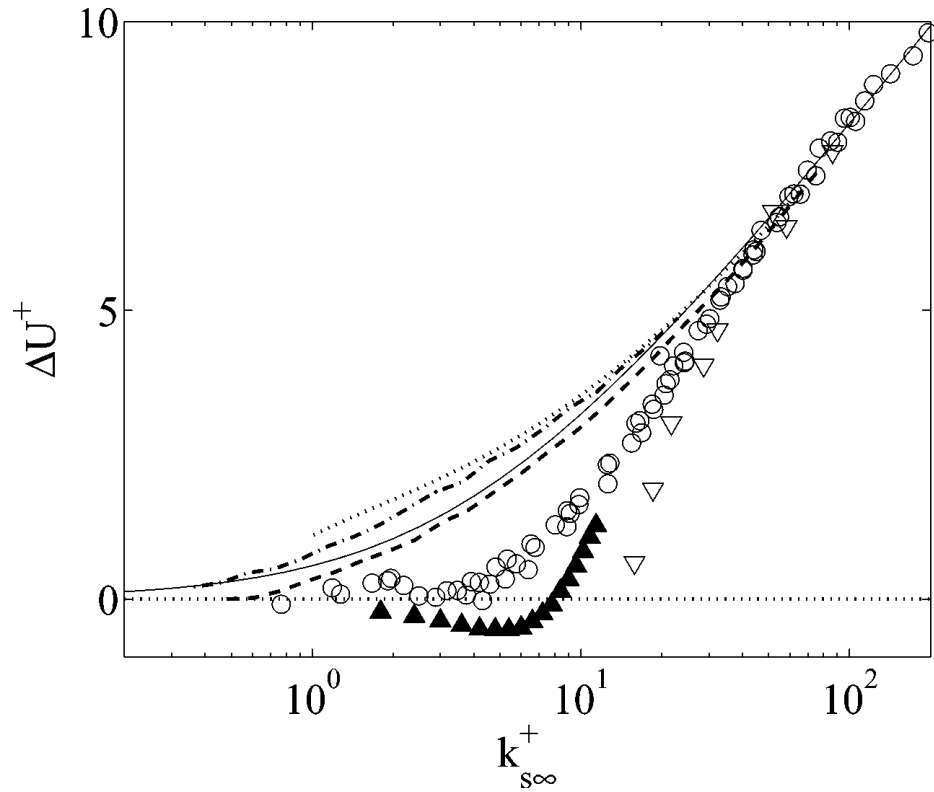


Fig. 3.8 - Roughness function for several transitionally rough surfaces, as a function of the Reynolds number based on the fully rough equivalent sand roughness.

Colebrook (1939) suggested that the reason for the gradual buildup of the roughness effects in industrial surfaces is that they contain irregularities of different sizes, and that each element becomes active when it individually reaches a critical Reynolds number. The overall smooth evolution of the drag is the sum of these individual transitions. Colebrook & White (1937) provided some support for this model in a series of experiments in which they used sand grains of different sizes to roughen the wall. Well-graded sand led to results

agreeing with Nikuradse (1933), but as little as 2.5% of larger grains were enough to substantially lengthen the transitional regime. The very sharp transition for the uniform tightly packed spheres included in Fig. 3.8 also supports this model.

Bandyopadhyay (1987) showed experimentally that  $h_+$  (upper) and  $h_+$  (lower) decrease as the aspect ratio  $\sigma_y$  increases, and that curves of  $\Delta U/u_\tau$  against  $h_+$  for different surfaces become similar when normalized by  $h_+$  (upper) and the value of  $\Delta U/u_\tau$  at  $h_+$  (upper). This was verified by Ligrani and Moffat (1986). Bandyopadhyay (1987) also correlated  $h_+$  (upper) and  $h_+$  (lower) with the Reynolds number associated with the onset of, and development of irregularities in, the vortex street shed from an isolated roughness element embedded in a laminar boundary layer.

For vegetation, viscous drag can still be important despite large values of  $h_+$  because the drag-inducing roughness elements have Reynolds numbers  $Ul/\nu$  orders of magnitude smaller than  $h_+$  (where  $l$  is an element dimension such as a pine needle diameter or a leaf width, and  $U$  is the ambient velocity about the element). For pine needles  $Ul/\nu$  is around 30-200; for wheat leaves, around 500-2000. Thom (1968) estimated the ratio of form to viscous drag on a typical bean leaf as 3:1. Thus, viscosity provides significant drag in many canopies.

There is another interesting interpretation of figure 3.8; roughness has two effects in the transitional regime. In the first place it creates an extra form drag, which increases skin friction, but it also weakens the viscous generation cycle, which decreases it. The geometric offset in riblets is an example of the second effect, which is dominant in that case because the riblets, aligned with the mean flow, have little form drag. As  $h^+$  increases, and the viscous cycle is completely destroyed, the savings from that effect saturate, and the form drag eventually takes over. Different surfaces in Fig. 3.8 have different balances of both effects. In the case of surfaces with sparsely distributed roughness elements, the form drag increases before the viscous cycle is modified over most of the wall, and the savings are never realized. If this interpretation is correct, uniformly rough surfaces offer the best opportunity for drag-reducing roughness, and Fig. 3.8 suggests that it would be interesting to extend the experiments on packed spheres to lower  $h^+$ .

### 3.2 TURBULENCE ABOVE THE ROUGHNESS SUBLAYER

Because dimensional arguments establish many properties of the mean velocity field in a rough-wall boundary layer, it is worth examining the extent to which dimensional reasoning also determines properties of the turbulence, especially velocity variances and turbulence length scales. It turns out that a more physically based form of dimensional analysis is needed to understand the turbulence statistics. This section examines three complementary hypotheses about length and velocity scales for the turbulence above the roughness (or viscous) sublayer: the wall-similarity, equilibrium-layer, and attached eddy hypotheses. Together, they lead to a set of predictions for turbulence length scales and velocity variances which are comparable with the logarithmic profile law for the mean velocity. For this analysis, a sufficiently general turbulence statistic for consideration is the two-point velocity covariance

$$\overline{u_i(Y)u_j(Y+r)} = u_\tau^2 R_{ij}(Y, r, \delta, h, L_i, \nu/u_\tau) \quad (3.23)$$

in which the displaced height  $Y = y - d$  and the separation  $r$  are primary arguments, the outer and surface length scales are secondary arguments, and velocity scaling with  $u_\tau$  is assumed. However, similar dimensional arguments apply to higher velocity moments as well.

### 3.2.1 Wall similarity

The first hypothesis is one of flow similarity over different surface types:

*Outside the roughness (or viscous) sublayer, the turbulent motions in a boundary layer at high Reynolds number are independent of the wall roughness and the viscosity, except for the role of the wall in setting the velocity scale  $u_\tau$ , the height  $Y = y - d$  and the boundary-layer thickness  $\delta$ .*

This "wall similarity" hypothesis (our label) is an extension of the usual postulate of Reynolds number similarity, which Townsend (1976) expresses thus: "while geometrically similar flows are expected to be dynamically similar if their Reynolds numbers are the same, their structures are also very nearly similar for all Reynolds numbers which are large enough to allow (fully) turbulent flow." Provided that the Reynolds number is sufficiently high, Reynolds number similarity implies that, outside the viscous sublayer, the viscous length scale  $\nu/u_\tau$  has no influence in (3.23); the wall similarity hypothesis makes the further claim that, outside the roughness sublayer, the roughness length scales  $h$  and  $L_i$  are also irrelevant. It appears that Perry and Abell (1977) were the first to advance this hypothesis in essentially the form stated above; they called it the "Townsend hypothesis," since it is implicit in the similarity arguments of Townsend (1961, 1976). They supported the hypothesis with an analysis of scaling laws for velocity spectra in several overlapping spectral ranges, an idea extended later by Perry et al (1986, 1987).

For the velocity covariance, the wall similarity hypothesis is

$$\overline{u_i(Y)u_j(Y+r)} = u_\tau^2 R_{ij}(Y, r, \delta) \quad (3.24)$$

for large Reynolds numbers and for both  $Y$  and  $Y + r$  above the roughness sublayer. An *a priori* motivation for the hypothesis (not a derivation) is that (3.24) is a dimensional statement analogous to the outer-layer law (3.1) for the mean velocity  $U(Y)$ . The foregoing discussion of the mean velocity profile shows that both  $dU/dY$  and  $U(Y)$  itself, apart from a height-independent but roughness-dependent translational velocity, are independent of surface length scales ( $h$ ,  $L_i$ ,  $\nu/u_\tau$ ) in the outer layer, including the overlap region with the inner layer. Therefore, wall similarity holds for relative mean motion at all heights above the roughness sublayer. Since the turbulence maintains and is maintained by the mean velocity profile, it is unlikely that surface length scales which are irrelevant for the mean velocity profile are important for the dominant turbulent motions.

There is strong experimental support for the wall similarity hypothesis, of at least three kinds. Two of these (stress-to-shear relationships and measurements of single-point velocity moments) are reviewed now, while a third (two-point velocity covariance measurements) is considered in section 3.5.1.

*Stress-to-shear relationships:* Strong, though indirect, evidence that the turbulence structure is essentially independent of the nature of the wall is provided by the universal value of the von Karman constant  $k$  (the ratio of the turbulent velocity scale  $u_\tau$  to the normalized mean shear  $YdU/dY$  in the inertial sublayer). It is found that  $k$  is independent of

wall roughness to within experimental accuracy in both the laboratory and in the atmospheric boundary layer [see Yaglom (1977) for a review of atmospheric measurements]. Townsend (1976) pointed out the support that this fact provides for Reynolds number similarity, since the data span a Reynolds number range from  $10^4$  to  $10^8$ . The support for wall similarity is equally striking, since the data also span surface types from smooth walls to natural vegetation.

*Single-point measurements of velocity moments:* A consequence of (3.24) is that, provided that the Reynolds number is sufficiently large, vertical profiles of single-point velocity moments ( $\overline{u_i^2}, \overline{v_i^2}, \overline{w_i^2}, \overline{uv}$ , and higher moments) should collapse to common curves independent of wall roughness, when normalized with  $u_\tau$  and  $\delta$ . Figure 3.9 shows a data set from Raupach (1981) which tests this directly. Turbulence measurements were made with an X-wire probe in zero-pressure-gradient boundary layers over a smooth surface and five fully rough surfaces of different densities  $\lambda$ , all formed over the same splitter plate by sequentially adding roughness elements (cylinders with  $h = 6$  mm and  $l_x = l_z = 6$  mm).

The normalized profiles of  $\overline{uv}$  (Fig. 3.9a) and the standard deviations  $\sigma_u$ ,  $\sigma_v$  and  $\sigma_w$  (Fig. 3.9b) all collapse to common curves except in the roughness sublayers close to the surfaces. The same collapse is evident in Fig. 3.9c for the normalized third moments or generalized skewnesses

$$\begin{aligned} M_{30} &= \overline{uuu} / \sigma_u^3 & M_{21} &= \overline{uuv} / \sigma_u^2 \cdot \sigma_w \\ M_{12} &= \overline{uvv} / \sigma_u \cdot \sigma_w^2 & M_{03} &= \overline{vvv} / \sigma_w^3 \end{aligned}$$



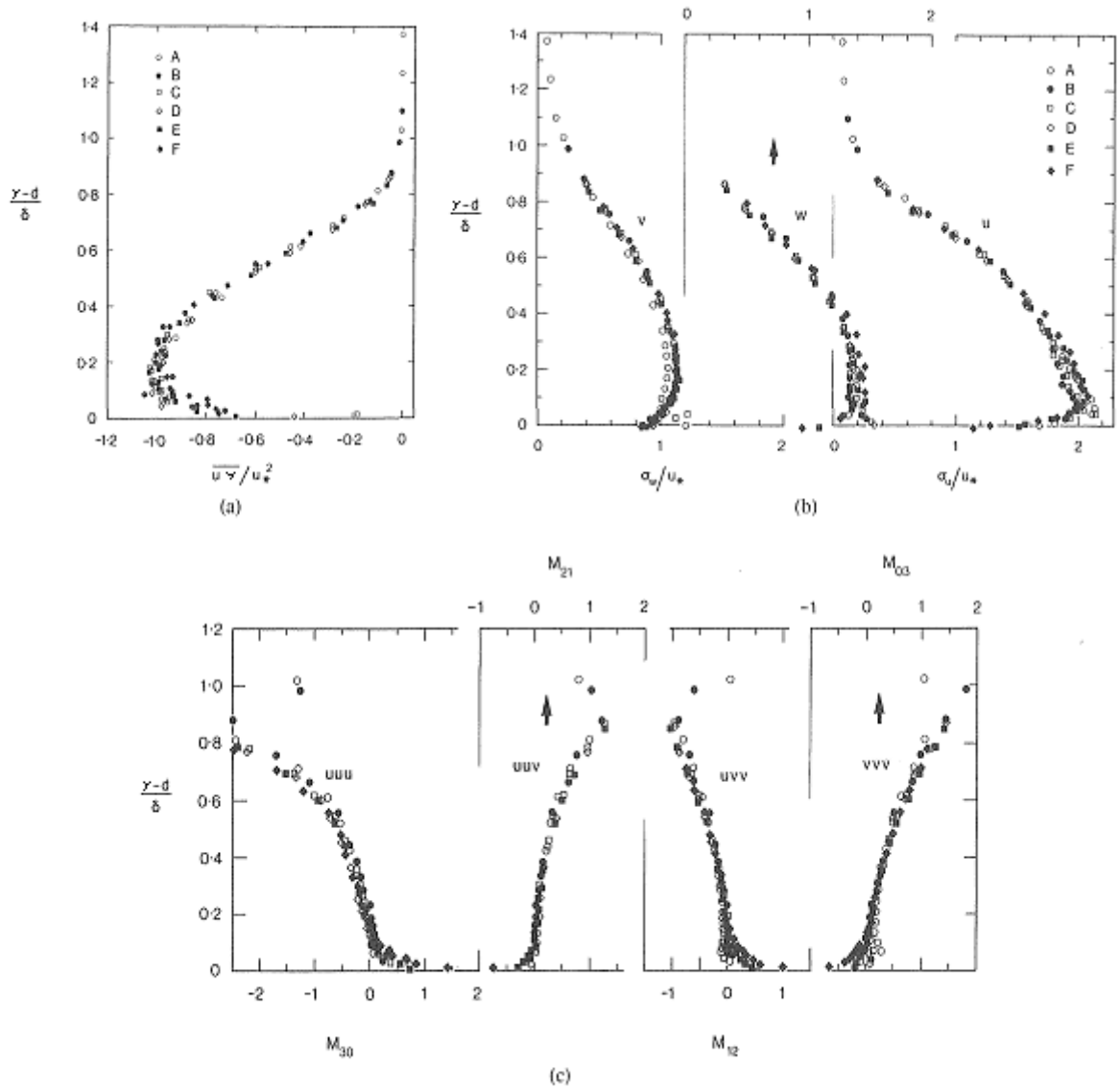


Fig. 3.9 - Profiles against  $Y/\delta$  of (a)  $\overline{uv}/u_\tau$ ; (b)  $\sigma_u$ ,  $\sigma_v$  and  $\sigma_w$  also normalized with  $u_\tau$ ; (c) the normalized third moments.

A similar collapse of second and third moments was observed by Andreopoulos and Bradshaw (1981), who compared boundary layers over smooth and sand-roughened walls. Kageyama et al (1982) presented a comparison between "d-type" roughwall and smooth-wall boundary layers in which the collapse, although reasonable, was not as complete as in Raupach's or Andreopoulos and Bradshaw's data (the main problem being with  $\sigma_u$  in the outer layer).

Care is required in making comparisons such as those above, because of (a) the influence of variations in flow configuration and (b) measurement errors. Regarding (a), configurational variations in boundary-layer flows can result from the choice between the tunnel wall or a splitter plate as the working surface, and also from the choice of boundary-layer tripping device, if any. Such variations are expected to influence mainly the largest

scales of motion and hence the velocity moments in the outer layer ( $Y \approx \delta$ ). Regarding (b), errors are well known to affect turbulence measurements with X-wire probes close to the surface, especially when the surface is rough (Raupach et al 1980, Perry et al 1987); these errors are responsible for the apparent decrease in  $|\overline{uv}|$  (and probably in  $\sigma_v$ , also) at low  $Y/\delta$  in Fig. 3.9, as discussed in more detail later. To minimize difficulties caused by both (a) and (b), the best approach is to compare profiles of velocity moments taken over a variety of surfaces (both smooth and rough) in the same experimental situation. All the experiments cited above are of this kind. Provided that the large-scale flow geometry (including the tripping technique) is held constant, problem (a) should be minimized. As for (b), constancy of instrumentation and experimental technique is no guarantee that measurement errors are minimized, or even independent of roughness or of position in the flow (since the errors worsen as turbulence intensity increases), but such constancy does remove gross variations from one experiment to another.

### 3.2.2. Turbulence velocity scales, length scales, and spectra

To obtain velocity and length scales for turbulence in the inner layer, Townsend (1961, 1976) used a set of arguments that have been very influential, to the extent that they have become part of the folklore of boundary-layer research. Therefore, the original argument is summarized here as accurately as possible. Townsend (1961) made the following "equilibrium layer hypothesis":

*In the inner layer, the local rates of turbulent kinetic energy production and dissipation are so large that aspects of the turbulent motion concerned with these processes are independent of conditions elsewhere in the flow.*

He called such a flow region an equilibrium layer; these layers exist not only in zero-pressure-gradient boundary layers but also in many other wall-bounded flows with pressure gradients or wall transpiration.

For zero-pressure-gradient boundary layers, dynamical constraints ensure that the inner or equilibrium layer is one of approximately constant stress. With usual boundary-layer approximations and at high Reynolds number (so viscous terms are negligible), the streamwise momentum equation in steady conditions is

$$U \frac{\partial U}{\partial x} + W \frac{\partial U}{\partial y} = -\frac{\partial P}{\partial y} - \frac{\partial \overline{uv}}{\partial y} \quad (3.25)$$

where  $P$  is the mean kinematic pressure. Given zero pressure gradient and slow streamwise development, this equation approaches  $\partial \overline{uv} / \partial y = 0$  as  $Y/\delta = (y - d)/\delta \rightarrow 0$  (but without going below the top of the roughness at  $y = h$ ). Hence there is a "constant-stress" layer near the surface in which  $\overline{uv}(y) \approx -u_\tau$ . In practice, the constant-stress layer is roughly the region  $h - d < y - d = Y < \delta/10$ . Its upper height limit can be regarded as the same as that of the inner layer, though both are only vaguely determined.

Townsend (1976) specified three conditions which must be satisfied in an equilibrium layer, the first being (clearly) that the turbulent kinetic energy budget must be in local equilibrium. To the same approximation as (3.25), the turbulent kinetic energy budget is

$$U \frac{\partial \overline{q^2}/2}{\partial x} + V \frac{\partial \overline{q^2}/2}{\partial y} = -\overline{uv} \frac{\partial U}{\partial y} - \frac{\partial \overline{vq^2}/2}{\partial y} - \frac{\partial \overline{vp}}{\partial y} - \varepsilon \quad (3.26)$$

Where  $\overline{q^2} = \overline{u^2} + \overline{v^2} + \overline{w^2}$  is twice the local turbulent kinetic energy,  $p$  is the fluctuating kinematic pressure, and  $\varepsilon$  is the average energy dissipation rate. Local equilibrium occurs when the advection terms (on the left-hand side) and transport terms (the second and third on the right-hand side) are negligible in comparison with local shear production and dissipation (the first and fourth terms on the right-hand side). Then, (3.26) reduces to

$$\overline{uv} \frac{\partial U}{\partial y} + \varepsilon = 0 \quad (3.27)$$

Local equilibrium is likely in the inner layer (but excluding the viscous or roughness sublayer) because the shear production term is proportional to  $1/Y$  and so increases rapidly as the surface is approached, but the advection and turbulent transport terms both remain small (in the case of transport, this assumption needs *a posteriori* confirmation).

The second requirement for an equilibrium layer is that the layer must be thin, with depth much less than  $\delta$ , so that the production and dissipation rates within it are independent of large eddies of scale  $\delta$ , and therefore of the large-scale flow geometry. Third, the shear stress variation across the layer must be small, to ensure that length scales associated with the height variation of shear stress are unimportant. In a zero-pressure-gradient boundary layer, this is satisfied by constancy of stress near the wall and the requirement that the layer be thin compared with  $\delta$ .

Given these constraints, dimensional analysis of the turbulent kinetic energy balance in an equilibrium layer can be based on  $u_\tau$  and  $Y$  as the only relevant velocity and length scales, since  $\delta$  has no influence because of the equilibrium-layer hypothesis, and the surface length scales ( $h$ ,  $L_i$ ,  $\nu/u_\tau$ ) are irrelevant by wall similarity (or Reynolds number similarity for a smooth wall). It follows that

$$\frac{\partial U}{\partial y} = \frac{u_\tau}{kZ} \quad -\overline{uv} = u_\tau^2 \quad \varepsilon = \frac{u_\tau^3}{kY} \quad (3.28)$$

Hence the argument yields the logarithmic mean velocity profile, recovers constant stress in the equilibrium layer, and also gives the additional result that the eddy length scale is proportional to  $Y$ , since in the last of (3.28)  $\varepsilon$  can be regarded as the cube of an eddy velocity scale divided by an eddy length scale. Townsend (1961) showed that these results for a zero-pressure-gradient boundary layer have counterparts for equilibrium layers in other wall-bounded flows with pressure gradients or wall transpiration, with modifications dependent on the stress distribution.

In the above argument, the restriction to "aspects of the turbulent motion concerned with energy production and dissipation" is crucial. If this restriction were not imposed, all aspects of the turbulence would scale on  $u_\tau$  and  $Y$  in the inner layer, so that the ratios  $\sigma_u/u_\tau$ ,  $\sigma_v/u_\tau$  and  $\sigma_w/u_\tau$  would all be universal constants independent of both surface type and pressure gradient. However, this is observed not to be true, especially in equilibrium layers with a range of pressure gradients (Bradshaw 1967a, 1967b). Observations such as these led Bradshaw (1967b) to divide the inner-layer turbulence into two components: a

universal, active component, responsible for vertical turbulent transfer and scaling with  $u_\tau$  and  $Y$ , and a larger-scale, inactive component arising from the effect of the outer-layer turbulence upon the inner layer. Bradshaw attributed the inactive component partly to irrotational motions due to pressure fluctuations generated in the outer layer, and partly to the large-scale vorticity field of the outer-layer turbulence which the inner layer sees as unsteadiness in the mean flow, or large-scale horizontal sloshing motions. These contribute to  $\sigma_u$  and  $\sigma_w$  but not to  $\sigma_v$  or  $\overline{uv}$ .

Following Townsend and Bradshaw, Perry and Abell (1977) and Perry et al (1986) developed scaling arguments to predict the form of the  $u$ ,  $v$ , and  $w$  turbulence spectra  $\phi_{uu}(k)$ ,  $\phi_{vv}(k)$ ,  $\phi_{ww}(k)$  (where  $k$  is the streamwise wavenumber), and thence (by integrating the spectra over  $k$ ) the variances of  $u$ ,  $v$ , and  $w$  as functions of height. They considered three spectral ranges, corresponding to inactive, active and fine scale eddies (in order of increasing  $A$ ), which respectively obey outer-layer, innerlayer, and Kolmogorov scaling:

$$\begin{aligned} \text{A: outer-layer scaling, on } u_\tau, \delta & \text{ — inactive eddies,} \\ \text{B: inner-layer scaling, on } u_\tau, Y & \text{ — active eddies,} \\ \text{C: Kolmogorov scaling, on } \varepsilon, \nu & \text{ — fine-scale eddies,} \end{aligned} \quad (3.29)$$

The ranges overlap in two wavenumber intervals AB and BC (where A overlaps B and B overlaps C, respectively). In range BC (usually called the inertial subrange) all spectra are dimensionally constrained to follow the Kolmogorov law  $\phi \propto \varepsilon^{2/3} k^{-5/3}$ , whereas in range AB, the  $u$  and  $v$  spectra are proportional to  $k^{-1}$ . Ranges A and AB do not exist in the  $w$  spectrum since the inactive eddies have negligible vertical motion.

Qualified support for the spectral scaling hypothesis (3.29) is provided by spectral measurements in both laboratory boundary layers and the atmospheric surface layer. Comprehensive laboratory spectral measurements were obtained by Perry et al (1987) over smooth and mesh-roughened walls. Figures 3.10 and 3.11 show their spectra over both wall types, which collapse in the outer (A, AB) and inner (AB, B, BC) spectral ranges when normalized with outer-layer and inner-layer scales, respectively. The Reynolds number  $\delta_+$  (sometimes called the von Karman number) in these experiments was between about 500 and 7000, not high enough to produce broad spectra with extensive  $k^{-1}$  and  $k^{-5/3}$  behaviors in spectral ranges AB and BC, respectively, a typical limitation in the laboratory. A further

problem is the spread of convection velocities at low wavenumbers, to which Perry et al attributed the less than satisfactory spectral collapse with outer-layer scaling over the rough wall (Fig. 3.11b). Considering these difficulties, the spectral data in Figs. 3.10 and 3.11 offer reasonable support for (3.29).

Atmospheric surface (inner) layer spectra are much broader than laboratory spectra, as  $\delta_+$  is typically  $10^7$  or more. Extensive spectral data have been measured in several major field experiments, one of the largest being at Kansas in 1968 (Kaimal et al 1972, Kaimal 1973). These data show that  $u$ ,  $v$ , and  $w$  spectra conform well to inner-layer and Kolmogorov scaling (ranges B and C), and exhibit extensive inertial subranges (BC) with spectra proportional to  $k^{-5/3}$ . However, the atmospheric  $u$  and  $w$  spectra do not generally conform well to the  $k^{-1}$  spectral slope prediction for range AB (Kaimal et al 1972), although a few atmospheric spectra do show both  $k^{-1}$  and  $k^{-5/3}$  regions, such as spectra measured over the sea by Pond et al (1966). A possible reason for the general absence of a  $k^{-1}$  region is that

outer-layer (range A) scaling is more complicated in the atmosphere than the laboratory, because of the effect of buoyancy forces which are almost always important for the largest eddies in the atmospheric boundary layer. These introduce an extra length scale, the Monin-Obukhov length  $L$ , into the scale analysis; the influence of  $L$ , or the associated dimensionless parameter  $Y/L$ , is largest at low wavenumbers, and therefore in ranges A and AB.

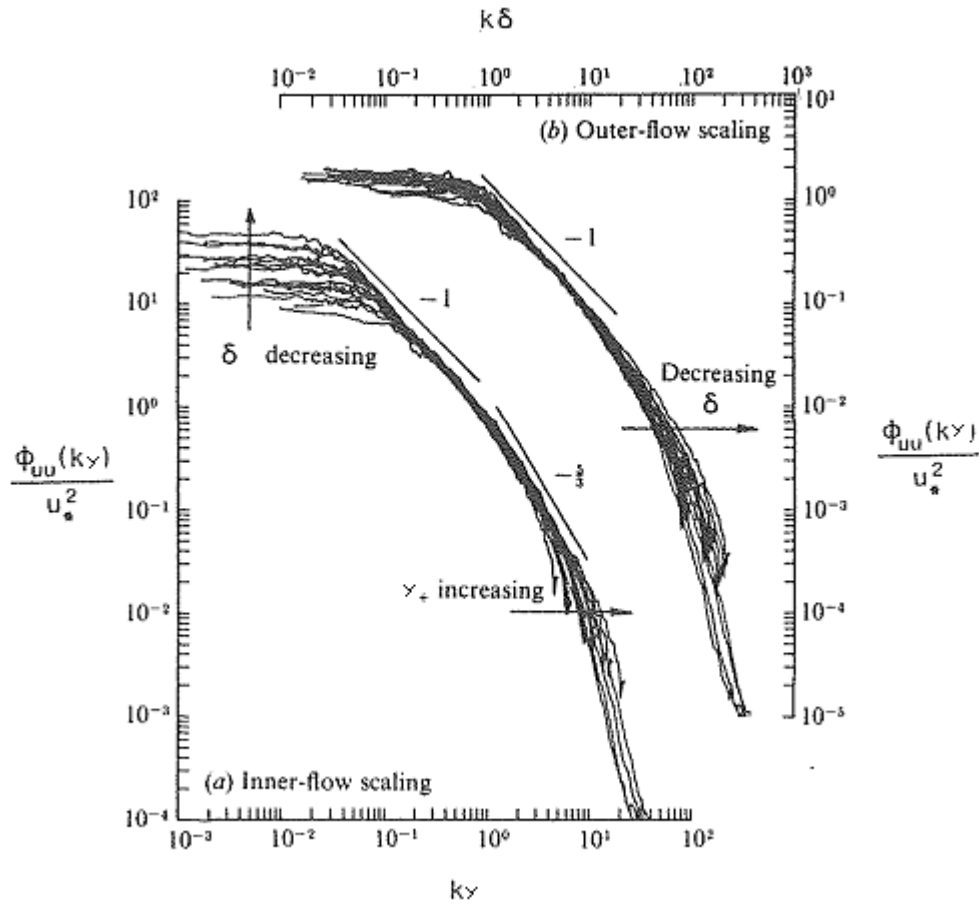


Fig. 3.10 -  $u$  spectra for varying values of  $Y/\delta$  in a smooth-wall boundary layer.

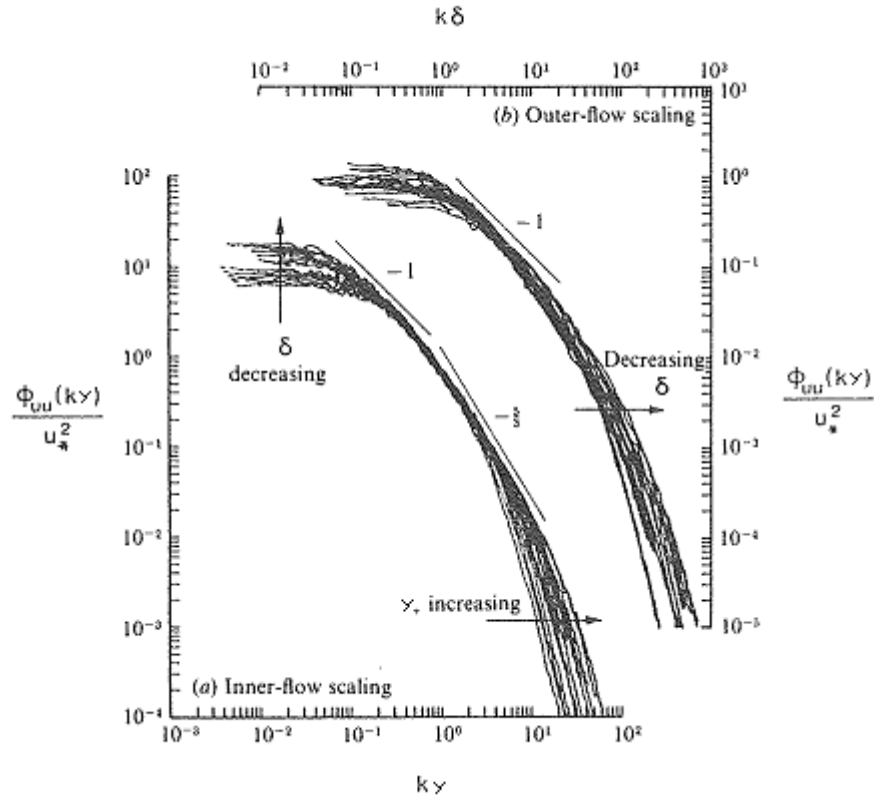


Fig. 3.11 -  $u$  spectra for varying values of  $Y/\delta$  in a rough-wall boundary layer.

The spectral scaling (3.29) has implications for the variances. By integrating over all spectral ranges, Perry et al (1986) used (3.29) to derive the following behavior for the variances in the inner layer:

$$\begin{aligned} \overline{u^2}/u_\tau^2 &= B_1 - A_1 \cdot \ln(Y/\delta) - E \cdot Y_+^{-1/2} \\ \overline{v^2}/u_\tau^2 &= B_2 - A_2 \cdot \ln(Y/\delta) - (4/3) \cdot E \cdot Y_+^{-1/2} \\ \overline{w^2}/u_\tau^2 &= A_3 - (4/3) \cdot E \cdot Y_+^{-1/2} \end{aligned} \quad (3.30)$$

The constants  $A_1, A_2, A_3$  and  $E$  are universal for all inner layers, whereas  $B_1$  and  $B_2$  depend on the large-scale flow geometry (thus,  $B_1$  and  $B_2$  are different for boundary layers, pipes, ducts, and so on). Perry et al (1987) deduced values for all these constants from their spectral data, obtaining slightly different values over smooth and rough walls for reasons which they attributed to measurement errors. Their rough-wall values were  $A_1 = 1.26, A_2 = 0.63, A_3 = 1.78, B_1 = 2.01, B_2 = 1.08$ , and  $E = 7.50$ . They emphasized that, for  $v/u_\tau \ll Y \ll \delta$  and  $h \ll Y \ll \delta$ , the scaling laws for smooth and rough surfaces should be indistinguishable; this is a requirement of the wall similarity hypothesis.

The strongest challenge has come from Krogstad et al. (1992) and Krogstad & Antonia (1994). They found that the one-point correlation times for all the velocity components are about twice shorter for rough than for smooth boundary layers below  $y/\delta < 0.5$ . Although the height of their mesh roughness,  $\delta/h \approx 50$  ( $\Delta U^+ = 11$ ), is marginal according to the criteria developed above, it is a little too large to dismiss the results on those grounds.

That observation has attracted a lot of interest, but it has been difficult for other investigators to reproduce it. Krogstad et al. (1992) and Krogstad & Antonia (1999) published frequency spectra for  $u$  and  $v$  over the same rough wall used by Krogstad & Antonia (1994), and there is little difference in the positions of their smooth and rough spectral peaks at  $y/\delta = 0.4$ – $0.5$ . The correlation time is only indirectly related to the spectral peak, but this disagreement suggests that the differences between rough and smooth flows are not associated with the most energetic velocity structures.

Nakagawa & Hanratty (2001) studied a channel over two-dimensional sinusoidal roughness ( $\delta/h \approx 60$ ,  $\Delta U^+ = 9$ ), and found correlation lengths,  $L/\delta$ , which are equal to those in smooth channels. Sabot et al. (1977) studied a very rough pipe with spanwise fences ( $\delta/h = 15$ ,  $\Delta U^+ = 17$ ) and found that the streamwise integral lengths for  $u$  and  $v$  change little with roughness. Comparing correlation lengths with times requires choosing an advection velocity, which changes both with the wavelength and with the distance to the wall (Krogstad et al. 1998). The question is not trivial, and the ratio between the smooth and rough times in Krogstad & Antonia (1994) varies between 1.6 and 2.5 depending on whether they are normalized with the friction, free-stream, or local velocities. The advection velocity also changes from rough to smooth flows, as a natural consequence of modifying the mean velocity profile. For example, Sabot et al. (1977) found that the advection velocity of the large scales is 1.3 times faster in their smooth pipe than in the rough one. However, none of these corrections is enough to fully account for the observed differences in the correlation times.

Krogstad & Antonia (1994) also measured the inclination angle of the twopoint correlation function of  $u$  between two  $y$  locations. They obtain  $38^\circ$  in the rough case against  $10^\circ$  in the smooth one. This disagreement is not as worrying as the one discussed above because it is done fairly near the roughness layer and may be a local effect, but Nakagawa & Hanratty (2001) found no change in this quantity. Because they used particle image velocimetry (PIV), which is a purely spatial procedure, they suggested that their disagreement with Krogstad & Antonia (1994) may be due to the previously discussed ambiguity of the advection velocity. Using different assumptions on the velocities reduces the angle to about  $25^\circ$  which, while still high, is closer to the smooth one. Because of these experimental uncertainties, and because of the marginal value of  $\delta/k$  in all these cases, the claim of large changes in the length scales above the roughness layer requires further confirmation.

### 3.2.3 The attached-eddy hypothesis

Earlier, Townsend (1976, pp 152-154) had obtained (3.30) (but without the viscous terms in  $y_+^{-1/2}$ ) from a different argument based on his "attached-eddy hypothesis." according to which *the turbulent flow field is a superposition of geometrically similar eddies with velocity distributions*

$$u_i(x) = u_0 \cdot f_i\left(\frac{x - x_a}{y_a}\right) \quad (3.31)$$

where  $x_a = (x_a, y_a, z_a)$  is the center of a particular eddy and  $u_0$  is its velocity scale. The term "attached" implies that all eddies are not only geometrically similar but have the same geometrical relationship with the wall, scaling with the center height  $y_a$ . By ensembleaveraging an eddy field consisting of a random superposition of eddies of the

form (3.31), imposing a continuity condition on  $f$  to account for the presence of the wall, and requiring  $\overline{uv}(z) = u_\tau^2 = \text{const}$ , Townsend derived the high Reynolds-number limit of (3.30) without further specifying  $f_i$ .

Perry and Chong (1982) were more specific about  $f_i$ , invoking flow visualizations of hairpin vortices in a smooth-wall boundary layer by Head and Bandyopadhyay (1981) to suggest a model attached eddy consisting of a " $\Lambda$ -vortex" inclined with the shear and with legs trailing along the wall. Although this structure leads to the spectral scaling laws (3.29), and to (3.30) for the velocity variances, it is apparent that many other choices for  $f_i$  lead to similar results. This suggests that observations of spectra and variances alone are insufficient to specify details of the eddy structure beyond those implied by the dimensional arguments given above.

### 3.2.4 Observations of velocity variances

One test of the wall similarity, equilibrium-layer, and attached-eddy hypotheses is a comparison of their predictions with laboratory and atmospheric data on the velocity variances  $\overline{u^2} = \sigma_u^2$ ,  $\overline{v^2} = \sigma_v^2$  and  $\overline{w^2} = \sigma_w^2$ . The wind tunnel data usually are at a fixed height (for instance  $Y/\delta = 0.1$ ) whereas the field data are generally from various heights in the atmospheric surface layer, typically in the height range 5-20 m.

These data are generally consistent with the wall similarity hypothesis. In laboratory boundary layers, the ratios  $\sigma_u/u_\tau$ ,  $\sigma_v/u_\tau$  and  $\sigma_w/u_\tau$  take values (at  $Y/\delta = 0.1$ ) of about  $2.1 \pm 0.2$ ,  $1.4 \pm 0.1$ , and  $1.1 \pm 0.1$ , respectively. Although there is scatter in the data, attributable to measurement errors, there is also a weak Reynolds number dependence consistent with that predicted by (3.30). There is some laboratory evidence for a dependence of  $\sigma_u/u_\tau$  and  $\sigma_v/u_\tau$  on  $Y/\delta$ , as suggested by (3.30), but the measurement problems are substantial. The careful measurements of Perry et al (1987) provide a good example: their X-wire turbulence data supported (3.30) quite well for the  $v$  component, partially for the  $u$  component, and rather poorly for the  $w$  component. Their work eliminated some of the problems with X-wire probes that had afflicted earlier experiments. However, they concluded that the remaining measurement difficulties (associated mainly with limited acceptance angles, crosstalk between  $v$  and  $v$ , and finite wire length) were great enough to account for the fact that (3.30) was only partly successful in describing their data. Later, Perry et al (1988) reported reasonable agreement between slightly modified forms of the third relation in (3.30) and carefully selected data for  $\sigma_v/u_\tau$ ; the data selection ensured that spatial resolution and cone angle problems were minimized and that the X-wire probes yielded values of  $\overline{uv}$  consistent with Clauser-chart or Preston-tube values.

In the atmosphere over grassland sites in flat terrain,  $\sigma_u/u_\tau$ ,  $\sigma_v/u_\tau$  and  $\sigma_w/u_\tau$  take values of about 2.4, 1.25, and 1.9, respectively, slightly higher than the typical laboratory values (2.1, 1.1, and 1.4, respectively). This trend is qualitatively consistent with (3.30) because the atmospheric data are obtained at lower  $Y/\delta$  and higher  $Y_+$  than the laboratory data, with both factors tending to increase the variances according to (3.30). An additional dynamical influence on the large-scale, inactive motions in the atmospheric planetary boundary layer is the Ekman spiral resulting from the rotation of the earth, which introduces a lateral, cross-isobaric shear amounting to a shift in wind direction of typically  $20^\circ$  through the depth of the planetary boundary layer (typically of order 1 km). This particularly affects  $\sigma_w$  and contributes to the larger difference in  $\sigma_w/u_\tau$  between laboratory and atmosphere relative to the other two components.



One significant point is the decrease in the values of  $\sigma_u/u_\tau$ ,  $\sigma_v/u_\tau$  and  $\sigma_w/u_\tau$  over very rough surfaces in the atmosphere (forests, corn crops) relative to grassland atmospheric or wind tunnel values. Over very rough atmospheric surfaces, the ratios are approximately 1.9, 1.2, and 1.4 at  $y \approx 2h$  and as low as 1.5, 1., and 1.3 at  $y \approx h$ . This is understandable because fetch and tower height limitations inevitably restrict measurement heights in these cases to the roughness sublayer ( $y$  less than about  $2h$ ). Hence, comparison with (3.30) and with other experiments, those which pertain to the inertial sublayer or equilibrium layer only, is not appropriate. However, there is significance in the large decreases in  $\sigma_u/u_\tau$ ,  $\sigma_v/u_\tau$  and  $\sigma_w/u_\tau$  in the roughness sublayer over tall vegetation. As argued later, the flow near the top of the canopy is dynamically more similar to a plane mixing layer than a boundary layer, because of a strong inflection point in the mean velocity profile. The values of  $\sigma_u/u_\tau$ ,  $\sigma_v/u_\tau$  and  $\sigma_w/u_\tau$  near  $y = h$  reflect this, as they bear little relationship to typical inertial-sublayer values and are much closer to typical values from the core of a plane mixing layer (Wyganski and Fiedler 1970).

### 3.2.5 Wake Intensity

Another indication of the effect of the roughness on the outer part of the boundary layer is its effect on the wake parameter  $\Pi$ . The classical result is again that  $\Pi$  changes little between rough and smooth boundary layers at the same Reynolds number (Hama 1954, Clauser 1956), but later authors reported substantial deviations. One problem is how to define  $\delta$  in flows without a well-defined logarithmic layer, such as those with low  $\delta^+$  or  $\delta/k$ , and the results from different investigators are not always comparable.

Tani (1987) reviewed several data sets using a uniform analysis scheme, and the conclusion from his work is that most differences are due to low values of  $\delta/k$ . Although for several  $k$ -surfaces he found  $\Pi \approx 0$ –0.8 when  $\delta/k < 60$ , they all tend to  $\Pi \approx 0.45$  when  $\delta/k > 100$ . This is close to the value  $\Pi \approx 0.52$  for smooth walls (Fernholz & Finley 1996).

$D$ -type surfaces are more interesting in this respect because the claim that their roughness length scale is proportional to the boundary-layer thickness suggests that the effect of the roughness might be felt throughout the layer. Tani (1987) compiled some of those cases and found  $\Pi = 0.6$ –0.7 for all of them, which is higher than the smooth-wall value, although only the data from Bandyopadhyay (1987) have  $\delta/k \geq 100$ . As with most available results for  $d$ -roughness, this one is tantalizing but requires confirmation.

### 3.2.6 Theoretical models

Numerical simulations, which have done so much to clarify other areas of turbulence, have still not left their mark on the understanding of rough-walled flows. There are numerous modifications to Reynolds-averaged simulation models that include roughness effects (Patel 1998, Durbin et al. 2001), but they are a posteriori applications of physical insight that are beyond our scope. From the point of view of a priori simulations the problem is computational cost. To be reasonably free from direct roughness effects we need  $\delta/h \geq 50$ , and to have well-developed roughness we should have  $h^+ \geq 80$ . To have a well-defined rough turbulent flow that is neither transitional in the sense of low  $h^+$ , nor of insufficient boundary layer thickness, we therefore need  $\delta^+ \geq 4000$ . The largest direct simulations of wall-bounded flows have at present  $\delta^+ \approx 2000$ . Large-eddy simulations could help in raising the Reynolds number, but they imply modeling the small scales, which is dangerous when trying to clarify the effect of small-scale roughness. Direct simulations

limited in one of the two parameters just mentioned are beginning to appear, (Bhaganagar & Kim 2002, Lee 2002, Leonardi et al. 2002, Nozawa et al. 2002). Direct simulations of the flow over riblets, in which the regime of interest is that of transitional  $h^+$ , have been available for some time (Chu & Karniadakis 1993, Choi et al. 1993, Goldstein et al. 1995), but they also have low  $\delta/h$ . In all these cases the emphasis is on the exact representation of the flow over the roughness elements, and on the details of the flow within the roughness layer. An alternative approach, which has to be applied with care because it involves modeling, but which bypasses some of the limitations of strict direct simulations, is to substitute the effect of the roughness layer by an “equivalent” wall-boundary condition. Low- $h^+$  riblets can be substituted by an offset between the locations of the streamwise and spanwise no-slip conditions. If we choose our origin at the no-slip position for  $u$ , and assume that the instantaneous velocity profile stays linear near the wall, we can write this as

$$w(x, 0, z) + \alpha \cdot \partial_y w(x, 0, z) = 0 \quad (3.32)$$

where  $\alpha$  is an adjustable parameter. Choi et al. (1993) used boundary conditions of this type as control devices to manipulate the skin friction in channel flows, obtaining changes in the drag coefficient of the order of  $\pm 50\%$  ( $h_s^+ \approx \pm 60$ ). Jiménez et al. (2001) used mixed boundary conditions that can be put in the form of Equation 15 for the wall-normal velocity to model the effect of a perforated wall. There is also in that case a large increase in the skin friction, which was traced to the appearance of large-scale instabilities of the mean velocity profile, in the form of large spanwise structures essentially spanning the full boundary-layer thickness. They originate from a lightly damped linear mode of the mean velocity profile over an impermeable wall, and connect to the Kelvin-Helmholtz instability of inflectional profiles in the limit of infinite permeability. Finnigan (2000) invoked similar inflectional instabilities to explain the properties of the roughness layer above plant canopies. It is interesting that such models generate effects similar to those of roughness without considering the details of the individual roughness elements, and that they produce length scales which are only linked to averaged properties of the wall. This brings to mind  $d$ -rough behavior, where the scale of the structures is determined by the boundary-layer properties instead of by the surface geometry. Although the details are beyond the space available in this chapter it is possible to devise artificial boundary conditions of the type of Equation 3.32 for  $v$  that arise naturally as approximations of the flow along the grooves of a  $d$ -wall under the effect of spanwise pressure gradients. Their stability has not been studied in detail but, in simple inviscid cases, they lead to instabilities of the mean flow for which the most unstable eigenmodes are large streamwise velocity streaks.

The flow over rough walls is generally too complicated to sustain streaks like the ones found over smooth walls, but Liu et al. (1966) and Djenidi et al. (1999) observed longitudinal streaks over  $d$ -surfaces. No direct simulations exist of fully turbulent flows with averaged boundary conditions designed to mimic high- $h^+$  directional wall roughness, but considerations such as the ones above suggest that they could help to clarify the dynamics of rough-wall turbulence in general, and of  $d$ -roughness in particular.

### 3.3 FLOW CLOSE TO AND WITHIN THE ROUGHNESS

Here the focus shifts from the overlying boundary layer to the flow in the roughness sublayer, where the roughness has an explicit dynamical influence and wall similarity does not apply. In this layer, especially in the region  $y < h$ , available mean and turbulent velocity data are mainly from field vegetation canopies or wind tunnel models of canopies. This bias occurs because (as already mentioned) most of the more traditional types of "engineering" rough surface, such as sandgrain roughness, do not admit measurements within the roughness, exceptions being flow visualization results from the region within the cavities of two-dimensional roughness (Liu et al 1966, Perry et al 1969). Therefore, most of the present section is drawn from field and wind-tunnel work on vegetation, though references to other types of roughness will be made wherever possible.

#### 3.3.1 Mean velocity

*Above the roughness:* As height decreases, the mean velocity profile begins to depart from the logarithmic profile law in the layer  $h < y < y_w$ , where  $y_w$  (dependent on geometric details of the roughness) is the upper height limit of the roughness sublayer. Laboratory studies over three-dimensional roughness (O'Loughlin 1965, O'Loughlin and Annambhotla 1969, Mulhearn and Finnigan 1978, Raupach et al 1980, 1986) agree that  $y_w$  is between  $2h$  and  $5h$ , and that in the layer  $h < y < y_w$  the shear  $dU/dy$  is less than the one obtained from the inertial-sublayer value. Because the momentum flux in the roughness sublayer is (nearly) constant with height for  $y > h$ , from (3.25) et seq, the reduced shear implies an enhanced turbulent diffusivity  $K$  for momentum in the roughness sublayer, relative to the inertial-sublayer form  $K = ku_t(Y - d)$ . An approximate form for  $K$  is  $K = ku_t(y_w - d)$ , independent of height for  $h < y < y_w$  (Raupach et al 1980).

Field work on the mean velocity profile close to rough surfaces has been prolific in the area of forest meteorology (Thorn et al 1975, Garratt 1978, 1980, Raupach 1979, Cellier 1984, 1986, Chen and Schwerdtfeger 1989, Shuttleworth 1989). The findings are similar to those from laboratory work, although the scatter is greater. The roughness-sublayer depth  $y_w$  has been found to be as great as  $5h$  for some rough, scrublike vegetated surfaces (Garratt 1980), but for closely spaced canopies with  $D \ll h$  such as wheat canopies,  $y_w$  is a little above  $h$ , and the near-surface enhancement of  $K$  above its inertialsublayer value is negligible (Thom 1971). To explain the variation in  $y_w$  Raupach et al (1980) suggested that  $y_w$  increases with roughness-element lateral dimension  $l_z$ ; Garratt (1980), on the other hand, suggested that  $y_w$  increases as the mean spacing  $D$  between plants increases.

It is worth noting the extension of these findings to the transfer of scalars, especially heat and water vapor. Just above the canopy, the eddy diffusivities  $K_H$  (for heat) and  $K_E$  (for water vapor) are found to exceed the momentum diffusivity  $K$  by factors between 2 and 4 (Thom et al 1975, Raupach 1979, Garratt 1980, Shuttleworth 1989). This contrasts with the inertial-sublayer situation where all diffusivities are nearly equal in thermally neutral conditions.

Several physical mechanisms contribute to the behavior of  $K$ ,  $K_H$  and  $K_E$  just above the roughness. First, the vertical velocity eddy length scale  $L_v$  is proportional to  $(y - d)$  in the inertial sublayer but scales with  $h$  (or with  $h - d$ ) in the roughness sublayer, taking values there which are larger than the extrapolated inertial-sublayer prediction. This is sufficient to account for the enhanced eddy diffusivities in the roughness sublayer, since the eddy

diffusivity is of order  $\sigma_v L_v$ . A second, closely related factor is the dynamical resemblance of the flow near  $y = h$  to a plane mixing layer rather than a boundary layer, which provides a reason for the difference between the momentum and scalar diffusivities, as the turbulent Prandtl number  $K/K_H$  is known to be substantially less than 1 in a mixing layer (Townsend 1976). Third, large eddies (inactive motions) make the flow nonstationary on the time scales of the active eddies responsible for vertical transfer; Townsend (1976, p 156) showed that this leads to an increase in the eddy diffusivity by a factor  $[1 + (\sigma_u^2 + \sigma_w^2)/(2U^2)]$ . Finally, working in the opposite direction, persistence of the turbulent motion on time scales of order  $L_v/\sigma_v$  leads to a reduction in effective vertical eddy diffusivities within heights of order  $L_v$  of sources or sinks of scalars and momentum (Deardorff 1978, Raupach 1987, 1989b). The profiles of eddy diffusivity just above (and within) the roughness are the result of all of these mechanisms.

*Within the roughness:* The mean wind profile within the roughness or canopy is exemplified in Fig. 3.12a by several profiles from field vegetation canopies and wind-tunnel models of vegetation. In general,  $U(y)$  is strongly sheared near  $y = h$ , with both  $U$  itself and the shear  $dU/dy$  attenuating within the canopy at a rate depending on the roughness density  $A$  and other geometrical properties. The upper part of the within-canopy  $U(y)$  profile is fairly well approximated by the empirical "exponential wind profile":

$$\frac{U(y)}{U(h)} = \exp\left[-\alpha\left(1 - \frac{y}{h}\right)\right] \quad (3.33)$$

where the coefficient  $\alpha$  tends overall to increase with  $\lambda$ , but with considerable scatter.

In the lower part of the canopy, some workers have reported "bulges" in the profile of  $U(y)$ ; see, for example, the data for Uriarra Forest in Fig 12a. Such a bulge, if real, implies countergradient momentum transfer in the region where  $dU/dy < 0$  (Shaw 1977). However, most of these data were gathered with cup anemometers which are prone to substantial overspeeding in the highly turbulent flow within the canopy, so that observations of bulges in  $U(y)$  within the canopy provide no proof of countergradient momentum transfer. By contrast, there is direct experimental evidence for countergradient scalar (heat, water vapor, and  $\text{CO}_2$ ) transfer, from measurements in Uriarra forest reported by Denmead and Bradley (1985, 1987). For a theoretical explanation, see Raupach (1987, 1989b).

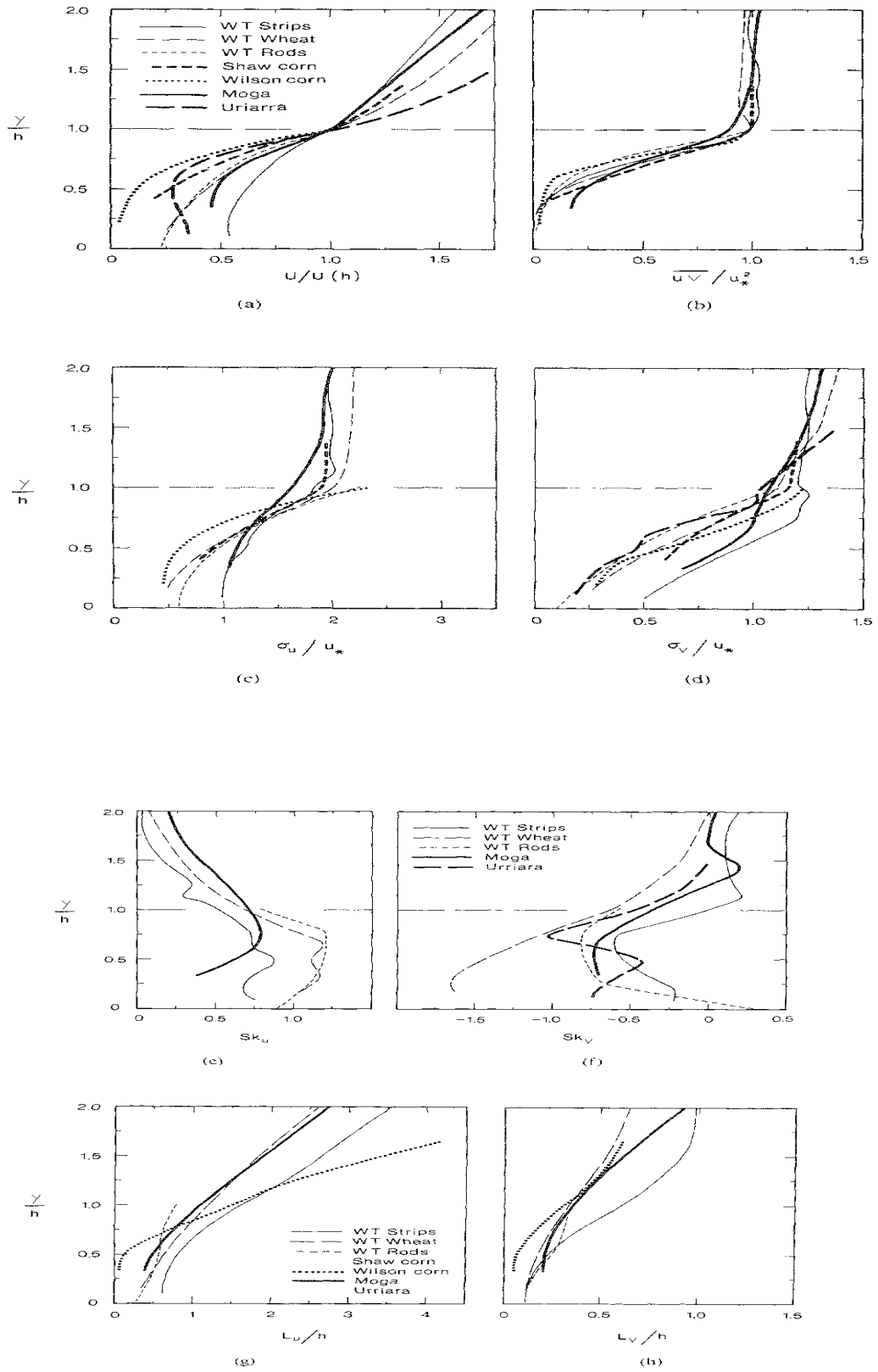


Fig. 3.12 - Profiles of  $y/h$  versus different functions, for different experiments. WT denotes wind tunnel. See Raupach (1988) for primary references.

### 3.3.2 Basic properties of the turbulence

Because the turbulence within the roughness sublayer has a very high intensity  $\sigma_u/U$  (typically between 0.5 and 5), its measurement is difficult, both in field canopies and in windtunnel models. Appropriate instrumentation includes sonic anemometers (Coppin and Taylor 1983) or servo-driven splitfilm anemometers (Shaw et al 1973) in the field, or coplanar triple-wire probes in wind-tunnel models (Kawall et al 1983, Legg et al 1984). This type of instrumentation has been developed only in the last 15 years or so. The earliest turbulence measurements in vegetation canopies were restricted to fluctuations in the horizontal wind component or the total wind speed (Uchijima and Wright 1964, Allen 1968, Meroney 1968, 1970, Sadeh et al 1971), and hence provided no direct information on the vertical eddy fluxes or vertical turbulent transfer. Only fairly recently, beginning with the turbulence measurements of Shaw et al (1974) in corn, has a substantial body of data been assembled on all three components of the turbulent wind field in canopies. Here we draw on a collation of seven comprehensive experiments on canopy turbulence: two in field crops, two in forests, and three in windtunnel model canopies. Figure 3.12 shows, for all seven canopies, roughness-sublayer profiles of velocity statistics, plotted against normalized height  $y/h$ . The mean velocity  $U(y)$  is normalized with  $U(h)$  and the turbulence statistics with  $u_\tau$ . Despite the wide range of canopy types represented, these measurements have some well-defined features in common. Properties of the mean velocity  $U(y)$  (Fig. 3.12a), especially its inflectional form, have already been noted. The normalized standard deviations  $\sigma_u/u_\tau$  and  $\sigma_v/u_\tau$  (Figs. 3.12c and 3.12d) approach typical surface-layer values (2.4 and 1.25, respectively) only well above the canopy; both ratios fall with decreasing  $y$ , so that at  $y = h$ ,  $\sigma_u/u_\tau$  is between 1.5 and 2.0 and  $\sigma_v/u_\tau$  between 1.0 and 1.1. Within the canopy,  $\sigma_u/u_\tau$  and  $\sigma_v/u_\tau$  fall more strongly as  $y$  decreases. The profile of shear stress  $-\overline{uv}$  (Fig. 3.12b) exhibits a constant-stress layer above the canopy and rapid attenuation as  $y$  decreases within the canopy. The correlation coefficient  $r_{uv} = \overline{uv}/(\sigma_u\sigma_v)$ , which is about -0.33 in the surface layer well above the canopy, increases with decreasing  $y$  to a maximum magnitude of about -0.5 at  $y = h$ ; with further decrease in  $y$ ,  $r_{uv}$  attenuates rapidly within the canopy. Hence, the turbulence at the top of the canopy is very efficient at downward momentum transfer, but deep within the canopy, the turbulence loses its ability to transfer momentum as well as its overall strength.

Figures 3.12e and 3.12f show the skewnesses of  $u$  and  $v$ ,  $Sk_u$  and  $Sk_v$  (in notation used in other sections  $Sk_u = M_{30}$  and  $Sk_v = M_{03}$ ). Despite variations due to morphological differences, the clear overall trend is for  $Sk_u$  to be strongly positive and  $Sk_v$  strongly negative within and just above the canopy, indicating that the strongest turbulent events there are downward-moving gusts. This indication can be made precise by quadrant analysis. Kurtoses for  $u$  and  $v$ , not shown here, reveal the same trend towards very high intermittency in the canopy (Maitani 1979).

The single-point Eulerian length scales  $L_u$  and  $L_v$  can be estimated from the single-point  $u$  and  $v$  integral time scales by applying Taylor's frozen-turbulence hypothesis:

$$L_v = \frac{U}{\sigma_v^2} \int_0^\infty \overline{v(t) \cdot v(t+\tau)} d\tau \quad (3.34)$$

and similarly for  $L_v$ . Near  $y = h$ ,  $L_u$  is of order  $h$  and  $L_v$  of order  $h/3$  (Figs. 3.12g and 3.12h), so that the turbulence length scales are comparable with  $h$ . It follows that the gusts inferred from the skewness profiles are large structures, coherent over streamwise and vertical distances of order  $h$ . The existence of such motions can be verified visually by watching "honami," the traveling wind waves seen on fields of grass, wheat, or barley on windy days (Inoue 1955, Finnigan 1979a, b).

Figure 3.12 suggests that the dominant velocity and length scales for the turbulence in the canopy are  $u_\tau$  and  $h$  (or the closely related length scale  $h - d$ ). These scales provide an approximate collapse of turbulence data from experiments in which  $h$  ranges over a factor of 400 and  $u_\tau$  over a factor of 10 or more. The scatter in the data indicates the influence on the canopy turbulence of other length and velocity scales related to canopy morphology, the fluttering of leaves and the waving of whole plants, and viscous (Reynolds number) effects which influence the drag on individual leaves (Thom 1968, 1971). In the field, an additional important complication is buoyancy, though its effects are absent from the data in Figure 3.12 which pertain only to thermally neutral or slightly unstable daytime conditions.

### 3.3.3 Measurement problems

We have referred several times to measurement problems in the high-intensity turbulence near and within the roughness. These have proved troublesome and (at times) confusing, especially in laboratory situations where X-wire probes have been the main turbulence sensors. The most obvious symptom is a decrease in the measured shear stress  $-\overline{uv}$  just above  $y = h$ , seen in most laboratory measurements over rough walls with X-wire probes. Examples are the X-wire TTvP profiles measured by Antonia and Luxton (1971a, b, 1972), Mulhearn and Finnigan (1978), and Raupach et al (1980) (see Fig. 3.9). Such a decrease, if real, would violate momentum conservation in the constant-stress layer close to the surface, unless an extra momentum transfer mechanism exists in the roughness sublayer.

There has been speculation that such a mechanism could be a systematic, time-averaged spatial variation in the mean velocity field imposed by the horizontal heterogeneity of the canopy, leading to a horizontally averaged momentum flux  $\langle U''V'' \rangle$ . Here, angle brackets denote a horizontal plane average and double primes a departure of a time-averaged quantity from its horizontal average. Fluxes of the type  $\langle U''V'' \rangle$  were identified by Wilson and Shaw (1977) for vegetation canopies, and labeled "dispersive fluxes." An early estimate by Antonia (1969) indicated that this type of momentum flux is unlikely to account for observations with X-wire probes of apparent stress decreases near transverse bar roughness. Later, detailed measurements by Mulhearn (1978) (bar roughness), Raupach et al (1980) (cylinder roughness), Raupach et al (1986) (model plant canopy), and Perry et al (1987) (mesh roughness) demonstrated that the magnitude of  $\langle U''V'' \rangle$  is less than a few percent of  $u_\tau^2$  at most. This leaves no possible explanation for the apparent stress decrease just above the roughness, other than the measurement errors of X-wire probes.

Further evidence that measurement error is the problem is provided by the  $\overline{uv}$  data in Fig. 3.12b, which show convincingly that no apparent stress decrease is found in field data measured with omnidirectional sonic anemometers, and in laboratory data obtained with coplanar triple-wire probes, which have far better directional response than X-wire probes (Kawall et al 1983, Legg et al 1984). All of these sensors indicate a layer of constant stress  $-\overline{uw}$  within the expected limits of the constant stress layer.

Theoretical and empirical error analyses on X-wire probes were made by Tutu and Chevray (1975), Raupach et al (1980), Legg et al (1984), and Perry et al (1987). All these studies agree that the main problem is the limited velocity-vector acceptance angle of  $\pm 45^\circ$  in a conventional X-wire probe, with secondary problems being contamination of streamwise and vertical velocity signals by the lateral velocity component, and finite wire length (in order of decreasing significance). Recent measurements of  $\overline{uv}$  have addressed some of these problems, and are of better quality than the earlier data. Perry et al (1987) showed that, by increasing the acceptance angle from the usual  $\pm 45^\circ$  to  $\pm 60^\circ$  and/or "flying" the probe in the streamwise direction to reduce the turbulence intensity  $\sigma_u/U$ , acceptable measurements can be made with X-wire probes. Acharya and Escudier (1987) confirmed the improvement in measurements resulting from  $\pm 60^\circ$  X-wire probes. Li and Perry's (1989) measurements of  $\overline{mv}$  over a rough-wall boundary layer, obtained with either a  $\pm 60^\circ$  stationary or a  $\pm 45^\circ$  flying X-wire probe, were in close agreement with an analytical expression of  $\overline{uv}$  obtained by integrating the mean streamwise momentum equation, using a logarithmic profile law and Coles wake function to specify  $U(y)$ .

### 3.3.4 Second-moment budgets

The mechanisms maintaining the turbulence in the roughness sublayer, both above and within the roughness, are partly elucidated by the turbulent kinetic energy and shear stress budgets. The budgets must be considered in a spatially (in practice, horizontally) averaged form because a significant dynamical role is played by processes associated with spatial heterogeneity at the length scales of individual roughness elements.

*Turbulent kinetic energy budget:* For a steady flow over a horizontal, immobile rough surface at high Reynolds number (so that molecular transport terms are negligible), and with negligible advection, thermal forcing, and mean pressure gradient, the horizontally average turbulent kinetic energy budget is

$$\frac{\partial \overline{q^2}/2}{\partial t} = 0 = P_s + P_w + T_t + T_d + T_p - \langle \varepsilon \rangle \quad (3.35)$$

with

$$\begin{aligned} P_s &= -\langle \overline{uv} \rangle \frac{\partial \langle U \rangle}{\partial y} \\ P_w &= -\left\langle \overline{u_i u_j} \frac{\partial \langle U_i \rangle}{\partial x_j} \right\rangle \\ T_t &= -\frac{\partial}{\partial y} \left\langle \frac{\overline{wq^2}}{2} \right\rangle \end{aligned} \quad (3.36)$$



$$T_d = -\frac{\partial}{\partial y} \left\langle \frac{W'' \overline{q'^2}}{2} \right\rangle$$

$$T_p = -\frac{\partial}{\partial y} \langle \overline{wp} \rangle$$

The terms denote shear production ( $P_s$ ), wake production ( $P_w$ ), turbulent, dispersive and pressure transport ( $T_t$ ,  $T_d$ ,  $T_p$ , respectively), and dissipation  $-\langle \varepsilon \rangle$ . It is convenient to write the wake production term in tensor notation, with  $x_i = (x, y, y)$ ,  $U_i = (U, V, W)$ ,  $u_i = (u, v, w)$ , and the summation convention effective. Of these terms,  $P_s$ ,  $T_t$ ,  $T_p$  and  $\langle \varepsilon \rangle$  are familiar as spatial averages of the corresponding terms in the single-point turbulent kinetic energy equation, whereas the less familiar terms  $P_w$  and  $T_d$  arise from spatial heterogeneity at roughness element length scales. The dispersive transport term  $T_d$  is the vertical gradient of a dispersive turbulent kinetic energy flux, directly analogous to the dispersive momentum flux  $\langle U''V'' \rangle$ . Since the dispersive momentum flux is negligible relative to the turbulent momentum flux, it is likely that the dispersive turbulent kinetic energy flux is likewise negligible, so that  $T_d$  is negligible relative to  $T_t$ .

The wake production term  $P_w$  is far from negligible (Wilson and Shaw 1977). It is the production rate of turbulent kinetic energy in the wakes of roughness elements by the interaction of local turbulent stresses and time-averaged strains. Like  $P_s$ ,  $P_w$  represents a conversion of mean to turbulent kinetic energy, but the two terms operate at different scales:  $P_s$  creates "shear turbulence" with a length scale of order  $h$  within and just above the canopy, whereas  $P_w$  creates "wake turbulence" with a length scale of the order of a typical roughness-element wake width. In vegetation canopies, wake turbulence is usually much smaller-scale than shear turbulence. It can be shown (Raupach and Shaw 1982) that  $P_w$  is approximately equal to the rate of working of the mean flow against drag:

$$P_w \approx -\langle U \rangle f_x \approx -\langle U \rangle \frac{\partial \langle \overline{uv} \rangle}{\partial y} \quad (3.37)$$

where  $f_x$  is the horizontally-averaged total force exerted by the elements on the flow, a negative quantity. Figure 3.13a shows measurements, from Raupach et al (1986), of the terms  $P_s$ ,  $P_w$  [using (3.37)] and  $T_t$  in the "WT strips" wind-tunnel model plant canopy. The curve  $D$  is the residual  $-P_s - P_w - T_t$ , equal to  $T_p - \langle \varepsilon \rangle$  if  $T_d$  is negligible as argued above. The main features are the peak in shear production  $P_s$  near  $y = h$ , the large wake production  $P_w$  in the upper part of the canopy, and the major role of turbulent transport  $T_t$  in carrying turbulent kinetic energy from the regions of strong production near  $y = h$  to lower levels in the canopy. In the lower part of the canopy, the turbulent kinetic energy budget reduces to an approximate balance between transport and dissipation. The importance of  $T_t$  is related to the dominant role of sweep motions, or gusts, in momentum transfer (section 3.4.2).

Two aspects of the turbulent kinetic energy budget do not emerge from Fig. 3.13a. First,  $T_p$  (which could not be measured) is probably significant. Maitani and Seo (1985) estimated it in a cereal canopy in the field from surface pressure measurements, concluding that  $T_p$  is comparable with  $T_t$  and likewise acts as a gain term in the budget deep in the canopy. Second,  $P_w$  converts not only mean kinetic energy but also large-scale (shear) turbulent kinetic energy into wake-scale turbulent kinetic energy. This conversion is not evident in

(3.37), which is spectrally integrated over all turbulence scales. However, since the small-scale wake turbulence is much more quickly dissipated than the larger-scale shear turbulence, the effect is that the dissipation rate of the shear turbulence within the canopy is much greater than would occur for free turbulence with similar velocity and length scales. The rapid dissipation rate of the wake turbulence also accounts (Raupach and Shaw 1982) for the fact that, in velocity spectra measured within canopies, little extra energy is seen at wavenumbers characteristic of element length scales, despite  $P_w$  being as large as or greater than  $P_s$  in the upper part of the canopy as in Fig. 3.13a.

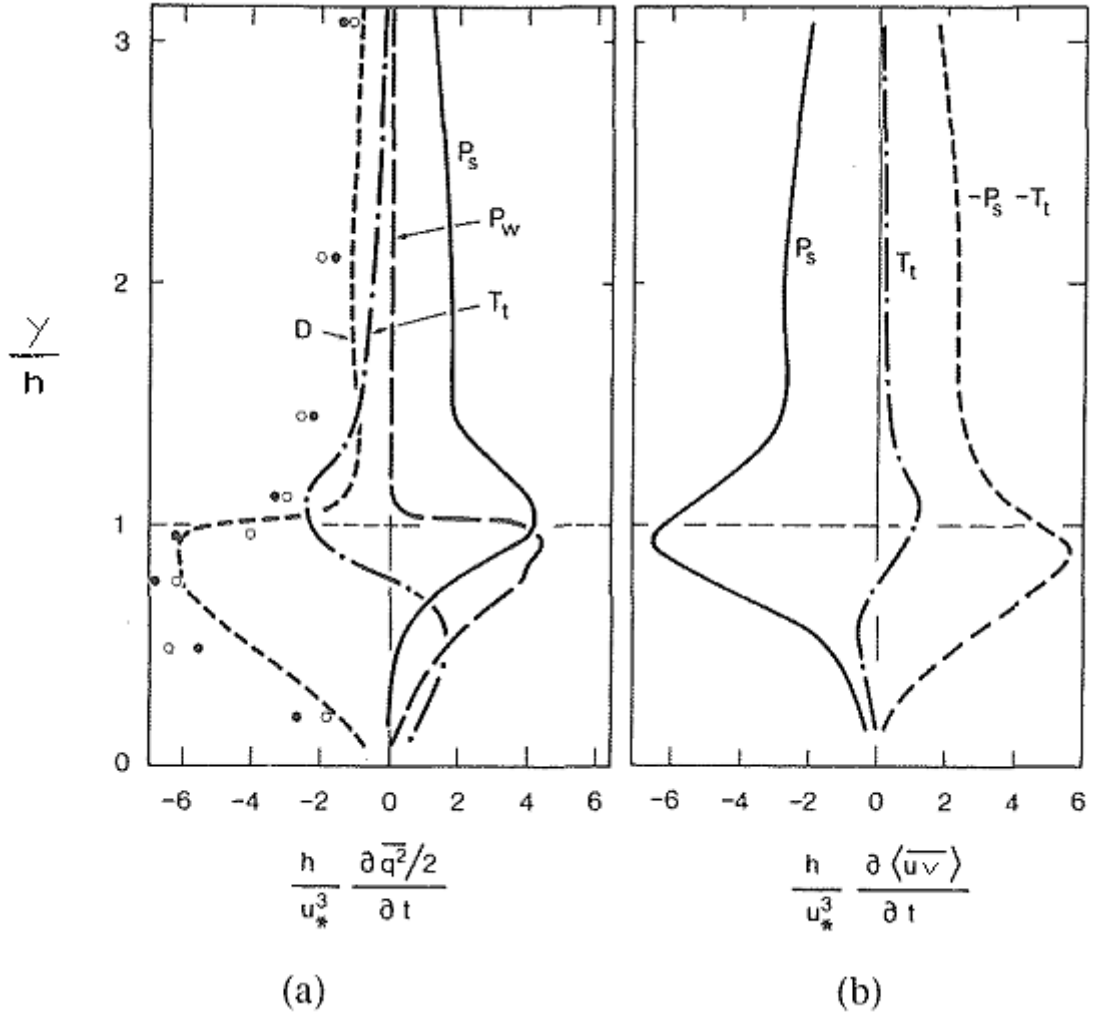


Fig. 3.13 - Terms in the second moment budgets in the “WT strips” canopy.

*Shear stress budget:* Under the same conditions as (3.35), the horizontally averaged shear stress budget is

$$\frac{\partial \langle uv \rangle}{\partial t} = 0 = P'_s + P'_w + T'_t + T'_d + T'_p + \Phi' \quad (3.38)$$

with

$$\begin{aligned}
P'_s &= -\left\langle \overline{v^2} \right\rangle \frac{\partial \langle U \rangle}{\partial y} \\
P'_w &= -\left\langle \overline{u_1 u_j''} \frac{\partial U_3''}{\partial x_j} + \overline{u_3 u_j''} \frac{\partial U_1''}{\partial x_j} \right\rangle \\
T'_t &= -\frac{\partial}{\partial y} \left\langle \overline{u y^2} \right\rangle \\
T'_d &= -\frac{\partial}{\partial y} \left\langle V'' \overline{u v''} \right\rangle \\
T'_p &= -\frac{\partial}{\partial y} \left\langle \overline{u p} \right\rangle \\
\Phi' &= \left\langle p \left( \frac{\partial u}{\partial y} + \frac{\partial v}{\partial x} \right) \right\rangle
\end{aligned} \tag{3.39}$$

The terms in (3.38), distinguished by primes, correspond in name and mnemonic to the terms in (3.35) except for the pressure-strain term  $\Phi'$ , which is the main destruction term for shear stress. The dispersive transport term  $T'_t$  is usually negligible in practice, just as for  $T_d$  in (3.36). However, in contrast to  $P_w$ , which plays a very important part in (3.35), the wake production term  $P'_w$  in (3.38) is also usually negligible.

Figure 3.13b shows direct measurements of the terms  $P'_s$  and  $T'_t$  in the shear stress budget (Raupach et al 1986). As for the turbulent kinetic energy budget, shear production peaks strongly near  $y = h$ , while turbulent transport is a loss near  $y = h$  and a gain lower down (noting that, because  $\overline{uw}$  is negative whereas  $\overline{q^2}/2$  is positive, gain terms are on the right of Fig. 3.13a but the left of Fig. 3.13b). The role of transport in the shear stress budget is relatively much smaller than in the turbulent kinetic energy budget, because the transport term ratio  $T'_t / T_t$  is of order only about 0.2 in the canopy, whereas the two production terms are comparable near  $y = h$ .

The main features of Figs. 3.13a and 3.13b are confirmed by a growing number of measurements from both wind-tunnel models and field canopies. However, the discussion has been restricted to vegetationlike roughness, for observational reasons already outlined. The conceptual framework of (3.35), (3.37), and (3.38) is valid for any roughness type, but the quantitative behavior of the budgets is another matter; although the main features of Fig. 3.13 probably carry over at least to threedimensional roughness such as sandgrain roughness, separate investigation is required for two-dimensional bar roughness, either widely-spaced ("k-type") or narrow-cavity ("d-type").

### 3.4 ORGANIZED MOTION IN ROUGH-WALL BOUNDARY LAYERS

It is now generally recognized that turbulent flows universally exhibit various forms of organized motion, sometimes referred to as coherent structures. The literature on these motions is vast: see, for example, the reviews of Cantwell (1981), Hussain (1986), and Fiedler (1987). Smooth-wall boundary layers are well represented in this extensive body of work; rough-wall boundary layers far less so.

#### 3.4.1 Two-point velocity correlation functions

A traditional but useful starting point for an examination of organized motion is the two-point, time-delayed velocity correlation function

$$r_{ij}(x, y, z, \tau, z_R) = \frac{\overline{u_i(x, y, z, t + \tau) \cdot u_j(0, y_R, 0, t)}}{\left[ \overline{u_i^2(y)} \cdot \overline{u_j^2(y_R)} \right]^{1/2}} \quad (3.40)$$

where  $y_R$  is the height of a reference sensor at  $(x, z) = (0, 0)$ . The correlation function depends explicitly on both the heights  $y$  and  $y_R$  because of vertical inhomogeneity, but depends only on the horizontal separation  $(x, z)$  and the time interval  $\tau$  because horizontal homogeneity and steady flow are assumed. The small-scale horizontal variability in the roughness sublayer is ignored in (3.40); this is justifiable for many vegetation canopies, including those discussed below, but may not be justifiable for two-dimensional laboratory roughness, for example.

*Above the roughness sublayer:* In the inertial sublayer and outer layer, data on  $r_{ij}$  over both rough and smooth walls generally show that  $r_{ij}$  is independent of the nature of the wall, thus providing direct support for the wall similarity hypothesis (section 3.2.1). For smooth-wall boundary layers, there are many measurements of  $r_{ij}$ ; see Townsend (1976) for primary references. Brown and Thomas (1977) crosscorrelated signals from a wall probe with  $u$  signals in a smoothwall boundary layer, finding that the maximum correlation occurred along a line in the  $xy$  plane sloping obliquely with the flow at an angle of about  $18^\circ$  to the horizontal. Comparable rough-wall data have been obtained by Bessem and Stevens (1984) and Osaka et al (1984), over "k-type" and "d-type" walls, respectively; in both cases, the locus of maximum  $u$  correlation was similar to that found by Brown and Thomas.

*Within the roughness sublayer:* Two-point correlations close to and within the roughness are available from work on vegetation canopies. Figure 3.14 shows contours, in the  $xy$  and  $yz$  planes, of the spatial  $u$  correlation at zero time delay,  $r_{11}(x, y, z, 0, y_R)$ , from the "WT wheat" canopy. The reference height was  $y_R = h$ . There is good correlation ( $r_{11} \geq 0.3$ ) within the region  $(-2h \leq x \leq 2h, 0 \leq y \leq 2h, -h \leq z \leq h)$ , a result which is consistent with the rough estimates of eddy length scales made in section 3.3.2 from single-point data. In the  $xy$  plane, the contours are roughly elliptical and slope obliquely with the flow; the slope is about  $18^\circ$  above the canopy and less within the canopy.

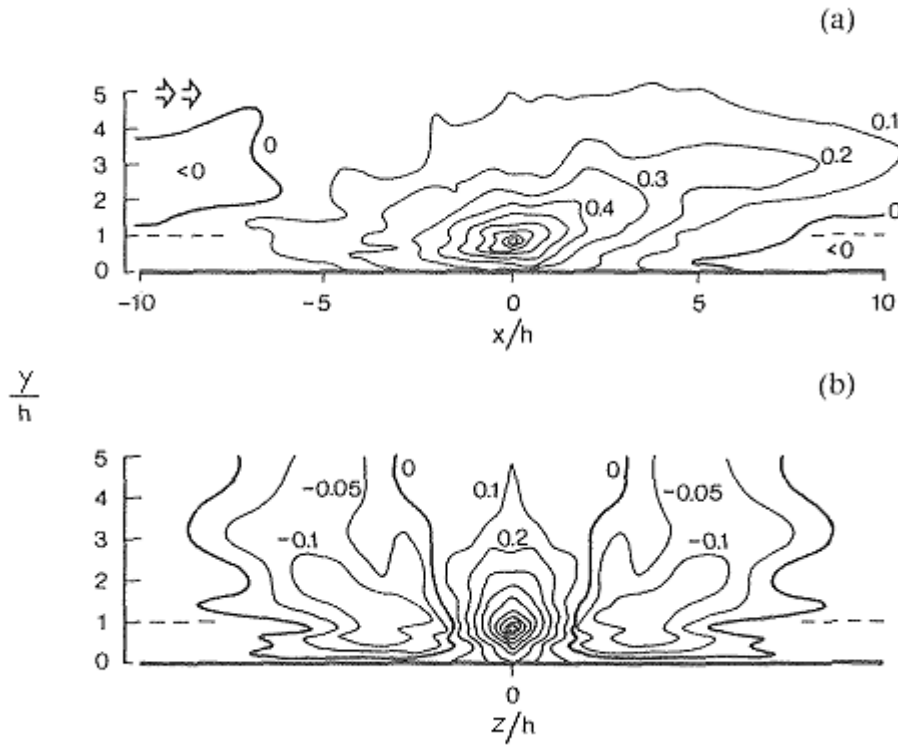


Fig. 3.14 - Contours of  $r_{11}(x, z, z, 0, y_R)$  in and above the "WT wheat" canopy.

A slightly different view is offered by space-time correlations with vertical separation,  $r_{ii}(0, y, 0, \tau, y_R)$ . Figure 3.15 shows these correlations for  $u$  and  $v$ , from "WT wheat," while Fig. 3.12 shows similar correlations for  $u$ ,  $v$ ,  $w$  and also for temperature  $\theta$ , from the "Moga" forest micrometeorology experiment (New South Wales, Australia). The field data in Fig. 3.16 are typical of several recent forest turbulence experiments (Gao et al 1989, Shaw et al 1989). The agreement between wind tunnel and field results underlines one of the themes of this review, that experiments on natural vegetation and laboratory roughness can provide complementary insights: field measurements with sonic anemometers offer an unambiguous resolution of all three velocity components which is not achievable in laboratory roughness sublayers, whereas laboratory measurements (Fig. 3.15) offer higher measurement density and reproducibility than the field.

A striking feature of Figs. 3.15 and 3.16 is the difference in the correlation functions for  $u$ ,  $v$ ,  $w$ , and  $\theta$ . For  $v$  and  $\theta$ , and to a lesser extent for  $u$ , the maximum correlation occurs at a time delay  $\tau$  which increases as the height separation increases, consistent with Fig. 3.14 and the Brown and Thomas (1977) result. It follows that the motions dominating the  $u$ ,  $w$ , and  $\theta$  correlations are inclined structures leaning with the shear. For  $v$ , however, the maximum correlation occurs with zero time delay, so that organized fluctuations in  $v$  are aligned vertically, both within and above the roughness. The region of strong  $v$  correlation is also more localized than for  $u$ ,  $w$ , or  $\theta$ . As with other features of  $r_{ij}$  these results agree well with smooth-wall data: Antonia et al (1988) found that the maximum  $v$  correlation over a smooth wall occurs at  $\tau = 0$  for a wide range of both  $y_R$  and  $y$ , again implying a vertical alignment of organized  $v$  fluctuations.

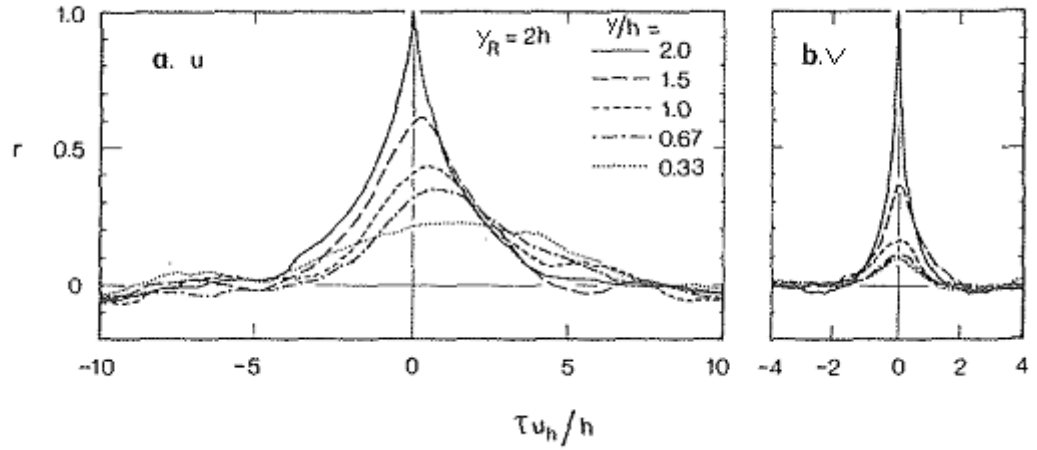


Fig. 3.15 - Vertically separated space-time correlations  $r_u(0, y, 0, \tau, y_R)$  in and above the “WT wheat” canopy.

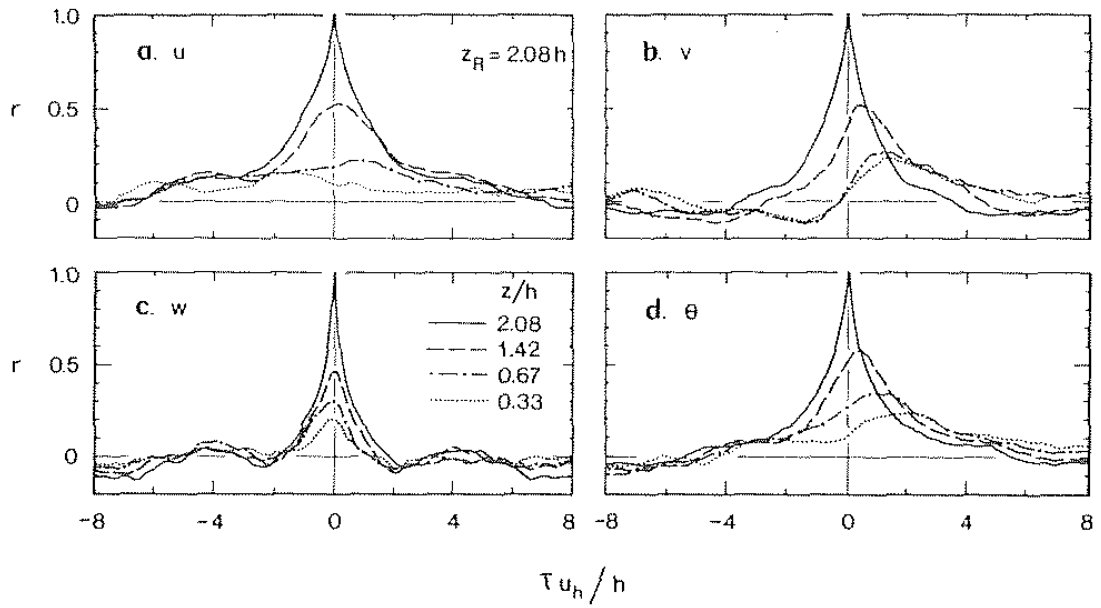


Fig. 3.16 - Vertically separated space-time correlations  $r_u(0, y, 0, \tau, y_R)$  in and above the Moga forest canopy.

In summary, two-point correlation functions confirm wall similarity above the roughness sublayer, and yield eddy length scales, orientations, and convection velocities both above and within the roughness sublayer. However, they are only weak indicators of the flow fields associated with organized motions; other type of analysis are required to elucidate these.

### 3.4.2 Manifestations of organized motion

Organized motion is manifested in a variety of quasicohherent features or structures; for example, Kline and Robinson (1990) identified eight types of structure in smoothwall boundary layers. Here we focus on four manifestations of organized motion: (a) low-speed streaks (mainly a smooth-wall phenomenon); (b) ejections and sweeps; (c) ramp-jump (sawtooth) structures in velocity and temperature signals; and (d) large-scale, outer-layer motions. Of these, (b) and (c) have received most attention in rough-wall work.

(a) *Low-speed streaks*: Kline et al (1967), Kim et al (1971) and many succeeding workers recognized low-speed streaks associated with streamwise vortical motion in the smooth-wall inner layer ( $y_+ \leq 100$ ). This body of work has also identified a "bursting process" in which the streaks are cyclically formed near the wall and ejected into the overlying flow. The whole phenomenon is often presumed to be the essential condition of the smooth-wall turbulent boundary layer.

The existence of low-speed streaks in rough-wall boundary layers is much more problematical. They are observed over certain rough walls: The flow visualizations of Liu et al (1966) and Osaka and Mochizuki (1987) have revealed low-speed streaks on narrow-cavity bar ("d-type") roughness, with the streaks forming and bursting continuously at a pseudowall defined by the tops of the bars. With increase in the gap space  $(D - l_x)/h$ , the streaky pattern disappeared, to reappear at high  $(D - l_x)/h$  in the reattached flow region between the bars. It is probable that these low-speed streaks are formed when the barroughened surface (or some part of it) acts dynamically like a smooth wall. In contrast, the near-wall flow over most rough surfaces is so disturbed by the roughness elements that longitudinal low-speed streaks are eradicated, as stressed by Liu et al (1966). However, there is still a possible rough-wall counterpart for at least some aspects of the smooth-wall "bursting process," as the following observations show.

(b) *Ejections and sweeps*: Grass (1971) used hydrogen bubble flow tracers and high-speed motion photography to obtain both a visual and a quantitative description of a free surface channel flow for three types of surface condition: smooth, transitional, and fully rough. The roughness was made of close-packed rounded pebbles of diameter 9 mm. The visualizations of the rough-wall flow clearly showed the fluid ejection and inrush (sweep) previously identified in the "bursting process" for a smooth wall. Grass concluded that the inrush and ejection events were present irrespective of the surface condition, but noted differences in these events between smooth-wall and rough-wall flows. For smooth-wall flows the ejection sequence draws on viscous sublayer fluid with an embedded structure of low-speed streaks, whereas for rough walls the source for ejected fluid is the low-momentum fluid trapped between the roughness elements. Grass noted that over a rough wall the ejections could be relatively violent, with ejected fluid "rising almost vertically from the interstices between the roughness elements." He also observed that the ejections were often coherent and identifiable through much of the flow; in contrast, coherent inrush or sweep motions were confined to the region close to the wall.

A quantitative measure of the relative importance of ejections and sweeps is provided by quadrant analysis, introduced for smooth-wall flows (Wallace et al 1972, Lu and Willmarth 1973, Brodkey et al 1974) and later applied to rough-wall flows by Nakagawa and Nezu (1977) and Raupach (1981) in the laboratory, Antonia (1977) and others in the atmospheric

inertial sublayer, and Finnigan (1979a) and Shaw et al (1983) in the atmospheric roughness sublayer over field vegetation. In this technique, instantaneous events are defined by quadrant in the  $uv$  plane, as outward interactions, ejections, inward interactions, and sweeps (the first, second, third, and fourth quadrants, respectively), with the total stress equal to the sum of the conditionally averaged contributions (denoted by double angle brackets) from each quadrant:

$$\overline{uv} = \langle\langle uv \rangle\rangle_1 + \langle\langle uv \rangle\rangle_2 + \langle\langle uv \rangle\rangle_3 + \langle\langle uv \rangle\rangle_4 \quad (3.41)$$

Nakagawa and Nezu (1977), using an open-channel water flow over glass-bead roughness, made several significant findings: (1) Sweep events are more important than ejection events for momentum transfer close to a rough wall, with the sweep-toejection ratio  $\langle\langle uv \rangle\rangle_4 / \langle\langle uv \rangle\rangle_2$  increasing with decreasing height and increasing roughness; (2) the events dominating momentum transfer are highly intermittent and occupy a small fraction of the time, with the fraction decreasing with decreasing height and increasing roughness; (3) a cumulant-discard analysis, using a third-order Gram-Charlier joint probability distribution for  $u$  and  $v$ , can account for the relationship between the quadrant decomposition of  $\overline{uv}$  and the normalized third moments of  $u$  and  $v$ . This last result provides a link between the organized motion of the flow (as quantified by quadrant analysis) and the turbulent energy budget (3.35), through the turbulent transport term which involves vertical gradients of the third moments. Raupach (1981), with wind-tunnel data from a smooth surface and five cylinder-roughened surfaces of progressively increasing roughness density, confirmed the importance of sweeps near rough walls and used Nakagawa and Nezu's cumulant discard analysis to relate the normalized third velocity moments to the difference between sweep and ejection contributions to stress:

$$\frac{\langle\langle uv \rangle\rangle_4 - \langle\langle uv \rangle\rangle_2}{\overline{uv}} = 0.37M_{30} = -0.75M_{21} = 0.73M_{12} = -0.63M_{03} \quad (3.42)$$

where  $M_{ij}$  are the normalized third moments or skewnesses. The constants in (3.42) are experimental, derived from measurements throughout the smooth-wall and rough-wall flows including the region within the roughness, but very similar values emerge from the cumulant-discard theory. Later measurements have confirmed that (3.42) also applies in a smooth-wall boundary layer, but only if the Reynolds number is sufficiently large. For vegetation, the early work of Finnigan (1979a) (with a small data set) was followed by Shaw et al (1983), who applied quadrant analysis to turbulence data from a corn canopy, finding  $\langle\langle uv \rangle\rangle_4 / \langle\langle uv \rangle\rangle_2$  values of about 2 near  $y = h$  and higher within the canopy, thus confirming that sweeps dominate the momentum transfer close to and within field canopies.

One dramatic visualization of the spatial structure of sweeps in a rough-wall boundary layer is the phenomenon of "honami," or traveling wind waves in cereal (wheat, barley, rice, grass) canopies. For one engaged in research on boundarylayer turbulence, watching these waves is time well spent. The phenomenon of honami was named and first studied by Inoue (1955), and has since been investigated in detail by Finnigan (1979a, b). He found that the waves are initiated by gust fronts, or sweeps, moving across the canopy at convection speeds substantially greater than the local mean wind speed. Each gust, as it



advances, bends over a patch of stalks which undergoes damped oscillation (typically for about two cycles) after the gust has passed, thus creating the impression of a wave moving through the canopy. By studying motion pictures of waving canopies and by analyzing short-time, vertically separated, space-time correlations, Finnigan found that the streamwise separation between gusts was about  $5h$ - $8h$ , close to the value  $8h$ ; inferred by several spectral and correlation methods for the typical streamwise separation between quasicohherent eddies.

(c) *Ramp-jump structures in signals:* Chen and Blackwelder (1978) observed correlated ramp-jump (sawtooth) patterns in temperature signals throughout a smooth-wall boundary layer, which they suggested to be a direct link between the wall region and the outer layer. This suggestion should be equally true in a rough-wall boundary layer. Indeed, such patterns were first observed in the (definitely rough-wall) atmospheric surface layer by Taylor (1958) and Priestley (1959), though the temperature structure in many of these early observations was largely determined by free convection rather than thermally near-neutral shear turbulence. Nevertheless, for moderately unstable conditions in the atmosphere, Antonia et al (1979) concluded that the observed similarity between laboratory and atmospheric ramp-jump temperature structures should be interpreted as the signature of an organized large-scale sheardriven motion, rather than as a consequence of the buoyancy field (which, of course, also produces large-scale organized motion). Wyngard (1988) reinforced the dominance of shear turbulence close to the surface, even in strongly unstable atmospheric boundary layers.

Many subsequent observations have confirmed that rampjump structures are universally observed in both rough-wall and smooth-wall boundary layers, in both the atmosphere (over land and sea) and the laboratory, and also for velocity components as well as temperature (for example, Antonia and Chambers 1978, Antonia et al 1979, Phong-Anant et al 1980, Antonia et al 1982). The velocity and temperature signals yielding the two-point correlation functions in Figs. 3.14-3.16 all exhibited these structures, to the extent that they substantially determine the shape of the correlation functions; Figs. 3.14-3.16 therefore indicate that the ramp-jump structures extend into the roughness itself. Further unpublished wind-tunnel measurements by us, over a slightly heated gravel roughness, have confirmed that temperature ramp-jumps are observed coherently throughout the whole (rough-wall) boundary layer, from  $y < h$  to  $y = \delta$ .

Direct observations from vegetation canopies indicate a close association between ramps and jumps in velocity components or temperature, and the sweeps which dominate momentum transfer within and close to the canopy (Finnigan 1979a, b, Denmead and Bradley 1985, 1987). A good example appears in Fig. 3.17, from a forest experiment at Camp Borden, Ontario, Canada (Gao et al 1989, Shaw et al 1989). This shows the ensemble-averaged potential temperature field for 10 temperature ramp-jump events during a 30-min run in slightly unstable conditions, the selection criterion being the presence of correlated temperature jumps at several levels within and above the canopy. Temperature contours are plotted in the  $(-t, y)$  plane (so that the horizontal axis corresponds to a  $+x$  axis with the frozen-field approximation), together with instantaneous wind fluctuation vectors  $(u, v)$  (shown as arrows) from sonic anemometers. The temperature jumps form a sharp, inclined microfront in space, dividing warmer, slower, ascending air ahead of the microfront from a well-defined region of cooler, descending, faster-moving air immediately behind. There is an intense sweep motion just behind the microfront near  $y = h$ ; in contrast, the strongest motion at higher levels ( $y \approx 2h$ ) is an

ejection just ahead of the microfront. This is consistent with the quadrant-analysis results discussed above. The microfront itself, involving a temperature fall of about  $1.2^\circ$  in 3 s, is somewhat smeared by the ensemble-averaging process and was even sharper in individual realizations. During the analyzed 30-min run, the 10 ensemble-averaged events occupied 33% of the time but accounted for over 75% of the heat and momentum transfer, indicating strongly that ramp-jump events coincide with the organized motions which dominate the transfer.

Although these results demonstrate that sweeps, ejections, and ramp-jump structures (or microfronts) are closely associated, the spatial relationship suggested by Fig. 3.17 must be interpreted with caution: The relationship is based on an ensemble-averaged result and may not apply instantaneously, largely because the ensemble average is taken over a set of two-dimensional streamwise slices through structures at random lateral displacements and stages of evolution. Some of the three-dimensional picture is indicated by the work of Robinson et al (1989), who found that, in a numerically simulated smooth-wall boundary layer, ejections and sweeps occur alongside quasi-streamwise "legs" of  $\Lambda$ -vortices (see next section), with sweeps most prevalent on the outward side of the necks of vortical arches and ejections most common just upstream and below vortical arches.

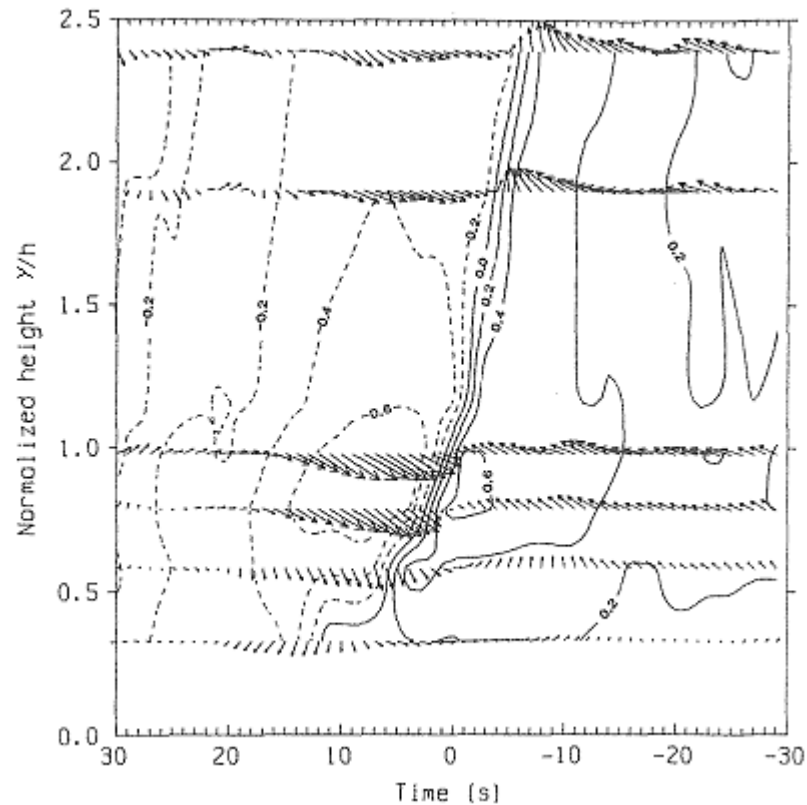


Fig. 3.17 - Vertical cross section of ensemble-averaged temperature and fluctuating velocity fields in Camp Borden forest.

(d) *Large-scale outer-layer motions:* The wall similarity hypothesis implies that organized motions should be the same in the outer parts of smooth-wall and rough-wall boundary layers, a contention supported by the available data. The turbulent-nonturbulent interface was first studied by Corrsin and Kistler (1955) in a boundary layer developing over a

corrugated rough wall. The properties of large-scale bulges in the boundary layer, inferred from ensemble-averaged velocity distributions conditioned with respect to the interface, are similar over a smooth wall (Kovaszny et al 1970) and widely spaced bar roughness (Antonia 1972). The latter paper showed that the outer-layer similarity between these two flows is also evident from profiles of mean velocity and a wide range of velocity moments, further supporting the wall similarity discussion in section 3.2.1.

### 3.4.3 Inferred structure of the organized motion

The above manifestations of organized motion are directly evident in flow visualizations or turbulence signals with minimal conditioning. In contrast, the complete structure of the organized motion near a rough wall, as for any turbulent flow, is not immediately evident in either point measurements or flow visualizations and must be inferred from all the above information (and more) by a variety of methods. Such inferences are difficult and contentious at present; the form of the organized motion near both rough and smooth walls is widely regarded as an unsolved problem. Nevertheless, we conclude the discussion of organized motion by mentioning a few current viewpoints.

A widely used, though not universally accepted, model for the dominant form of organized motion in a boundary layer is the inclined horseshoe, hairpin or A-vortex, sometimes identified with the inclined double-roller eddy of Townsend (1976); we will refer to this structure as a A-vortex. Such a structure was theoretically deduced long ago by Theodorsen (1952) and Hama (1963), inferred from two-point velocity correlations by Townsend (1976), and identified in smooth-wall flow visualizations by Falco (1977) and particularly Head and Bandyopadhyay (1981). Numerical support came from the direct numerical simulations of smooth-wall fully developed channel flow by Moin and Kim (1985). In a review of rapiddistortion theory, Savill (1987) concluded that the total turbulent kinetic energy in a boundary layer is partitioned in the ratio 60:20:20 between A-vortices, transverse vortices (possibly identifiable with the loops joining the "legs" of the A-vortices at the top), and fine-scale turbulence (present as a result of the stretching, spin-up and decay of the A-vortices). Perry and Chong (1982) used a hierarchy of A-vortices to construct a detailed theoretical model of a smooth-wall boundary layer, which predicts realistic mean velocity profiles, second velocity moments and spectra.

Despite the popularity of the A-vortex model, it is almost certainly an oversimplification. Direct numerical simulations of smooth-wall boundary-layer and channel flows (Robinson 1989, Moin and Spalart 1987) indicate that many other types of vortical structures are also present besides A-vortices. The near-wall region ( $y_+ < 100$ ) is dominated by quasistreamwise vortices with an outward tilt, whereas spanwise and  $45^\circ$  vortices are more likely to occur in the outer region. Robinson (1989) found that evidence for the dominance of particular forms such as horseshoes, hairpins, and so on is not yet conclusive. Despite these caveats, the A-vortex model is a simple picture with a degree of theoretical support, experimental verification, and predictive power not available from other models, so we shall continue to base the present discussion around it.

Almost all of the above evidence on vortical structures comes from smooth-wall boundary layers. However, the wall similarity hypothesis implies that the dominant organized vortical motions in smooth-wall and rough-wall boundary layers must be similar, except in the viscous or roughness sublayers. On this basis, the A-vortex model should describe organized motion in the bulk of the rough-wall boundary layer (in and above the inertial sublayer), with similar caveats as for a smooth-wall boundary layer. One direct piece of

supporting evidence, from a rough-wall channel flow, is the three-dimensional velocity and vorticity fields constructed by Grass (1983) from digitized marked-particle tracks: the constructed vorticity field contained evidence of A-vortices, though their importance, both in terms of frequency of occurrence and contribution to the transfer process, could not be established.

Finally, we return to a sharper form of the question posed in the introduction of this section: how are vortical structures in the bulk of the boundary layer (possibly A-vortices) coupled to the nearwall motion in the roughness sublayer (for a rough wall) or the viscous sublayer (for a smooth wall)?

Near the roughness, one expects to find organized vortical structures in roughness-element wakes which are absent in smooth-wall flow. For two-dimensional bar roughness, several vortical structures have been observed in the cavities between elements, as reviewed by Wood and Antonia (1975). For three-dimensional roughness, Bandyopadhyay and Watson (1988) proposed "necklace" vortices straddling the roughness elements near their bases. However, such proposals (especially in the three-dimensional case) are necessarily rather specific about roughness type, as the element shape determines the nature of the wake. In contrast, there is attraction in a mechanism for organized motion in the roughness sublayer which is largely independent of roughness type and individual element wakes, in part because the wakes are often not the most energetic features of the flow (for vegetated surfaces it is almost impossible to detect them as discrete vortices), but also because of the simplifying property of such a mechanism. The following "wake-independent" suggestion centers on vegetation and similar types of roughness but may have wider applicability.

Raupach et al (1989) postulated that the flow near the top of the canopy is dominated by the intense shear layer centered on the inflection point in  $U(y)$  near  $y = h$  (see Fig. 3.16a). The length scale for the depth of this layer is  $h - d$ ,  $d$  being zeroplane displacement. Associated with the inflection point is an intense, inviscid (Rayleigh) instability leading to rapidly growing, transverse vorticity perturbations with a streamwise wavelength determined by  $h - d$  (typically, the wavelength is about  $30(h - d)$  or  $8h$ ). These motions, together with subsequent, three-dimensional secondary instabilities, are the fastest-growing perturbations near  $y = h$ ; and are therefore likely progenitors for the fully developed, highly energetic turbulence field near  $y = h$ . This field retains as its length scale "signature" that of the original, inviscid, inflection-point instability. The secondary instabilities lead to A-vortex structures (Pierrehumbert and Widnall 1982, Bayly et al 1988) within the roughness sublayer, just as in the overlying boundary layer; this is consistent with the observations of microfronts and lines of maximum twopoint  $u$ ,  $w$ , and  $\theta$  correlation within and just above the canopy, similar to those in the inertial sublayer and above (Figs. 3.14-3.17). A similar inflectional instability process occurs in a plane mixing layer, leading likewise to a turbulent length scale proportional to the local layer depth (Wyganski and Fiedler 1970). This explains one attribute already noted in section 3.4 and elsewhere: near the top of a vegetation canopy, basic turbulence properties (such as the ratios  $\sigma_w/u_\tau$  and  $\sigma_v/u_\tau$ , the skewness profiles, and the turbulent energy budget, especially the role of turbulent transport) tend to be more reminiscent of a mixing layer than a boundary layer.

This proposed mechanism is fairly easy to visualize for vegetation and similar roughness where the element (leaf) length scales are small compared with  $h$  and horizontal heterogeneity is relatively unimportant. For laboratory three-dimensional and two-dimensional roughness with element dimensions comparable with  $h$ , individual roughness elements can generate strong wakes (for example, streamwise vortices in the case of

discrete three-dimensional roughness elements) which may play a role in the transfer process. However, there is almost always a strong vertical shear just above the elements, so the effects of individual element wakes may well be considered as superposed upon some more general process such as that just described.

In conclusion, in order to understand the meaning of the work done and explained in the next chapters, here we have attempted to place within a single framework two bodies of research which, till now, have been largely separate: laboratory and theoretical work on rough-wall turbulent boundary layers, and micrometeorological studies in the atmospheric surface layer. By combining insights from both fields, a fairly complete picture of the rough-wall turbulent boundary layer emerges. The hypothesis of wall similarity, that rough-wall and smooth-wall boundary layers at sufficiently high Reynolds numbers are structurally similar outside the roughness (or viscous) sublayer, is well supported by many kinds of observation. The flow in the roughness sublayer is more difficult to measure than that in the overlying boundary layer, not only because of spatial heterogeneity but also because of high turbulence intensities, which introduce unacceptable errors with many laboratory velocity sensors, including X-wire probes. However, careful measurement techniques in the laboratory, using flying X-wire probes or coplanar triple-wire probes, have eliminated some of these difficulties. For field vegetation, threedimensional sonic anemometers provide an unambiguous measure of all three velocity components superior to anything obtainable with current laboratory sensors. Together, these techniques have facilitated the exploration of the main properties of the roughness sublayer, including its spatial heterogeneity, its turbulence structure in terms of velocity moments and second-moment budgets, and the organized motion within it. To a surprising extent, these properties are common across a wide variety of roughness types.

An important fundamental role for the study of rough-wall boundary layers is in tackling the general problem of boundary layer turbulence and its dominant forms of organized motion. It is clear that conditions at the wall can be drastically altered by roughness without changing the main boundary-layer structure (outside the roughness or viscous sublayer) in any fundamental way. This provides a strong clue about the selforganizing properties of boundary-layer turbulence, which, when properly understood, will offer much to the study of turbulence in general.

## 4. Problem Formulation

In this chapter, we introduce the problem formulation. First we present the governing equation, then numerical method and the boundary conditions used are discussed. We conclude by describing in detail the immersed boundary method used to simulate the roughness.

### 4.1 Governing equations

The equations of conservation of momentum and mass for incompressible flow are

$$\frac{\partial u_i}{\partial t} + \frac{\partial}{\partial x_j} (u_i u_j) = -\frac{1}{\rho} \frac{\partial p}{\partial x_i} + \nu \cdot \nabla^2 u_i \quad (4.1)$$

$$\frac{\partial u_i}{\partial x_i} = 0 \quad (4.2)$$

The large-eddy simulation equations are derived from (4.1) and (4.2) by applying a filtering operation (Leonard, 1974), defined as

$$\overline{f}(x) = \int f(x') \cdot G(x, x'; \overline{\Delta}) dx' \quad (4.3)$$

where  $G$  is a filter function with a characteristic length,  $\overline{\Delta}$ . Applying filtering to both sides of (4.1) and (4.2), one obtains

$$\frac{\partial \overline{u}_i}{\partial t} + \frac{\partial}{\partial x_j} (\overline{u_i u_j}) = -\frac{1}{\rho} \frac{\partial \overline{p}}{\partial x_i} + \nu \cdot \nabla^2 \overline{u}_i \quad (4.4)$$

$$\frac{\partial \overline{u}_i}{\partial x_i} = 0 \quad (4.5)$$

Here the overbar denotes the filtered quantities. Defining the residual-stress tensor  $\tau_{ij}^R$

$$\tau_{ij}^R = \overline{u_i u_j} - \overline{u}_i \overline{u}_j \quad (4.6)$$

the anisotropic residual-stress tensor

$$\tau_{ij}^r = \tau_{ij}^R - \frac{1}{3} \cdot \tau_{ij}^R \delta_{ij} \quad (4.7)$$

and including the isotropic portion of the residual stress into the modified filtered pressure

$$\bar{P} = \bar{p} + \frac{1}{3} \cdot \rho \cdot \tau_{ij}^R \quad (4.8)$$

then (4.4) becomes

$$\frac{\partial \bar{u}_i}{\partial t} + \frac{\partial}{\partial x_j} (\bar{u}_i \bar{u}_j) = -\frac{1}{\rho} \frac{\partial \bar{P}}{\partial x_i} + \nu \cdot \nabla^2 \bar{u}_i - \frac{\partial \tau_{ij}^r}{\partial x_j} \quad (4.9)$$

This equation, together with (4.5), will be solved in this study.

## 4.2 Sub-grid scale model

A linear eddy-viscosity model is used to link the residual stress tensor to the filtered rate of strain,

$$\tau_{ij}^r = -2\nu_T \bar{S}_{ij} \quad (4.10)$$

where  $\nu_T$  is the eddy viscosity, and the filtered rate of strain is

$$\bar{S}_{ij} = \frac{1}{2} \cdot \left( \frac{\partial \bar{u}_i}{\partial x_j} + \frac{\partial \bar{u}_j}{\partial x_i} \right) \quad (4.11)$$

Thus the momentum equation becomes

$$\frac{\partial \bar{u}_i}{\partial t} + \frac{\partial}{\partial x_j} (\bar{u}_i \bar{u}_j) = -\frac{1}{\rho} \frac{\partial \bar{P}}{\partial x_i} + \frac{\partial}{\partial x_j} \left[ (\nu + \nu_T) \frac{\partial \bar{u}_i}{\partial x_j} \right] + \frac{\partial}{\partial x_j} \left[ (\nu + \nu_T) \frac{\partial \bar{u}_j}{\partial x_i} \right] \quad (4.12)$$

The eddy viscosity is modeled as

$$\nu_T = l_s^2 \cdot \bar{S} = c \cdot \bar{\Delta}^2 \cdot \bar{S} \quad (4.13)$$

where  $l_s$  is the subgrid-scale length scale, which is taken to be proportional to the grid filter width,  $\bar{\Delta} = (\Delta x \Delta y \Delta z)^{1/3}$ , and  $\bar{S}$  is the grid-filtered strain-rate

$$\bar{S} = (2\bar{S}_{ij} \bar{S}_{ij})^{1/2} \quad (4.14)$$

In the current study,  $c$  is modeled by the Lagrangian Dynamic Eddy-Viscosity model (Meneveau et al., 1996).

$$c = -\frac{1}{2} \cdot \frac{\zeta_{LM}}{\zeta_{MM}} \quad (4.15)$$

where  $\zeta_{LM}$  and  $\zeta_{MM}$  represent the averages  $\langle M_{ij} L_{ij} \rangle$  and  $\langle M_{ij} M_{ij} \rangle$  along particle paths, and are calculated as follows. First  $L_{ij}$  and  $M_{ij}$  are obtained from:

$$L_{ij} = \overline{u_i u_j} - \overline{u_i} \overline{u_j} \quad (4.16)$$

$$M_{ij} = \alpha^2 \overline{\Delta}^2 \overline{\tilde{S} S_{ij}} - \overline{\Delta}^2 \overline{\tilde{S}} \overline{S_{ij}} \quad (4.17)$$

where  $\overline{(\cdot)}$  denotes filtering by the test filter, and  $\alpha = \overline{\Delta} / \Delta$  is the ratio of the test filter width to the grid filter width. Then,  $P_{LM}$  and  $P_{MM}$  are calculated as

$$P_{LM} = L_{ij} M_{ij} \quad P_{MM} = M_{ij} M_{ij} \quad (4.18)$$

The new numerator and denominator of (4.15) at the  $(n+1)^{\text{th}}$  time step are obtained from:

$$\zeta_{LM}^{n+1} = \varepsilon^n P_{LM}^{n+1} + (1 - \varepsilon^n) \zeta_{LM}^n \quad (4.19)$$

$$\zeta_{MM}^{n+1} = \varepsilon^n P_{MM}^{n+1} + (1 - \varepsilon^n) \zeta_{MM}^n \quad (4.20)$$

where  $\varepsilon^n = \Delta t^n / (\Delta t^n + T^n)$ ,  $\Delta t$  is the time step,  $T$  is a time constant defined as

$$T^n = 1.5 \overline{\Delta} \times (-8 \zeta_{LM}^n \zeta_{MM}^n)^{-1/8} \quad (4.21)$$

### 4.3 Time-advancement and discretization

The fractional time-step method (Chorin, 1968; Kim & Moin, 1985) is used to solve the governing equation (4.9) and (4.5). First the predicted value of the velocity field is solved from the momentum equation without the pressure term. Second-order Crank-Nicolson time advancement is applied on the wall-normal viscous and wall-normal subgrid-scale viscosity terms. The explicit Adams-Bashforth time-advancement is applied for all other terms. For the  $u$ -momentum equation,

$$\left\{ 1 - \frac{1}{2} \Delta t \frac{\partial}{\partial y} \left[ (\nu + \nu_T^n) \right] \right\} \tilde{u} = \bar{u}^n + \Delta t \left( \frac{3}{2} F_u^n - \frac{1}{2} F_u^{n-1} \right) + \frac{1}{2} \Delta t \frac{\partial}{\partial y} \left[ (\nu + \nu_T^n) \frac{\partial \bar{u}^n}{\partial y} \right] \quad (4.22)$$

where



$$\begin{aligned}
F_u^n = & -\frac{\partial \bar{u}^n \bar{u}^n}{\partial x} - \frac{\partial \bar{u}^n \bar{v}^n}{\partial y} - \frac{\partial \bar{u}^n \bar{w}^n}{\partial z} + \frac{\partial}{\partial x} \left[ (\nu + \nu_T^n) \frac{\partial \bar{u}^n}{\partial x} \right] + \frac{\partial}{\partial z} \left[ (\nu + \nu_T^n) \frac{\partial \bar{u}^n}{\partial z} \right] + \\
& \left[ \frac{\partial}{\partial x} \left( \nu_T^n \frac{\partial \bar{u}^n}{\partial x} \right) + \frac{\partial}{\partial y} \left( \nu_T^n \frac{\partial \bar{v}^n}{\partial x} \right) + \frac{\partial}{\partial z} \left( \nu_T^n \frac{\partial \bar{w}^n}{\partial x} \right) \right] - \frac{1}{\rho} \frac{\partial \bar{P}^n}{\partial x}
\end{aligned} \tag{4.23}$$

In analogy, for  $v$ -momentum

$$\left\{ 1 - \frac{1}{2} \Delta t \frac{\partial}{\partial y} \left[ (\nu + \nu_T^n) \right] \right\} \bar{v}^n = \bar{v}^n + \Delta t \left( \frac{3}{2} F_v^n - \frac{1}{2} F_v^{n-1} \right) + \frac{1}{2} \Delta t \frac{\partial}{\partial y} \left[ (\nu + \nu_T^n) \frac{\partial \bar{v}^n}{\partial y} \right] \tag{4.24}$$

where

$$\begin{aligned}
F_v^n = & -\frac{\partial \bar{v}^n \bar{u}^n}{\partial x} - \frac{\partial \bar{v}^n \bar{v}^n}{\partial y} - \frac{\partial \bar{v}^n \bar{w}^n}{\partial z} + \frac{\partial}{\partial x} \left[ (\nu + \nu_T^n) \frac{\partial \bar{v}^n}{\partial x} \right] + \frac{\partial}{\partial z} \left[ (\nu + \nu_T^n) \frac{\partial \bar{v}^n}{\partial z} \right] + \\
& \left[ \frac{\partial}{\partial x} \left( \nu_T^n \frac{\partial \bar{u}^n}{\partial y} \right) + \frac{\partial}{\partial z} \left( \nu_T^n \frac{\partial \bar{w}^n}{\partial y} \right) \right] - \frac{1}{\rho} \frac{\partial \bar{P}^n}{\partial y}
\end{aligned} \tag{4.25}$$

and for  $w$ -momentum

$$\left\{ 1 - \frac{1}{2} \Delta t \frac{\partial}{\partial y} \left[ (\nu + \nu_T^n) \right] \right\} \bar{w}^n = \bar{w}^n + \Delta t \left( \frac{3}{2} F_w^n - \frac{1}{2} F_w^{n-1} \right) + \frac{1}{2} \Delta t \frac{\partial}{\partial y} \left[ (\nu + \nu_T^n) \frac{\partial \bar{w}^n}{\partial y} \right] \tag{4.26}$$

where

$$\begin{aligned}
F_w^n = & -\frac{\partial \bar{w}^n \bar{u}^n}{\partial x} - \frac{\partial \bar{w}^n \bar{v}^n}{\partial y} - \frac{\partial \bar{w}^n \bar{w}^n}{\partial z} + \frac{\partial}{\partial x} \left[ (\nu + \nu_T^n) \frac{\partial \bar{w}^n}{\partial x} \right] + \frac{\partial}{\partial z} \left[ (\nu + \nu_T^n) \frac{\partial \bar{w}^n}{\partial z} \right] + \\
& \left[ \frac{\partial}{\partial x} \left( \nu_T^n \frac{\partial \bar{u}^n}{\partial z} \right) + \frac{\partial}{\partial y} \left( \nu_T^n \frac{\partial \bar{v}^n}{\partial z} \right) + \frac{\partial}{\partial z} \left( \nu_T^n \frac{\partial \bar{w}^n}{\partial z} \right) \right] - \frac{1}{\rho} \frac{\partial \bar{P}^n}{\partial z}
\end{aligned} \tag{4.27}$$

After the prediction step, the Poisson equation is solved

$$-\nabla^2 \Phi^{n+1} = \frac{1}{\Delta t} \frac{\partial \bar{u}_i}{\partial x_i} \tag{4.28}$$

where  $\Phi$  satisfies

$$\frac{\partial \Phi}{\partial x_i} + \frac{\partial}{\partial x_j} \left[ \nu \Delta t \frac{\partial^2 \Phi}{\partial x_i \partial x_j} \right] = \frac{\partial \delta \bar{P}}{\partial x_i} \quad (4.29)$$

in which

$$\delta \bar{P} = \bar{P}^{n+1} - \bar{P}^n \quad (4.30)$$

The velocity is then corrected to obtain a divergence-free velocity field

$$\bar{u}_i^{n+1} \stackrel{\leftarrow}{=} \bar{u}_i - \Delta t \frac{\partial \Phi}{\partial x_i} \quad (4.31)$$

Second-order central differencing is used for all terms. For the convective term, a reverseweighting (or volume-weighting) (Ham et al., 2002) technique is used to interpolate the velocity field to evaluate derivatives at a staggered location. Define the averaging operators:

$$\bar{\Phi}^{\bar{x}} \Big|_{i,j,k,n} \equiv \frac{(x_{i+1/2} - x_i) \Phi_{i+1/2,j,k}^n + (x_i - x_{i-1/2}) \Phi_{i-1/2,j,k}^n}{2} \quad (4.32)$$

and

$$\bar{\Phi}^x \Big|_{i,j,k,n} \equiv \frac{\Phi_{i+1/2,j,k}^n + \Phi_{i-1/2,j,k}^n}{x_{i+1/2} - x_{i-1/2}} \quad (4.33)$$

where  $\Phi$  is a staggered variable, and the  $x$  superscript denotes interpolation in the  $x$  direction. Taking the convection terms in the u-momentum equation for an example, the convection term in the discretized u-momentum equation is obtained as

$$\frac{\partial(uu_j)}{\partial x_j} = \frac{\delta \bar{u}^x \bar{u}_j^{\bar{x}}}{\delta x_j} \quad (4.34)$$

in which summation is applied for repeating subscript, and  $\delta$  denotes discrete differencing.

#### 4.4 Boundary conditions

Periodic boundary conditions are applied in the spanwise direction and for the outflow. At the inflow, the recycling method is used. At the free stream the same setup used in previous studies of this flow (Piomelli et al., 2000; De Prisco et al., 2007; Piomelli &

Scalo, 2010) is applied here: a profile of the streamwise timeaveraged velocity is assigned, and the mean free-stream wall-normal velocity component,  $V_\infty(x)$ , is derived from mass conservation (Lund et al., 1998)

$$V_\infty = U_\infty \frac{\partial \delta^*}{\partial x} + (\delta^* - h) \frac{\partial U_\infty}{\partial x} \quad (4.35)$$

and the irrotational condition

$$\left. \frac{\partial U}{\partial y} \right|_\infty + \frac{\partial V_\infty}{\partial x} = 0 \quad (4.36)$$

where  $\delta^*$  is the local displacement thickness and  $h$  the domain height.

## 4.5 Immersed boundary method

Immersed boundary methods (IBM) are widely used to handle moving or deforming bodies with complex surface geometries embedded in a flow. They do not require the Eulerian grid to be body-conforming, since the no-slip boundary condition is imposed on the boundary surface by spreading boundary forces to the Eulerian cells. The IBM was first introduced by Peskin (1972), who calculated the boundary force on the Lagrangian grid points as a singular function using Hooke's law, and spread it on to the neighbouring Eulerian cells with regularized delta functions. With a similar approach, Goldstein et al. (1993) obtained the forcing function from a feed-back mechanism. These approaches, however, require some empirical parameters, and pose strict constraints on the time step or the deformation from immersed boundary. Direct formulations of the forcing function were introduced by Fadlun (2000), who modified the discretized momentum equation so that the interpolated velocity at the interface equals the required value, giving sharp interfaces. However, the interpolation is easy to carry out only for simple and regular interface geometries. Balaras (2004) extended the approach to complex geometries. In this study, to represent the random roughness elements while maintaining the simplicity of the Cartesian approach, we use an IBM based on the volume-of-fluid approach. This technique was first applied by Scotti (2006) to the study of roughness with DNS.

The volume-of-fluid (VOF) IBM method was first introduced by Hirt & Nichols (1981) to study the interface between different types of fluid. In this method, the volume fractions  $\Phi$  in surface cells are calculated (for incompressible fluids) from a conservation equation,

$$\left. \frac{\partial \Phi}{\partial t} \right| + \nabla \cdot (\Phi \vec{v}) = 0 \quad (4.37)$$

then, the amount of fluid transferred from the upstream cell to the downstream one is calculated from the product of  $\Phi$  and the flux boundary area. This method is simple and effective. It describes immersed interfaces in a piecewise-linear sense, and ensures conservation of mass for each type of fluid (with conservation of total  $\Phi$ ).

In this study, the interface is between steady surface roughness and a fluid; thus both the time-derivative term and the convection term in (4.37) equal zero. Instead, the volume fraction of each cell occupied by fluid,  $\Phi$ , is calculated in pre-processing. Note that, due to the staggered grid arrangement, different volume fractions are used for the three velocity components and the subgrid-scale viscosity. A force is imposed on the right-hand side of the momentum equation to reduce the velocity proportionally to the solid volume in each cell. This method is less accurate than, for instance, direct forcing (Fadlun et al., 2000); it is, however, adequate for the present application, since the description of the rough surface is only an approximation to real sandpaper. The IBM is imposed by calculating the forcing term

$$f_i^n = -\left(1 - \Phi\right) \frac{\bar{u}_i}{\Delta t} \quad (4.38)$$

after the prediction step. Afterwards, the prediction step is carried out for a second time with the forcing term as the source term, and the modified intermediate filtered velocity is obtained (taking the filtered  $u$ -momentum equation as an example),

$$\left\{1 - \frac{\Delta t}{2} \frac{\partial}{\partial y} \left[ (\nu + \Phi \nu_T^n) \frac{\partial}{\partial y} \right] \right\} \bar{u}_i = \left\{1 + \frac{\Delta t}{2} \frac{\partial}{\partial y} \left[ (\nu + \Phi \nu_T^n) \frac{\partial}{\partial y} \right] \right\} \bar{u}_i^{n-1} + \Delta t \left[ \frac{3}{2} (RHS^n + f_x^n) - \frac{1}{2} (RHS^{n-1} + f_x^{n-1}) \right] \quad (4.39)$$

where

$$\begin{aligned} RHS^n = & -\frac{\partial \bar{u}^n \bar{u}^n}{\partial x} - \frac{\partial \bar{u}^n \bar{v}^n}{\partial y} - \frac{\partial \bar{u}^n \bar{w}^n}{\partial z} - \frac{1}{\rho} \frac{\partial \bar{P}^n}{\partial x} + \\ & \frac{\partial}{\partial x} \left[ (\nu + \Phi \nu_T^n) \frac{\partial \bar{u}^n}{\partial x} \right] + \frac{\partial}{\partial z} \left[ (\nu + \Phi \nu_T^n) \frac{\partial \bar{u}^n}{\partial z} \right] + \\ & \Phi \frac{\partial}{\partial x} \left[ \nu_T^n \frac{\partial \bar{u}^n}{\partial x} \right] + \Phi \frac{\partial}{\partial y} \left[ \nu_T^n \frac{\partial \bar{v}^n}{\partial x} \right] + \Phi \frac{\partial}{\partial z} \left[ \nu_T^n \frac{\partial \bar{w}^n}{\partial x} \right] \end{aligned} \quad (4.40)$$

and, to accommodate the change of filter length in cells cut by the immersed boundaries, the eddy viscosity in these cells is also reduced proportionally to the volume of fluid.

## 5. Model Validation

This chapter describes the validation of the model, with particular stress on the implementation of the IBM, whose spatial and temporal accuracy are analyzed. This is done in two cases. First, a two-dimensional channel flow is studied, in which the channel is tilted with respect to the wall, to investigate the behaviour of the IBM on immersed boundaries that are not aligned to the cell boundaries, in a case for which the analytical solution is known. Then, the flow over a stationary cylinder is studied to investigate the average effect of random cutting of grid cells by the immersed boundary, and the accuracy of the method in an unsteady flow. Finally, an open-channel flows with a varying roughness surface is studied to validate the roughness modeling within the LES framework, and the grid resolution required for adequate resolution of the roughness. The results are compared to those obtained by Scotti (2006).

### 5.1 Tilted plane-channel flow

First, a two-dimensional, laminar flow in a channel tilted with respect to the grid lines is studied. A velocity profile is given at the inlet, and convective outflow boundary condition directions respectively, where  $l$  is the channel width. Three progressively refined meshes are used to study the spatial accuracy of the current scheme compared to the analytical result. The channel is tilted by  $45^\circ$ . Here the reference length is the channel height  $l = 1$ , and the reference velocity is the maximum velocity magnitude  $V_{max} = 1$  (where  $V = (u^2 + v^2)^{1/2}$ ). The Reynolds number, based on  $l$  and  $V_{max}$ , is equal to 1. A uniform mesh is used throughout the domain; immersed boundaries are applied to model the no-slip condition on both walls of the channel.

The contours of the volume-of-fluid  $\Phi$  and the velocity-magnitude contours are presented in figure 5.1. The velocity is zero outside the channel boundaries, and within the channel a parabolic profile is obtained. The magnified plot of  $\Phi$  shows the non-zero values of  $\Phi$  at the cells that are either cut by the immersed boundary, or are outside the immersed object. The magnified plot of velocity magnitude shows that velocity is non-zero at the cells that are partly occupied by the immersed object.

To determine the spatial accuracy of the method, three different resolutions are studied with a fixed time-step size  $\Delta t^* = 3 \times 10^{-4}$  (where  $\Delta t^* = \Delta t V_{max}/l$ ). The number of grid points (in  $x$  and  $y$ ) is  $96 \times 125$ ,  $192 \times 250$ , and  $384 \times 500$ . The number of grid points used to describe the channel-flow profile (perpendicular to the center-line) is 12, 24, 48, respectively.

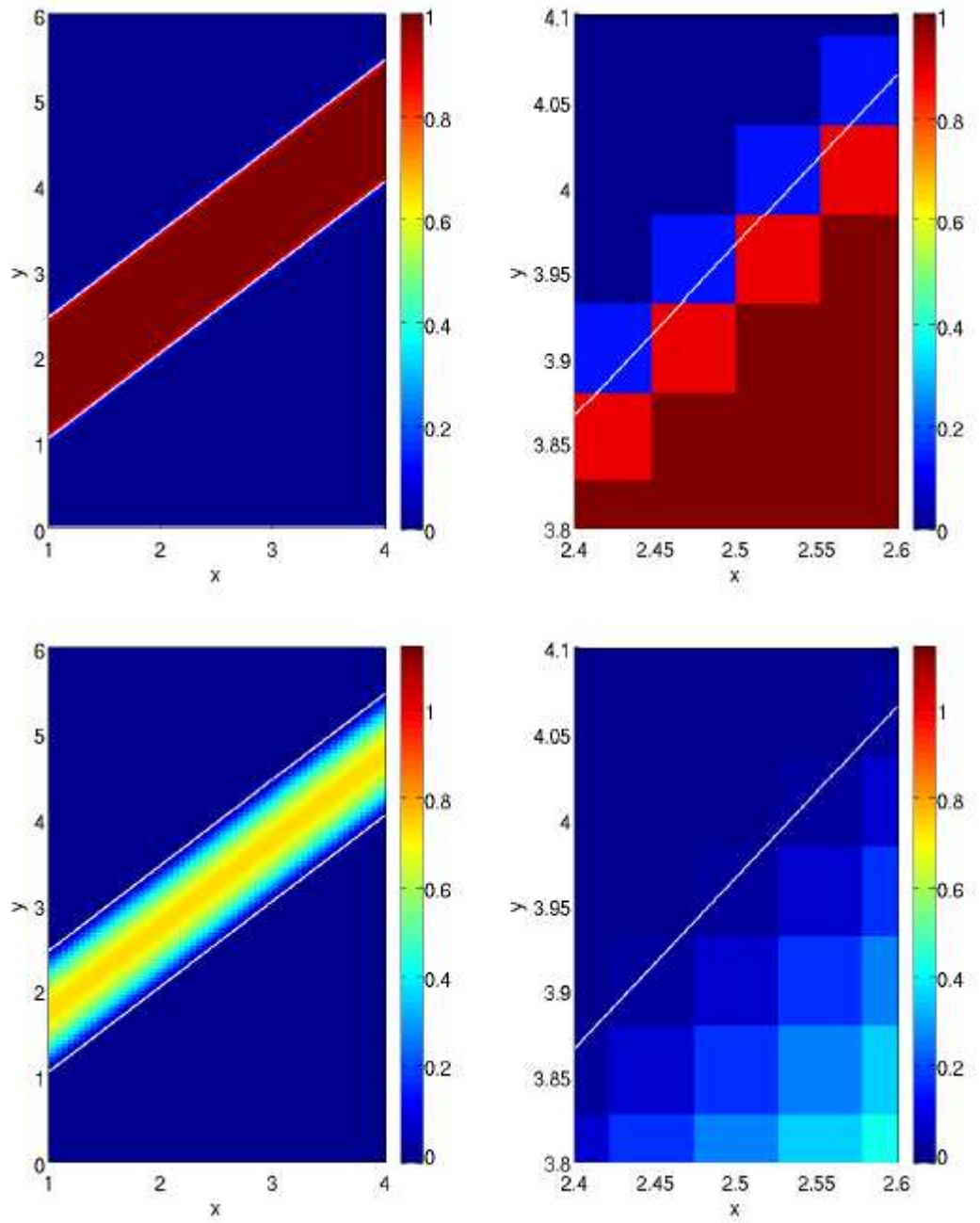


Fig. 5.1 - Contours of volume of fluid  $\Phi$  (top) and velocity magnitude (bottom) in the tilted channel. Magnified plots of a region near the top wall are shown on the right. 96 x 125 grid points are used in  $x$  and  $y$ . The white lines mark the exact locations of the channel walls.

The resulting velocity profiles are compared with the analytical profile in Fig. 5.2. We observe two types of error: near the wall, the no-slip condition is not verified on the grid cell intersected by the boundary; furthermore, the centreline velocity tends to be higher than the analytical solution. The combination of these errors yields first-order accuracy, as shown in figure 5.3, in which the  $L_2$  and  $L_\infty$  norms are shown for various grid resolutions. The error norms here are averaged over the streamwise direction.

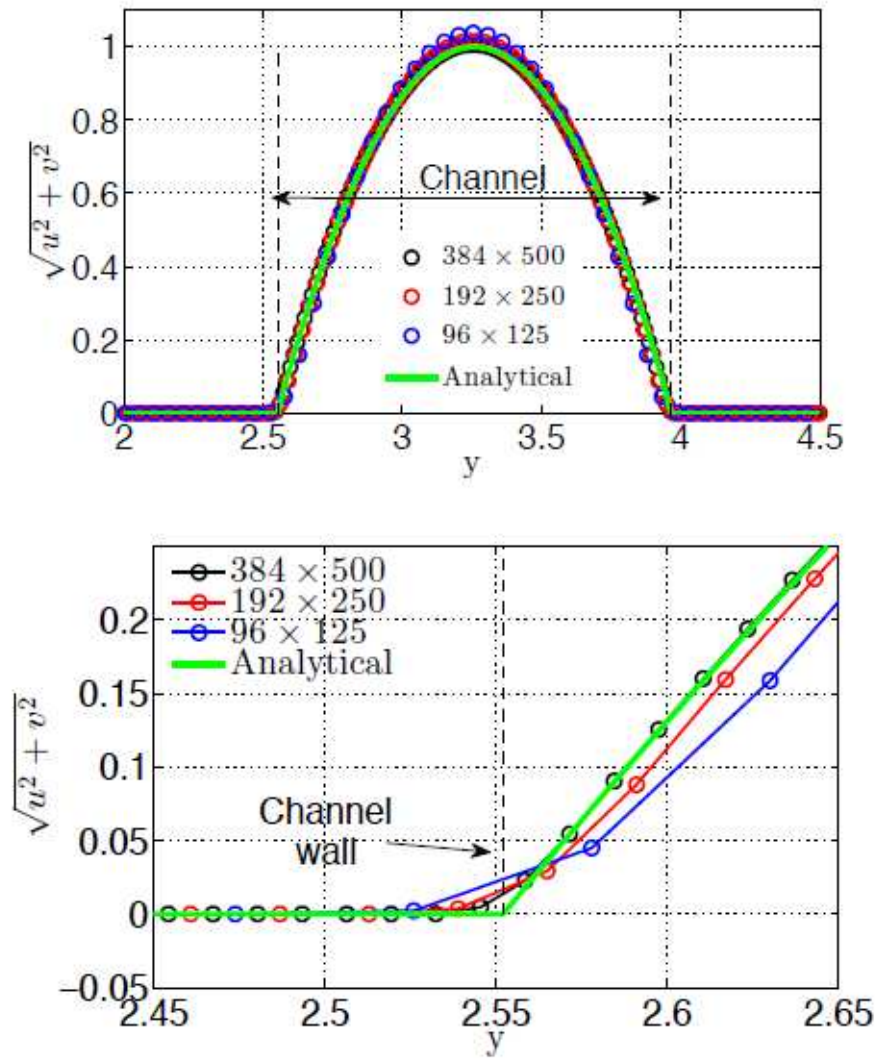


Fig. 5.2 - Profiles of velocity magnitude for the flow in a tilted channel at  $x = 2.5l$  (top) and its magnified plot (bottom).

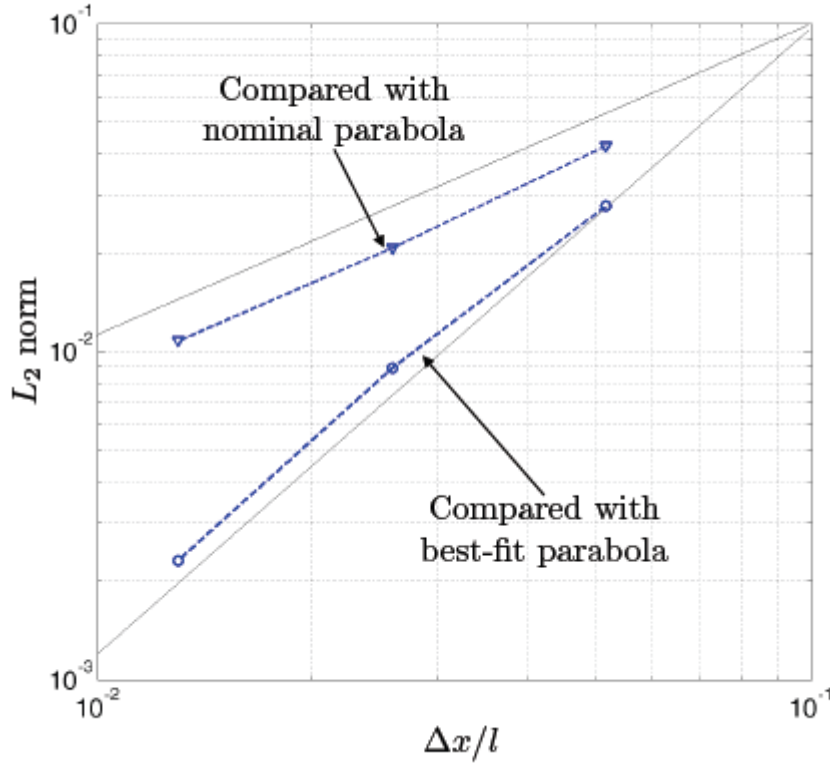


Fig. 5.3 - Spatial accuracy for the flow in a tilted channel. The lines correspond to first and second-order accuracy, respectively.

The first-order accuracy of the IBM is due to the fact that the VOF yields a diffused interface, whose exact location can be determined only to the order of the grid size. With reference to figure 5.2, one notices that extrapolating the velocity profile from the last two inner points to zero gives a virtual position of the wall that corresponds to a narrower channel than the nominal one. This naturally yields (since mass is conserved) a higher centerline velocity.

To clarify this issue, at each  $x$ -location we computed the parabola that best fits (in a least-squares sense) the velocity profile (Fig. 5.4). We then use the zero crossings of the parabola to determine the “real” location of the wall (indicated with a triangle in the figure). If we compare the numerical solution with the best-fit parabola, we obtain second order accuracy (Fig. 5.3); however, if we compare the difference between the “real” and nominal location of the walls (Fig. 5.5), we observe that the difference decreases with first-order accuracy only.



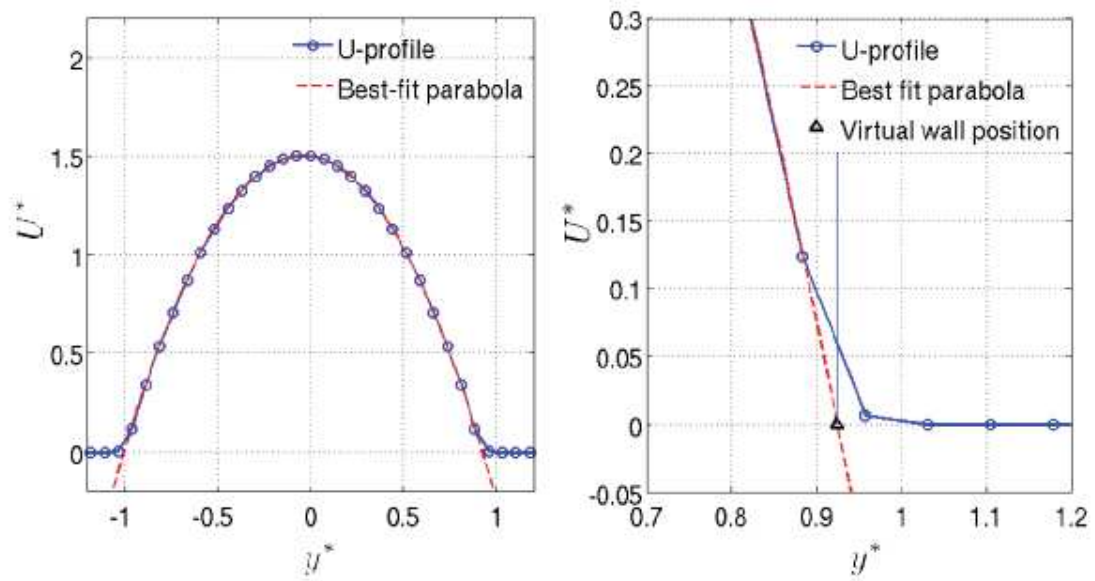


Fig. 5.4 - Comparison of the numerical solution with the best-fit parabola (left) and the magnified plot (right).

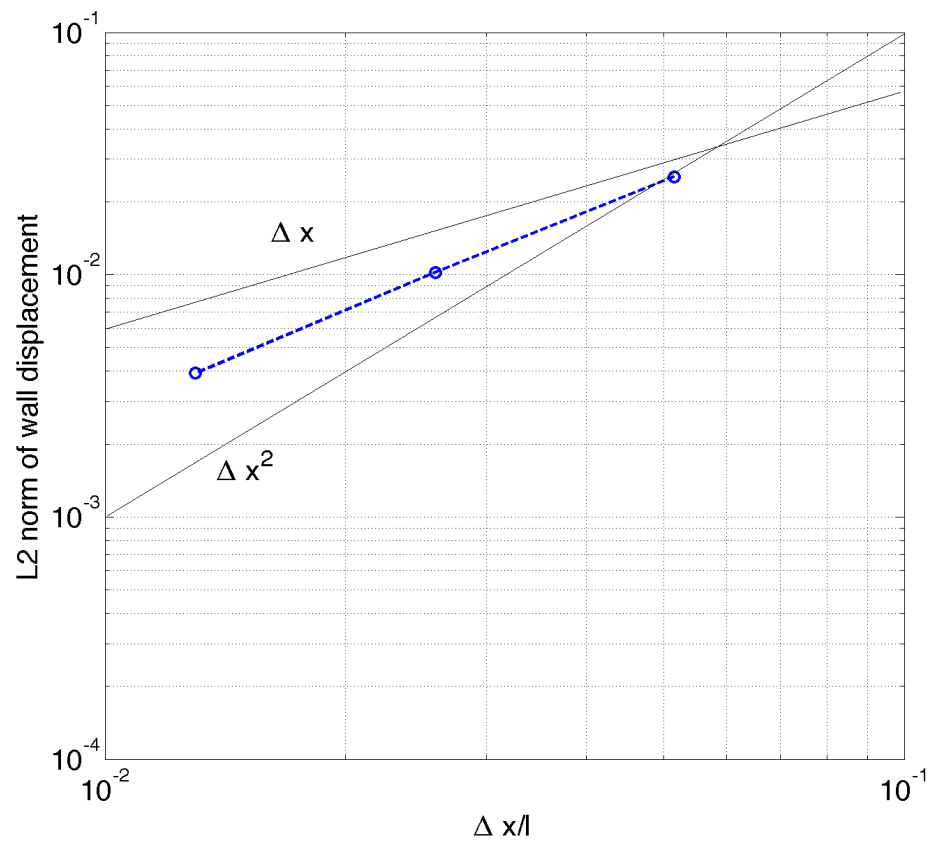


Fig. 5.5 - Difference between the “nominal” and the “real” wall locations. The lines correspond to first- and second-order accuracy, respectively.

The conclusion of this test is that the main limitation of the VOF-based IBM method comes from the difficulty in determining the exact location of the interface. For problems in which the geometry of the immersed boundary can be described with high accuracy, this limitation may be significant. In the application studied here, the flow over a rough wall, on the other hand, the description of the boundary is only approximate, and this error is not expected to affect the results significantly.

Although this problem is steady state, we demonstrate in figure 5.6 that the solution depends weakly on time-step size. This might be due to the time-dependence of the forcing defined for the IBM. As  $\Delta t^*$  reduces asymptotically to zero, the error approaches an asymptotic non-zero value, with the “real” location of the wall approaches the one corresponding to zero -  $\Delta t^*$ .

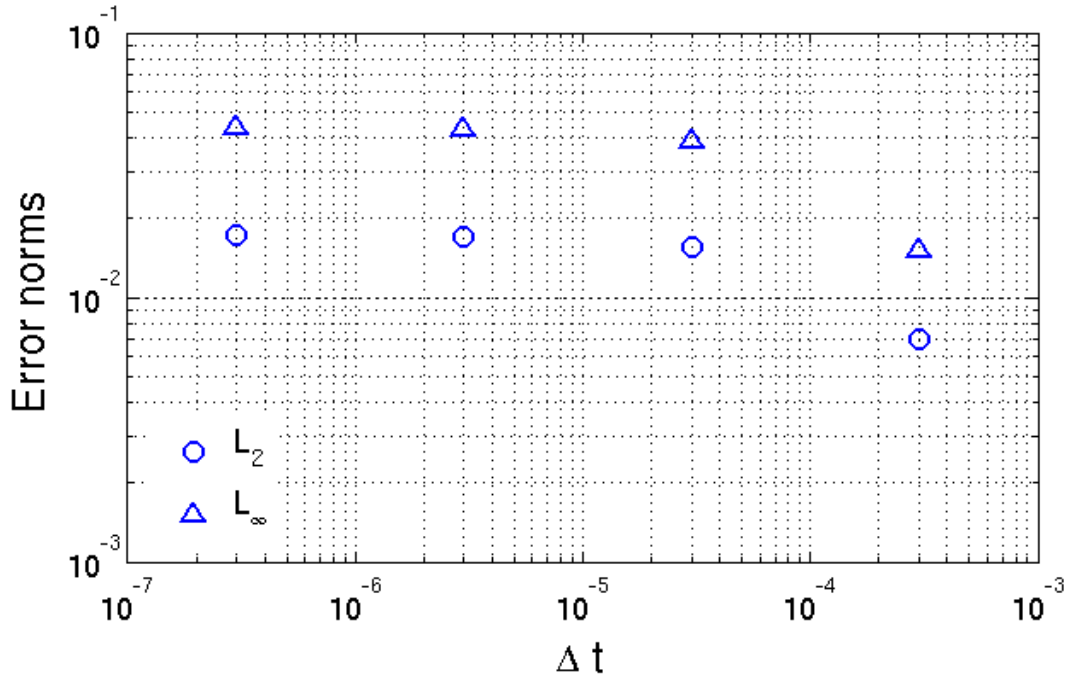


Fig. 5.6 - Dependence of the error on the time step in a tilted channel. The error is defined as the difference from the case with smallest time-step size.

## 5.2 Flow over a two-dimensional circular cylinder

To study the flow over a general shape described by the immersed boundary, we investigate the use of IBM in simulating a stationary two-dimensional cylinder. Uniform free-stream velocity in the  $x$ -direction is assigned at the inflow. At the outflow the convective boundary condition is applied. Free-slip boundary conditions are used for both the top and bottom boundaries. The reference length and velocity are the cylinder diameter  $d$  and the uniform inlet velocity  $U_\infty$ , both of which are set to a unit value. The domain is  $[0, 49d]$  and  $[0, 60d]$  in  $x$  and  $y$ , with the cylinder at  $[9d, 30d]$ . The Reynolds number based on  $d$  and  $U_\infty$  is 20.

To carry out the grid refinement study, two resolutions are used (Table 5.1). Grids are stretched in both  $x$  and  $y$  directions. Close to the cylinder ( $8.4 < x/d < 10$ , and  $29 < y/d <$

31) the mesh is uniform and takes the smallest value across the domain:  $\Delta x = \Delta y = \Delta_{min}$ . The grid starts to be stretched outside of this region, with a stretching rate less than 3% for  $23 < y/d < 37$  and  $5.5 < x/d < 16.5$ . A constant time-step  $\Delta t^* = \Delta t U_\infty/d = 1 \times 10^{-4}$  is used in all cases. In Table 5.2, the present results are compared to those in the study by Taira & Colonius (2007), where a direct-forcing immersed boundary method was used, with domain size  $[-30d, 30d] \times [-30d, 30d]$ , and the cylinder at  $[0, 0]$ . Also the experimental studies by Tritton (1959) and Coutanceau & Bouard (1977) are listed. The size and shape of the wake is characterized by lengths  $l$ ,  $a$ ,  $b$ , and  $\theta$ , which are illustrated in figure 5.7.

|                  | Case B           | Case A           | Taira B          | Taira A          |
|------------------|------------------|------------------|------------------|------------------|
| $n_x \times n_y$ | $400 \times 500$ | $300 \times 420$ | $300 \times 300$ | $150 \times 150$ |
| $\Delta_{min}$   | $0.02d$          | $0.04d$          | $0.02d$          | $0.04d$          |

Table 4.1 - Grid resolutions used in cylinder flow simulation compared to previous simulations (Taira & Colonius, 2007).

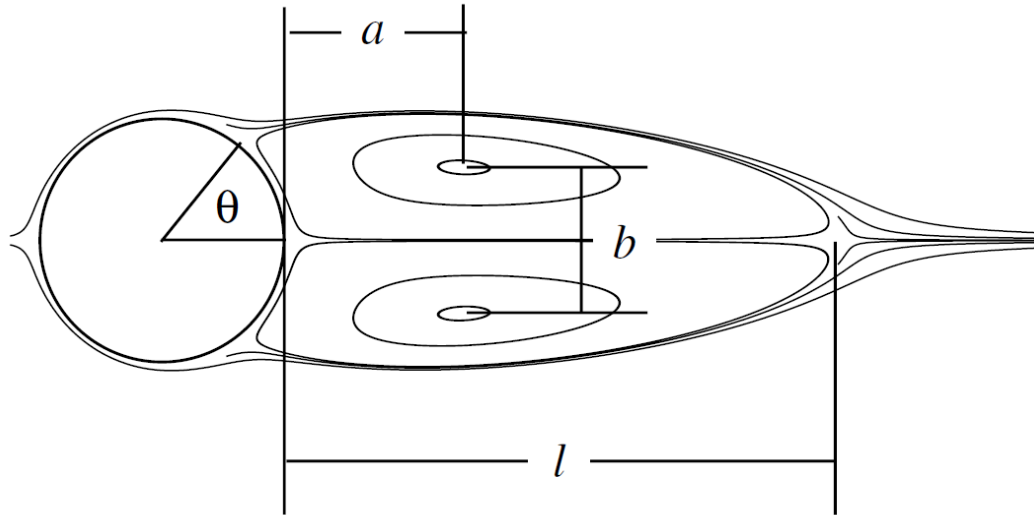


Fig. 5.7 - Definition of the characteristic dimensions of the wake structure.

The drag coefficient is defined as

$$C_d = \frac{F_x}{1/2 \rho U_\infty^2 A} \quad (5.1)$$

where the reference area  $A$  is taken to be  $d \times 1$  in the current two-dimensional flow, and  $F_x$  is the total drag force summed within the two-dimensional domain with unit depth,

$$F_x = \int_V f_x dv \quad (5.2)$$

where  $V$  is the whole domain area and  $f_x$  is the local forcing imposed by the IBM,

$$f_x = \frac{\partial uu}{\partial x} + \frac{\partial uv}{\partial y} + \frac{1}{\rho} \frac{\partial p}{\partial x} - \nu \frac{\partial^2 u}{\partial x^2} - \nu \frac{\partial^2 v}{\partial y^2} \quad (5.3)$$

In general, the results match each other very well. The grid resolution slightly influences the characteristic lengths of the cylinder wake.  $b/d$  is the least sensitive to resolution, while there is a 2% increase for  $a/d$  and a 2% decrease for  $l/d$  from the coarsest case to the finest case. Both simulations give higher values of  $a/d$  and  $l/d$  than the experimental results.  $C_d$  in this study is systematically higher than the reference numerical and experimental results by about 10%, probably because of the error due to the smearing effect of the virtual boundary. This error slowly decreases as the mesh is refined.

|          | Case B | Case A | Taira B | Taira A | C.B. expt. | T. expt. |
|----------|--------|--------|---------|---------|------------|----------|
| $C_d$    | 2.23   | 2.26   | 2.06    | 2.07    | —          | 2.09     |
| $a/d$    | 0.37   | 0.36   | 0.37    | 0.39    | 0.33       | —        |
| $b/d$    | 0.44   | 0.44   | 0.43    | 0.43    | 0.43       | —        |
| $l/d$    | 0.97   | 0.99   | 0.94    | 0.97    | 0.93       | —        |
| $\theta$ | 44.6°  | 45.0°  | 43.3°   | 44.1°   | 45.0°      | —        |

Table 5.2 - Grid convergence study on the flow over a stationary cylinder.  $\Delta t^* = 0.0001$ . Here, “C.B. expt.”, and “T. expt.” Indicates experimental studies by Coutanceau & Bouard (1977) and Tritton (1959).

It is shown again here that the steady solution depends on the time step. Calculations were carried out for the grid of Case D, with  $\Delta t^* = 0.0012$ , 0.0003, and 0.0001. The results reported in Table 5.3 show some effect of time-step, which changes the flow-field length scales by approximately 2% over the range of  $\Delta t^*$  considered. For steady-state problems, this dependence is built into the formulation of the VOF-based IBM. As  $\Delta t^*$  goes to zero, in any cell with  $\Phi < 1$  the velocity eventually goes to zero too. In this case, the virtual boundary is no longer smooth, but becomes pixellated, with a scale proportional to the grid size; this increases local forcing, and consequently leads to higher values of  $C_d$ . Such effective roughness may exert a visible influence in laminar flows. In turbulent flows, however, in which local grid size is supposed to be smaller than the viscous sublayer thickness, it will still result in a hydrodynamically smooth surface. Besides, the drag force from the rough wall in the study of turbulent boundary layers in the next chapter is calculated from global momentum balance for each vertical slice of the domain; this approach decreases the influence of local error brought by the IBM. Therefore, the error in  $C_d$  as is found in the current testcase could be considered negligible in the discussion in chapter 6.

| $\Delta t^*$ | 0.0012 | 0.0003 | 0.0001 |
|--------------|--------|--------|--------|
| $C_d$        | 2.19   | 2.25   | 2.26   |
| $a/d$        | 0.37   | 0.38   | 0.38   |
| $b/d$        | 0.44   | 0.44   | 0.44   |
| $l/d$        | 0.97   | 0.98   | 0.99   |
| $\theta$     | 45.0°  | 45.0°  | 45.0°  |

Table 5.3 - Influence of  $\Delta t$  on cylinder wake and drag coefficient with the resolution in Case A.

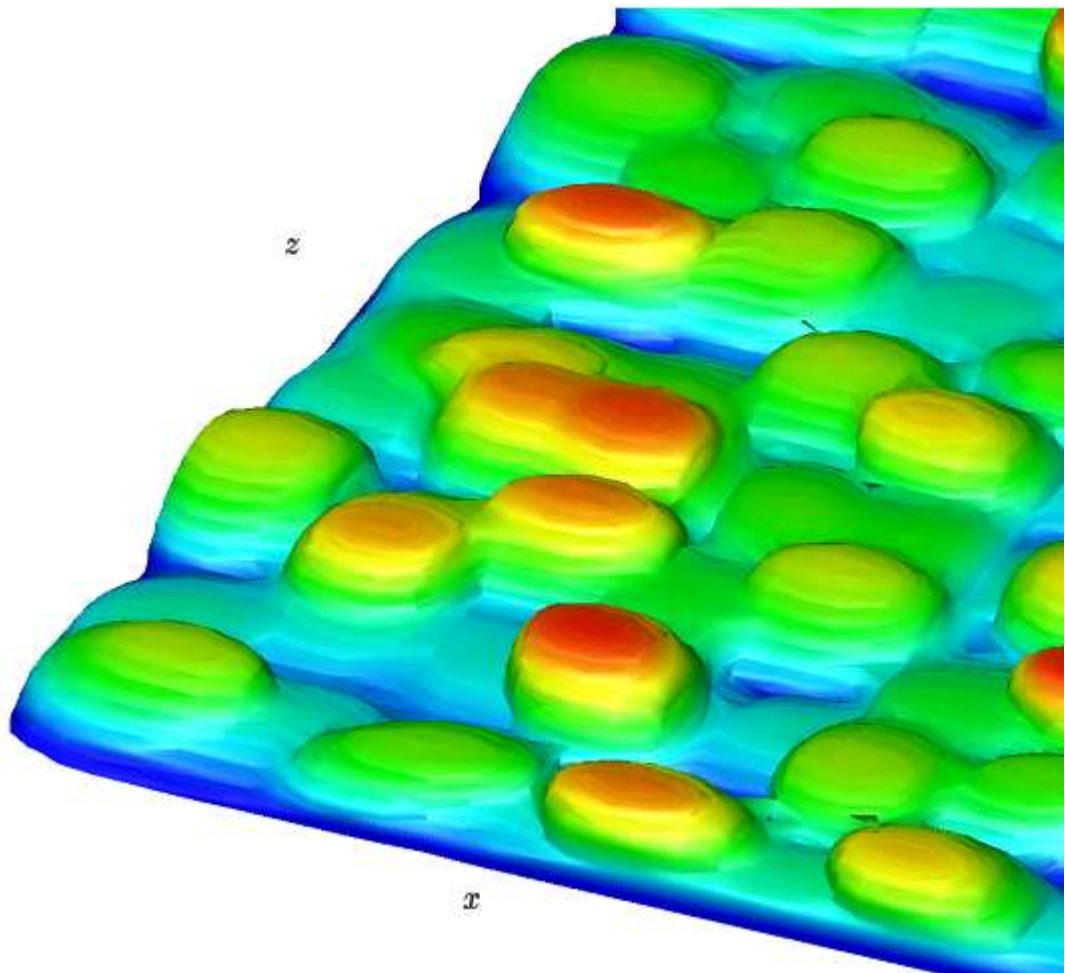


Fig. 5.8 - Iso-surface of  $\Phi$  (coloured by  $y/h$ ) showing a section of the rough wall used in the open-channel testcase, with  $h = 0.04$ . Here  $\Phi = 0.9$ .

### 5.3 Rough-wall channel flow

To validate the roughness simulated by the IBM, and to carry out a grid-resolution study, we perform LES of channel flow with roughness. Here an open channel is chosen in order to reduce the domain size required. Periodic boundary conditions are applied in the spanwise and streamwise directions; and the streamwise pressure gradient is constant through out the domain; a free-slip boundary condition is used for the top boundary. At the bottom, roughness elements are modeled using the IBM.

We use the virtual sand-paper roughness model proposed by Scotti (2006): the sandgrains are represented by uniformly distributed but randomly oriented ellipsoids of the same size (larger than the cell size) and shape. Only one parameter, the equivalent sandroughness height  $h_s$ , is needed to describe the roughness geometry and distribution, with the semi-axes of the ellipsoids set to  $h_s$ ,  $1.4 h_s$ , and  $2 h_s$ , and a separation of  $2 h_s$  between centers of neighboring ellipsoids in streamwise and spanwise directions, (i.e., the bottom wall is discretized into tiles of the size  $2 h_s \times 2 h_s$ , and each of them contains a roughness element). The roughness height  $h_s$  is chosen to be  $0.025l$ ,  $0.05l$ , where  $l = 1$  is the half-channel height. Since  $h_s$  alone can describe the roughness surface, from here on we call it “roughness height” for simplicity and denote it by  $h$ . The iso-surface of the volume fractions  $\Phi$ , defined in section 4.5, in particular  $\Phi = 0.9$ , with  $h = 0.04l$  on a section of the bottom wall is presented in figure 5.8, which shows the shape and distribution of roughness elements.

Scotti’s model of roughness is very useful, since satisfies the following requirements:

- It is characterized by a small set of parameters;
- It is easy to implement numerically;
- the effects on the bulk properties of the flow (velocity defect, friction coefficient,...) is known a priori;
- the boundary layer has properties that match observations.

We want to remark that in Scotti’s model of roughness the volume fraction is calculated once for a given cartesian grid and roughness height  $h$ ;  $\Phi$  is then used to include the effect of the rough boundary at each time step based on the following procedure:

- 1) compute the intermediate velocity field which includes the effects of advection and diffusion;
- 2) multiply the intermediate field by  $\Phi$  to include the effect of roughness;
- 3) calculate the pressure field necessary to project the corrected intermediate field onto the space of divergenceless fields;
- 4) apply the pressure correction to obtain the velocity field at the end of the time step.

The appeal of this method is that it is extremely simple to implement numerically. Of course, it is possible to use an immersed boundary method to achieve the same result with higher accuracy (sand grains, trees, etc.) whose surface is not known if not approximatively. However, the computational cost would be higher, without a clear benefit, since we are interested in boundaries (sand grains, trees, etc.) whose surface is not known if not approximatively.

The domain size we used in our open channe is  $6l \times l \times 3l$  in  $x$ ,  $y$ , and  $z$  directions; the reference velocity and length scales are  $u_\tau$  and  $l$ . The Reynolds number  $Re_\tau$ , based on  $u_\tau$  and  $l$ , is 800, which gives  $h^+ = 20$  and 40 respectively for  $h_s = 0.025l$  and  $0.05l$ . A uniform mesh, with constant step, is used in the streamwise and spanwise directions.

The situation is different for the  $y$  domain: here we want to focus on the rough wall, hence this region must be solved carefully: we used a  $y$ -mesh which is uniform ( $\Delta y^+ < 1$ ) within the region  $y < 1.5h$  (which includes the highest point of roughness elements). For  $y > 1.5h$ ,  $\Delta y^+$  increases with a stretching rate of less than 2% through out the boundary layer with a hyperbolic tangent behaviour.

Two progressively refined grid resolutions are compared, together with the one used in the DNS in open-channel flows in Scotti (2006).

Table 5.4 lists the number of grid points (in  $x$ ,  $y$  and  $z$  direction), grid size in wall unit, as well as the number of grid points per roughness element,  $N_i$  and  $N_k$ , in the streamwise and spanwise directions; they are defined, respectively, as  $2h/\Delta x$  and  $2h/\Delta z$ .

| <i>Mesh</i>        | <i>A</i>      | <i>B</i>        | <i>Scotti (2006)</i> |
|--------------------|---------------|-----------------|----------------------|
| Grid size          | 96 x 152 x 96 | 192 x 152 x 192 | 386 x 256 x 386      |
| $N$ ( $h=0.025l$ ) | 0.8 x 1.6     | 1.6 x 3.2       | 2.57 x 7.72          |
| $N$ ( $h=0.05l$ )  | 1.6 x 3.2     | 3.2 x 6.4       | 5.14 x 15.44         |
| $\Delta x^+$       | 50            | 25              | 15.2                 |
| $\Delta z^+$       | 25            | 12.5            | 5.2                  |

Table 5.4: Grid size and grid resolution for each mesh, compared to Scotti (2006)

$\Delta y^+$  (1) is less than 1 for all cases. Also, focus is not given on  $N_j$ , since the roughness elements are much better resolved vertically than they are horizontally.

For smooth-wall flows, to resolve the spanwise streaks in LES,  $\Delta x^+ \approx 60$  and  $\Delta z^+ \approx 25$ . In the transitionally rough regime, the roughness elements interfere with the buffer-layer production cycle, but do not completely destroy it; thus, the influence of roughness on the forming of streaks is limited: the characteristics of the near-wall structures are still comparable to those over a smooth wall. Therefore, we expect that this near-wall flow-structure constraint also applies to rough walls. Meshes A and B both satisfy this requirement. Another constraint is imposed by a reasonable description of the shape of the roughness elements: it has been widely presented in the literature that the effects of roughness vary with the element shape (as widely described in chapter 3). Table 5.4 shows that the lower resolution, which marginally resolves the near-wall structures from the point of view of the smooth-wall criteria, also describes the shape of roughness elements, at least marginally (e.g.,  $N_i = 0.8$  and  $1.6$  in Mesh A).

The grid-refinement study is carried out considering first- and second-order turbulent statistics. For the mean flow, the roughness effect is represented by the roughness function  $\Delta U^+(y^+)$ , which is plotted against  $h^+$  in figure 5.9 for each resolution. It is clear that both mesh A and mesh B resolve well the mean momentum absorption by roughness, and the results obtained fit very well with Scotti's.

From now on to compare the two meshes we consider only the lowest roughness height  $h^+ = 20$ , for which the shape description is the most critical (the size of the roughness is smaller).

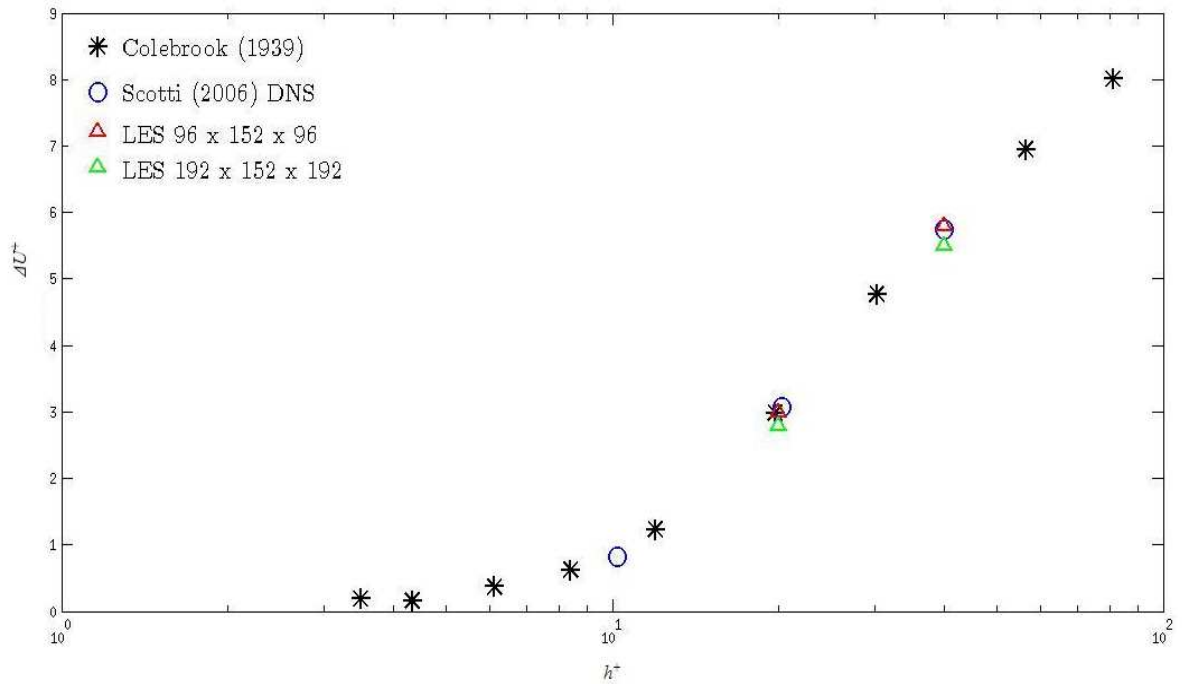


Fig. 5.9 – Grid refinement study: roughness function. LES and DNS results compared to experiment results in Colebrook (1939).

Fig. 5.10 shows that, when the zero-plane displacement  $d$  is added to the y-axis, curves of both the meshes collapse well with the DNS and smooth-wall experimental results.

Thus Meshes A and B adequately resolve the mean flow;  $d$  could be either calculated as the centroid of drag profile exerted by the roughness elements (Jackson, 1981), or obtained by fitting measured mean velocity profiles to assumed forms (Bandyopadhyay, 1987). Here  $d$  is calculated from the first method based on the temporal- and spatial-averaged  $u$ -momentum equation (refer to Scotti (2006) for details) and is found very close to  $0.8h$  for both Case A and Case B, consistent with the value obtained in Scotti (2006). This indicates that the general effect of drag force on the mean flow outside of the roughness sublayer is well resolved and our model is validated with Scotti's one.

In figure 5.11, the three components of turbulent fluctuation are compared to the smooth- and rough-wall DNS results and the smooth-wall experimental results from Wei & Willmarth (1991). For  $100 < y^+ < 500$ , both results obtained with Mesh A and Mesh B collapse very well with the reference data in the spanwise and vertical directions, while for the streamwise direction the LES results is slightly lower than the DNS and experimental results.



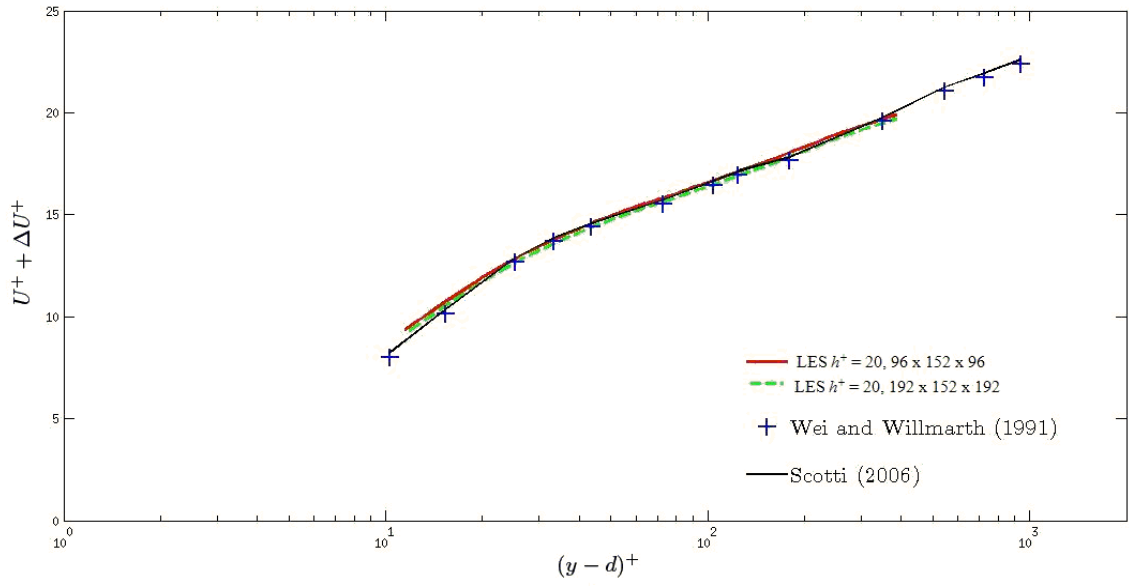


Fig. 5.10 – Mean velocity profiles for  $h^+ = 20$ ; comparison between grids.

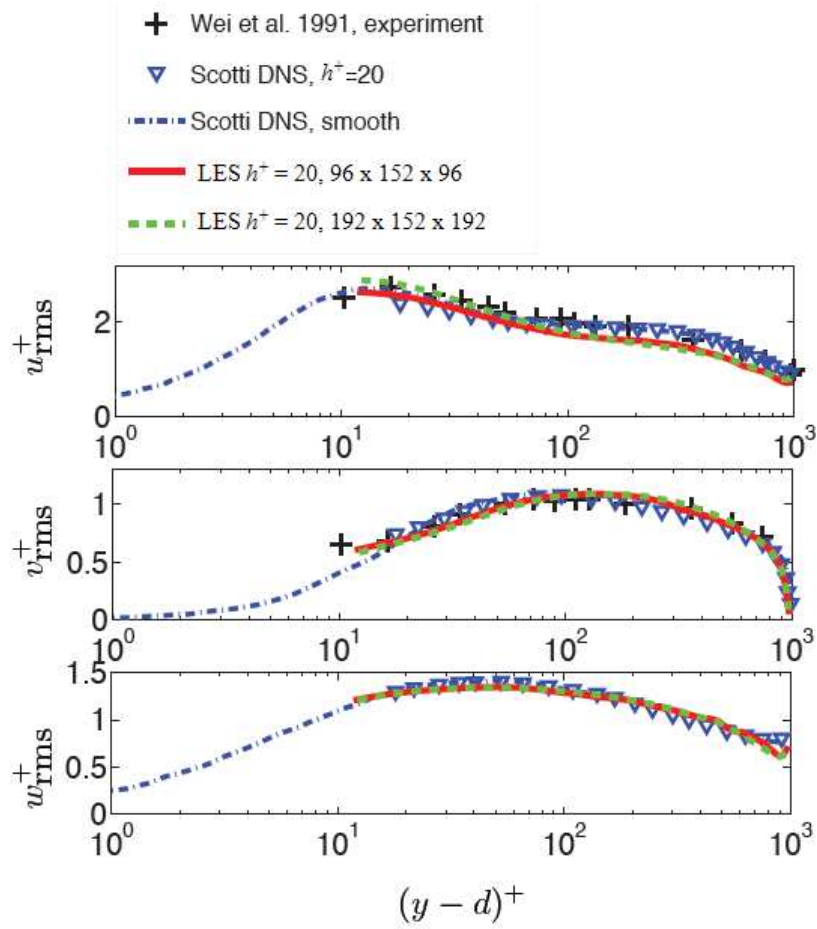


Fig. 5.11 – Influence of grid resolution on the velocity fluctuations for LES of open channel flow over a rough wall.

Overall, the results satisfy the wall similarity hypothesis proposed by Raupach et al. (1991). The results also show that Mesh A resolves the flow statistics well for the rough-wall open-channel flow even with a lower resolution than Mesh B. Thus, one concludes that for this given roughness model and conditions, at least one and two grid points per roughness element in the streamwise and spanwise directions, respectively, are required to resolve the roughness effect on the first- and second-order statistics.

As the grid resolution increase, the change in resolved roughness effects on the mean flow and turbulent fluctuations is not apparent, probably due to the nature of randomness for this roughness model: a range of element shapes would produce the same effect outside of the roughness sublayer. An accurate description of element shape is not necessary to resolve the time- and space-averaged roughness effects on low-order flow statistics for this roughness model.

## 6. Results

In this chapter we present the results of the study of open channel flows over smooth and rough walls, where the dimension and geometry of the patches, together with the roughness height, are the parameters we vary. First, a summary of all the cases is presented, with an introduction of the problem setup and explanations regarding the choices made; then, we describe and show the geometry of the smooth-rough patches; after that, the calculations of the zero-plane displacement for developing flows and the wall shear stress are described.

Finally, plots and figures of mean velocity, Reynolds stresses and turbulent structure are shown and described, in order to understand completely the behavior of the flow.

### 6.1 Case setup

Here we present a summary of all the cases generated. They are summarized in Table 6.1, together with some important parameters.

Our goal was to maintain for all the cases  $Re_\tau$  around the value 800, with an error less than 5%, over the rough patches, in order to be able to do a reasonable comparison. So, where the Reynolds number is lower, for instance in the 2P4 case, the value indicated is the global  $Re_\tau$ , evaluated through all the domain; we verified that only in the rough region  $Re_\tau$  satisfies our requirement. Moreover, the  $Re_b$  is constant for every case with the same  $h^+$ , which implies that the conditions over the rough patches should not be very different from the completely rough case, where  $Re_\tau$  is actually very close to 800.

From Table 6.1 one can see that the domain size along the spanwise direction isn't constant for every case. In fact we used a bigger domain for the  $h^+ = 40$  cases, in order to obtain a better sampling of the roughness: in fact, when we obtain the 2d statistics, which means that all the quantities are averaged in time and in the spanwise direction, we have a worse sampling of the roughness for the cases in which  $h$  is higher, and that leads to higher fluctuations of our variables, in particular the wall shear stress. To avoid this problem, and to have the same number of roughness elements in the  $z$  direction, we used a double wide domain when  $h^+ = 40$  (double than  $h^+ = 20$ , so the number of roughness elements is constant).

Cases R2B, R4B and R4S were used to analyze the effect of the spanwise domain on the results: case R2B was run with the same conditions of case R2, but with double wide domain, and double number of point in  $z$  direction, in order to maintain the same resolution. The same for cases R4S, R4 and R4B, in which the  $z$  domain and  $n_k$  are increased by a factor of 2 every time.

For all the cases we respected the conclusion of the grid size presented in section 5.3, in order to resolve the roughness effect on the first- and second-order statistics.

All the cases were run for more than 400 time units, defined as  $l/U_b$ , to achieve steady state and to accumulate statistics. We started from the smooth case, then the final field was used as an initial condition for  $h^+ = 20$ , and so on for the  $h^+ = 40$  cases. Statistical convergence is gauged by measuring the deviation of the total stress (turbulent and viscous) from a linear profile; convergence is deemed satisfactory when the discrepancy is less than 0.5%. The output sampling frequency was taken equal to 10 time units.

| <i>Case</i> | <i>number of patches</i> | $h^+$   | $Re_b$ | $Re_\tau$ | <i>domain</i>            | $n_i \times n_j \times n_k$ |
|-------------|--------------------------|---------|--------|-----------|--------------------------|-----------------------------|
| S           | 0                        | 0       | 16000  | 839       | $6l \times l \times 3l$  | $96 \times 152 \times 192$  |
| R2          | 1                        | 19 – 21 | 12400  | 792       | $6l \times l \times 3l$  | $96 \times 152 \times 192$  |
| R2B         | 1                        | 19 – 21 | 12400  | 801       | $6l \times l \times 6l$  | $96 \times 152 \times 384$  |
| R4          | 1                        | 38 – 42 | 10100  | 789       | $6l \times l \times 6l$  | $96 \times 152 \times 192$  |
| R4B         | 1                        | 38 – 42 | 10100  | 772       | $6l \times l \times 12l$ | $96 \times 152 \times 384$  |
| R4S         | 1                        | 38 – 42 | 10100  | 792       | $6l \times l \times 3l$  | $96 \times 152 \times 96$   |
| 2P2         | 2                        | 19 – 21 | 12400  | 754       | $6l \times l \times 3l$  | $96 \times 152 \times 192$  |
| 2P4         | 2                        | 38 – 42 | 10100  | 744       | $6l \times l \times 6l$  | $96 \times 152 \times 192$  |
| 4P2         | 4                        | 19 – 21 | 12400  | 776       | $6l \times l \times 3l$  | $96 \times 152 \times 192$  |
| 4P4         | 4                        | 38 – 42 | 10100  | 765       | $6l \times l \times 6l$  | $96 \times 152 \times 192$  |
| 8P2         | 8                        | 19 – 21 | 12400  | 798       | $6l \times l \times 3l$  | $96 \times 152 \times 192$  |
| 8P4         | 8                        | 38 – 42 | 10100  | 825       | $6l \times l \times 6l$  | $96 \times 152 \times 192$  |

Table 6.1 - Case summary with parameters.

## 6.2 Patches generation

In this section we described the geometry and the proceeding we used to obtain the rough patches, which were used in the 2P2, 2P4, 4P2, 4P4, 8P2 and 8P4 cases.

At first we generated the roughness with Scotti's method, as explained in section 5.3: the said grains are represented by uniformly distributed but randomly oriented ellipsoids of the same size and shape. In this way we obtained the completely rough cases (R2, R2B, R4, R4B and R4S). In this section, for simplicity, we will focus on the  $h^+ = 20$  cases, since the method used for the  $h^+ = 40$  cases is exactly the same. Figure 6.1 shows the iso-surface of  $\Phi$  ( $\Phi = 0.9$ ) for the R2 case; we can see that all the channel is completely rough.

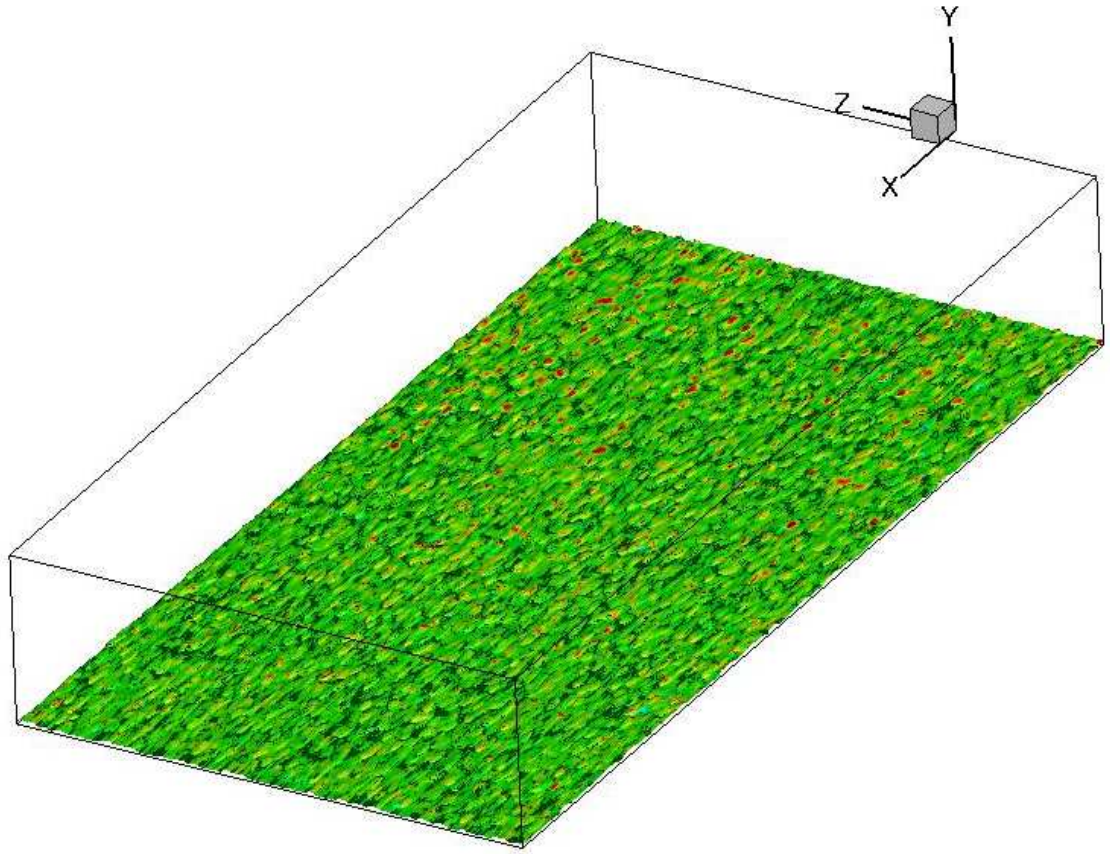


Fig. 6.1 - Iso-surface of  $\Phi$  ( $\Phi = 0.9$ ) coloured by  $u/U_\infty$  for case R2.

After that, without generating new randomly oriented ellipsoids but keeping the same, we multiply the volume of fluid  $\Phi$  obtained for the completely rough case by a function  $f(x)$ , plotted in Figs. 6.2, 6.4 and 6.6 for, respectively, cases 2P2, 4P2 and 8P2. Figs 6.3, 6.5 and 6.7 show the iso-surface of  $\Phi$  ( $\Phi = 0.9$ ) for the same cases.

Where  $f = 1$   $\Phi$  is not modified in any way and the surface is the same as the completely rough case. Where  $f = 0$ , instead, the roughness is removed and we have a smooth wall. The transition between patches is realized with a hyperbolic tangent behavior, and the slope is maintained the same for every case. Since we are using periodic boundary condition in the streamwise direction, the position of the rough and smooth patches is not important; thus the rough patches are placed in the middle of the domain.

For every patch-case, the section of the channel which is rough is exactly the same as the smooth section; that implies that half the domain is smooth and half is rough.

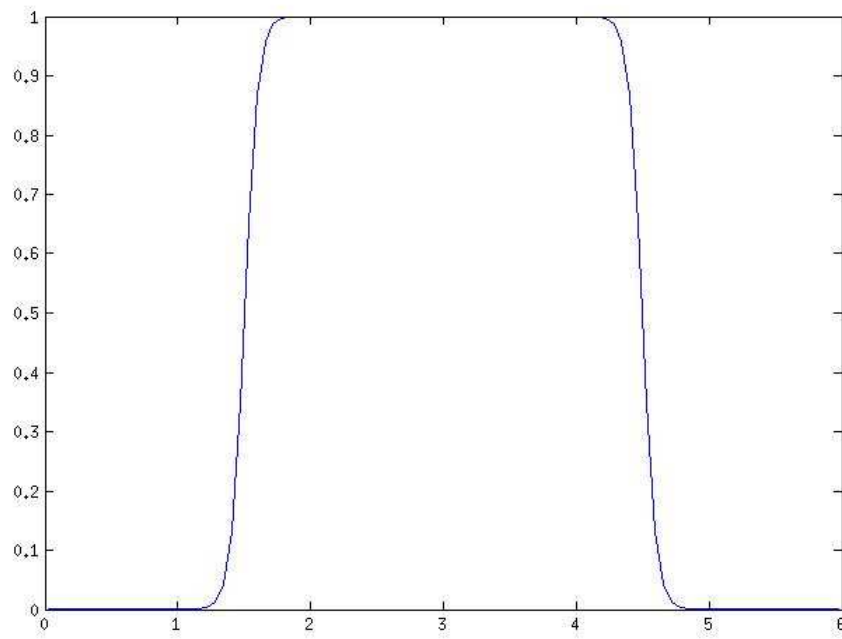


Fig 6.2 - Function  $f$  as a function of  $x$  for the case 2P2.

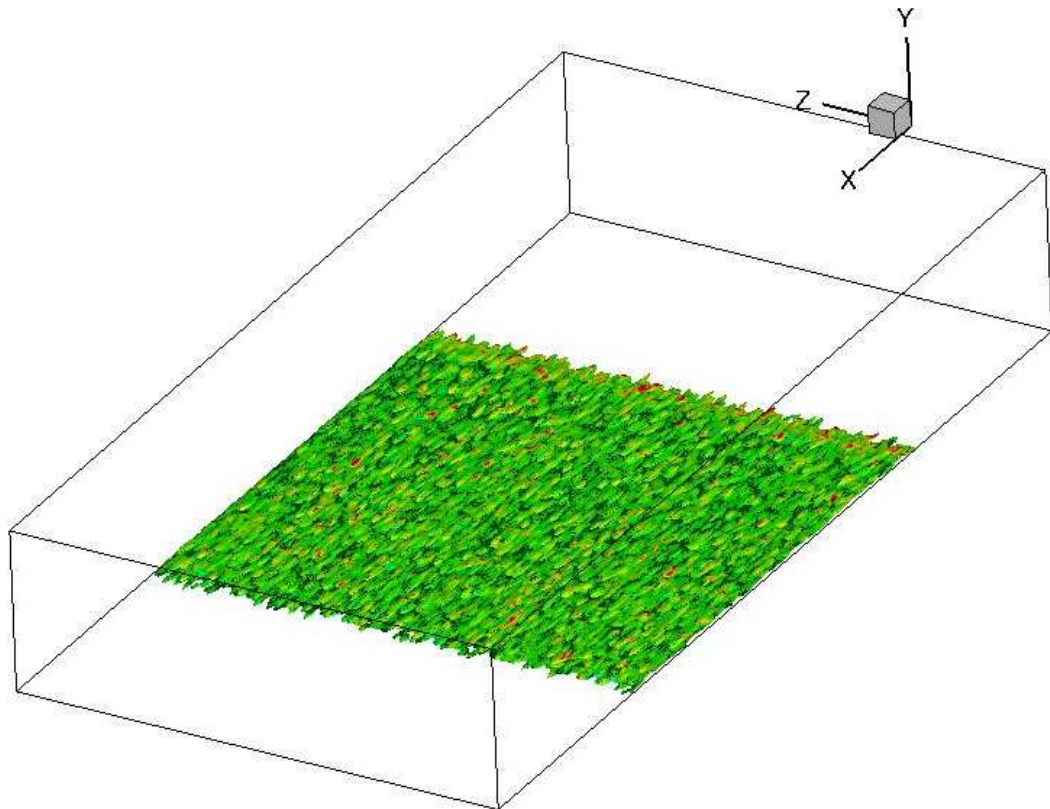


Fig. 6.3 - Iso-surface of  $\Phi$  ( $\Phi = 0.9$ ) coloured by  $u/U_\infty$  for case 2P2.

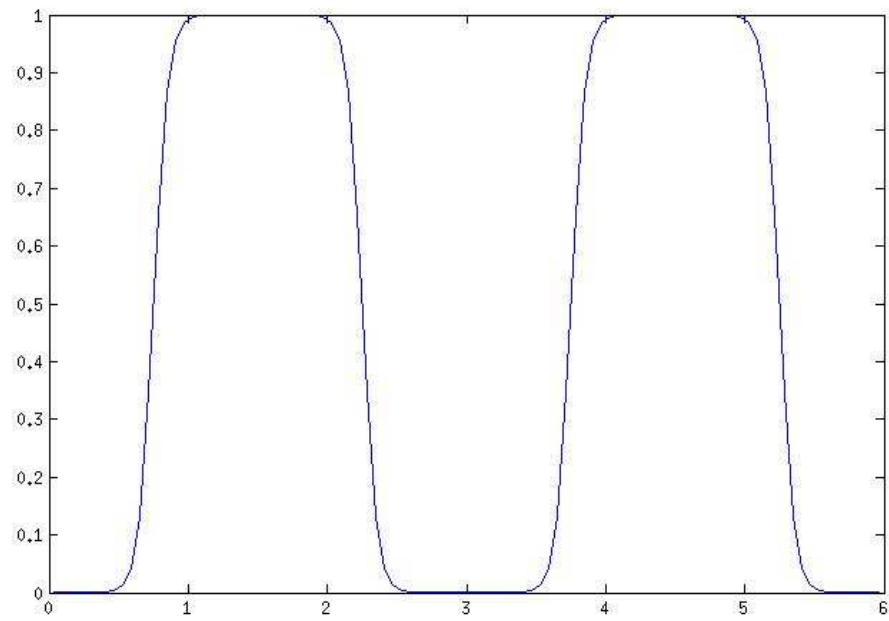


Fig. 6.4 - Function  $f$  as a function of  $x$  for the case 4P2.

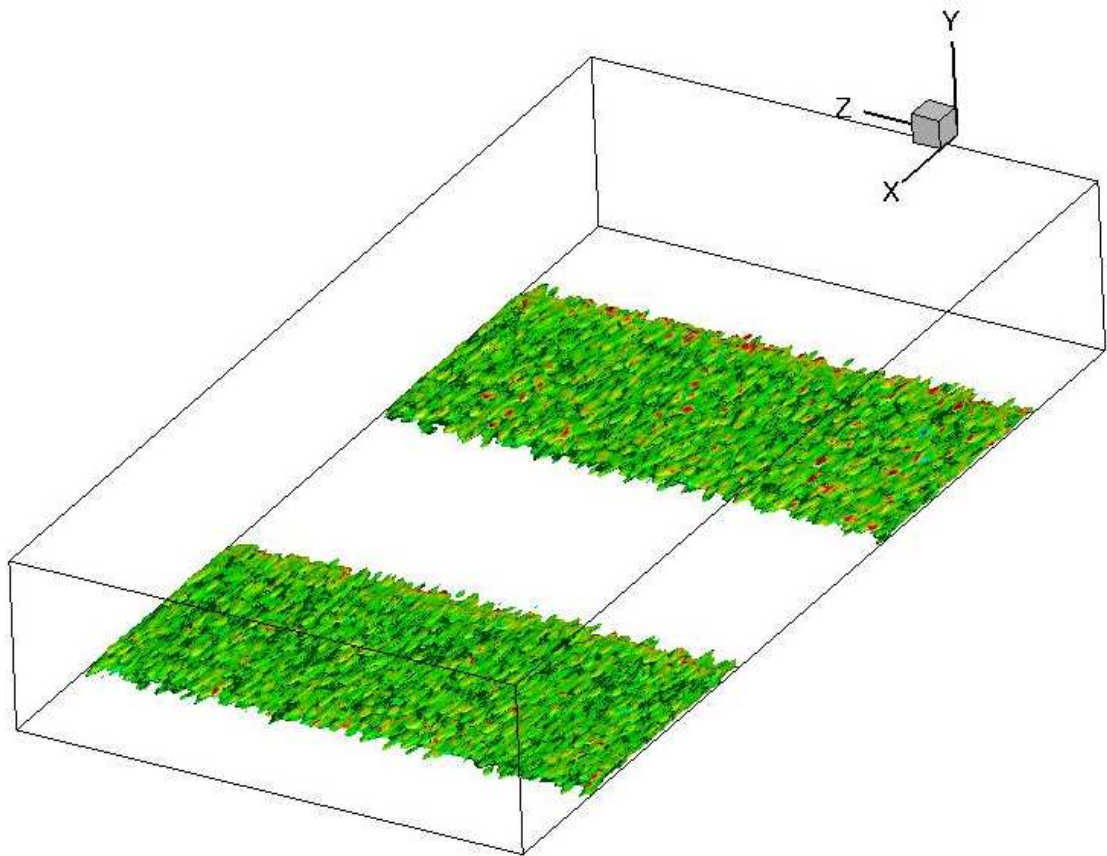


Fig. 6.5 - Iso-surface of  $\Phi$  ( $\Phi = 0.9$ ) coloured by  $u/U_\infty$  for case 4P2.



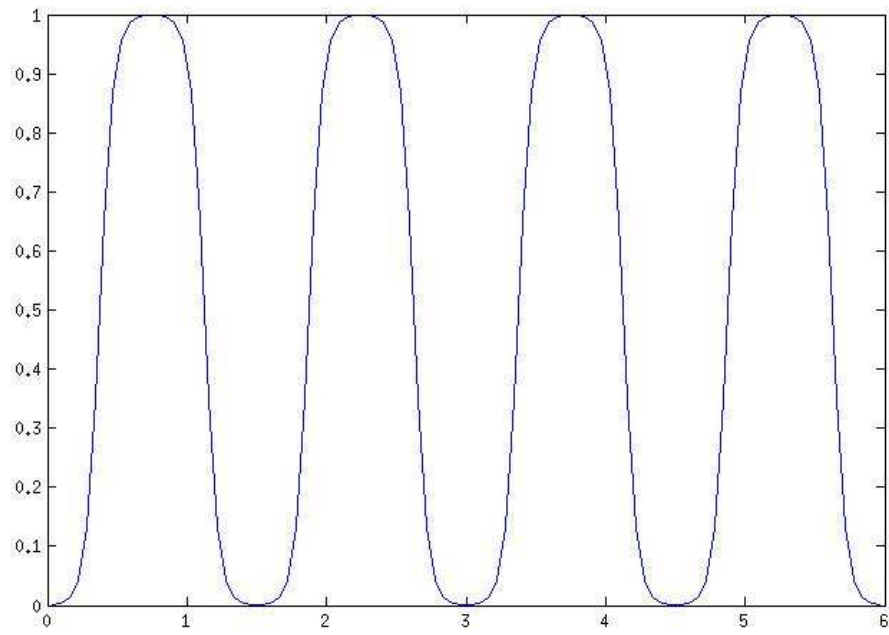


Fig. 6.6 - Function  $f$  as a function of  $x$  for the case 8P2.

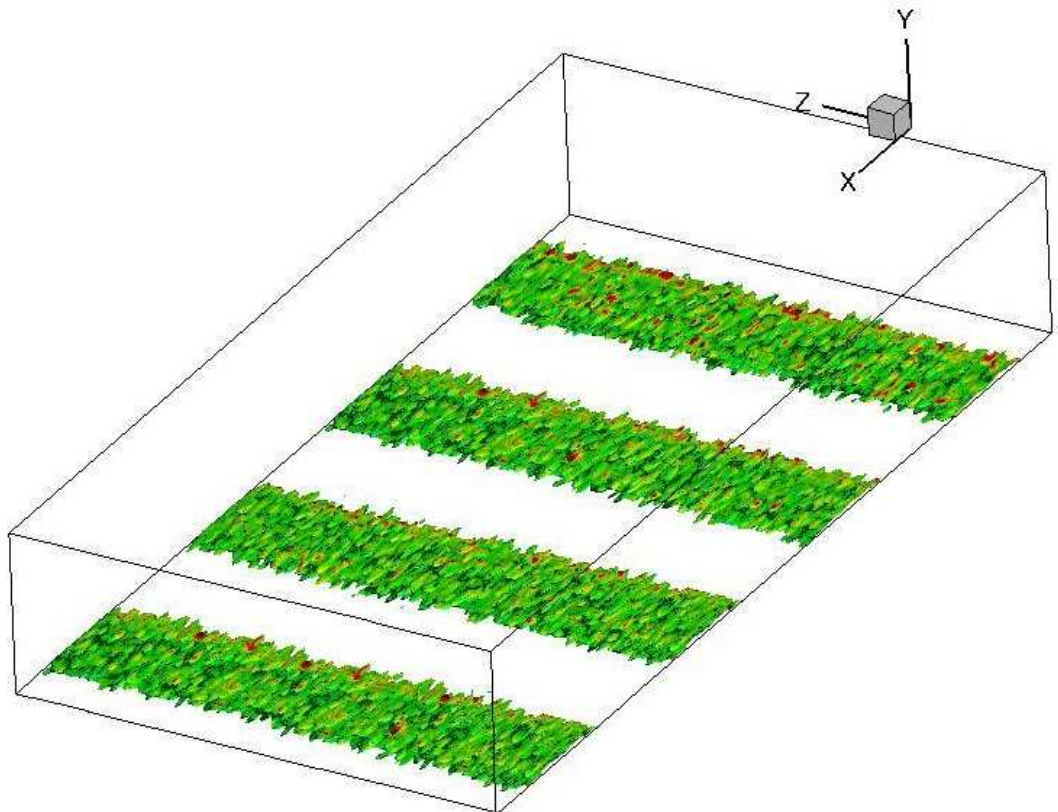


Fig. 6.7 - Iso-surface of  $\Phi$  ( $\Phi = 0.9$ ) coloured by  $u/U_\infty$  for case 8P2.



## 6.3 Preliminary calculation

### 6.3.1 Calculation of zero-plane displacement $d$

The approach described in Scotti (2006) is used to calculate  $d$ , except that the streamwise flow development is also considered. First the instantaneous local drag  $f_i$  is calculated from the governing equation:

$$f_i = \frac{\partial \bar{u}_i}{\partial t} + \frac{\partial (\bar{u}_i \bar{u}_j)}{\partial x_j} + \frac{\partial \bar{p}}{\partial x_i} - \frac{\partial}{\partial x_j} \left[ (\nu + \nu_T) \frac{\partial \bar{u}_i}{\partial x_j} \right] - \frac{\partial}{\partial x_i} \left[ (\nu + \nu_T) \frac{\partial \bar{u}_j}{\partial x_i} \right] \quad (6.1)$$

Then, its streamwise component  $f_x$  is averaged in both time and the spanwise direction, and is used to calculate  $d$  from

$$d(x) = \frac{\int_0^y \langle f_x(x, y) \rangle dy}{\int_0^y \langle f_x(x, y) \rangle dy} \quad (6.2)$$

The result for case R2B is plotted in figure 6.8, which shows that  $d/l$  remains around 0.8, which is the same result obtained by Scotti (2006). Again, this result validates our model and our results.

However  $d/l$  is found to be very sensitive to insufficient statistical sampling, as shown by the scatter of the data. From here on we will set  $d/l = 0.8$  through out the domain for simplicity.

Note that, if we take for instance case R2B, the one plotted in Fig. 6.8, and we average  $d/l$  also in streamwise direction (which is exactly Scotti's method to obtain  $d/l$ ), we obtain as a result  $d/l = 0.8168$ , very close to his value.

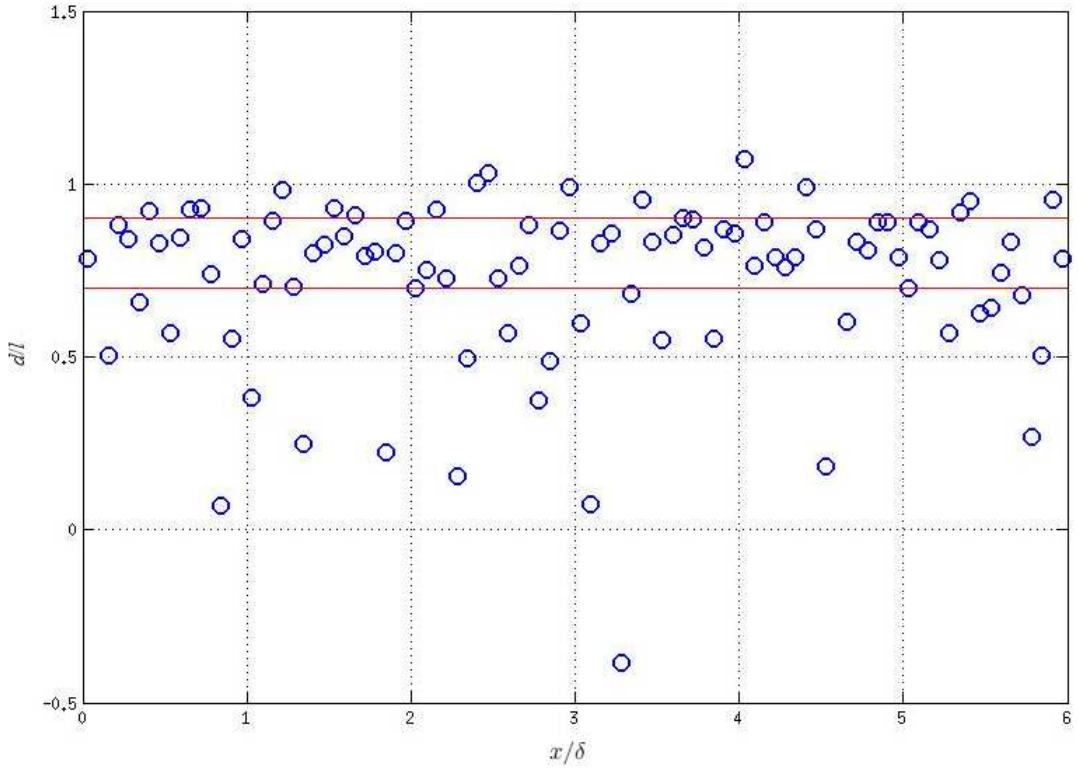


Fig. 6.8 – Streamwise distribution of  $d/l$  in case R2B. The two red lines show  $d/l = 0.7$  and  $0.9$ .

### 6.3.2 Calculation of $\tau_w$

In the present simulation, the drag force exerted on the rough wall is due to the sum of viscous and form drags. Integrating the streamwise momentum equation from  $y = 0$  to the top of the domain,  $y = l$ , gives

$$\begin{aligned}
 & -\int_0^l \frac{\partial}{\partial y} \left[ (\nu + \nu_T) \frac{\partial \bar{u}}{\partial y} \right] dy - \int_0^l f_x dy = \\
 & -\int_0^l \frac{\partial \bar{u}}{\partial t} dy - \int_0^l \left( \frac{\partial \bar{u}\bar{u}}{\partial x} + \frac{\partial \bar{u}\bar{v}}{\partial y} + \frac{\partial \bar{u}\bar{w}}{\partial z} \right) dy - \frac{1}{\rho} \int_0^l \frac{\partial \bar{P}}{\partial x} dy + \nu \int_0^l \left( \frac{\partial^2 \bar{u}}{\partial x^2} + \frac{\partial^2 \bar{u}}{\partial z^2} \right) dy + \\
 & \int_0^l \left[ 2 \frac{\partial}{\partial x} \left( \nu_T \frac{\partial \bar{u}}{\partial x} \right) + \frac{\partial}{\partial y} \left( \nu_T \frac{\partial \bar{v}}{\partial x} \right) + \frac{\partial}{\partial z} \left( \nu_T \frac{\partial \bar{u}}{\partial z} \right) + \frac{\partial}{\partial z} \left( \nu_T \frac{\partial \bar{w}}{\partial x} \right) \right] dy
 \end{aligned} \tag{6.3}$$

where  $f_x$  represents the drag force in the streamwise direction due to roughness. Note that this integration includes the solid part of the domain (beneath the top of the roughness elements), where the right-hand side is zero trivially. The left-hand side of (6.3) represents the (local and instantaneous) stress on the rough wall,  $\tau_w(x, z, t)$ . Note that, the second term on the left-hand side of (6.3) contains most of the form drag and the viscous drag; the first term is nearly zero, since, under such roughness model, the argument of the integral at the

bottom boundary is nearly zero due to the roughness blockage. The instantaneous  $\tau_w$  can then be averaged in both the spanwise direction and time to get  $\langle \tau_w \rangle$ . The friction coefficient  $C_f$  can then be obtained from

$$C_f = \frac{\langle \tau_w \rangle}{\rho \cdot U_\infty^2 / 2} \quad (6.4)$$

as profusely described in chapter 2 (equation 2.14).

## 6.4 Description of the flow

In this section, we give a description of the flow and show the boundary layer quantities. The goal is to describe, at first, the flow behaviour for a turbulent boundary layer over a smooth wall and a rough wall. Then, the patch cases are introduced and compared with the previous cases, to show the influence of the geometry. The roughness height  $h^+$  is the other parameter which has been varied and its effects on the flow are shown. To help us in the explanation of the flow behaviour we show local streamwise velocity  $u$  and contour of the different terms that come out the momentum equation.

### 6.4.1 Streamwise development of $\tau_w$ and $C_f$ - smooth and rough cases

The streamwise development of  $C_f$ , obtained as defined in (6.4), is plotted in figure 6.9 for cases S and R2. The smooth case was obtained using the vof method, as for the rough cases, but setting  $\Phi = 0$  everywhere in the domain, in order not to have roughness. The result obtained is in accord with the classic smooth turbulent open channel flow, at the same Reynolds number, obtained without using the immerse boundary method; thus our technique to obtain the wall shear stress from momentum equation (section 6.3.2) is validated.

When roughness is introduced, the fluctuations of  $C_f$  (which are due to fluctuations of  $\tau_w$ ) are quite large in magnitude and high in frequency (red line). We investigated the nature of those fluctuations, and we saw that they are due to a problem of sampling the roughness: even if the ellipsoids, generated with Scotti's method, are randomly oriented, there are some favored structures and locations, and the roughness, averaged in  $z$ , is not homogeneous.

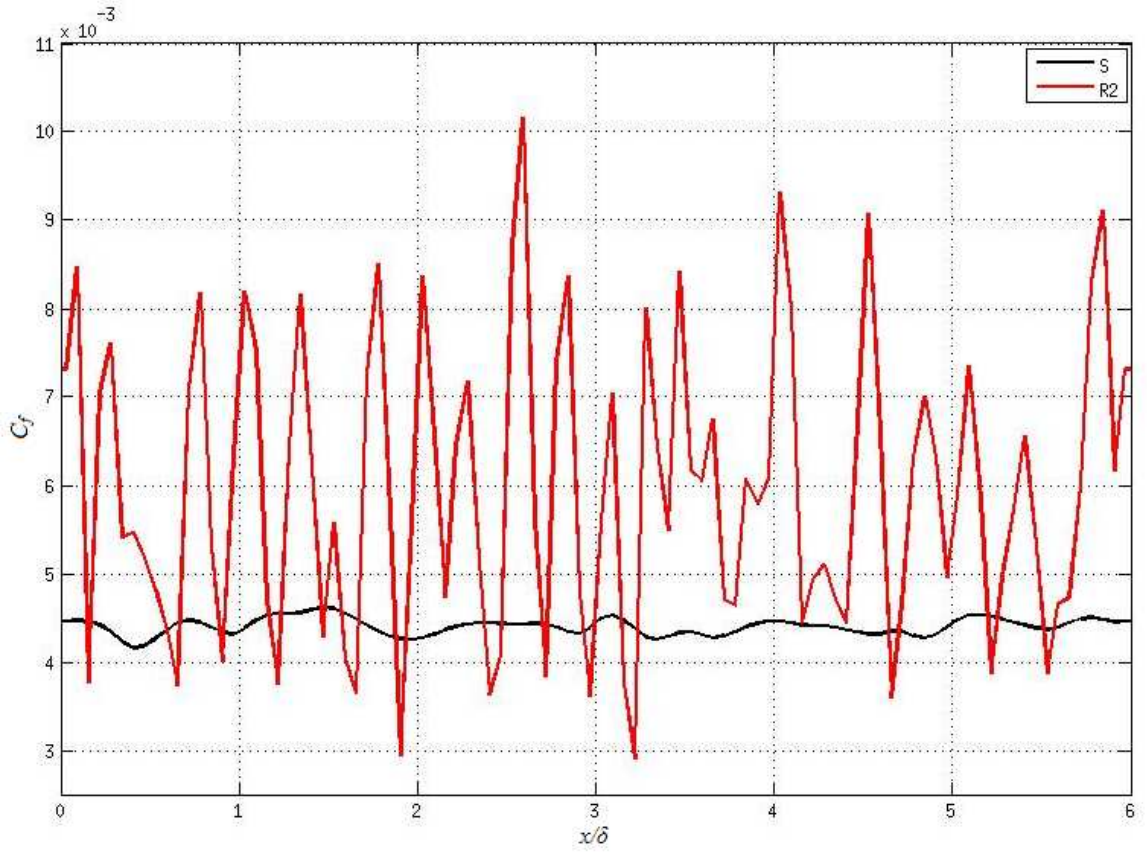


Fig. 6.9 - Streamwise development of  $C_f$  for case S (black line) and for case R2 (red line).

In figure 6.10 the wall shear stress  $\tau_w$  and contour of volume of fluid  $\Phi$  for case R4 are shown. In this figure, and in all the following plots,  $\tau_w$  is nondimensionalized with the density  $\rho$  and the square of the bulk velocity  $U_b$ , as defined in chapter 2.  $\Phi$ , which is a local variable and a function of  $x, y, z$ , has been averaged in the spanwise direction. It is possible to see the strong relation between  $\tau_w$  and  $\Phi$ : since the roughness is not perfectly random and there are peaks and valleys, those same peaks and valleys are found also in the  $\tau_w$  streamwise development.

This phenomenon is more relevant for cases in which  $h^+ = 40$ , because the roughness height is double and so there are also fewer ellipsoids per spanwise unit. That's why, in order to reduce the fluctuations and improve the sampling of the roughness, the main rough cases with  $h^+ = 40$  were computed using a bigger spanwise domain, with  $l_z = 6l$ , as described in table 6.1.

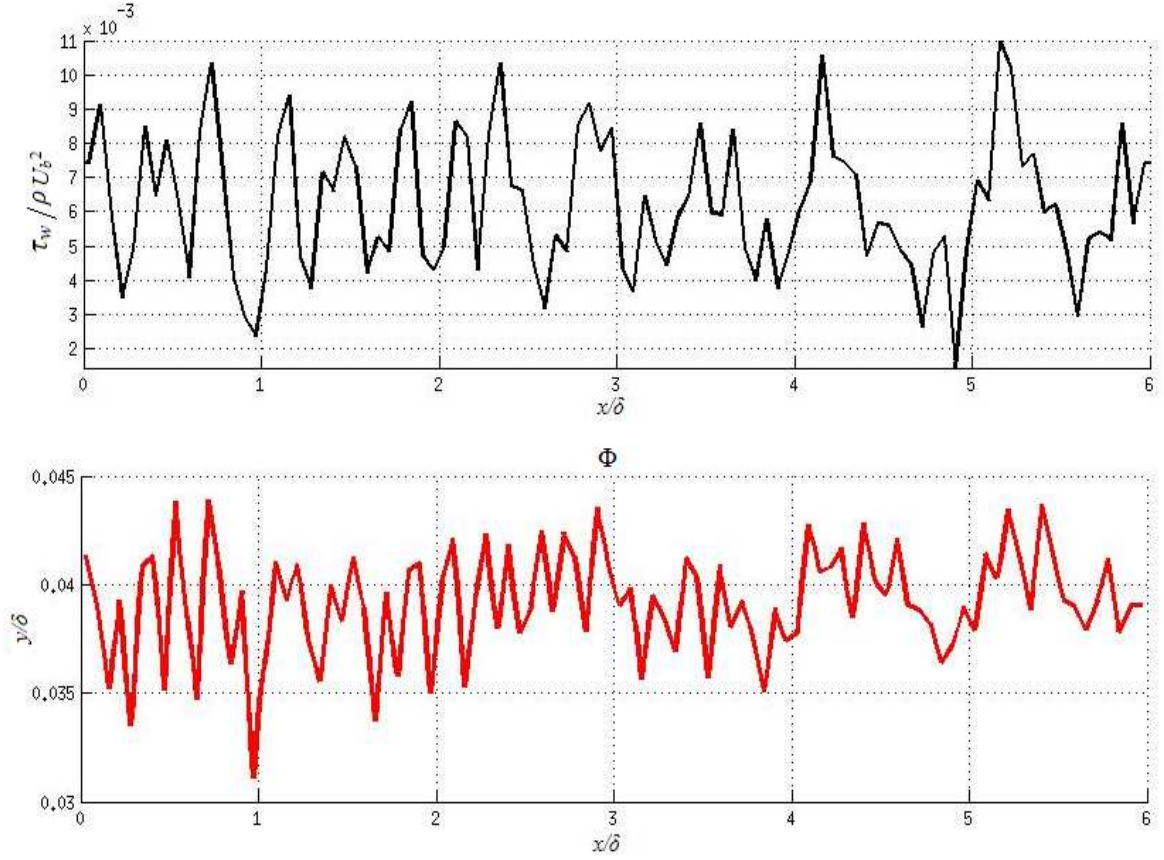


Fig. 6.10 - Streamwise development of  $\tau_w/\rho U_b^2$  and contour of  $\Phi$  ( $\Phi = 0.8$ ) averaged in spanwise direction for case R4.

The effect of the spanwise domain is shown in Tab. 6.2, where domain, mean wall shear stress and its standard deviation are shown for cases R4S, R4 and R4B. We define the standard deviation  $\sigma$  as

$$\sigma = \sqrt{\frac{1}{N} \sum_{i=1}^N (x_i - \mu)^2} \quad (6.5)$$

where the mean value is defined as

$$\mu = \frac{1}{N} \sum_{i=1}^N x_i \quad (6.6)$$

One can see that the standard deviation decreases with the increase of the domain, but the decrease is not linear.

| <i>Case</i> | <i>domain</i>            | $\sigma$ | $\langle \tau_w \rangle$ |
|-------------|--------------------------|----------|--------------------------|
| R4S         | $6l \times l \times 3l$  | 0.03     | 0.0062                   |
| R4          | $6l \times l \times 6l$  | 0.02     | 0.0061                   |
| R4B         | $6l \times l \times 12l$ | 0.015    | 0.0059                   |

Table 6.2 – Effect of the spanwise domain in the roughness sampling.

To better show the global effect of roughness, we filter  $\tau_w$  with wavelet transform. Wavelets are mathematical functions that cut up data into different frequency components, and then study each component with a resolution matched to its scale. They have advantages over traditional Fourier methods in analyzing physical situations where the signal contains discontinuities and sharp spikes. The fundamental idea behind wavelets is to analyze according to scale.

Wavelet, exactly as Fourier transform, are linear operations that generate a data structure that contains  $\log_2 n$  segments of various lengths, usually filling and transforming it into a different data vector of length  $2^n$ .

The mathematical properties of the matrices involved in the transforms are similar as well. The inverse transform matrix for both of them is the transpose of the original. As a result, both transforms can be viewed as a rotation in function space to a different domain. For the Fourier transform, this new domain contains basis functions that are sines and cosines. For the wavelet transform, this new domain contains more complicated basis functions called wavelets, mother wavelets, or analyzing wavelets.

Both transforms have another similarity: the basis functions are localized in frequency, making mathematical tools such as power spectra (how much power is contained in a frequency interval) and scalegrams useful at picking out frequencies and calculating power distributions.

Nevertheless, the most interesting dissimilarity between these two kinds of transforms is that individual wavelet functions are localized in space: Fourier sine and cosine functions are not. This localization feature, along with wavelets localization of frequency, makes many functions and operators using wavelets "sparse" when transformed into the wavelet domain. This sparseness, in turn, results in a number of useful applications such as data compression, detecting features in images, and removing noise from time series.

Figure 6.11 shows the wall shear stress for case R4 before and after the filtering process: the magnitude of the fluctuations has been reduced; to quantify this reduction the standard deviation is indicated in the legend:  $\sigma$  decreases by half after the filtering process; however, the local behavior of  $\tau_w$ , due to roughness, is maintained and only the highest wavenumbers are removed.

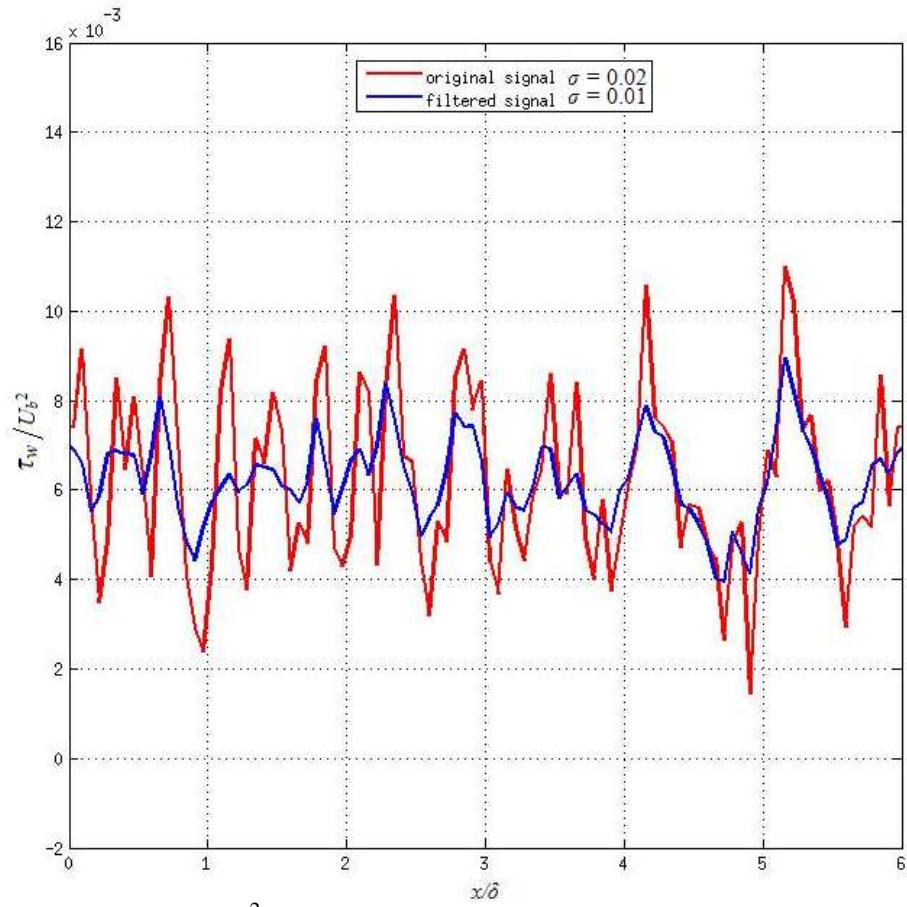


Fig. 6.11 -  $\tau_w/\rho U_b^2$  for case R4 before and after the filtering process.

In figure 6.12 the filtered  $\tau_w$  for cases S, R2 and R4, together with the free-stream velocity  $U_\infty$  and the friction coefficient  $C_f$  are compared.  $\tau_w$  increases passing from the smooth case, to the  $h^+ = 20$  case and again to the  $h^+ = 40$  case, in accord to the fact that the higher is the roughness, the bigger is the effect of viscosity on the computation of the wall shear stress.  $U_\infty$  increases as well with the increase of the roughness height due to an upward shift of the flow: the roughness creates a blockage for the flow, which moves upward in order to preserve the mass flux.



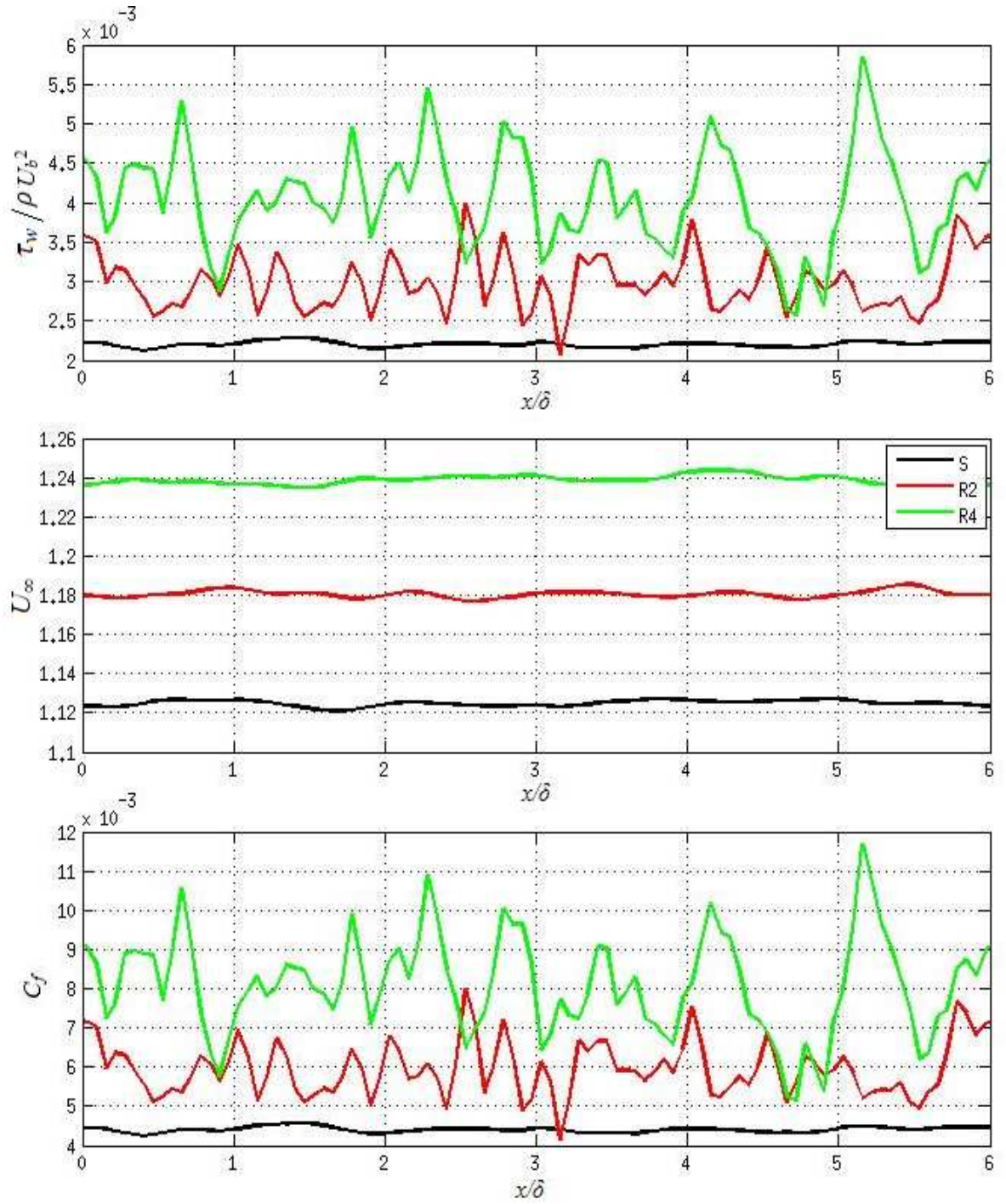


Fig. 6.12 - Streamwise development of the nondimensionalized wall shear stress  $\tau_w/\rho U_b^2$ , free-stream velocity  $U_\infty$  and friction coefficient  $C_f$  for cases S, R2, R4 after filtering.

From now on we will apply always our filtering process and we will use the filtered wall shear stress by default; in fact, the filtering signal is preferable because, as we will see in the next section, it is closer to  $\tau_w$  obtained from the log law assumption, in which the local fluctuations are very small.



#### 6.4.2 $\tau_w$ from the log law assumption

At this point we compare the wall shear stress obtained from momentum equation and filtered with wavelets, the one shown in Fig. 6.12, with  $\tau_w$  obtained from the assumption of the log law: in fact, the standard approach to calculate the wall stress in boundary layers over rough surfaces is to assume that in the overlap region

$$U^+(y^+) = \frac{1}{k} \cdot \ln(y^+ - d) + B - \Delta U^+(h^+) \quad (6.7)$$

where  $k$  is the Von-Karman constant (typically the value 0.41 is used),  $5 < B < 5.5$  a universal constant,  $\Delta U^+$  the roughness-dependent velocity defect (Fig. 6.13), and  $d$  the location of the virtual wall. Usually, experimental data points are fitted to equation 6.7 to determine appropriate values of  $B$ ,  $d$ ,  $\Delta U^+$ , and  $u_\tau$  in an iterative method. And that is the procedure we adopted to obtain a new streamwise development of  $\tau_w$ , fitting the log law in the region  $200 < (y - d)^+ < 230$ . The two different functions are plotted in Figs. 6.14 and 6.15 for two different cases. We can see that  $\tau_w$  obtained from log law is more stable, but it can not capture the large fluctuations due to the roughness. However, the interesting result is that the mean value of  $\tau_w$  within all the domain is the same for the two methods, with an error less than 5%. This result allows us to say that, for the completely rough cases, the log law is valid through all the domain, our model of roughness agrees with existing data, from which the roughness function has been built, and the procedure we used to obtain  $\tau_w$  from momentum gives reasonable result.

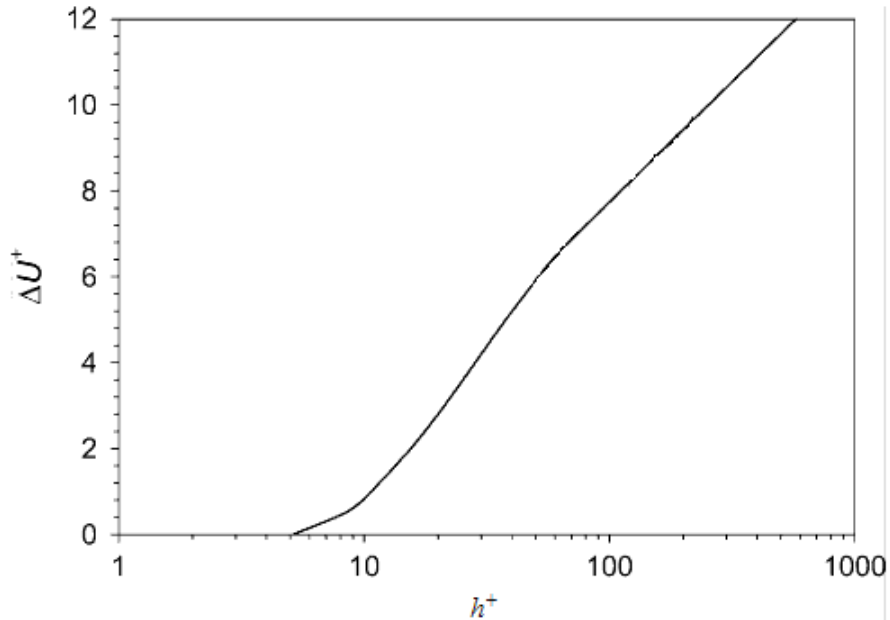


Fig. 6.13 - Roughness functions  $\Delta U^+$  versus  $h^+$ .

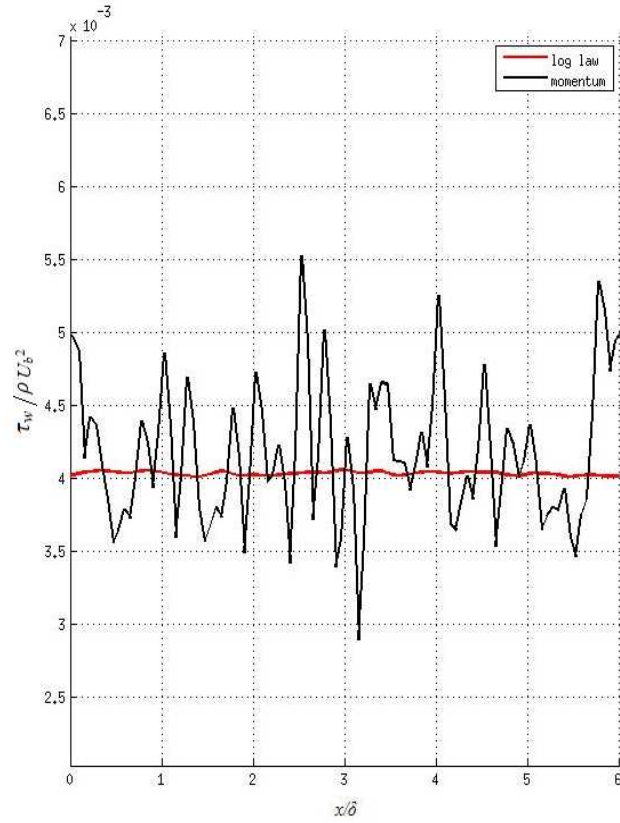


Fig. 6.14 - Streamwise development of  $\tau_w/\rho U_b^2$  obtained by fitting the log law (red line) and by the momentum equation (black line) for case R2.

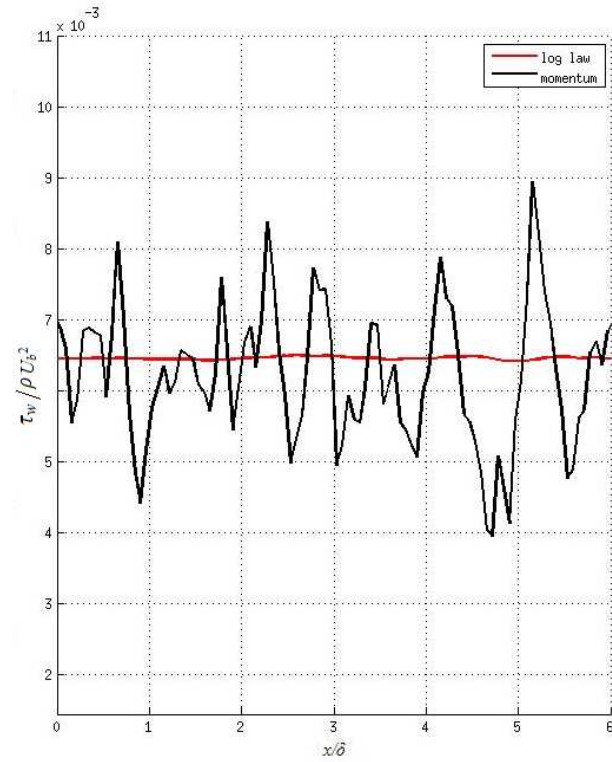


Fig. 6.15 - Streamwise development of  $\tau_w/\rho U_b^2$  obtained by fitting the log law (red line) and by the momentum equation (black line) for case R4.

### 6.4.3 Streamwise development of $\tau_w$ and $C_f$ - patch cases

In this section we analyze the streamwise development of  $\tau_w$  and  $C_f$  for the patches cases, which are the cases where the domain is partly smooth and partly rough; the geometry of these patches varies from one case to another as longly explained in section 6.2.

The wall shear stress  $\tau_w$  for case 2P2 is plotted in figure 6.16, obtained with the two different methods explained. The interesting result is that this time there is a discrepancy between  $\tau_w$  obtained from momentum and from the log law: even if the mean values of the two functions are the same,  $\tau_w$  from log law is built from an *a priori* assumption (the existing of the log law through all the  $x$  domain).  $\tau_w$  from momentum, instead, is obtained from the balance of the momentum equation, thus it is sensitive to the local variation of such quantities as the pressure gradient, the convective term, the viscous term and the reynolds stress term. From this  $\tau_w$  we can see that there is a huge peak just at the beginning of the rough patch, for  $x = 1.5l$ . Note that the transition between patches is not abrupt, but smoothed with an hyperbolic tangent function, as explained in section 6.2. This peak is physical, as we can see from the momentum equation terms plotted in Figs. 6.17 - 6.19.

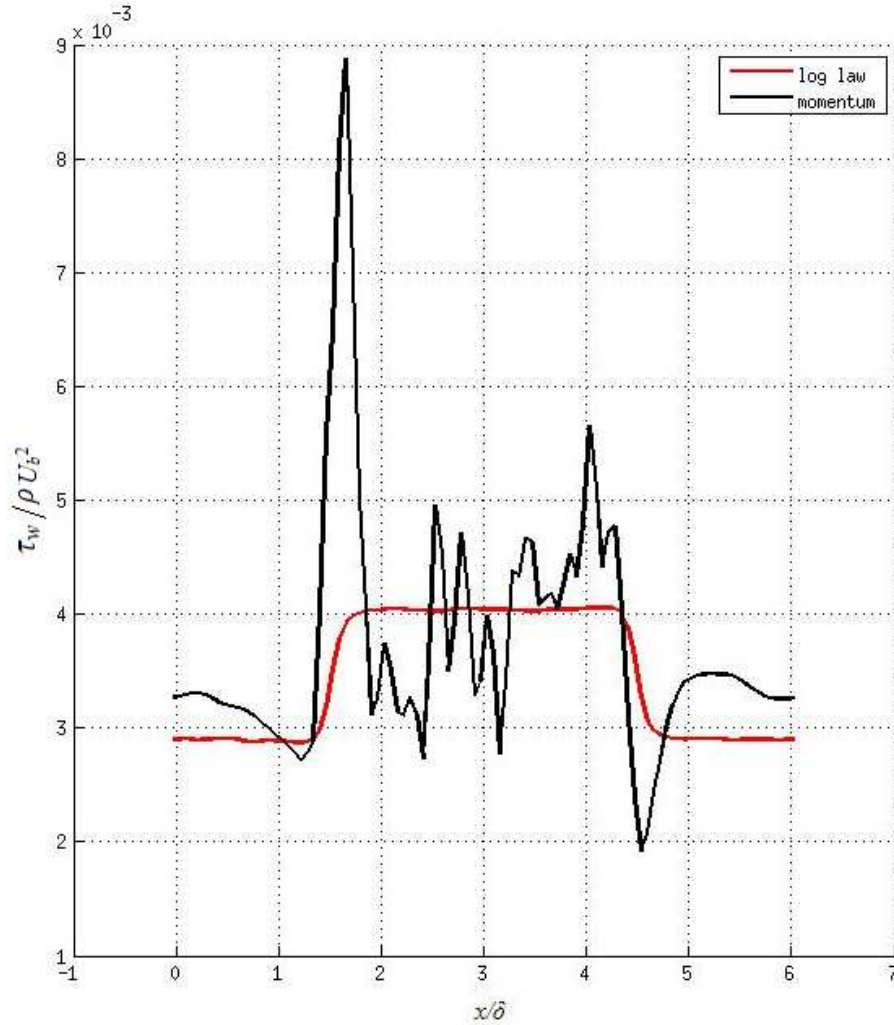


Fig. 6.16 - Streamwise development of the nondimensionalized wall shear stress  $\tau_w / \rho U_b^2$  obtained by fitting the log law (red line) and by the momentum equation (black line) for case 2P2.

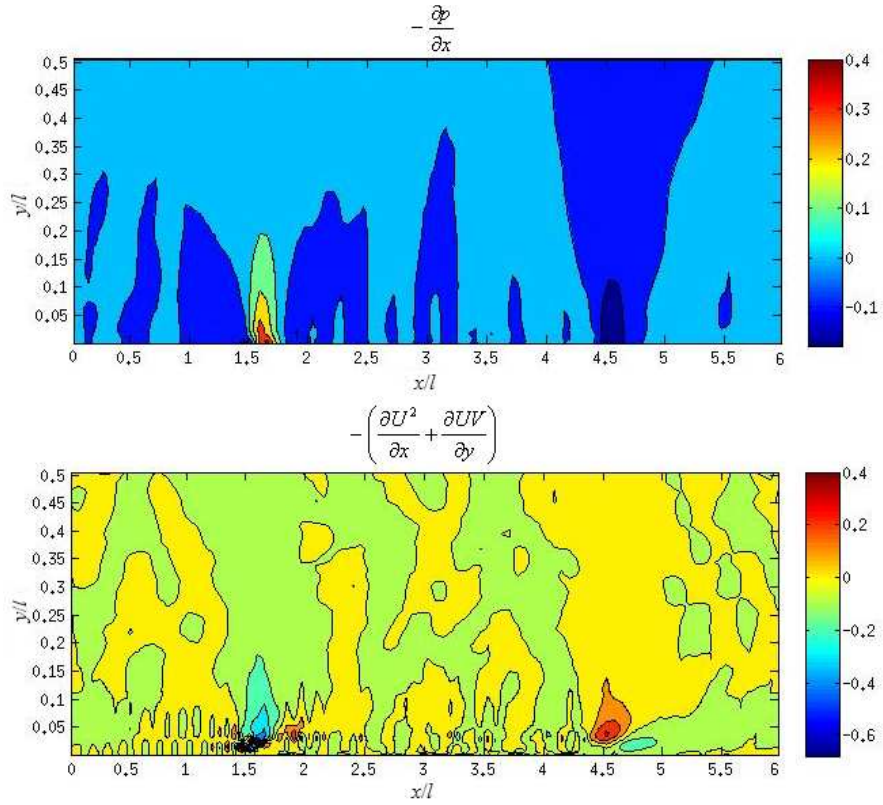


Fig. 6.17 - Pressure term and convective term in the momentum equation for case 2P2.

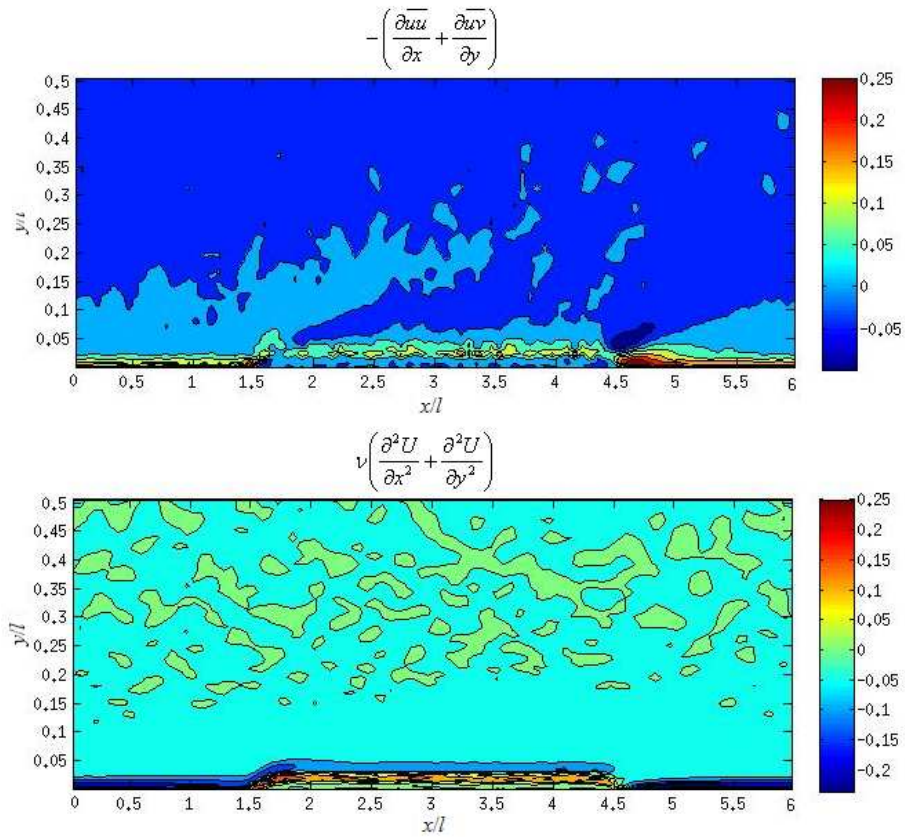


Fig. 6.18 - Reynolds stress term and viscous term in the momentum equation for case 2P2.

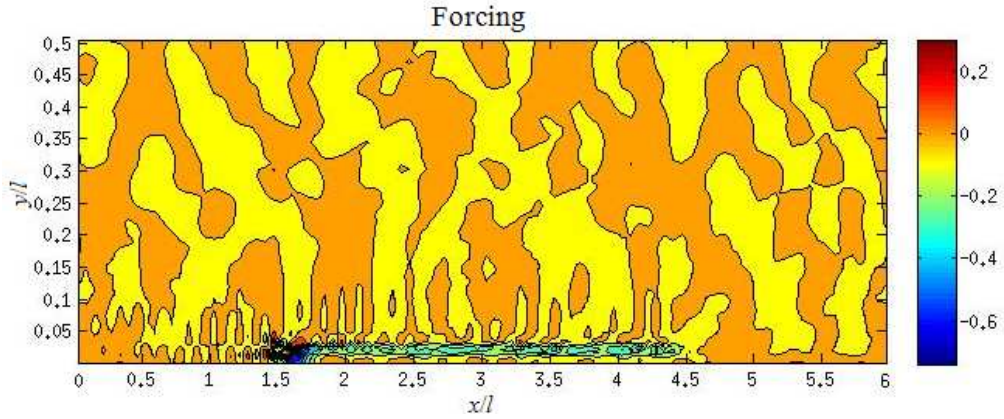


Fig. 6.19 - Forcing term in the momentum equation for case 2P2.

From Figs 6.17 - 6.19 we can see that at  $x = 1.5l$  the momentum equation terms increase suddenly (in absolute value) due to presence of roughness, which introduces a drag force against the flow; thus the wall shear stress increases at the same location, with a local behaviour that can not be seen from the log law assumption.

A similar situation occurs at the end of the rough patch, at  $x = 4.5l$ : here the flow comes across an adverse pressure gradient (APG) and, due to the relatively low Reynolds number and high roughness height, it separates creating a recirculation region, which leads to very low value of  $\tau_w$ . In fact, our  $\tau_w$  is averaged in the spanwise direction, but locally, at some  $z$  locations,  $\tau_w$  assumes negative value just at the the end of the rough patch, as we can see from Fig. 6.20: it shows the streamlines and the contour of the streamline velocity  $U^2$  at  $4 < x/l < 6$  and  $z = l$  for the case 2P2, together with the volume of fluids  $\Phi$  for the same case in the same streamwise location. The recirculation region is clearly visible at the end of the roughness, with negative value of  $U$  which leads to local negative value of  $\tau_w$ .

In figure 6.21 and 6.22 comparisons between the smooth case, the completely rough case and the 2 patch case are shown. In Fig. 6.21  $h^+ = 20$ , while in Fig. 6.22  $h^+ = 40$  for the rough cases. We can notice that the 2 patch case behaves close to the smooth case in the smooth region and close to the rough case in the rough region. The only two irregularities are in the transition regions smooth-rough patch and rough-smooth patch, as observed before.

In Fig. 6.23 - 6.25 friction coefficient  $C_f$  and the free-stream velocity  $U_\infty$  are plotted, respectively for the 2 patch cases, 4 patch cases and 8 patch cases; cases with different roughness height are plotted together, to show the effect of this parameter. When the roughness height is higher,  $\tau_w$  and  $U_\infty$  increase, as we've already noticed in the completely rough cases.

From these plots we notice that the patch cases behave in a pretty similar way: the peak exists always at the beginning of a rough patch and its magnitude remains almost constant in the differen patch cases; the same for the valleys at the end of rough patches. Hence the influence of the geometry is little.



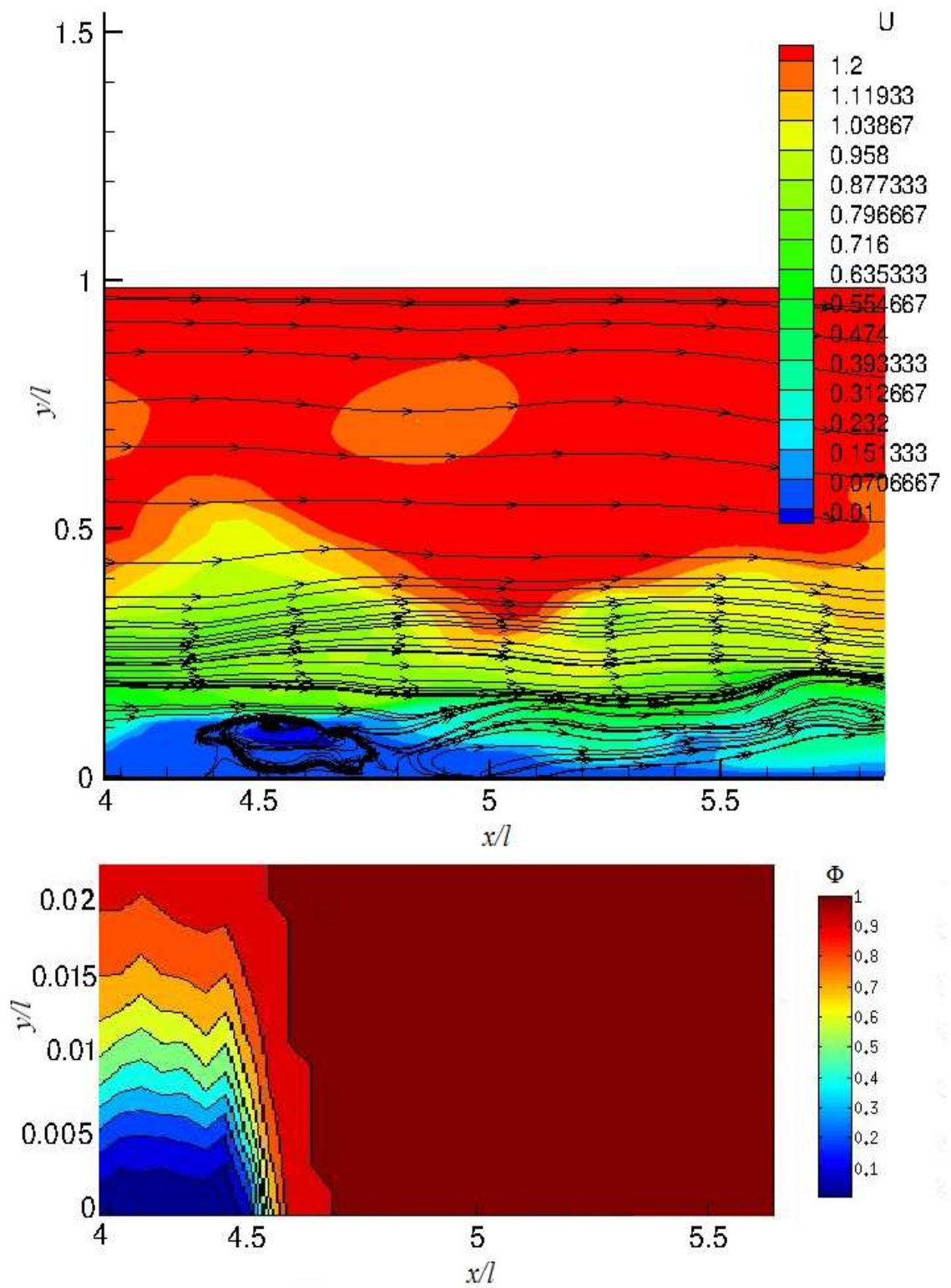


Fig. 6.20 - Streamlines and the contour of the streamline velocity  $U^2$  at  $4 < x/l < 6$  and  $z = l$  for case 2P2, together with the volume of fluids  $\Phi$  for the same case and at the same streamwise location.

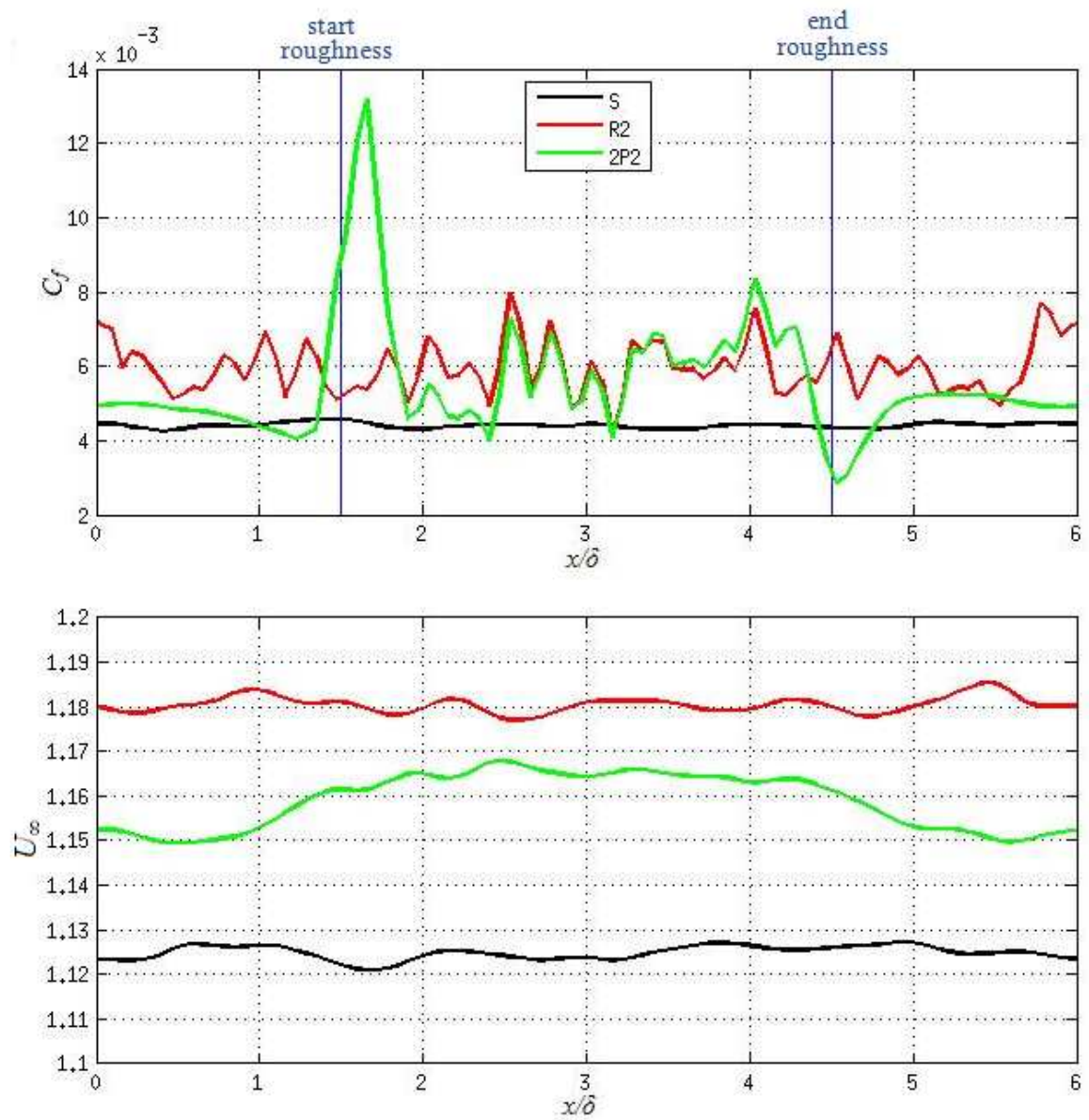


Fig. 6.21 - Streamwise development of the friction coefficient  $C_f$  and the free-stream velocity  $U_\infty$  for cases S, R2, 2P2. Blue lines show locations of roughness for 2P2 case.

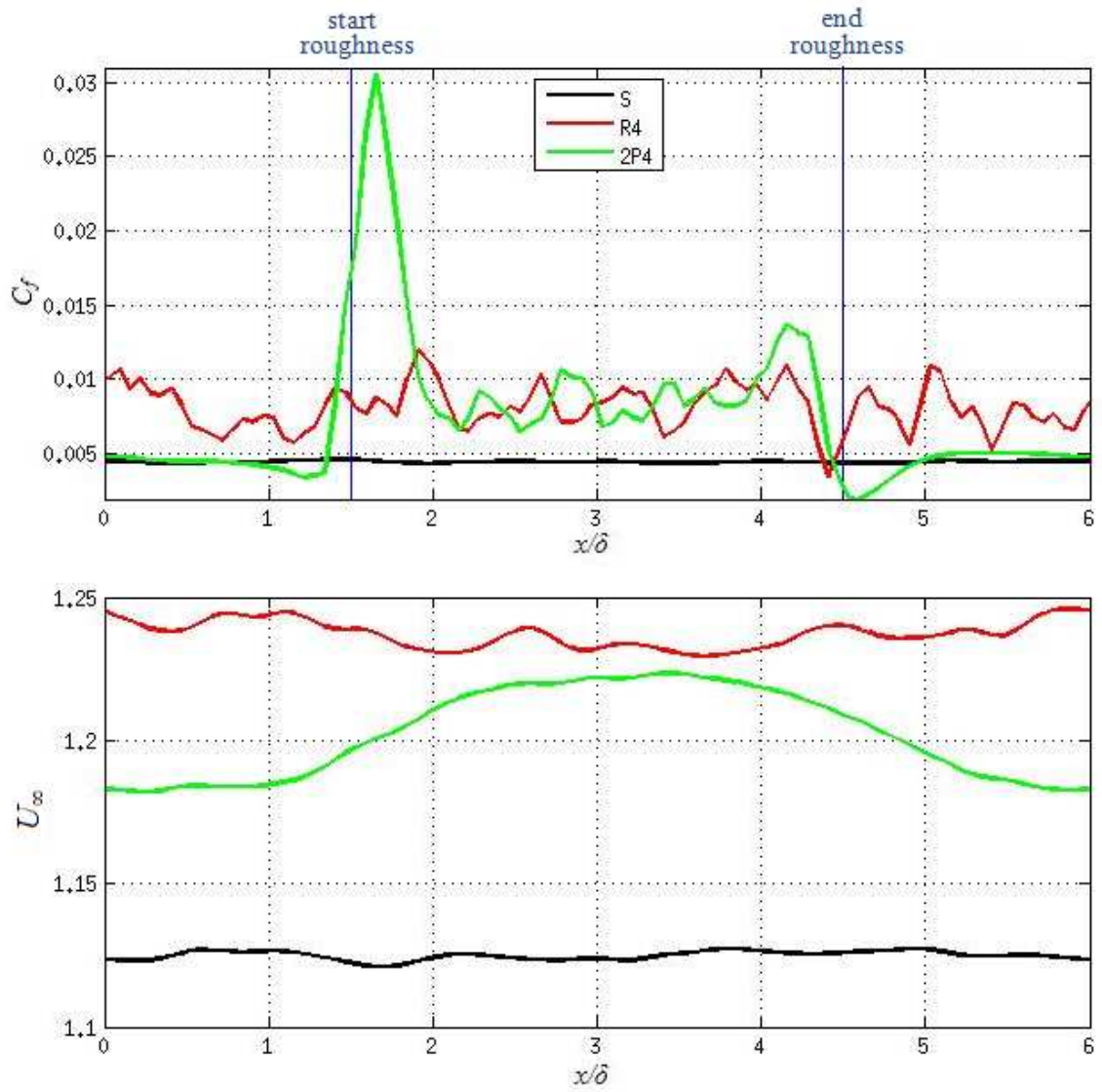


Fig. 6.22 - Streamwise development of the friction coefficient  $C_f$  and the free-stream velocity  $U_\infty$  for cases S, R4, 2P4. Blue lines show locations of roughness for 2P4 case.

Note that for the 4 patch cases and 8 patch cases we avoid the problem of sampling the roughness using a phase space average along the streamwise direction: all the quantities, which are already averaged in time and spanwise direction, are also averaged along the  $x$  domain, with a space shift depending on the number of rough patches. For instance, the streamwise velocity  $u$  for the 4 patches cases becomes:



$$\begin{aligned}
u\left(0 < x < \frac{n_i}{2}, y\right) &= \frac{1}{2} \left[ u\left(0 < x < \frac{n_i}{2}, y\right) + u\left(\frac{n_i}{2} + 1 < x < n_i, y\right) \right] \\
u\left(\frac{n_i}{2} + 1 < x < n_i, y\right) &= u\left(0 < x < \frac{n_i}{2}, y\right)
\end{aligned} \tag{6.8}$$

where  $n_i$  is the number of point in the  $x$  direction, indicated in Table 6.1 for every case. The 8 patches cases allow us to average even more, since there are more patches:

$$\begin{aligned}
u\left(0 < x < \frac{n_i}{4}, y\right) &= \frac{1}{4} \left[ u\left(0 < x < \frac{n_i}{4}, y\right) + u\left(\frac{n_i}{4} + 1 < x < \frac{n_i}{2}, y\right) + \right. \\
&\quad \left. u\left(\frac{n_i}{2} + 1 < x < \frac{3 \cdot n_i}{4}, y\right) + u\left(\frac{3 \cdot n_i}{4} + 1 < x < n_i, y\right) \right] \\
u\left(\frac{n_i}{4} + 1 < x < \frac{n_i}{2}, y\right) &= u\left(\frac{n_i}{2} + 1 < x < \frac{3 \cdot n_i}{4}, y\right) = \\
u\left(\frac{3 \cdot n_i}{4} + 1 < x < n_i, y\right) &= u\left(0 < x < \frac{n_i}{2}, y\right)
\end{aligned} \tag{6.9}$$

Thanks to the phase average we can average the domain, in particular the rough domain, the one which gives problem with the sampling, in more point, still maintaining the main behavior of the flow above rough or smooth patches.

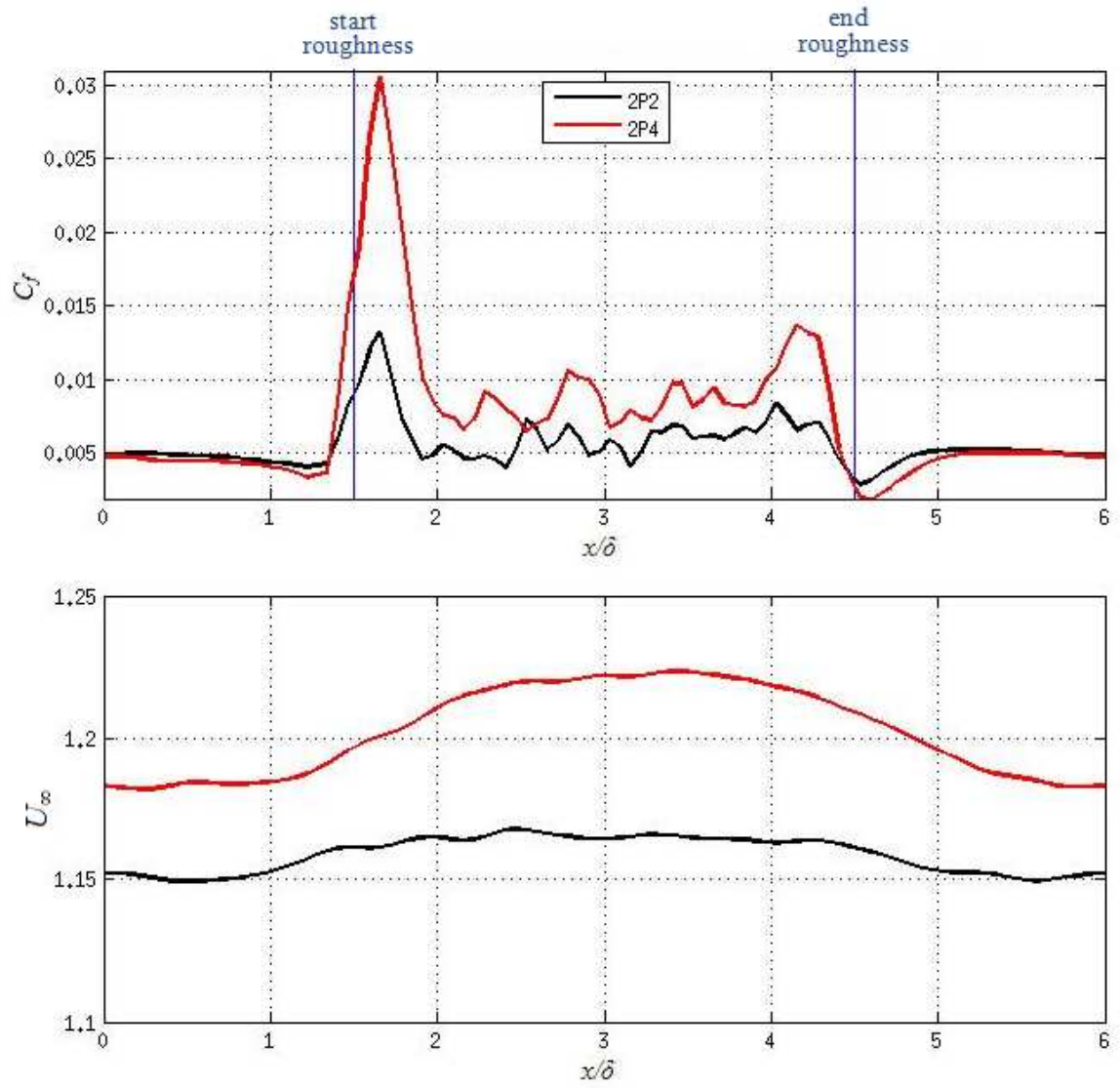


Fig. 6.23 - Streamwise development of the friction coefficient  $C_f$  and the free-stream velocity  $U_\infty$  for cases for cases 2P2 and 2P4. Blue lines show locations of roughness.

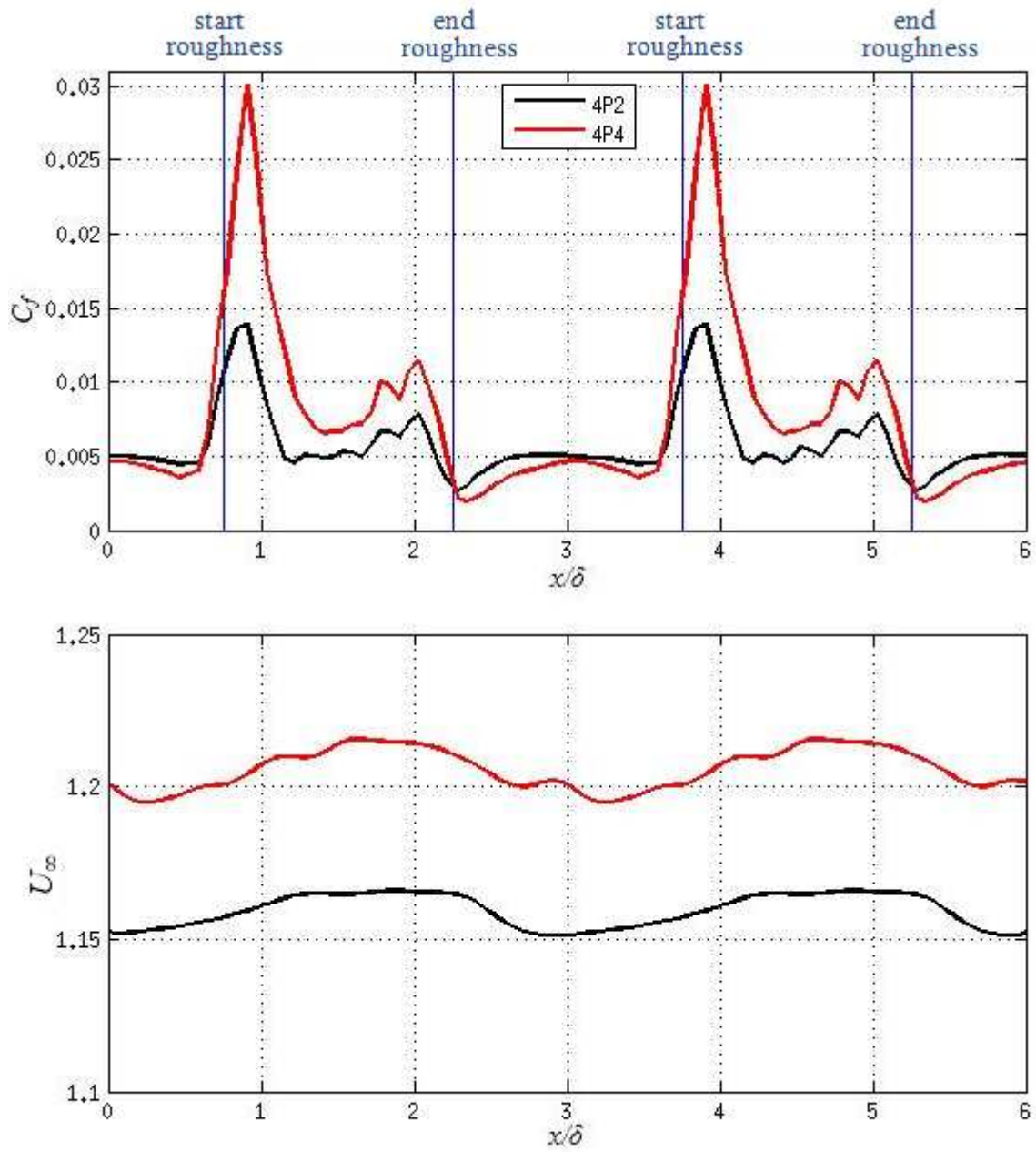


Fig. 6.24 - Streamwise development of the friction coefficient  $C_f$  and the free-stream velocity  $U_\infty$  for cases for cases 4P2 and 4P4. Blue lines show locations of roughness.

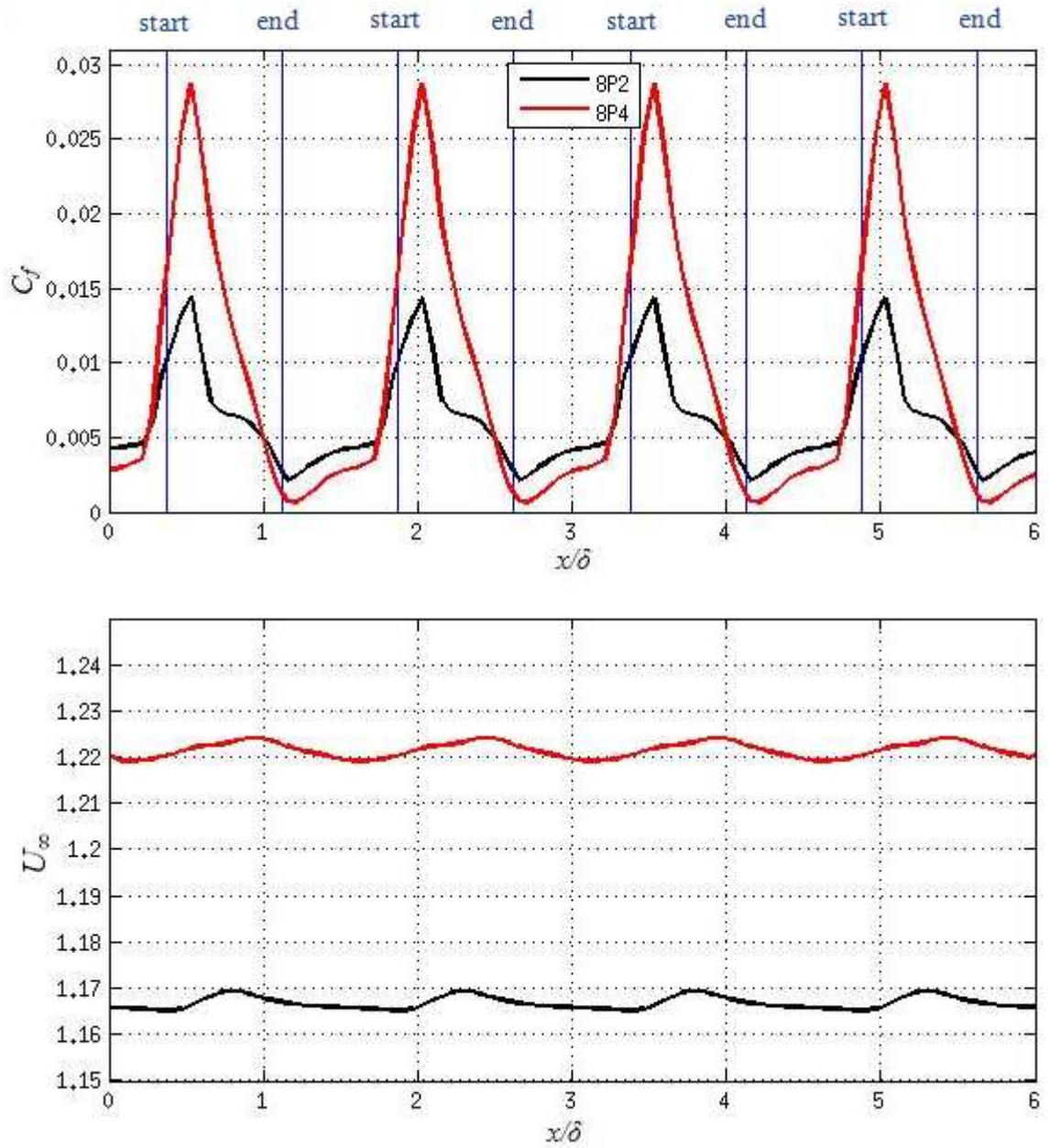


Fig. 6.25 - Streamwise development of the friction coefficient  $C_f$  and the free-stream velocity  $U_\infty$  for cases for cases 8P2 and 8P4. Blue lines show locations of roughness.

We can notice the similarities between the 2 patch case and 8 patch case also comparing the momentum equation terms from Figs. 6.18 and 6.19 (case 2P2) with following Figs. 6.26 and 6.27 (case 8P2). The influence and magnitude of the different terms above the patches are the same.

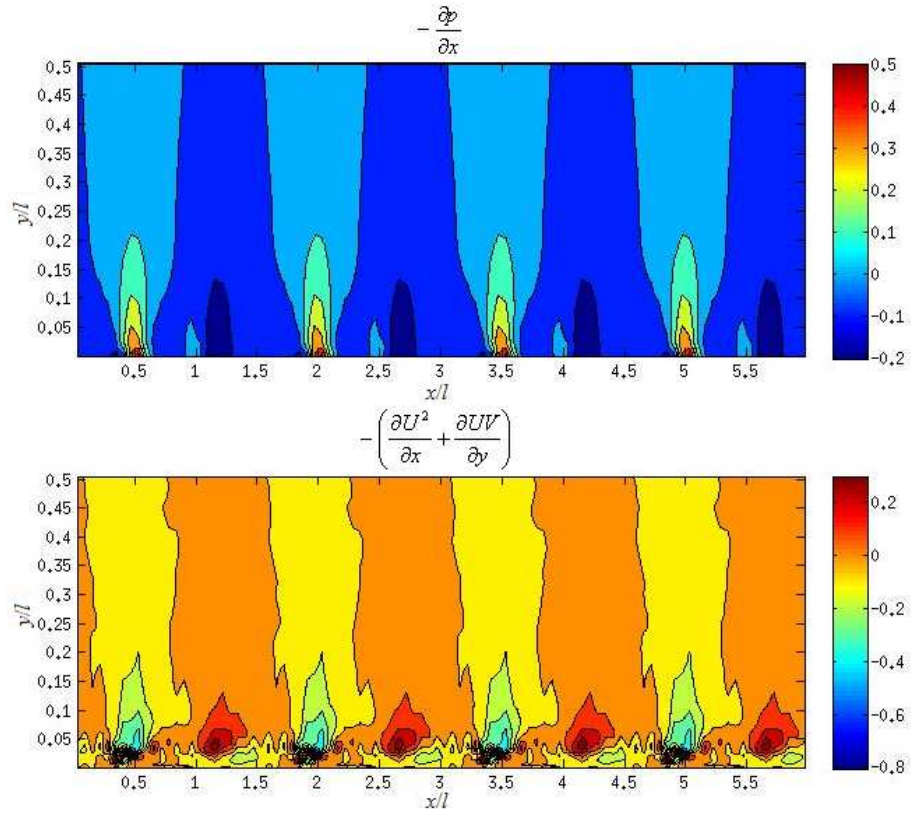


Fig. 6.26 - Pressure term and convective term in the momentum equation for case 8P2.

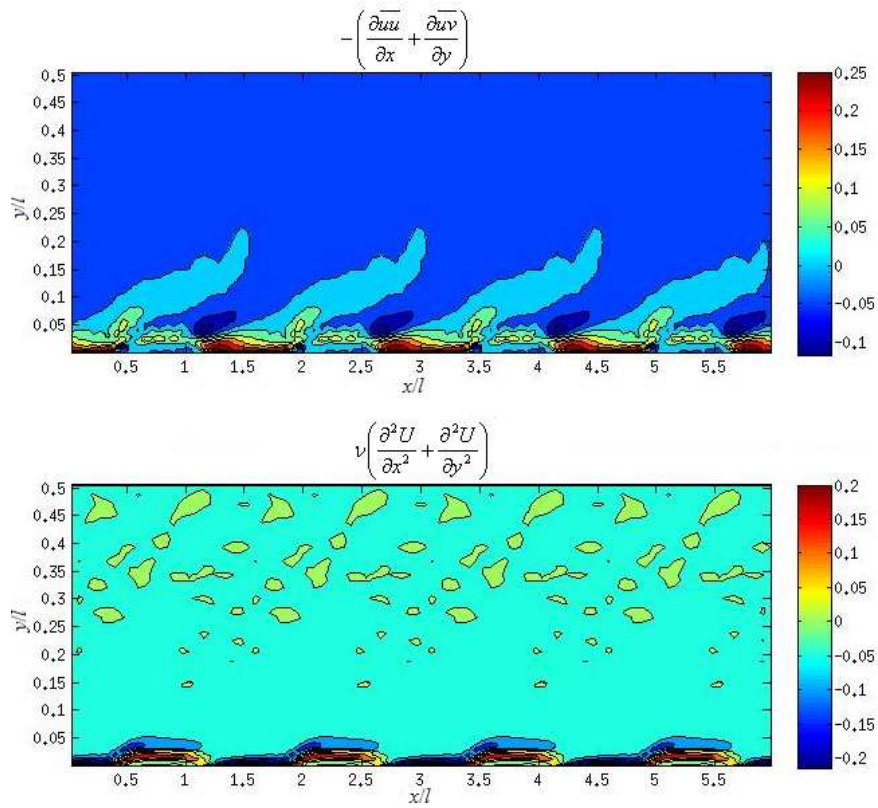


Fig. 6.27 - Reynolds stress term and viscous term in the momentum equation for case 8P2.

## 6.5 Mean velocity

In this section we show the mean velocity of the patch cases in different  $x$  locations, and we compare them with the rough cases, with the same roughness height  $h^+$ , and the smooth case, in order to study the effect of local roughness on the flow. For rough cases, the vertical location is shifted by the zero-plane displacement  $d$ , as defined in (6.2), while  $d = 0$  for smooth case. Both inner and outer scalings are used, although the inner scaling is more interesting since we maintained  $Re_\tau$  constant for every case.

Figs. 6.28 shows the mean velocity plots for the smooth case and the two completely rough cases; we can notice that, under inner scaling, profiles are similar in the outer layer, except for an offset depending on the roughness height. Furthermore, the log law, represented by a thin black line, is respected in all the cases.

Note that the  $x$  location is not indicated, since it doesn't affect the plots; Thus only one position is sufficient to show the mean velocity for these cases.

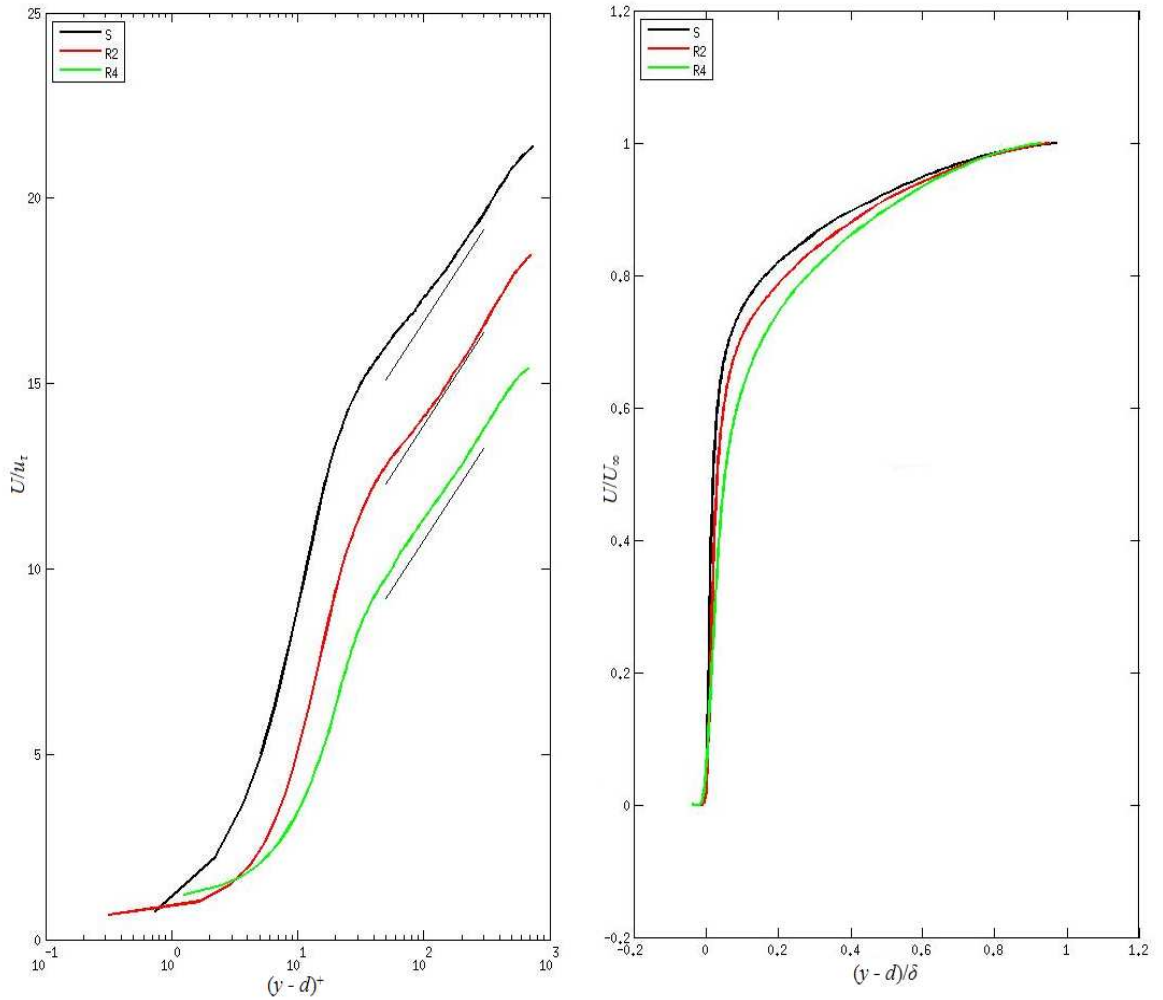


Fig. 6.28 - Profiles of streamwise mean velocity for cases S, R2, R4 with inner (left) and outer (right) scalings. Thin black lines in the inner scaling represent the log law.



Now we focus on the patch cases: Fig. 6.29 shows the inner scaling for case 2P2, compared with the completely rough case R2 and the smooth case S. In all the following plots we decided not to consider the zero-plane displacement  $d$ , since the value of  $d$  is not well determined in the transition region, where it is neither 0 (smooth patches) nor 0.08 (rough patches) and it could bring to unphysical and misunderstood results.

The  $x$  location of the plots are chosen through all the domain, with a step equal to  $x/\delta = 0.5$ , in order to study the effect of local roughness. We can notice that over the smooth patch,  $x/\delta = 0.5$  and 1, the patch case fits well the smooth case; then the transition to roughness begins and, at  $x/\delta = 1.5$ , the mean velocity of the patch case is approaching the one of the rough case; this transition ends quickly, and at  $x/\delta = 2$  the surface is completely rough and the patch case collapses with the rough case. This superposition between case R2 and 2P2 is evident over all the rough domain, since  $x/\delta = 4$ ; then transition to smoothness begins, and at  $x/\delta = 4.5$ , the patch case departs from the rough case. At  $x/\delta = 5$  the patch case collapses again with the smooth one. We can notice that the plots at  $x/\delta = 6$  and  $x/\delta = 0.5$  are very close, since periodic boundary conditions are imposed and this process is repeated every time.

A similar analysis can be done for cases S, R4 and 2P4 (Fig. 6.30), where this time the roughness height is  $h^+ = 40$ .

Figure 6.31 shows a comparison of mean velocities for cases S, R4, 2P4, the same of Fig. 6.30, with outer scalings, which give the advantage that the wall shear stress doesn't affect the results: we can see that in the outer layer the three curves collapse perfectly, at every  $x$  location. Instead in the inner layer we can notice a streamwise development of the patch case, similar to the one observed under the inner scalings.

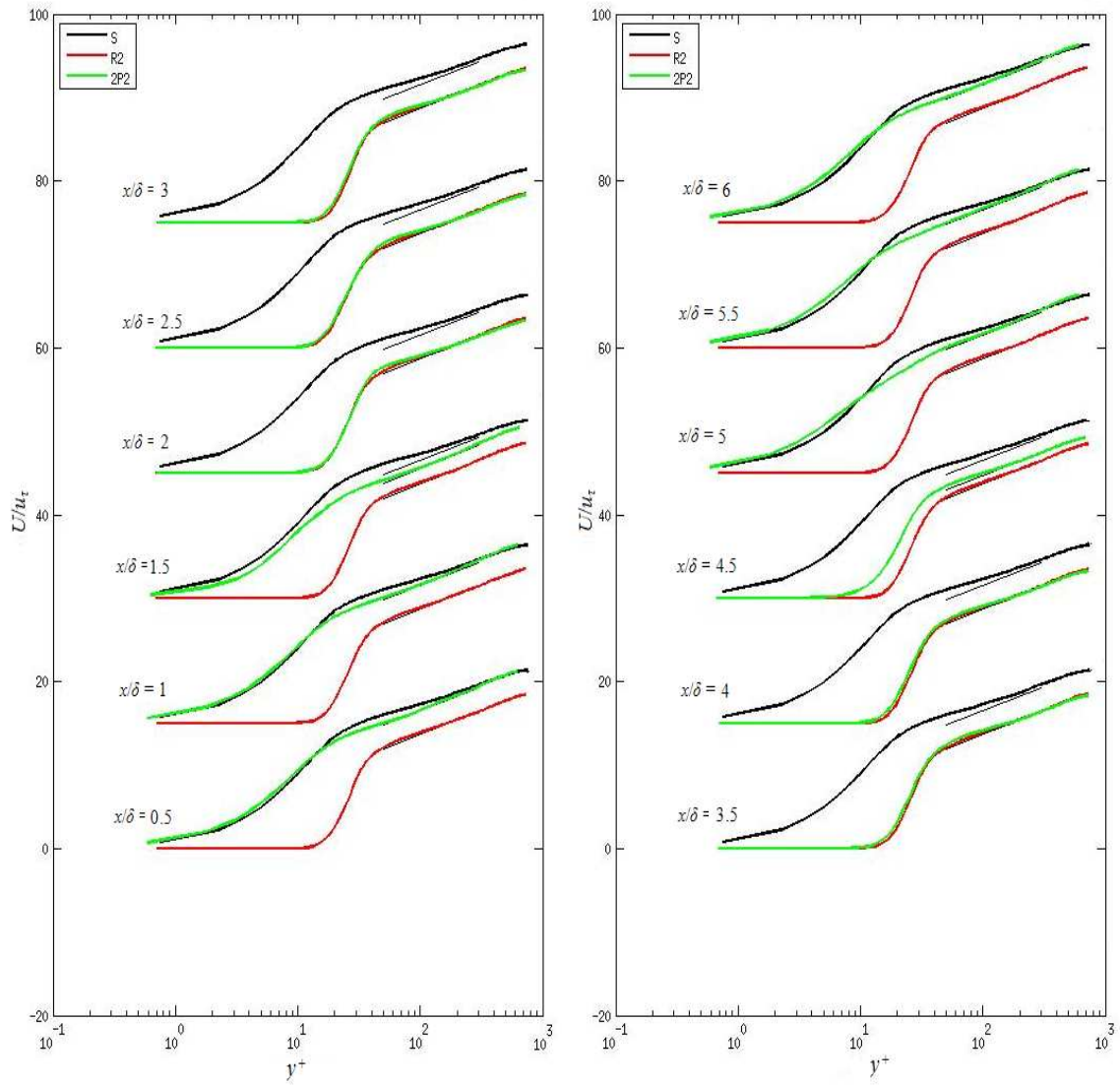


Fig. 6.29 - Profiles of streamwise mean velocity for cases S, R2, 2P2 with inner scalings. Thin black lines represent the log law.



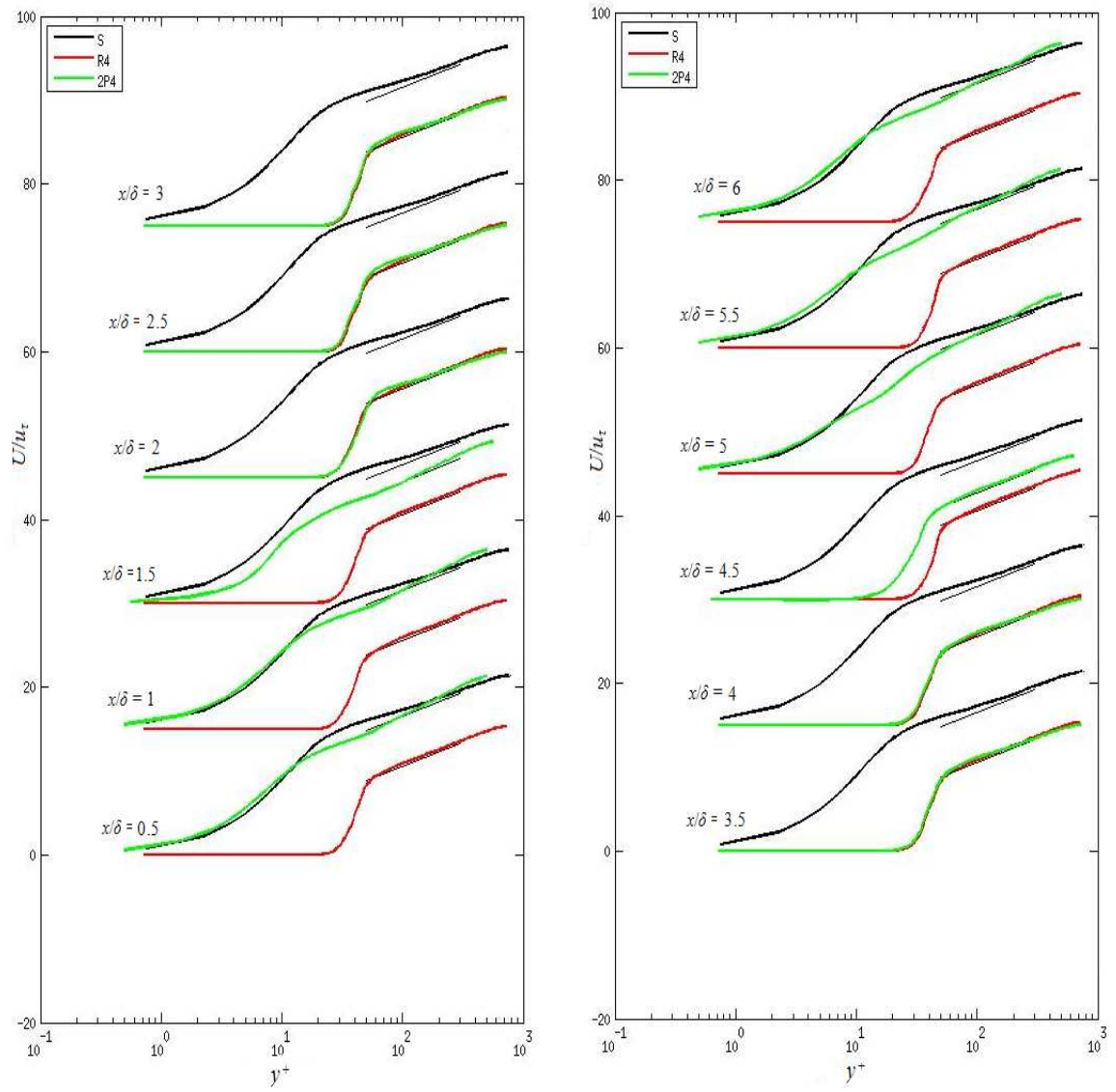


Fig. 6.30 - Profiles of streamwise mean velocity for cases S, R4, 2P4 with inner scalings. Thin black lines represent the log law.

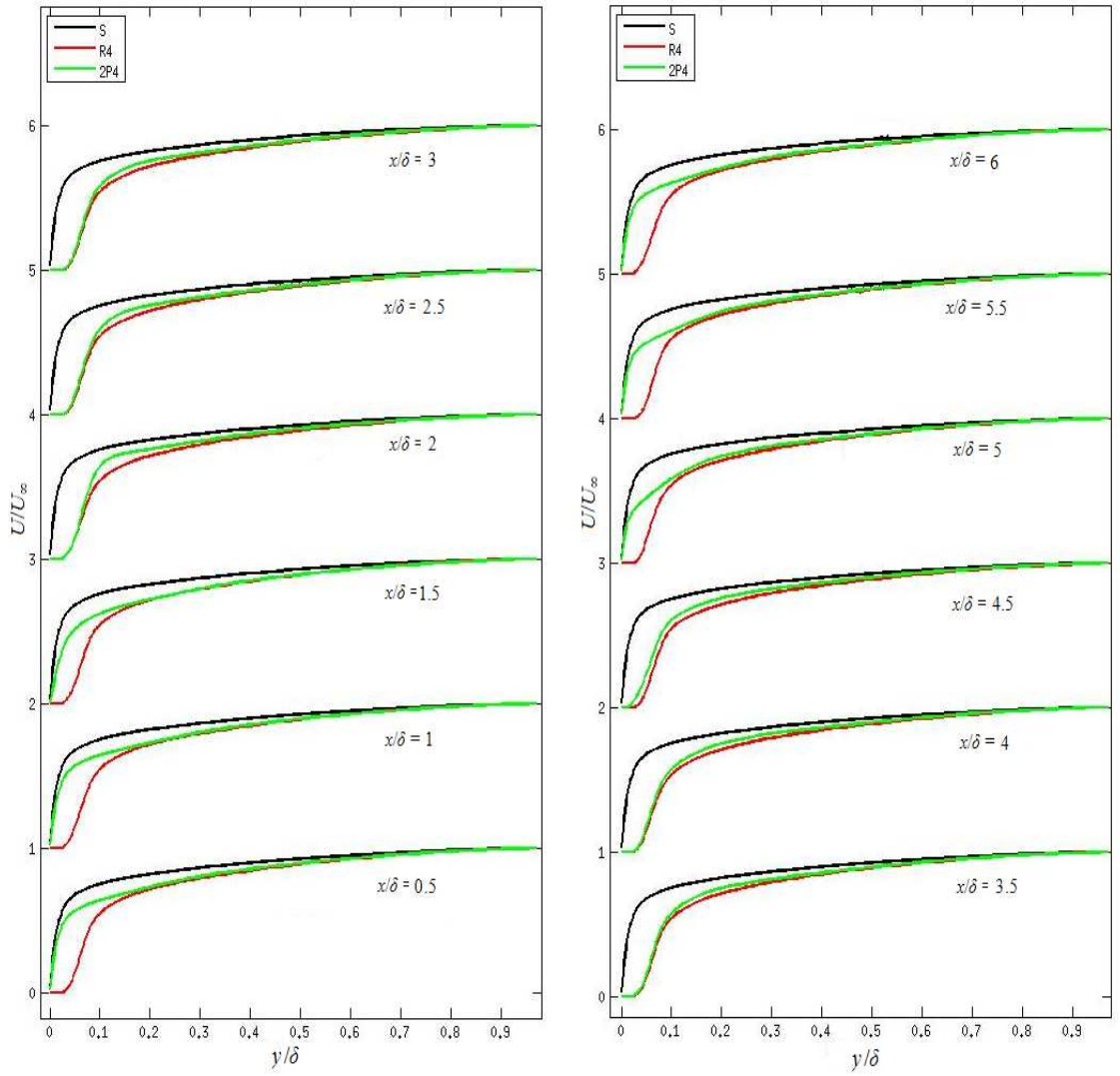


Fig. 6.31 - Profiles of streamwise mean velocity for cases S, R4, 2P4 with outer scalings.

Finally, we focus on the number of patches, the other parameter we are studying: in figure 6.33 - 6.35 patch cases are compared. To make a reasonable comparison the  $x$  location of the plots are different, since the position of the patches changed between cases. We defined 4 stations, with the same step, but shifted, in order to study the smooth-rough and rough-smooth transitions. The positions of the stations are summarized in fig. 6.32, where the transition functions  $f$  are plotted for different cases. The precise positions of the stations are summarized in Table 6.3. Note that in the 4 and 8 patch cases, the phase average has been applied (equations (6.8) and (6.9)); hence, the behavior of the flow is the same over every patches.

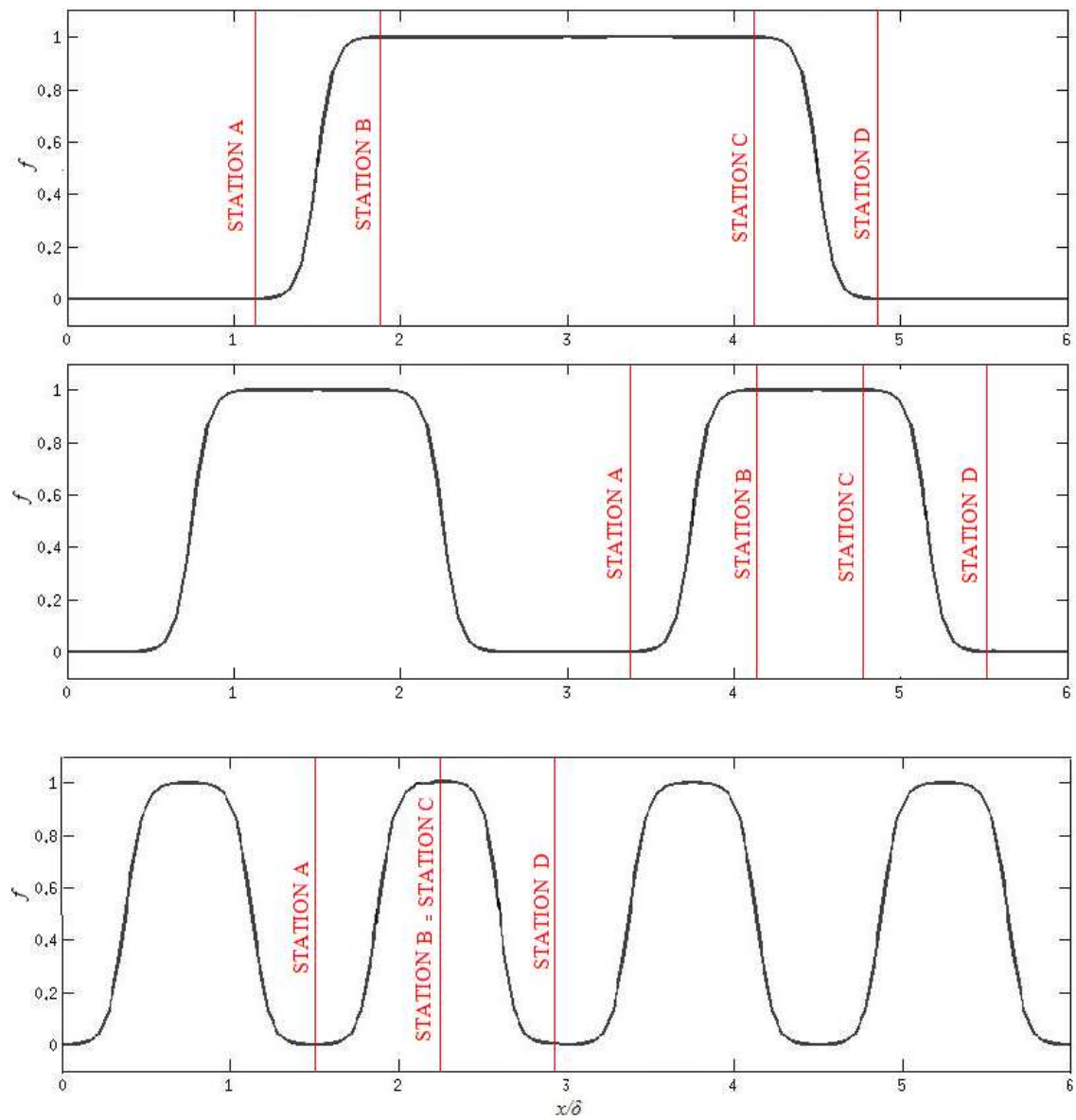


Fig. 6.32 – Transition functions  $f$  for cases 2P2, 2P4 (above), 4P2, 4P4 (middle) and 8P2, 8P4 (below) with indicated the positions of the stations.

| <i>Case</i> | <i>Station A</i><br>$x/\delta$ | <i>Station B</i><br>$x/\delta$ | <i>Station C</i><br>$x/\delta$ | <i>Station D</i><br>$x/\delta$ |
|-------------|--------------------------------|--------------------------------|--------------------------------|--------------------------------|
| 2P2, 2P4    | 1.125                          | 1.875                          | 4.125                          | 4.875                          |
| 4P2, 4P4    | 3.375                          | 4.125                          | 4.875                          | 5.625                          |
| 8P2, 8P4    | 1.5                            | 2.25                           | 2.25                           | 3                              |

Table 6.3 – Positions of the stations used in the mean velocity compare plots.

From figure 6.33 we notice that the  $h^+ = 20$  cases are not influenced by the number of patches: when the roughness is low, the three curves agree very well over the smooth, rough and transition domain. The situation is different for the  $h^+ = 40$  cases (Fig. 6.34): here we notice that the 8 patch case doesn't fit the 2 and 4 patch cases at the station A, at the end of a smooth region, where we notice that in the buffer layer the green line is lower than the others, closer to the situation we have over a rough patch instead of a smooth one. We can say that the influence of rough patch frequency more significantly affects the ability of the flow to adapt from rough to smooth than from smooth to rough, since the agreement with the other cases is respected at station F. Hence, under the present conditions that we used for these simulations, the critical number of patches is between 4 and 8, since for 8 patches the smooth and rough regions change too frequently for the flow to reach the smooth equilibrium status.

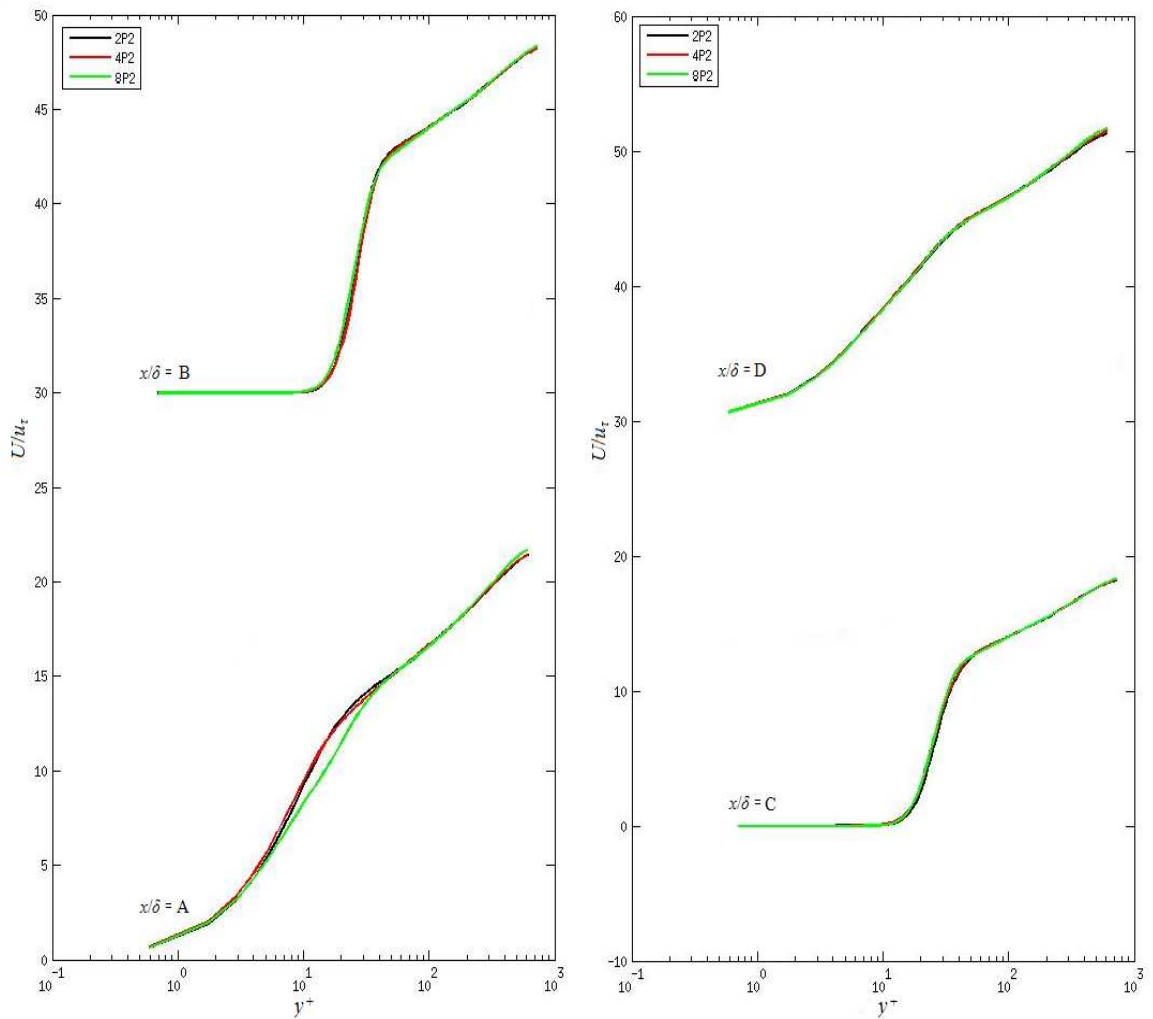


Fig. 6.33 - Profiles of streamwise mean velocity for cases 2P2, 4P2 and 8P2 with inner scalings.

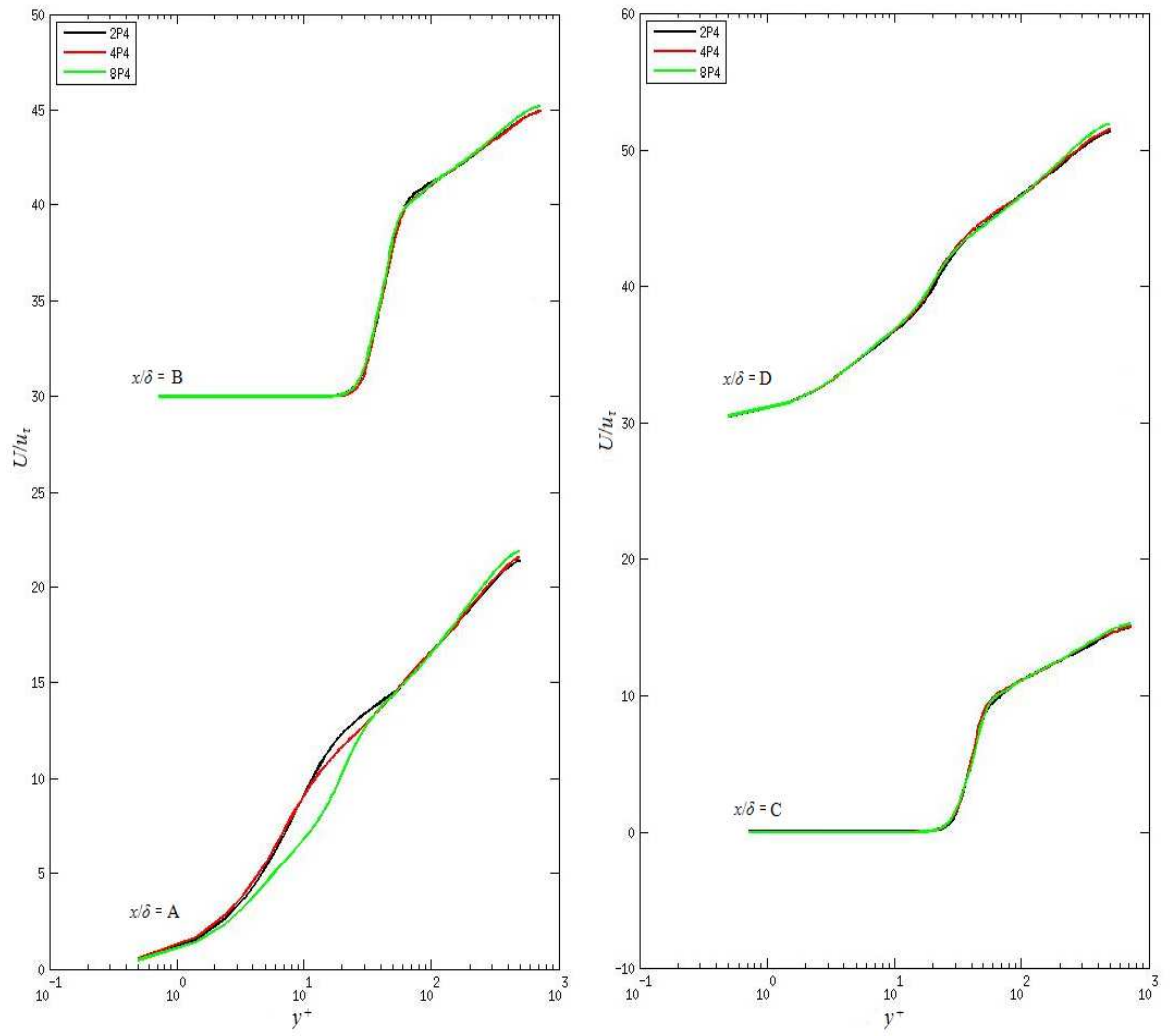


Fig. 6.34 - Profiles of streamwise mean velocity for cases 2P4, 4P4 and 8P4 with inner scalings.

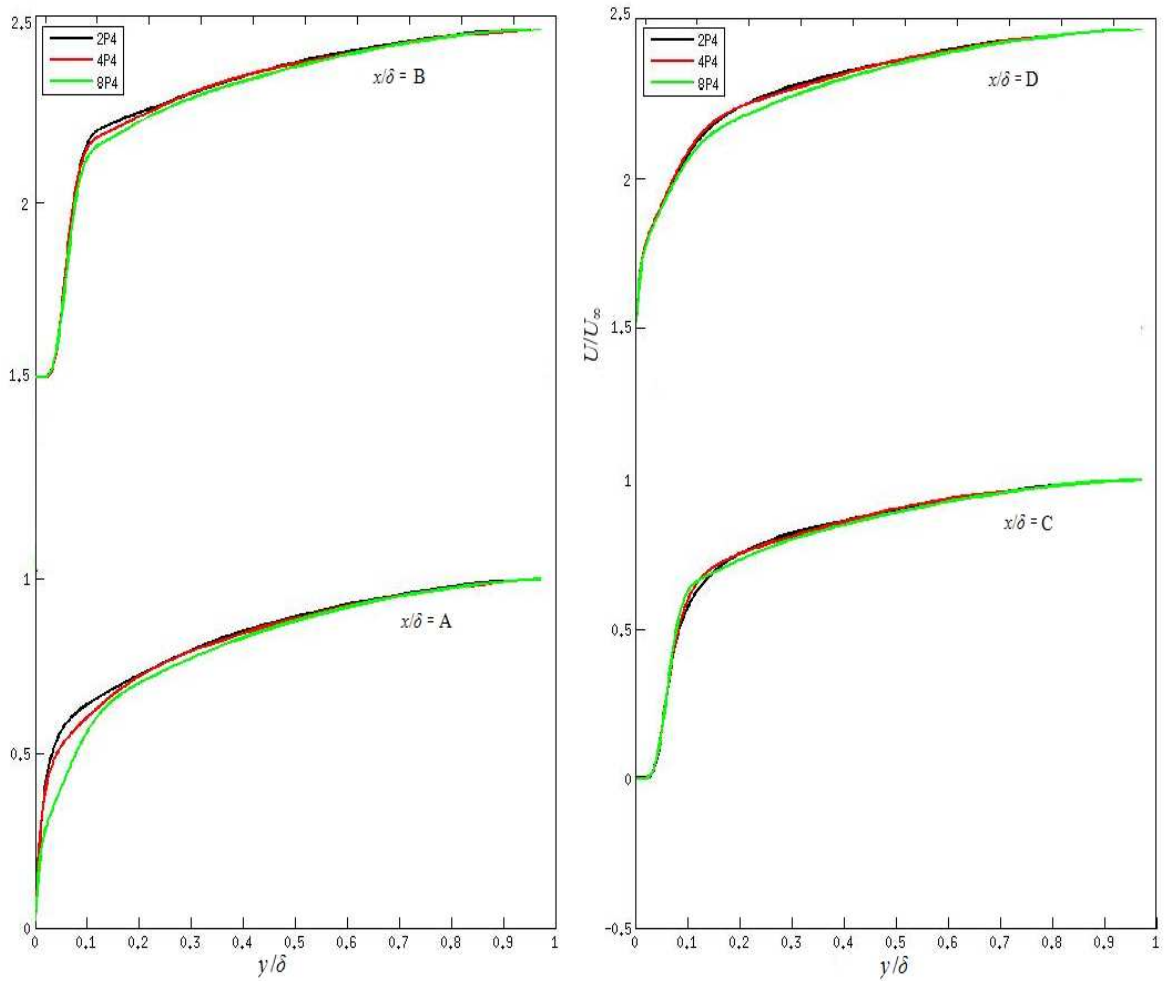


Fig. 6.35 - Profiles of streamwise mean velocity for cases 2P4, 4P4 and 8P4 with outer scalings.

## 6.6 Reynolds stresses

In this section Reynolds stresses are shown and presented, plotted against both the normal wall direction and the streamwise one.

At first a comparison between the smooth and the completely rough cases is shown in figure 6.36. Reynolds stresses are normalized with local  $u_\tau$ . The  $x/\delta$  parameter is not indicated since it doesn't affect the completely smooth and rough cases. A single large peak is observed for the smooth case, and the magnitude of the components are in agreement with the smooth turbulent channel flow theory (section 2.6); for the completely rough cases the peak is shifted and localized in a thinner region inside the outer layer; This indicates that for high  $h$  the turbulence generation mechanism is noticeably altered by the roughness, and the near-wall roughness-induced active turbulence motions meet the inactive motions farther away from the wall.



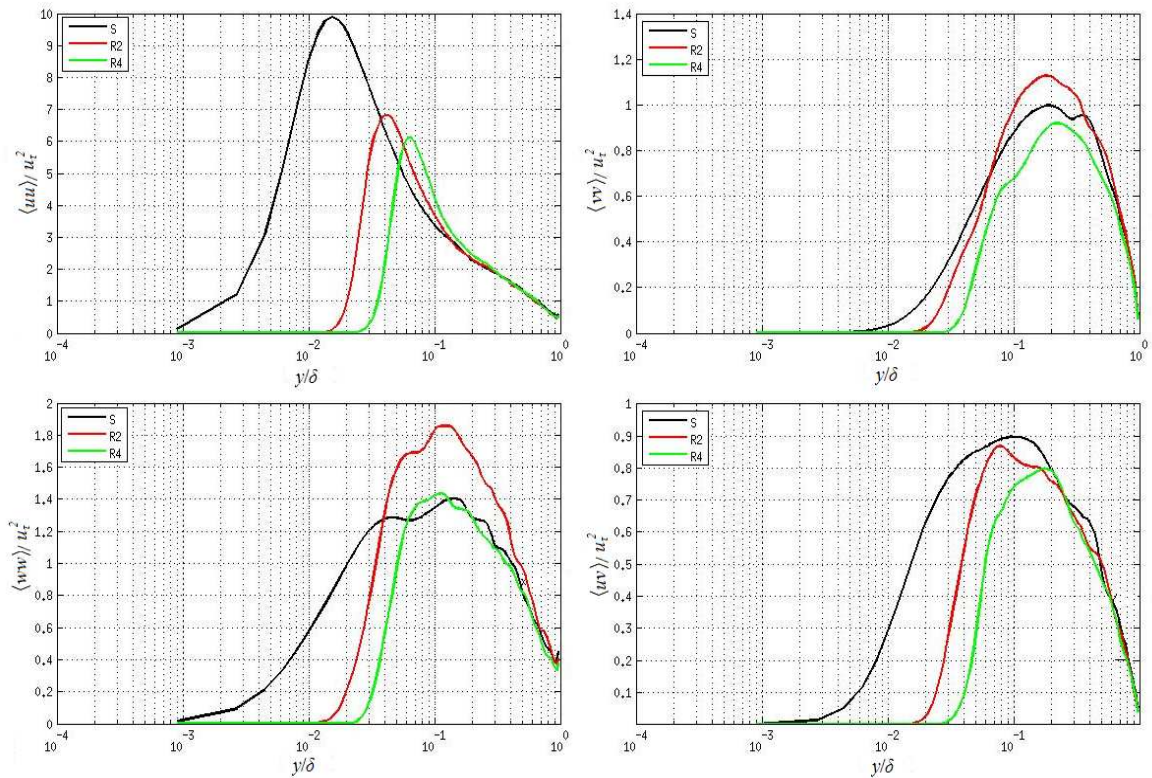


Fig. 6.36 - Components of Reynolds stress tensor for cases S, R2 and R4 plotted against  $y/\delta$ . The profiles are shifted for clarity.

For case 2P2 (plotted in Figs. 6.37 and 6.38 at different  $x$  locations), we observe that, over a rough patch ( $x/\delta = A$  and  $x/\delta = F$ ), the rough case collapses very well with the corresponding completely rough one, and the Reynolds stresses are very close; instead, over a smooth patch ( $x/\delta = C$  and  $x/\delta = D$ ), the situation is more complicated:  $\langle uu \rangle$  component of Reynolds stress is lower than the smooth case and extend in the same region; other components, in particular  $\langle ww \rangle$ , have got higher stresses than the smooth one: they extend in a wide region (both in the inner and outer layer), like the smooth case, but the magnitude is higher. This indicates that the flow is affected by the presence of the roughness, which increases the stresses also over the smooth region. Similar results occur in case 2P4, plotted in figure 6.39 - 6.40.

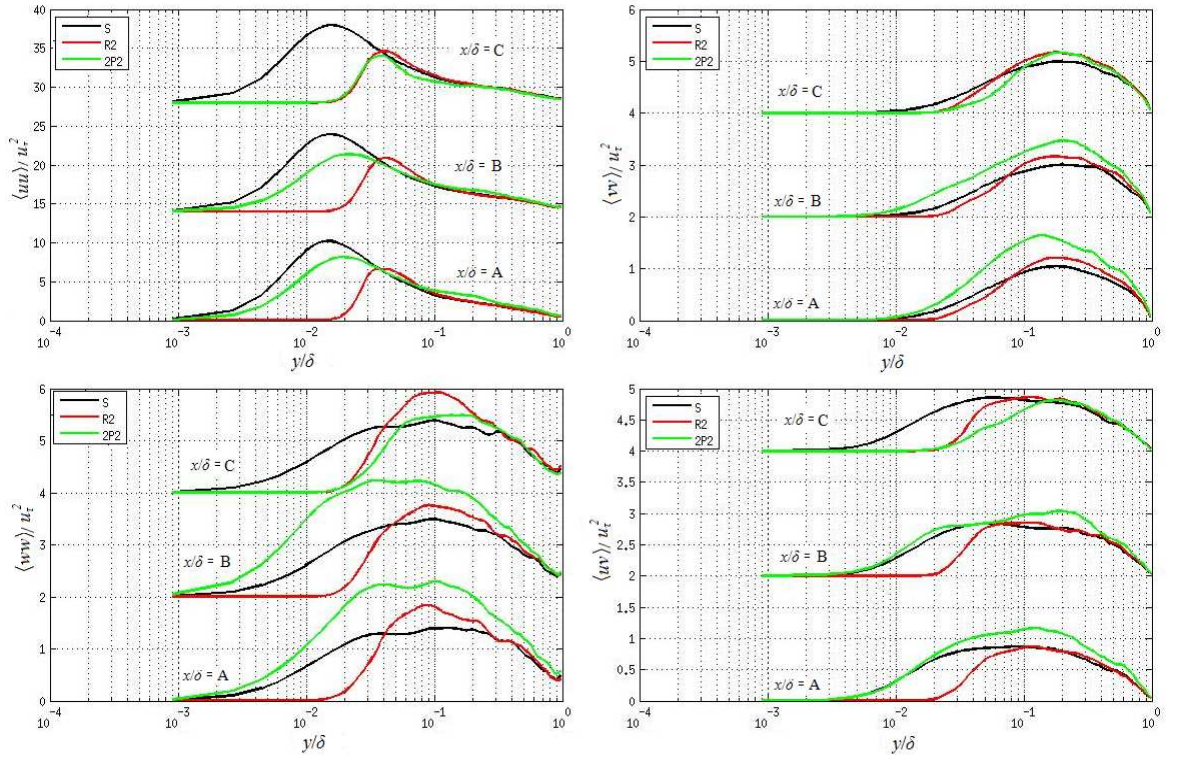


Fig. 6.37 - Components of Reynolds stress tensor for cases S, R2 and 2P2 plotted against  $y/\delta$ . The profiles are shifted for clarity.

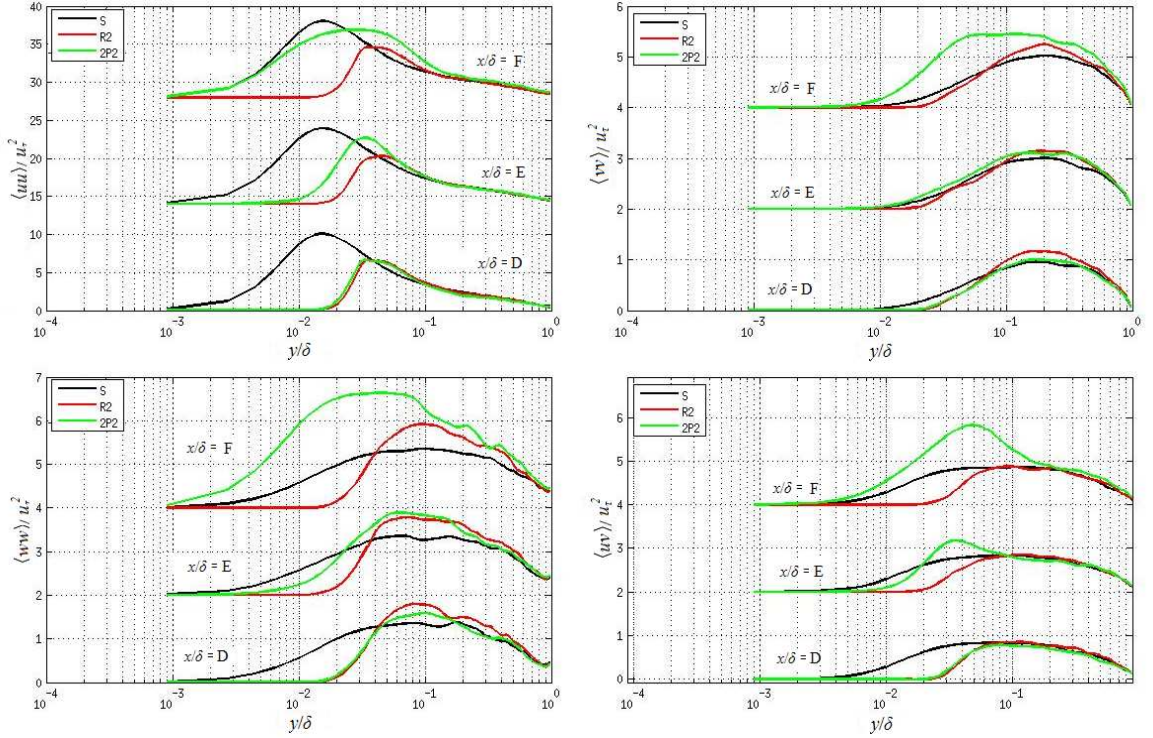


Fig. 6.38 - Components of Reynolds stress tensor for cases S, R2 and 2P2 plotted against  $y/\delta$ . The profiles are shifted for clarity.



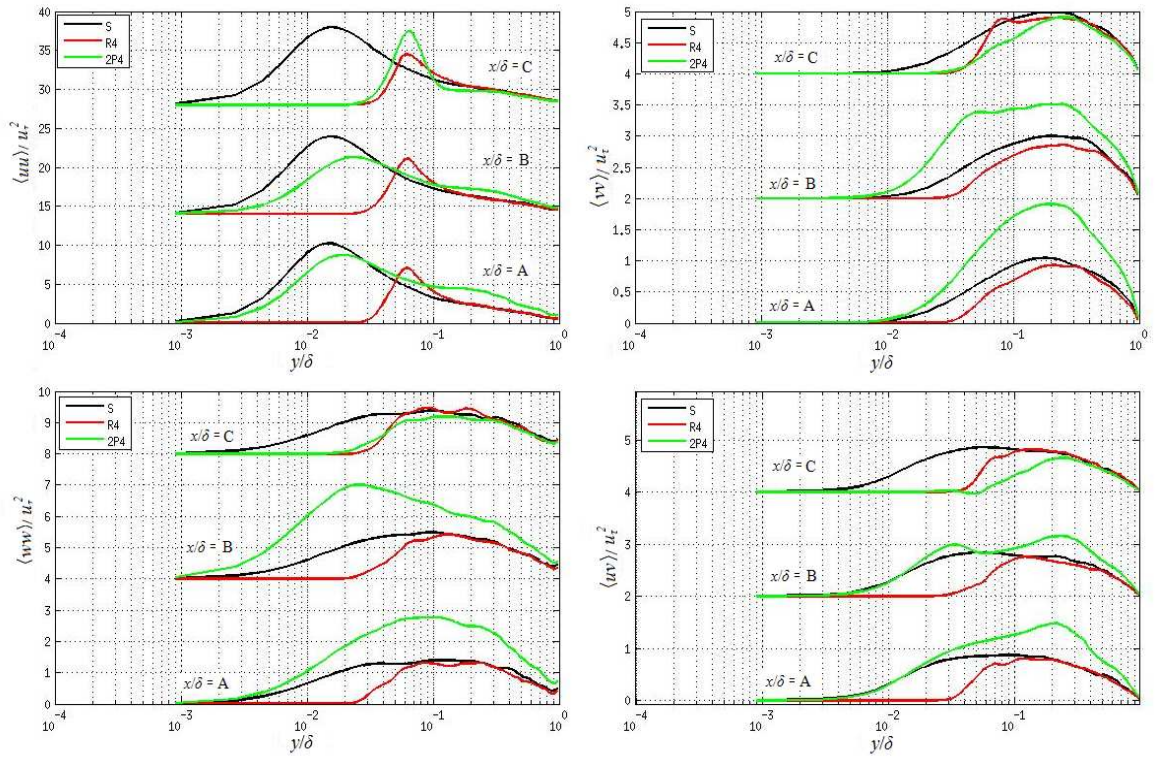


Fig. 6.39 - Components of Reynolds stress tensor for cases S, R4 and 2P4 plotted against  $y/\delta$ . The profiles are shifted for clarity.

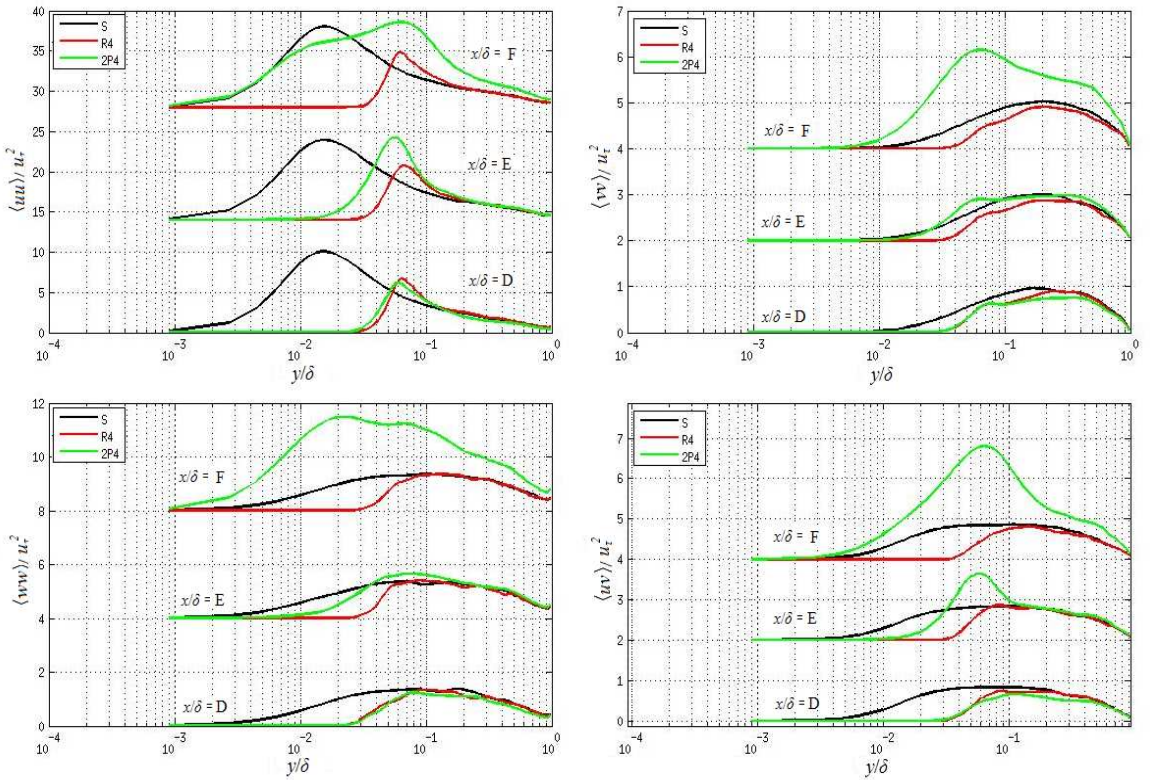


Fig. 6.40 - Components of Reynolds stress tensor for cases S, R4 and 2P4 plotted against  $y/\delta$ . The profiles are shifted for clarity.

In the next figures we show contours of Reynolds stresses, normalized with  $U_\infty$ , through the  $x$  and  $y$  domain for the patch cases. Also a streamline starting from  $y/d = 0.2$  is plotted in every components. At first the three  $h^+ = 20$  cases are plotted in Figs. 6.41 - 6.43 with the same scale in the legend in order to compare the results. Then the  $h^+ = 40$  case are shown, with a higher scale, since Reynolds stresses are, in general, higher through all the domain.

We can see a high increase of  $\langle uu \rangle$  component above the rough patches; this component is the most affected by local roughness. Also the  $\langle uv \rangle$  component has a very interesting behavior: it suddenly decreases just before a rough patch, assuming also negative values, and, in a similar way, it increases very rapidly at the end of the patches. This increase is due to recirculation regions and possibly separation of the flow, as shown in Fig. 6.21. The phenomenon is emphasized for the  $h^+ = 40$  cases, plotted in Figs. 6.44 - 6.46.

We can also notice that the streamlines, starting at  $y/d = 0.2$ , are deflected, since the flow shifts upwards over the rough patches due to their blockage effect.

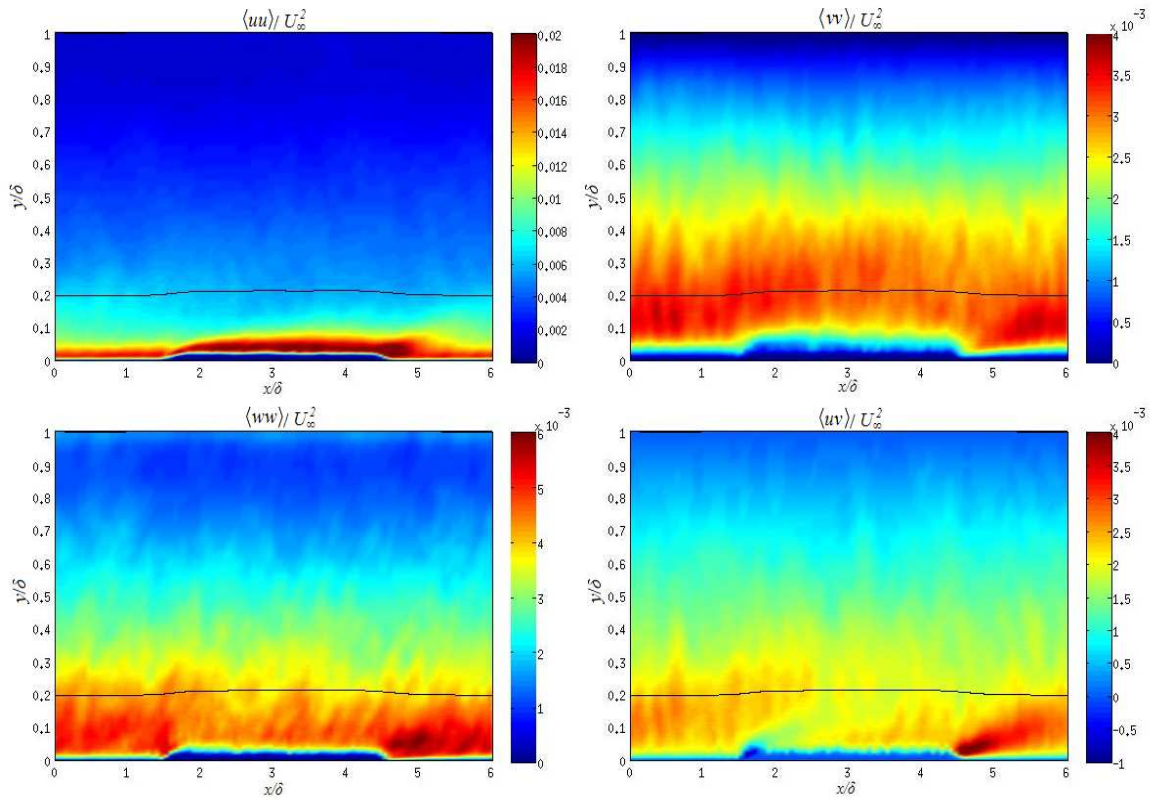


Fig. 6.41 - Contours of Reynolds stress tensor components for case 2P2. Black lines are streamlines at  $y/d = 0.2$ .



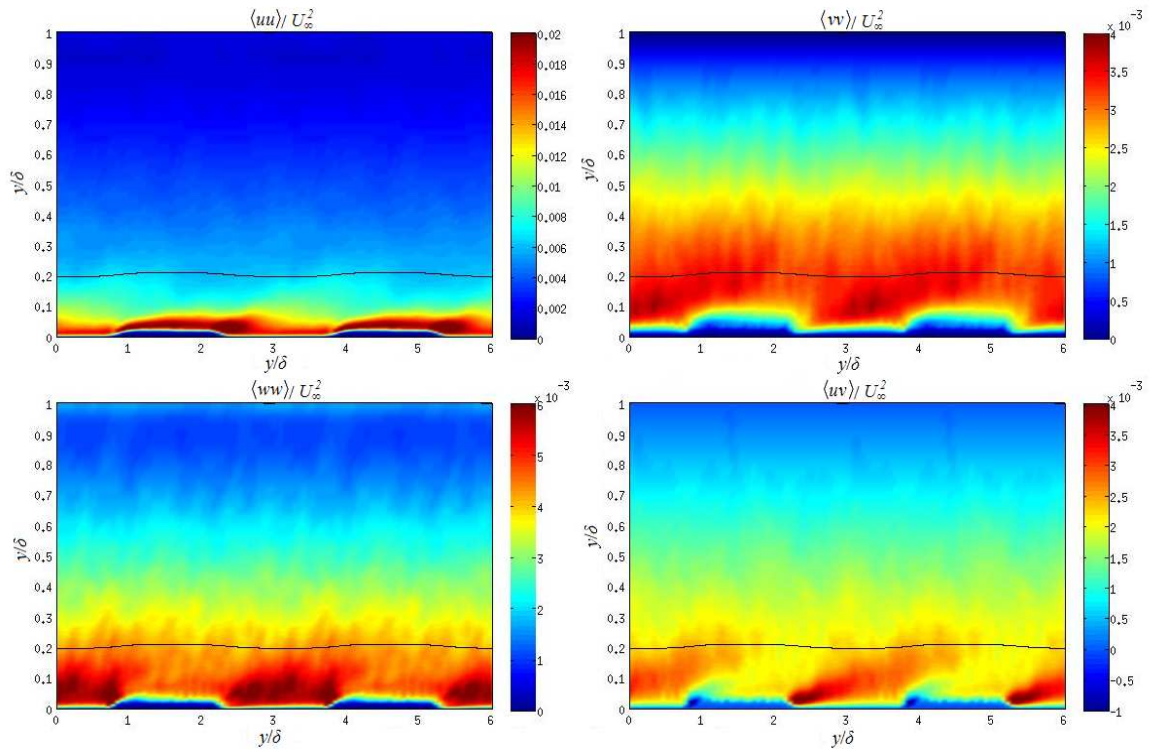


Fig. 6.42 - Contours of Reynolds stress tensor components for case 4P2. Black lines are streamlines at  $y/d = 0.2$ .

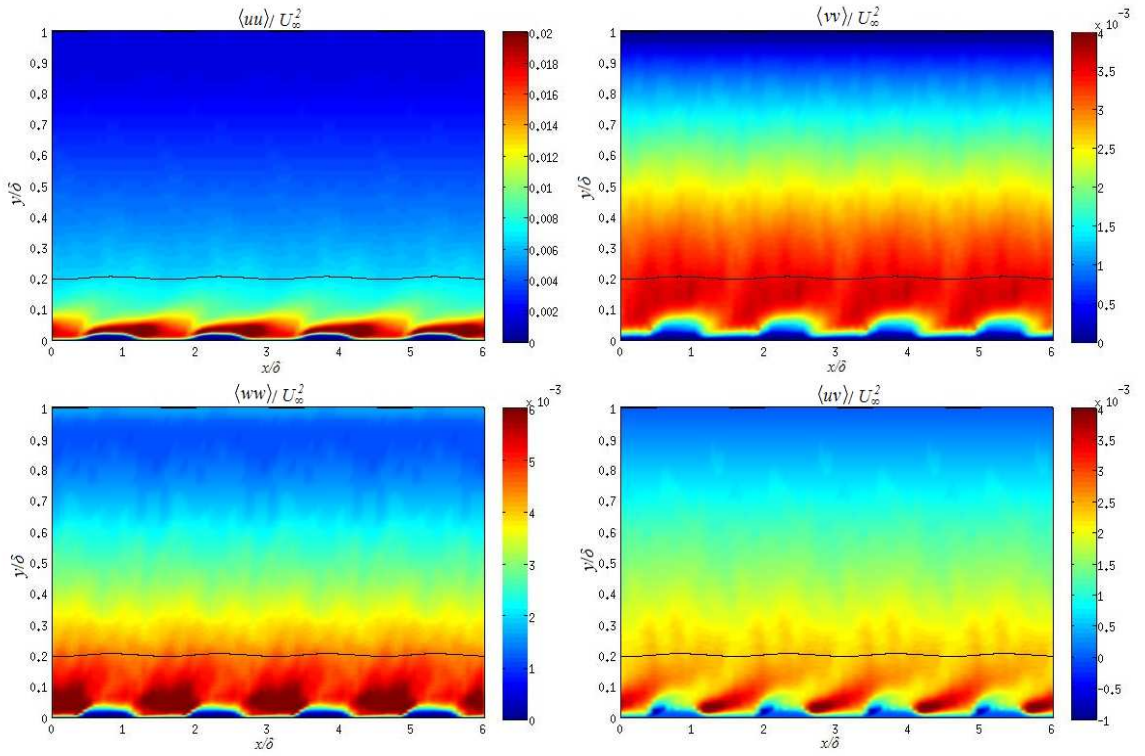


Fig. 6.43 - Contours of Reynolds stress tensor components for case 8P2. Black lines are streamlines at  $y/d = 0.2$ .

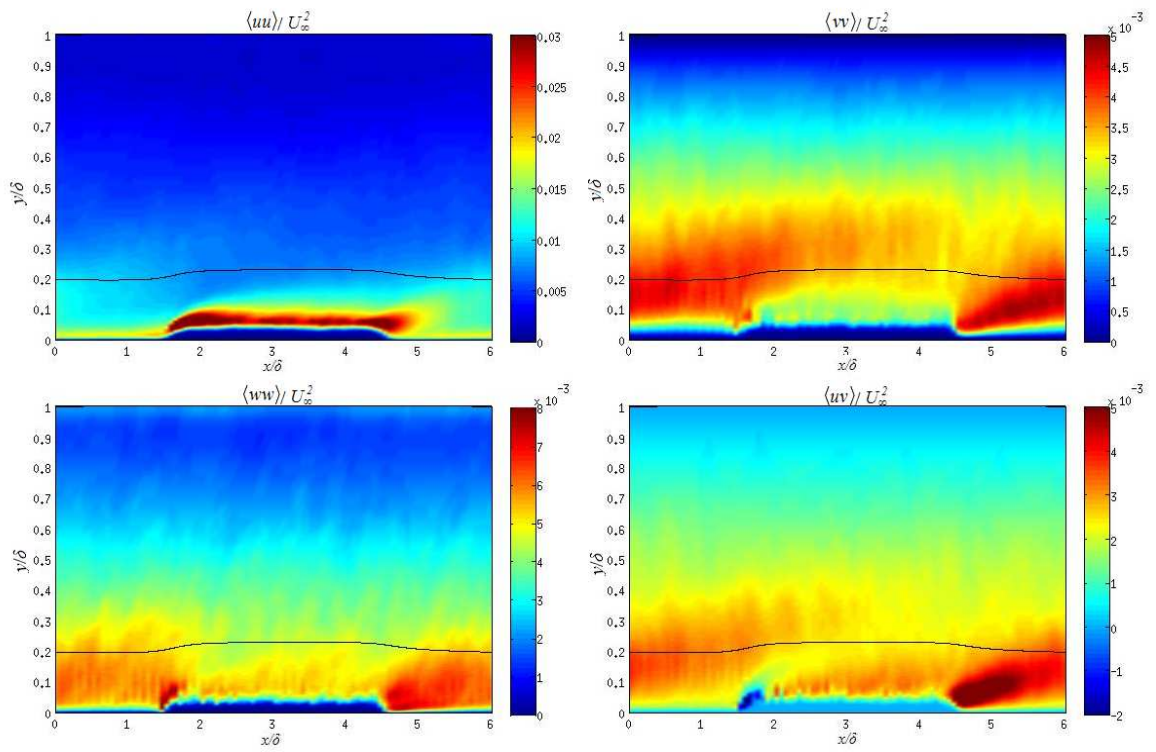


Fig. 6.44 - Contours of Reynolds stress tensor components for case 2P4. Black lines are streamlines at  $y/d = 0.2$ .

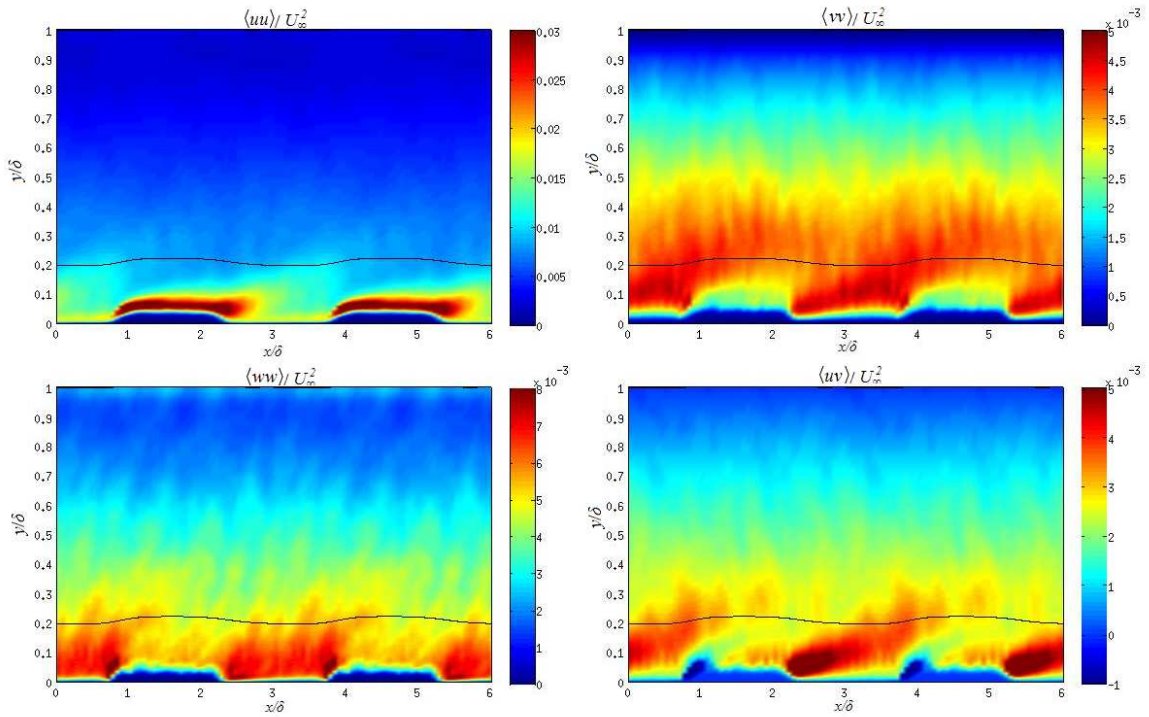


Fig. 6.45 - Contours of Reynolds stress tensor components for case 4P4. Black lines are streamlines at  $y/d = 0.2$ .

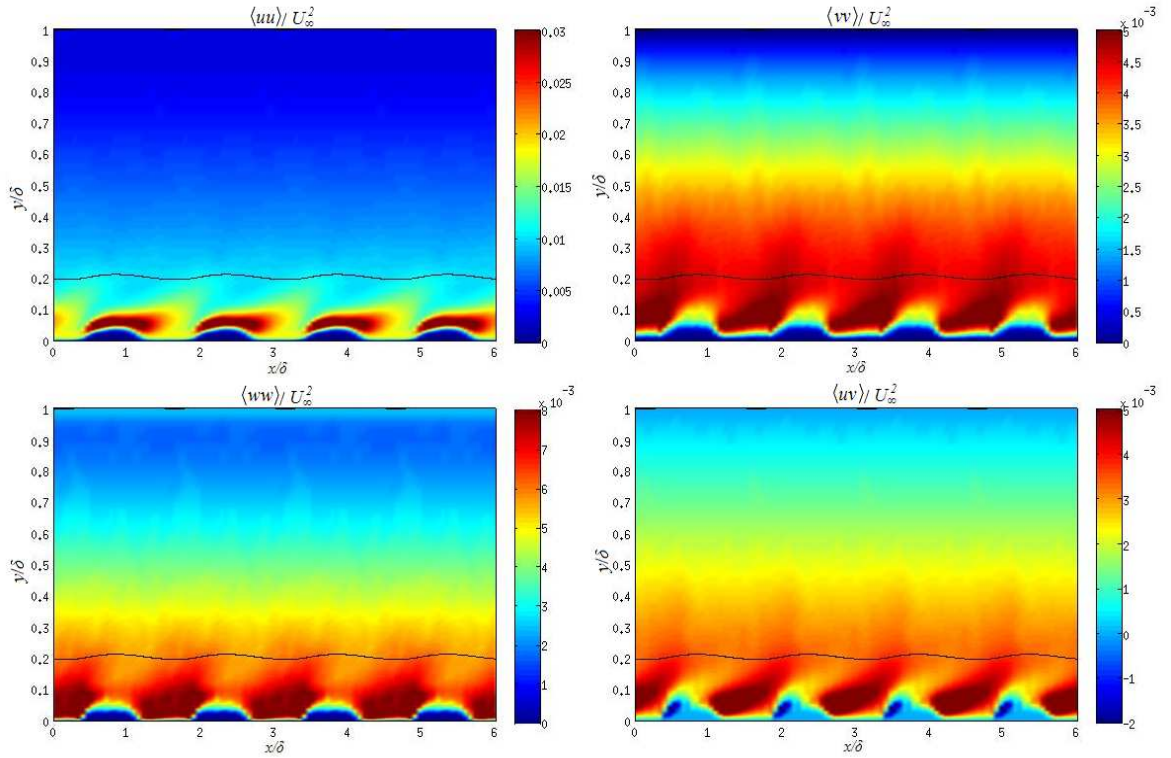


Fig. 6.46 - Contours of Reynolds stress tensor components for case 8P4. Black lines are streamlines at  $y/d = 0.2$ .

## 6.7 Turbulent structures

The roughness effects on flow reversion in the near-wall region can be illustrated by instantaneous contours of the velocity fluctuations  $u'$  in a plane near the wall. Figures 6.47 - 6.48 compare  $u'$  contours in the smooth case (S) and the completely rough cases (R2 and R4). The wall-distance of the planes are chosen at the same location (in wall units) in the buffer layer, which extends in the region  $5 < y^+ < 30$ ; in the rough cases the zero-displacement  $d$  is taken in account for the for the  $y$  location. In the smooth case, we observe the well-known establishment of very elongated streaks of high-low streamwise velocity, an indication of the stabilization of the inner layer and the reduction of the burst cycle. When the roughness is present, the elongated streaky structures are barely established and are not so clear; they are significantly disrupted by local disturbance and the generation of a turbulent spot is observed in Fig. 6.48. In the highest rough case ( $h^+ = 40$ ) the structures are difficult to see and the velocity fluctuations appears more disuniform.

The patch cases are shown in Figs. 6.49 - 6.51; we observe the local disturbance induced by the roughness over the rough patches; there are region where the flow is more turbulent, the velocity fluctuations are higher in absolute value; these regions are easily visible when the roughness is higher. Only when the frequency of the patches is too high (8 patch cases) the separation between smooth and rough regions is not any more easy to observe. Note that one should take in account the change in the length scale: the viscous length scale,  $\nu/u_\tau$ , increases as a result of the decrease of  $u_\tau$  over the smooth patches. Also the zero-plane displacement  $d$  is actually varying from 0 over the smooth patches to  $0.08l$  over the rough



ones. In figures 6.49 – 6.51 we consider  $d/l = 0.08$  (as in the completely rough case), but we have to remember that, in the smooth patches, we are visualizing the velocity in a lower level of the buffer layer, since  $d = 0$ . That can bring to a lower velocity in these regions. The significance of the roughness disruption is determined by the importance of the roughness-induced burst cycle, which depends on the extension of the roughness sublayer into the buffer layer.

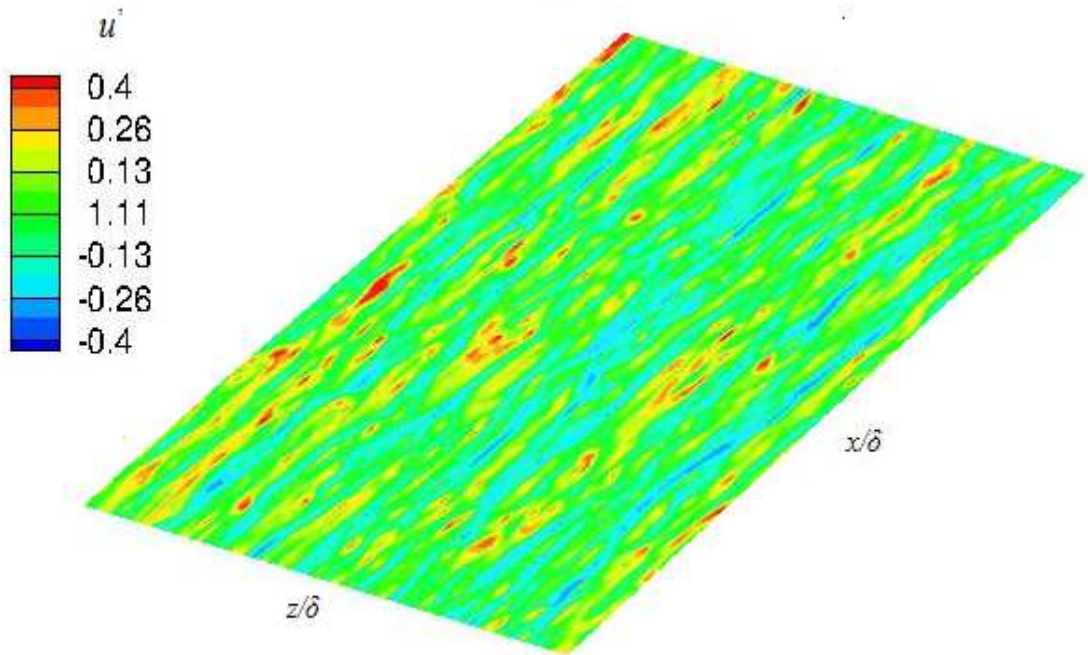


Fig. 6.47 - Contours of streamwise velocity fluctuations  $u'$  for case S (in the plane  $y^+ = 10 - 20$ ).

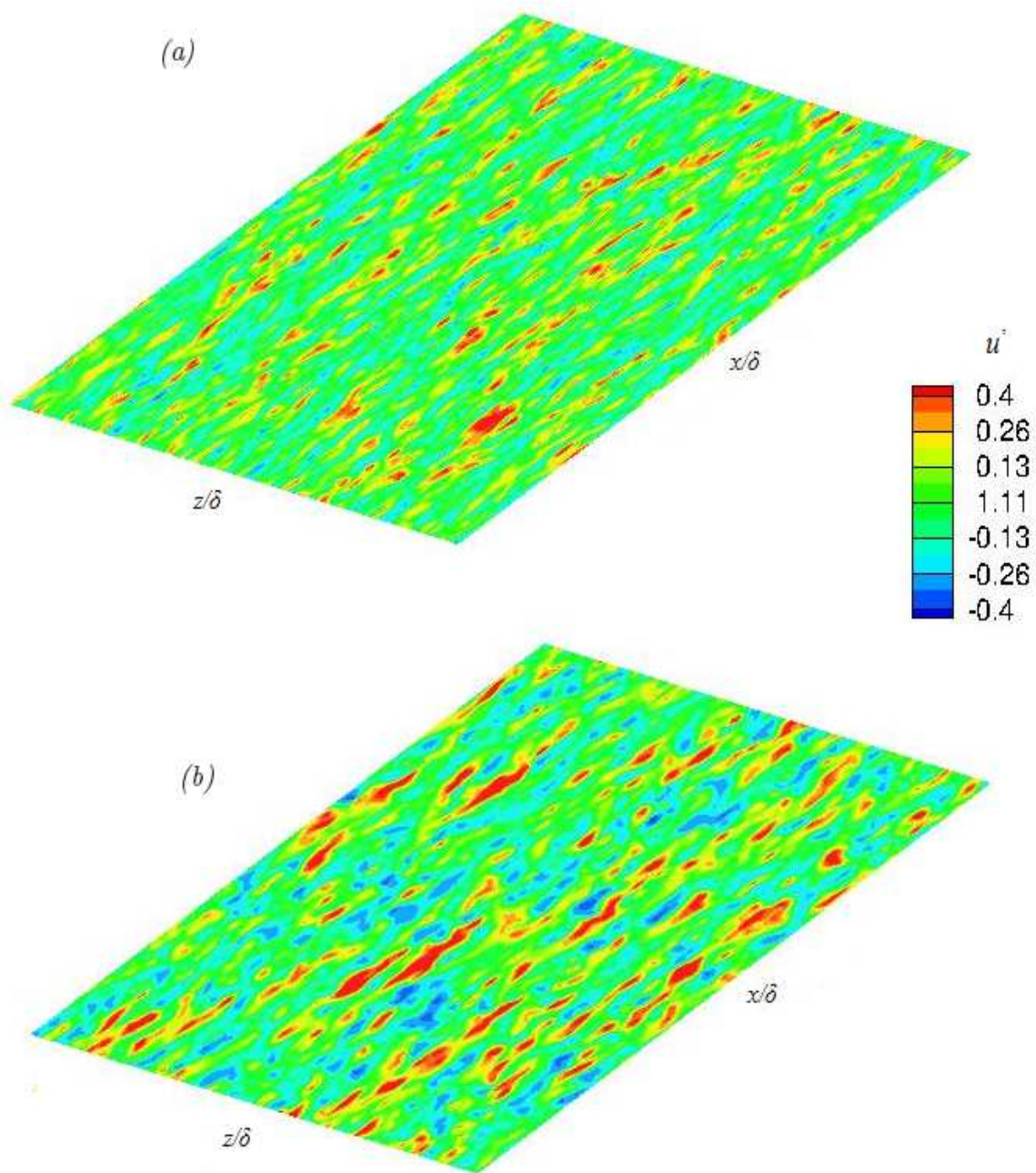


Fig. 6.48 - Contours of streamwise velocity fluctuations  $u'$  for (a) case R2 and (b) case R4 in the plane  $(y - d)^+ = 10 - 20$ .

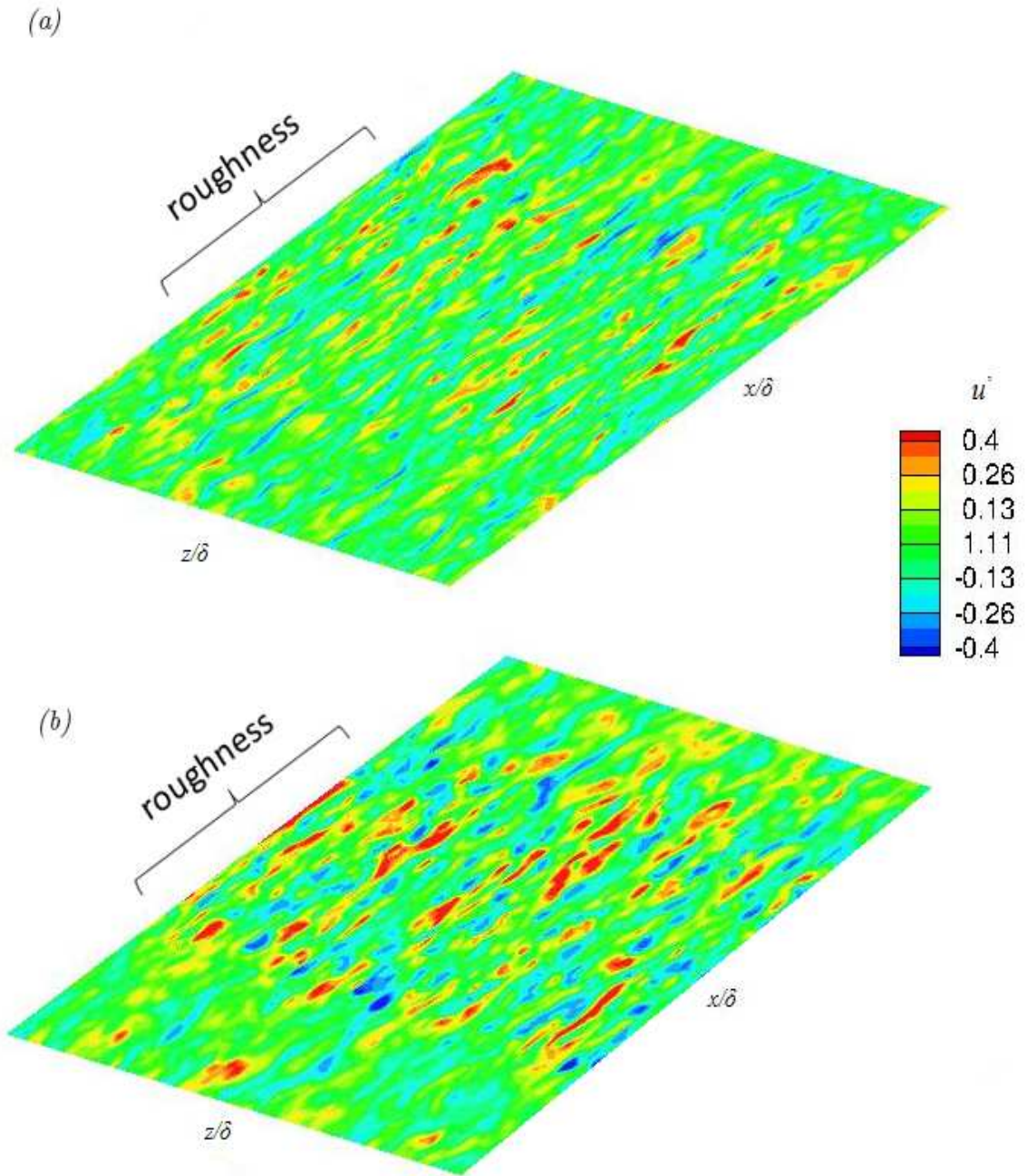


Fig. 6.49 - Contours of streamwise velocity fluctuations  $u'$  for (a) case 2P2 and (b) case 2P4 in the plane  $(y - d)^+ = 10 - 20$ .



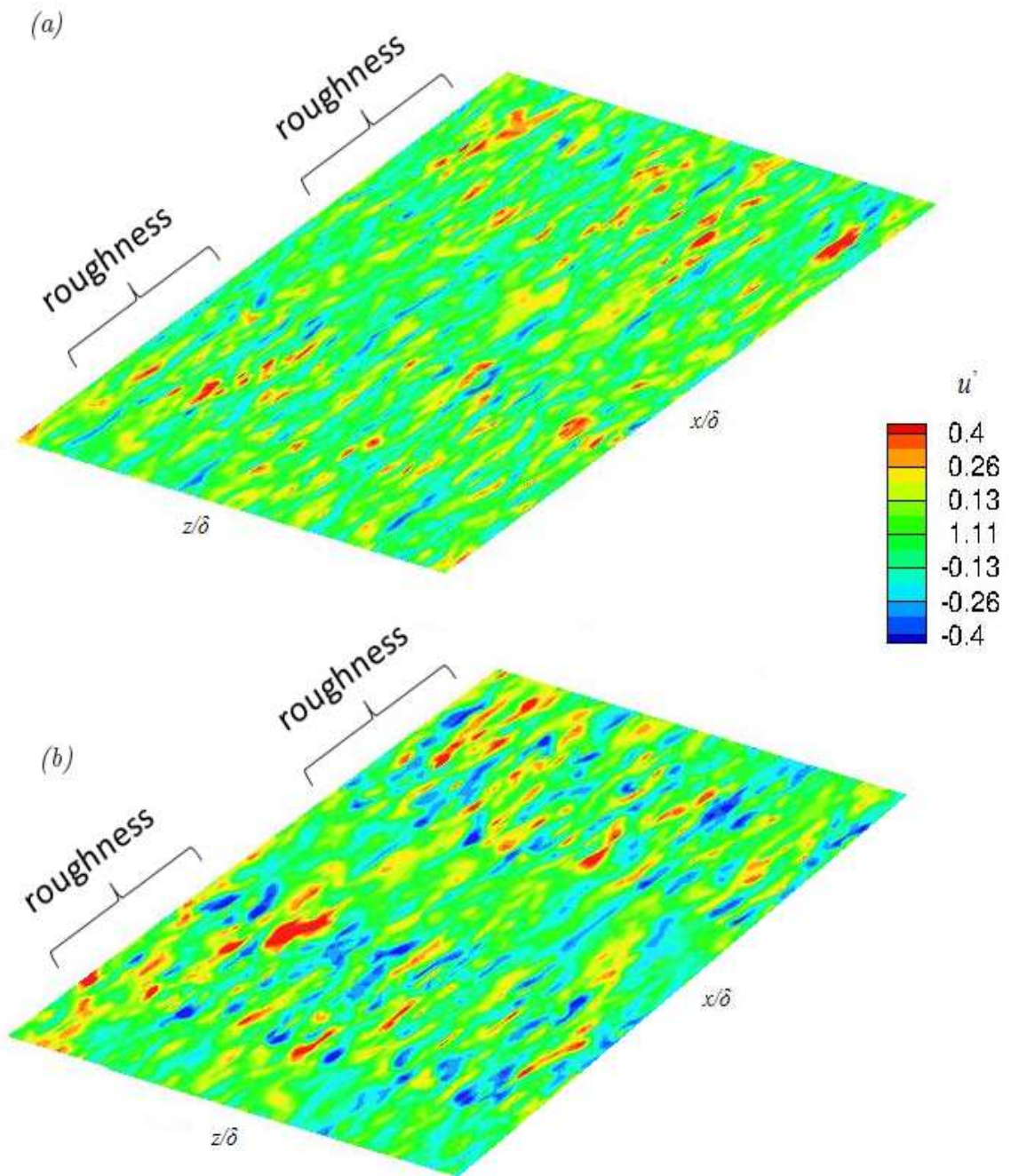


Fig. 6.50 - Contours of streamwise velocity fluctuations  $u'$  for (a) case 4P2 and (b) case 4P4 in the plane  $(y - d)^+ = 10 - 20$ .

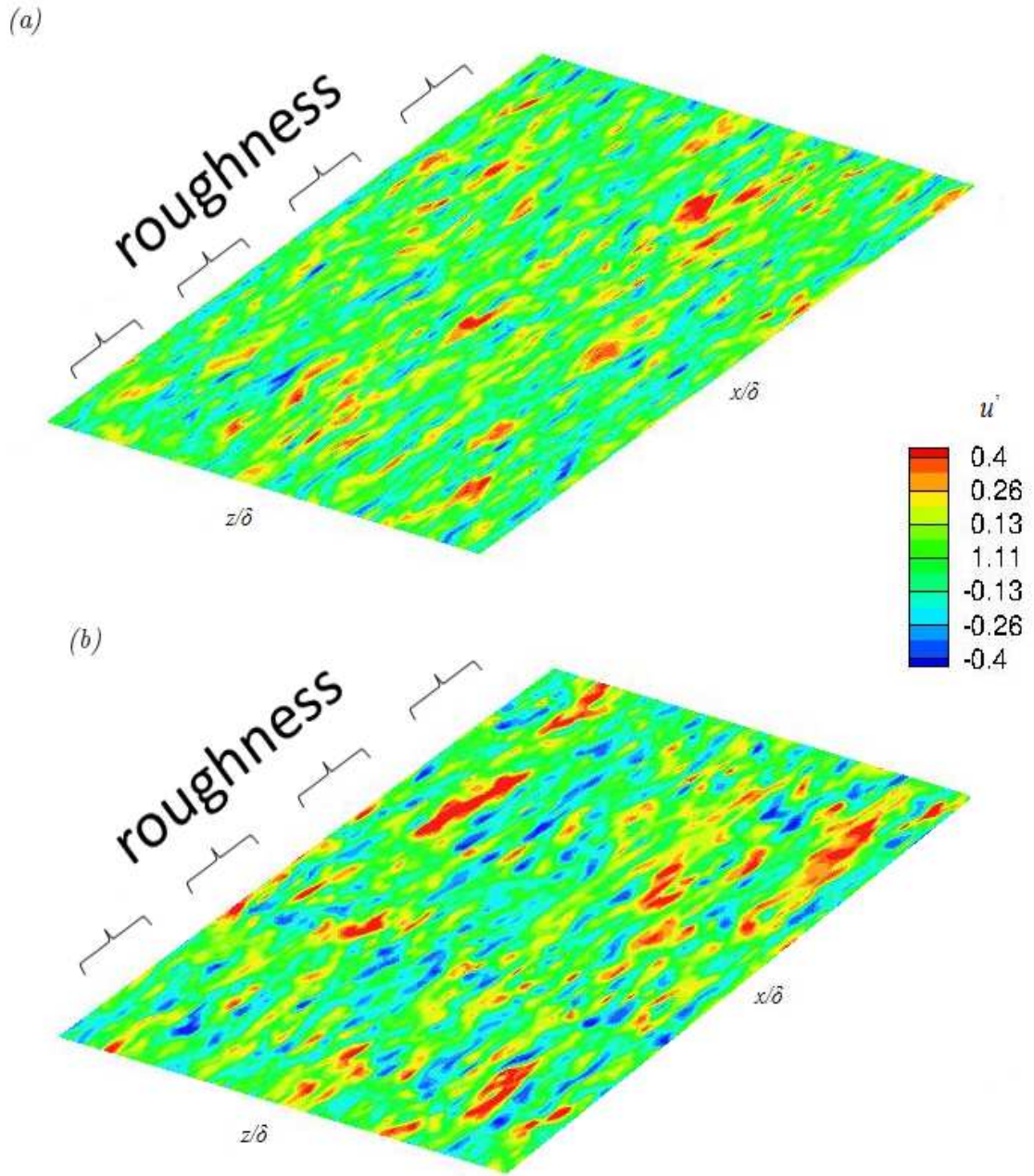


Fig. 6.51 - Contours of streamwise velocity fluctuations  $u'$  for (a) case 8P2 and (b) case 8P4 in the plane  $(y - d)^+ = 10 - 20$ .

### 6.7.1 The Q-criterion

Turbulent structures can be visualized with the so called Q criterion. The easier way to visualize turbulent structures is looking for high vorticity modulus  $\omega$ : it's a possible candidate for coherent-vortex identification, especially in free shear flows. For instance, Comte et al. (1998) extensively discussed the dynamics of streamwise vortices in a mixing layer on the basis of  $\omega$ -isosurfaces. In the presence of a wall, however, like our study, the

mean shear created by the no-slip condition is usually significantly higher than the typical vortical intensity of the near-wall vortices. A more sophisticated criterion is therefore required to distinguish vortices from internal shear layers in those types of flow.

A fluid parcel winding around a vortex needs to be (in a frame moving with the parcel) in approximate balance between centrifugal and (static) pressure-gradient effects, according to the following Euler equation:

$$\frac{\partial u}{\partial t} + \omega \times u = -\frac{1}{\rho} \nabla P \quad (6.10)$$

If, as a condition, coherent vortices should approximately keep their shape during a time  $T_c$  far enough in front of the local turnover time  $\omega^{-1}$ , then, in a frame moving with a coherent vortex and supposed locally to be Galilean, the ratio of the second to the first terms on the left-hand side of (6.10) is of the order of  $T_c \omega$ . Thus the equation reduces to the cyclostrophic balance:

$$\omega \times u = -\frac{1}{\rho} \nabla P \quad (6.11)$$

Under the assumptions implied by (6.11), the dynamic pressure should decrease inside a vortex tube in order to counterbalance the centrifugal effects. Isosurfaces of pressure have also been used by Comte et al (1998), and Robinson's (1991) investigation of coherent structures in a turbulent boundary layer suggests the superiority of pressure as a vortex eduction criterion rather than the vorticity modulus. However, the threshold to be used for proper isopressure surfaces strongly depends on the pressure surrounding the vortical structure. In regions of high concentrations of vortices, this criterion may fail to capture the details of the vortical organization.

The criterion which is here presented study shares some properties with both the vorticity and the pressure criterion. The Q-criterion was named after the second invariant of velocity gradient tensor  $\nabla u$  by Hunt et al (1998). The second invariant Q is:

$$Q = \frac{1}{2} (\Omega_{ij} \Omega_{ij} - S_{ij} S_{ij}) \quad (6.12)$$

where  $\Omega_{ij} = (u_{i,j} - u_{j,i})/2$  and  $S_{ij} = (u_{i,j} + u_{j,i})/2$  are respectively the antisymmetric and the symmetric components of  $\nabla u$ . In other words, Q is the balance between the rotation rate  $\Omega^2 = \Omega_{ij} \Omega_{ij}$  and the strain rate  $S^2 = S_{ij} S_{ij}$ . The implication of the latter observation is fairly straightforward: positive Q isosurfaces isolate areas where the strength of rotation overcomes the strain, thus making those surfaces eligible as vortex envelopes. Further support can be found by recasting (6.12) in a form which relates to the vorticity modulus:

$$Q = \frac{1}{4} (\omega^2 - 2S_{ij} S_{ij}) \quad (6.13)$$

Since vorticity should increase as the centre of the vortex is approached, Q can be expected to remain positive in the core of the vortex. This speculation, which arises from good

sense, can be proven providing a few approximations and subsequently linked to pressure lows. One should be reminded that  $Q$  is equal to half the Laplacian of pressure:

$$Q = \frac{1}{2} \left( \frac{1}{2} \omega^2 - S_{ij} S_{ij} \right) = -\frac{1}{2} \left( S_{ij} + \frac{1}{2} \varepsilon_{ijk} \omega_k \right) \left( S_{ij} + \frac{1}{2} \varepsilon_{ijk} \omega_k \right) =$$

$$-\frac{1}{2} u_{i,j} u_{i,j} = -\frac{1}{2} \partial_i [u_j u_{i,j}] = -\frac{1}{2} \partial_i \partial_j [u_i u_j] = \frac{1}{2\rho} \nabla^2 p \quad (6.14)$$

According to the maximum principle, the pressure maximum occurs only on the boundary if  $Q$  is strictly positive and the pressure minimum occurs only on the boundary if  $Q < 0$ . As stated by Jeong and Hussain (1995), there is no necessary implication for the pressure to reach a minimum within a region of positive  $Q$ . Although it has been suggested that a minimum of pressure might not be appropriate within an agglomeration of vortices, one should check the correspondence of the pressure criterion with the  $Q$  criterion for an isolated vortex tube which contains a pressure low. However, the  $Q$  criterion ( $Q > 0$ ) is a necessary condition for the existence of a thin low-pressure tube.

The isosurfaces of the second invariant of the velocity tensor  $Q$  shown in figures 6.52 - 6.54 help to explain some of the phenomena observed. While in the smooth case the isosurfaces are few, in the rough cases we observe a nearly homogeneous distribution of eddies. These eddies are generated by the wakes of the roughness elements, and are essentially locked to the roughness element. They may increase flow mixing, and play a role in the break-up of the streaks that would otherwise be stabilized in a smooth case. This happens because the roughness-generated eddies are large enough to reach the layer where the majority of the energy is generated, so they disturb the stabilized structures.



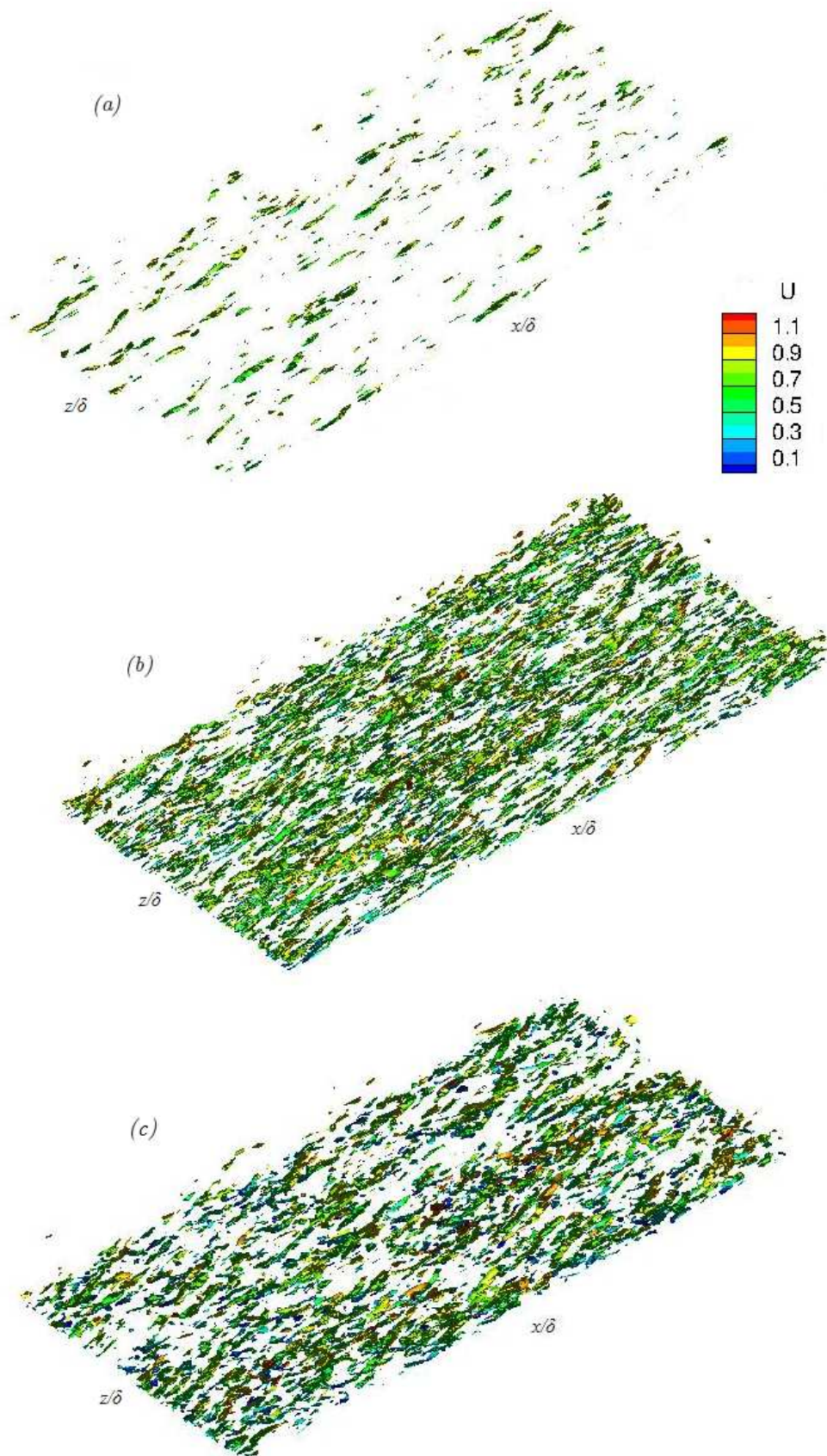


Fig. 6.52 - Isosurfaces of  $Q$  ( $Q = 10$ ), coloured by  $U$ , in cases S (a), R2 (b), and R4 (c).

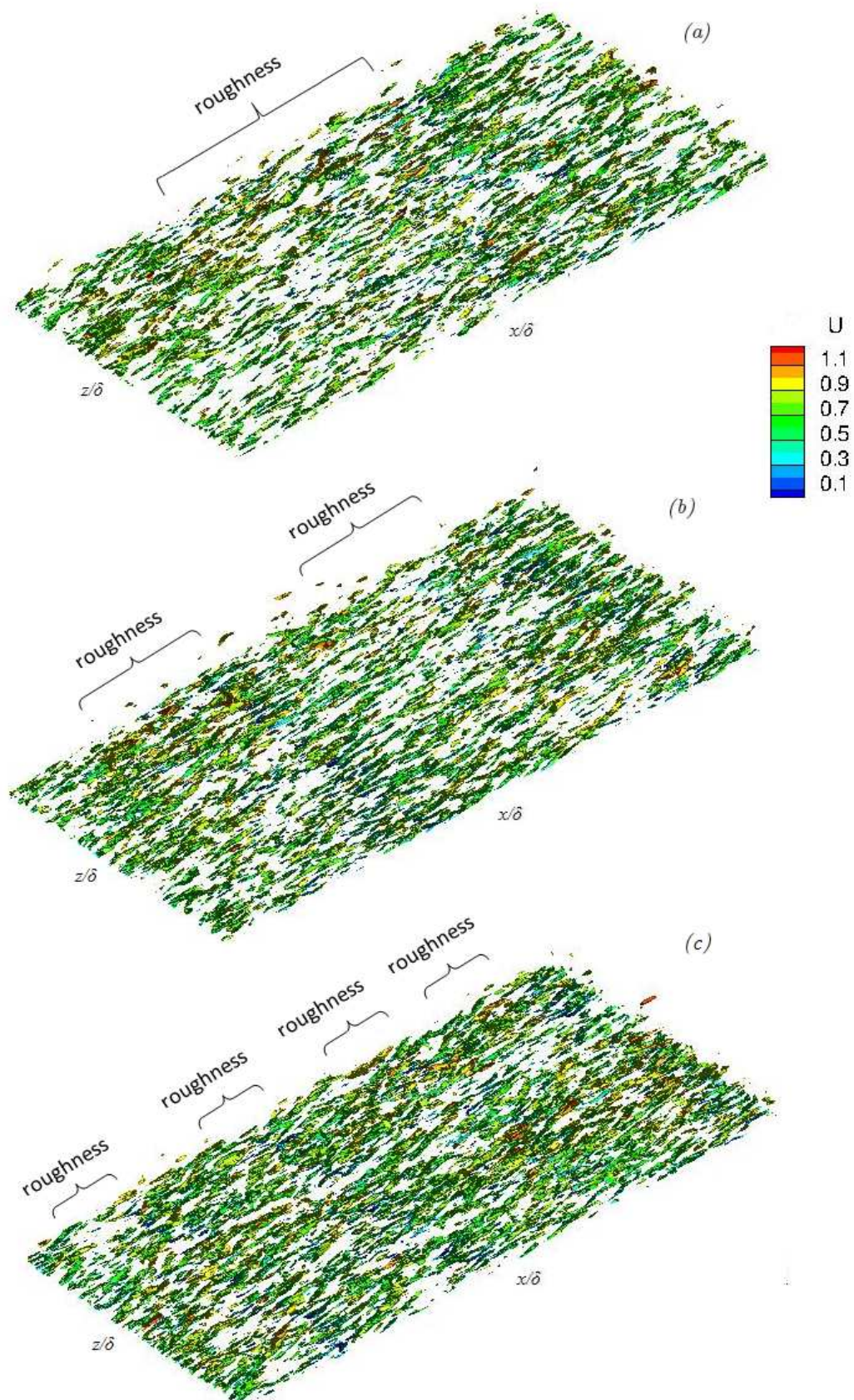


Fig. 6.53 - Isosurfaces of  $Q$  ( $Q = 10$ ), coloured by  $U$ , in cases 2P2 (a), 4P2 (b), and 8P2 (c).



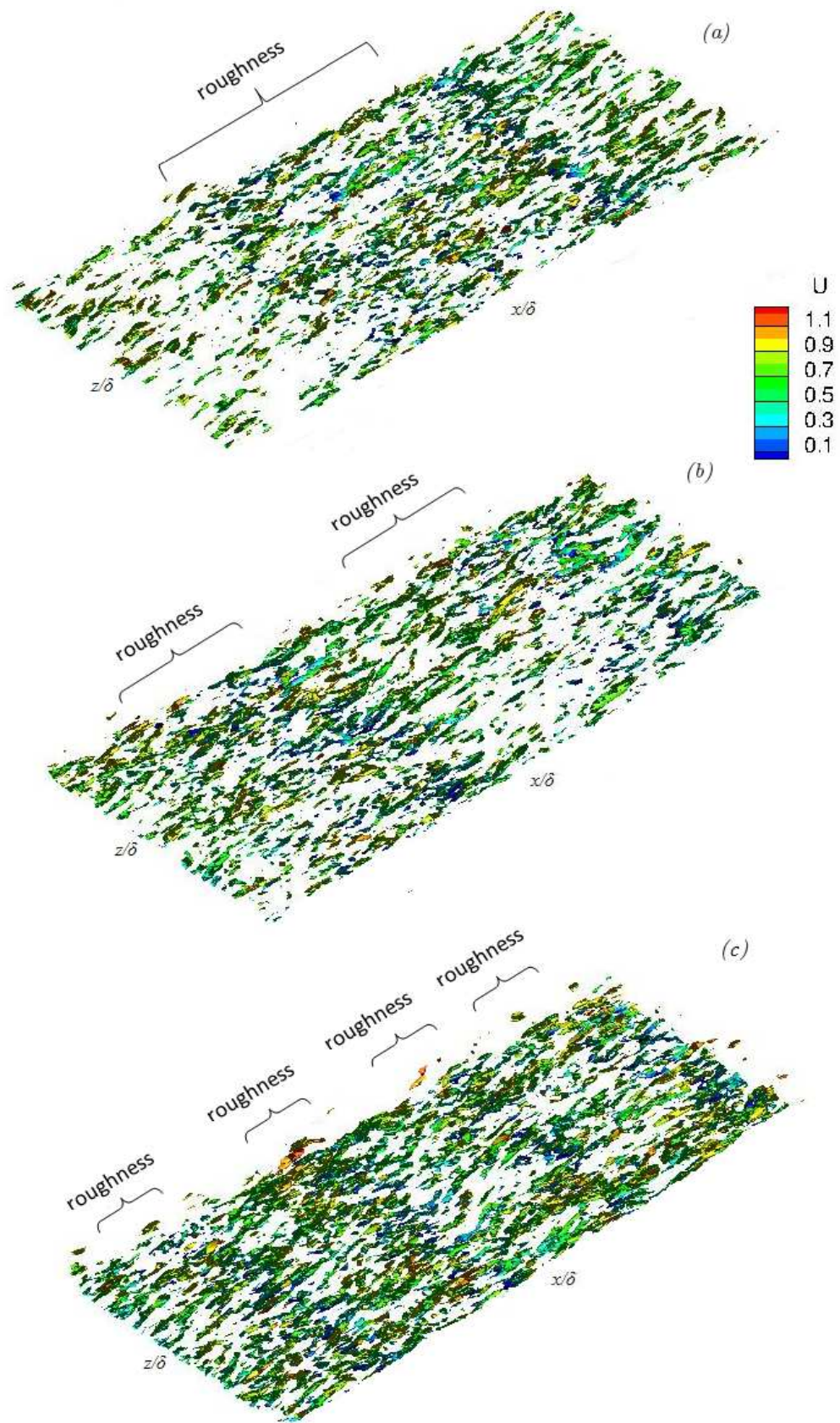


Fig. 6.54 - Isosurfaces of  $Q$  ( $Q = 10$ ), coloured by  $U$ , in cases 2P4 (a), 4P4 (b), and 8P4 (c).

## 7. Conclusions

We carried out large-eddy simulations of open channel flows over smooth and rough walls. Parameters studied include the roughness height ( $h$ ), the dimension and geometry of the smooth and rough patches, and the Reynolds number based on the friction velocity ( $Re_\tau$ ). A sand-grain roughness model (Scotti, 2006) was used, with the no-slip boundary conditions on the solid-fluid interface imposed with an immersed boundary method based on the volume of fluid.

First of all, we presented and discussed the theory of turbulent channel flows, at first for a regular smooth wall, and then introducing the roughness and analyzing its effects on the flow. We summarized the current knowledge on this matter, putting together, within a single framework, laboratory and atmospheric rough-wall studies.

After that, we presented the problem formulation, and explained the numerical method used to solve the flow. This model was, then, validated: the spatial and temporal accuracies of the immersed boundary method were studied with two test-cases: a two-dimensional open channel at an angle with respect to the grid, and flows over a stationary cylinder at  $Re = 20$  based on the uniform inflow velocity and the cylinder diameter. Also, simulations on equilibrium rough-wall open-channel flows were carried out, giving results that match the reference DNS results in the mean flow (in terms of the mean velocity profile, the roughness function), and Reynolds normal stresses. The calculation of zero-plane displacement  $d$  matched Scotti's results (2006), although  $d/l$  was found to be very sensitive to insufficient statistical sampling, as shown by the scatter of the data. A requirement on the LES grid resolution was given to resolve the forcing exerted by the roughness for equilibrium turbulent flows. It was verified that the current method with such grid resolution resolves well the flow for the smooth-wall and rough-wall open channel from the comparison with previous DNS and experimental results.

After describing the parameters and the procedure used to obtain the rough patches, results of the simulations were presented. From the streamwise development of the wall shear stress  $\tau_w$  and the friction coefficient  $C_f$  we noticed large magnitude fluctuations above the roughness, due to a problem of insufficient sampling: even if the ellipsoids, generated with Scotti's method, are randomly oriented, there are some favored structures and locations; this phenomenon can be reduced increasing the spanwise domain or filtering the signal with wavelet transform, which allows us to analyze according to scale and, thus, to remove only the highest wavenumbers. Comparing with  $\tau_w$  obtained from the assumption of the log law (the standard approach to analyze velocity profiles in boundary layers over rough surfaces, based on an a priori assumption) we saw two different results between completely rough cases and patch cases: for rough cases even if  $\tau_w$  from the log law can't capture fluctuations due to local roughness, the mean value of the two functions is very similar, with a difference less than 5%, letting us to say that the log law is valid through all the domain and the procedure we used to obtain  $\tau_w$  from momentum gives reasonable result. For patch cases, instead, in the smooth-rough transition and rough-smooth transition the two functions behave quite different:  $\tau_w$  from the log law can't capture the local variation of flow quantities close to the wall, where, for example, the pressure gradient increases abruptly when the flow runs into roughness, making  $\tau_w$  from momentum increase as well. Moreover, when a rough patch ends, the flow comes across an adverse pressure gradient (APG) and, due to the relatively low Reynolds number and high roughness height, it



separates creating a recirculation region ( $U < 0$ ), which leads also to local negative values of  $\tau_w$ .

From smooth and completely rough mean velocity profiles we saw that, under inner scaling, profiles are similar in the outer layer, except for an offset depending on the roughness height. Furthermore, the log law is respected in all the cases. Also the velocity profiles (with outer scaling) shifted by the virtual origin  $d$  match well the smooth and rough wall profiles in the outer layer under the same equilibrium or non-equilibrium state. Studying mean velocity profiles for the patch cases at different  $x$  locations, we observed the influence of the number of patches: when  $h^+ = 20$  profiles for 2, 4 and 8 patches agree very well over the smooth, rough and transition domains; the situation is different for  $h^+ = 40$  cases: here we noticed that, only above smooth regions, the 8 patch case mean velocity profile is lower than the corresponding 2 and 4 patch cases within the buffer layer; the influence of rough patch frequency more significantly affects the ability of the flow to adapt from rough to smooth than from smooth to rough, as their agreement is respected elsewhere. Hence, under the present conditions and only for high roughness height, the critical number of patches is between 4 and 8, since for 8 patches the smooth and rough regions change too frequently for the flow to reach the smooth equilibrium status.

Close to the wall, the presence of roughness increases the Reynolds stresses and creates inner peaks in the Reynolds-stress profiles. For higher  $h$ , the magnitude of such increase is higher, and this peak moves towards the overlap region, until it merges with the outer peak of the Reynolds stress profile, indicating that the turbulence generation mechanism is noticeably altered by the roughness, and the near-wall roughness-induced active turbulence motions meet the inactive motions farther away from the wall. For a low value of  $h$ , however, the region of increased Reynolds stress due to the roughness is well separated from the outer peak. In general, roughness tends to make the Reynolds stresses more isotropic, consistent with experimental results obtained in quasi-equilibrium flows (Cal et al., 2009). When patch cases are plotted, we noticed that the frequently shift between rough and smooth patches tended to increase Reynolds stresses over smooth regions, in particular  $|\langle uv \rangle|$ , probably due to the presence of separation regions already observed in those areas.

The visualizations of isosurfaces of the second invariant of the velocity tensor  $Q$  helped to explain some of the phenomena observed: while in the smooth case the isosurfaces are few, in the rough cases we observe a nearly homogeneous distribution of eddies; these eddies are generated by the wakes of the roughness elements, and are essentially locked to the roughness element. They may increase flow mixing, and play a role in the break-up of the streaks that would otherwise be stabilized in a smooth case. This happens because the roughness-generated eddies are large enough to reach the layer where the majority of the energy is generated, so they disturb the stabilized structures.

This study shows that the roughness affects directly only the flow close to the wall: its blockage effect extends only to  $y = d$  in the mean flow; also, it increases the Reynolds stresses and decreases the Reynolds-stress anisotropy within limited region near the wall. As a result, the roughness affects significantly the inner-layer quantities like  $\tau_w$  and  $C_f$  but the outer layer quantities are not sensitive to the variation of the surface condition.

## Bibliography

- Albertson, J. D., and M. B. Parlange (1999b), Surface length-scales and shear stress: Implications for land-atmosphere interaction over complex terrain. *Water Resour. Res.* 35(7), 2121–2132.
- Aupoix, B. & Spalart, P. R. 2003 Extensions of the Spalart–Allmaras turbulence model to account for wall roughness. *Int. J. Heat Fluid Flow* 24, 454–462.
- Balaras, E. 2004 Modeling complex boundaries using an external force field on fixed cartesian grids in large-eddy simulations. *Comput. Fluids* 33, 375–404.
- Balaras, E. 1995 Finite difference computations of high Reynolds-number flows using the dynamic subgrid-scale model. *Theor. Comput. Fluid Dyn.* 7, 207.
- Bandyopadhyay, P. R. 1987 Rough-wall turbulent boundary layers in the transition regime. *J. Fluid Mech.* 180, 231–66.
- Bhaganagar, K., Coleman, G. N. & Kim, J. 2007 Effect of roughness on pressure fluctuations in a turbulent channel flow. *Phys. Fluids* 19, 028103.
- Bhaganagar, K., Kim, J. & Coleman, G. N. 2004 Effect of roughness on wall-bounded turbulence. *Flow, Turb. Combust.* 72, 463–492.
- Blackwelder, R. F. & Kovasznay, L. S. G. 1972 Large-scale motion of a turbulent boundary layer during relaminarization. *J. Fluid Mech.* 53 (01), 61–83.
- Bou-Zeid, E., Meneveau, C., Parlange, M. B. 2004 Large-eddy simulation of neutral atmospheric boundary layer flow over heterogeneous surfaces: blending height and effective surface roughness. *Water Resour. Res.* 40, W02505.
- Bradshaw, P. 2000. A note on critical roughness height and transitional roughness. *Phys. Fluids* 6, 1611–14.
- Chang, Y., Scotti, A. 2003 A numerical study of entrainment and suspension of sediments into a turbulent flow over ripples. *J. Turbul.* 4.
- Chen, H., Castro, I. P. 2002 Near-wall flow over urban-like roughness. *Boundary-layer Meteorol.* 104, 229–59.
- Choi, H., Moin, P., Kim, J. 1994 Active turbulence control and drag reduction in wall-bounded flows. *J. Fluid Mech.* 262, 75–110.
- Chorin, A. J. 1968 Numerical solution of Navier-Stokes equations. *Math. Comput.* 22 (104), 745–762.

- Chu, D. C., Karniadakis, G.E. 1993 A direct numerical simulation of laminar and turbulent flow over riblet-mounted surfaces. *J. Fluid Mech.* 250, 1–42.
- Colebrook, C. F. 1939 Turbulent flow in pipes with particular reference to the transition region between smooth- and rough-pipe laws. *J. Inst. Civil Eng.* 11, 133–56.
- Coutanceau, M. & Bouard, R. 1977 Experimental determination of the main features of the viscous flow in the wake of a circular cylinder in uniform translation. Part 1. Steady flow. *J. Fluid Mech.* 79 (2), 231–256.
- Dean, R. B. 1978 Reynolds number dependence of skin friction and other bulk flow variables in two-dimensional rectangular duct flow. *J. Fluids Eng.* 100, 215.
- Durbin, P. A., Medic, G., Seo, J. M., Eaton, J. K., Song, S. 2001 Rough wall modification of  $k - \varepsilon$ . *J. Fluids Eng.* 123, 16–21.
- De Prisco, G., Keating, A., Piomelli, U. & Balaras, E. 2007 Large-eddy simulation of accelerating boundary layers. *Springer Proceedings in Physics*.
- Fadlun, E. A., Verzicco, R., Orlandi, P. & Mohd-Yusof, J. 2000 Combined immersedboundary finite-difference methods for three-dimensional complex flow simulations. *J. Comput. Phys.* 161, 35–60.
- Fiedler, H. & Head, M. R. 1966 Intermittency measurements in the turbulent boundary layer. *J. Fluid Mech.* 25 (4), 719–735.
- Finnigan, J. 2000 Turbulence in plant canopies. *Annu. Rev. Fluid Mech.* 32, 519–71.
- Flack, K. A., Schultz, M. P. & Connelly, J. S. 2007 Examination of a critical roughness height for outer layer similarity. *Phys. Fluids* 19, 095104.
- Flack, K. A., Schultz, M. P. & Shapiro, T. A. 2005 Experimental support for Townsend's Reynolds number similarity hypothesis on rough walls. *Phys. Fluids* 17, 035102.
- Garratt, J. R. 1990 The internal boundary layer - A review. *Boundary Layer Meteorol.* 50, 171–203.
- Germano, M., Piomelli, U., Moin, P. & Cabot, W. H., 1991 A dynamic subgrid-scale eddy viscosity model. *J. Comp. Phys.* 161, 35-60.
- Goldstein, D., Handler, R. & Sirovich, L. 1993 Modeling a no-slip flow boundary with an external force field. *J. Comput. Phys.* 105, 354–366.
- Goode, K., Belcher, E. 1999 On the parameterization of the effective roughness length for momentum transfer over heterogeneous terrain. *Water Resources Research* 40, 1-18.

- Grass, A. J. 1971 Structural features of turbulent flow over smooth and rough boundaries. *J. Fluid Mech.* 50 (2), 233–255.
- Ham, F. E., Lien, F. S. & Strong, A. B. 2002 A fully conservative second-order finite difference scheme for incompressible flow on nonuniform grids. *J. Comput. Phys.* 177, 117–133.
- Hirt, C. W. & Nichols, B. D. 1981 Volume of fluid (vof) method for the dynamics of free boundaries. *J. Comput. Phys.* 39, 201–225.
- Ikeda, T. & Durbin, P. A. 2007 Direct simulations of a rough-wall channel flow. *J. Fluid Mech.* 571, 235–263.
- Jackson, P. S. 1981 On the displacement height in the logarithmic velocity profile. *J. Fluid Mech.* 111, 15–25.
- Jiménez, J. 2004 Turbulent flows over rough walls. *Annu. Rev. Fluid Mech.* 36, 173–96.
- Jiménez, J., Uhlmann, M., Pinelli, A., Kawahara, G. 2001 Turbulent shear flow over active and passive porous surfaces. *J. Fluid Mech.* 442, 89–117.
- Johnson, T. A., Patel, V. C. 1999 Flow past a sphere up to a Reynolds number of 300. *J. Fluid Mech.*, 285, 69–94.
- Jones, W. P. & Launder, B. E. 1972 Some properties of sink-flow turbulent boundary layers. *J. Fluid Mech.* 56 (02), 337–351.
- Kim, J. & Moin, P. 1985 Application of a fractional step method to incompressible Navier-Stokes equations. *J. Comput. Phys.* 59, 308–323.
- Kotey, N. A., Bergstrom, D. J., Tachie, M. F. 2003 Power laws for rough wall turbulent boundary layers. *Physics of Fluids*, 15: 1396–1404.
- Krogstad, P.-A. 1991 Modification of the van Driest damping function to include the effects of surface roughness. *AIAA J.* 29 (6), 888–894.
- Krogstad, P.-A. & Antonia, R. A. 1999 Surface roughness effects in turbulent boundary layers. *Exp. Fluids* 27, 450–60.
- Krogstad, P.-A., Antonia, R. A. & Browne, L. W. B. 1992 Comparison between rough and smooth-wall turbulent boundary layers. *J. Fluid Mech.* 245, 599–617.
- Kunkel, G. J., Allen, J. J. & Smits, A. J. 2007 Further support for Townsend's Reynolds number similarity hypothesis in high Reynolds number rough-wall pipe flow. *Phys. Fluids* 19, 055109.
- Launder, B. E. 1964 Laminarization of the turbulent boundary layer by acceleration. *M.I.T. Gas Turbines Lab. Rep. No. 77*.

- Lee, J. & Paynter, G. C. 1996 Modified Spalart-Allmaras one-equation turbulence model for rough wall boundary layers. *J. of Propulsion* 4, 809-812.
- Lee, J. H., Sung, H. J. & Krogstad, P.- A 2011 Direct numerical simulation of the turbulent boundary layer over a cube-roughened wall. *Bull. Am. Phys. Soc.* 47(10), 111.
- Lee, S.-H. & Sung, H. J. 2007 Direct numerical simulation of the turbulent boundary layer over a rod-roughened wall. *J. Fluid Mech.* 584, 125–146.
- Leonard, A. 1974 Energy cascade in large-eddy simulations of turbulent fluid flows. *Adv. Geophys.* 18A, 237–248.
- Leonardi, S., Orlandi, P., Smalley, R. J., Djenidi, L., Antonia, R. A. 2003 Direct numerical simulations of turbulent channel flow with transverse square bars on one wall. *Journal of Fluid Mechanics* 491, 229-238
- Ligrani, P. M., Moffat, R. J. Structure of transitionally rough and fully rough turbulent boundary layers. *J. Fluid Mech.* 162, 69–98.
- Lund, T. S., Wu, X. & Squires, K. D. 1998 Generation of inflow data for spatially-developing boundary layer simulations. *J. Comput. Phys.* 140, 233–258.
- Marusic, I., Monty, J. P., Hutchins, N. and Smits, A. J. 2010 Spatial resolution and Reynolds number effects in wall-bounded turbulence. *Engineering Turbulence, Modelling and Measurements*.
- Meneveau, C., Lund, T. S. & Cabot, W. H. 1996 A Lagrangian dynamic subgrid-scale model of turbulence. *J. Fluid Mech.* 319, 353–385.
- Miyake, Y., Tsujimoto, K., Agata, Y. 2000 A DNS of a turbulent flow in a rough-wall channel using roughness elements models. *JSME Int. J., Ser. B* 43, 233
- Mukund, R., Viswanath, P. R., Prabhu, A. & Crouch, J. D. 2006 Relaminarization in highly favourable pressure gradients on a convex surface. *J. Fluid Mech.* 566, 97–115.
- Nakagawa, S., Hanratty, T. J. 2001 Particle image velocimetry measurements of flow over a wavy wall. *Phys. Fluids* 13, 3504–7.
- Narasimha, R. & Sreenivasan, K. R. 1973 Relaminarization in highly accelerated turbulent boundary layers. *J. Fluid Mech.* 61, 417–447.
- Nozawa, K., Tamura, T., Cao, S. 2002 LES study on streamwise spatial variation of turbulence structures in rough-wall boundary layer. *Bull. Am. Phys. Soc.* 47(10), 55–56.
- Olsen, R. B., Stokseth, S. 1995 Three-dimensional numerical modelling of water flow in a river with large bed roughness. *J. Hydraul. Res.* 33, 571.

- Orlandi, P., Leonardi, S. 2008 Direct numerical simulation of three-dimensional turbulent rough channels: parameterization and flow physics. *J. Fluid Mech.* 606, 399–415.
- Orlanski, I. 1976 A simple boundary condition for unbounded hyperbolic flows. *J. Comput. Phys.* 21, 251–269.
- Ovchinnikov, V., Piomelli, U. & Choudhari, M. M. 2004 Inflow conditions for numerical simulations of bypass transition. *AIAA Paper* 2004-0491.
- Peskin, C. S. 1972 Flow patterns around heart valves: a numerical method. *J. Comput. Phys.* 10, 252–271.
- Perry, A. E., Schofield, W. H., Joubert, P. 1969 Rough wall turbulent boundary layers. *J. Fluid Mech.* 37, 383–413
- Piomelli, U., Balaras, E. & Pascarelli, A. 2000 Turbulent structures in accelerating boundary layers. *J. Turbul.* 1 (1), 1–16.
- Piomelli, U. & Scalo, C. 2010 Subgrid-scale modelling in relaminarizing flows. *Fluid Dyn. Res.* 42, 045510.
- Piomelli, U. 1999 Large-eddy simulation: Achievements and challenges. *Progress in Aerospace Sciences* 35, 335–362.
- Piomelli, U. 1993 High Reynolds number calculations using the dynamic subgrid-scale stress model. *Phys. Fluids A* 5 (6), 1484.
- Piomelli, U., Lawrence Ong, B., Wallace, C. J., 1993 Reynolds stress and vorticity in turbulent wall flows. *Phys. Fluids A* 1, 609–611.
- Piomelli, U., Cabot, W. H., Moin, P., Lee, S. 1991 Subgrid-scale backscatter in turbulent and transitional flows. *Phys. Fluids A* 3, 1766–1771.
- Piomelli, U., Ferziger, J., Moin, P. 1989 New approximate boundary conditions for large eddy simulations of wall-bounded flows. *Phys. Fluids.* 1, 1061–1068.
- Piomelli, U., Moin, P., Ferziger, J. H., 1988 Model consistency in large eddy simulation of turbulent channel flows. *Phys. Fluids A* 31, 1884-1891.
- Poggi, D., Porporato, A., Ridolfi, L. 2003 Analysis of the small-scale structure of turbulence on smooth and rough walls. *Phys. Fluids* 15, 35.
- Pope, S. B. 2005 Turbulent Flows. *Cambridge University Press*.
- Porte'-Agel, F., C. Meneveau, and M. B. Parlange 2000 A scale-dependent dynamic model for large-eddy simulation: Application to a neutral atmospheric boundary layer. *J. Fluid Mech.* 415, 261– 284.

- Raupach, M. R., 1981 Conditional statistics of reynolds stress in rough-wall and smooth-wall turbulent boundary layers. *J. Fluid Mech.* 108, 363–82.
- Raupach, M. R., Antonia, R. A. & S., Rajagopalan 1991 Rough-wall boundary layers. *Appl. Mech. Rev.* 44, 1–25.
- Rotta, J. C. 1962 Turbulent boundary layers in incompressible flow. *Prog. Aero. Sci.* 2 (1).
- Scaggs, W. F., Taylor, R.P., Coleman, H. W. 1988 Measurement and prediction of rough wall effects on friction factor - Uniform roughness. *J. Fluid Eng.* 110, 385–91.
- Schultz, M. P. & Flack, K. A. 2005 Outer layer similarity in fully rough turbulent boundary layers. *Exp. Fluids* 38 (3), 328–340.
- Schultz, M. P. & Flack, K. A. 2007 The rough-wall turbulent boundary layer from the hydraulically smooth to the fully rough regime. *J. Fluid Mech.* 580, 381–405.
- Scotti, A. 2006 Direct numerical simulation of turbulent channel flows with boundary roughened with virtual sandpaper. *Phys. Fluids* 18, 031701.
- Simpson, R. L. 1973 A generalized correlation of roughness density effects on the turbulent boundary layer. *AIAA J.* 11, 242–44.
- Smagorinsky, J. 1963 General circulation experiments with the primitive equations. *Mon. Weather Rev.* 91, 99.
- Spalart, P.R. 1986 Numerical study of sink-flow boundary layers. *J. Fluid Mech.* 172, 307–328.
- Sreenivasan, K. R. 1982 Laminar, relaminarizing and retransitional flows. *Acta Mechanica* 44, 1–48.
- Tachie, M. F., Bergstrom, D. J. & Balachandar, R. 2003 Roughness effects in low-Re  $\theta$  open-channel turbulent boundary layers. *Exp. Fluids* 35, 338–346.
- Tachie, M. F. & Shah, M. 2008 Favorable pressure gradient turbulent flow over straight and inclined ribs on both channel walls. *Phys. Fluids* 20.
- Taira, K. & Colonius, T. 2007 The immersed boundary method: A projection approach. *J. Comput. Phys.* 225, 2118–2137.
- Tani, I. 1988 Drag reduction by riblet viewed as a roughness problem. *Proc. Jpn. Acad. B* 64, 21–24.
- Tani, I. 1987 Turbulent boundary layer development over rough surfaces. In *Perspectives in Turbulence Studies*, ed. HU Meier, P Bradshaw, 223–49. Berlin: Springer-Verlag.

- Taniguchi, Y., Evans, J. W. 1993 Some measurements of the penetration of turbulence into small cavities. *Int. J. Heat Mass Transf.* 36, 961–65.
- Tarada, F. 1990 Prediction of rough-wall boundary layers using a low reynolds number  $k-\epsilon$  model. *Int. J. Heat Fluid Flow* 11 (4), 331–345.
- Taylor, R. P., Coleman, H. W., Hodge, B. K., 1985 Prediction of turbulent rough-wall skin friction using a discrete element approach. *J. Fluid Eng.* 107, 251–57.
- Townsend, A. A., 1976 The structure of turbulent shear flows. *Cambridge, UK: Cambridge Univ. Press.* 429 pp. 2nd ed.
- Townsin, R. L. 1991 The correlation of added drag with surface roughness parameters. *In Recent Developments in Turbulence Management*, ed. K-S Choi, 181–91. *Amsterdam: Kluwer.*
- Tritton, D. J. 1959 Experiments on the flow past a circular cylinder at low reynolds numbers. *J. Fluid Mech.* 6, 547–567.
- Vanella, M., Piomelli, U. & Balaras, E. 2008 Effect of grid discontinuities in large-eddy simulation statistics and flow fields. *J. of Turbulence* 9, 1-23.
- Volino, R. J., Schultz, M. P. & Flack, K. A. 2007 Turbulence structure in rough-and smooth-wall boundary layers. *J. Fluid Mech.* 592, 263–293.
- Waigh, D. R., Kind, R. J., 1998 Improved aerodynamic characterization of a regular three-dimensional roughness. *AIAA J.* 36, 1117–19.
- Wei, T. & Willmarth, W. W. 1991 Examination of  $v$ -velocity fluctuations in a turbulent channel flow in the context of sediment transport. *J. Fluid Mech.* 223, 241–252.
- Wei, T. & Willmarth, W. W. 1989 Reynolds number effects on the structure of a turbulent channel flow. *J. Fluid Mech.* 204, 57.
- Wood, D. H., Antonia, R. A., 1975 Measurements in a turbulent boundary layer over a  $d$ -type surface roughness. *J. Appl. Mech.* 42, 591–97.